9-1-2006

Load Carrying Capacity of Steel Orthotropic Deck Panel with Trapezoidal Shaped Longitudinal Stiffeners

WanChun Jen

Ben T. Yen

Recommended Citation

Jen, WanChun and Yen, Ben T., "Load Carrying Capacity of Steel Orthotropic Deck Panel with Trapezoidal Shaped Longitudinal Stiffeners" (2006). ATLSS Reports. ATLSS report number 06-15:.
http://preserve.lehigh.edu/engr-civil-environmental-atlss-reports/82

Load Carrying Capacity of Steel Orthotropic Deck Panel with Trapezoidal Shaped Longitudinal Stiffeners

WanChun Jen, Ph.D.
jew2@lehigh.edu

Ben T. Yen, Ph.D.
bty0@lehigh.edu

ATLSS Report No. 06-15
September , 2006

ATLSS is a National Center for Engineering Research
on Advanced Technology for Large Structural Systems

117 ATLSS Drive
Bethlehem, PA 18015-4728

Phone: (610)758-3525
Fax: (610)758-5902

www.atlss.lehigh.edu
Email: inatl@lehigh.edu

ACKNOWLEDGEMENTS

The study presented in this report was supported by the Engineering Research Center for Advanced Technology for Large Structural Systems (ATLSS) through the program of Pennsylvania Infrastructure Technology Alliance (PITA). The test specimens were secured from the prototype model deck from Weidlinger Associates, Inc. and Triborough Bridge and Tunnel Authority (TBTA) of New York City for an earlier study on fatigue behavior. The support of all these organizations is highly appreciated. The assistance of Mr. Qi Ye and Mr. Guang-Nan Fanjiang of Weidinger, Inc., on the prototype model deck, is acknowledged. The advice and assistance of Dr. Wagdy G. Wassef of Modjeski and Masters, Inc. and Drs. John W Fisher, Le-Wu Lu, James M. Ricles and Alexis Ostapenko of ATLSS and the Department of Civil and Environmental Engineering, Lehigh University, is sincerely appreciated.

Many thanks are due Mr. Frank E. Stokes and the technical and administrative staff of the laboratories of ATLSS for their assistance.

TABLE OF CONTENTS

LIST OF TABLES

LIST OF FIGURES

ABSTRACT

An examination of the static strength of steel orthotropic deck panels with trapezoidal shaped longitudinal stiffeners (ribs) was conducted through experimental and analytical studies. A prototype deck was utilized for evaluating the local effects of wheel loads. Individual rib specimens were cut from the deck for beam, column and beam-column strength testing. Finite element analyses of the test specimens and of orthotropic deck panels were made. A procedure of summation of component strength for analytical prediction of static strength of ribs and deck panels was developed and verified by the finite element analysis.

Chapter 1 Introduction

1.1 Steel Orthotropic Deck System

The word “orthotropic” is derived from two words, “orthogonal” and “anisotropic”, meaning material or structural properties exhibiting differences in two directions at a right angle. The orthotropic theory of deck design and construction was developed primarily in Europe following World War II as an answer to the shortage of construction materials. The orthotropic bridge theory is the results of efforts to obtain optimum structural performance of steel materials. The concept evolved from the battledeck floor (Figure 1-1), the gridwork systems (Figure 1-2 and 1-3), and the cellular systems (Figure 1-4), in the 1930s and early 1950s.

Steel orthotropic plates as a load-carrying element have larger reserves of safety margin than one-dimensional beam members and are considered as an efficient utilization of steel material. The steel orthotropic deck has become an excellent choice for long span bridges for weight and strength.

The basic orthotropic deck system contains the deck plate, longitudinal ribs, floor beams, and main girders. The open rib (torsionally soft) and closed rib (torsionally stiff) framing system for orthotropic deck bridges are shown in Figures 1-5 and 1-6. Closed ribs provide considerable torsional rigidity and contribute to the transverse load distribution. Because the ribs participate in the primary action of the deck and the bridge system, the resulting stresses are high. Hence, the ribs are made continuous though the web of floor beams, either by welding or through slots in the web of the floor beams.

In earlier years, the buckling of orthotropic deck components or the deck panel was considered as the load carrying capacity of the deck system. The design philosophy was to make the buckling stresses of the component plates and individual ribs higher than the yield stress of the material. With the change from the yield stress based Allowable Stress Design (ASD) to the load carrying capacity based Load and Resistance Factor Design (LRFD), the load carrying capacity of the deck panels needs to be evaluation. The static strength of orthotropic deck panels is the topic of this study.

Another major concern regarding the deck system is the possible fatigue cracking of steel component details. As more orthotropic decks are used in new constructions and in replacement decks of older bridges and the number of vehicles traveling over the decks increases drastically, fatigue cracks have developed. The most vulnerable detail is the rib to floor beam / diaphragm connection. At the present, most of the studies on orthotropic decks are on the fatigue strength of components at the connections. Fatigue damage of deck components is not the topic of this study.

1.2 Literature Review

Many studies have been carried out on steel orthotropic deck systems, including elastic analysis of stiffened plates, buckling analysis of deck plate components, and strength evaluation of orthotropic deck and components.

1.2.1 Orthotropic Plate Theory

The analysis of an isotropic plate was first presented by Gehiring (1860) and Boussinesq (1879). The complete solution for isotropic plate was presented by Huber (1914). The differential equation giving the relationship between the lateral deflection and the loading of an orthotropic deck, Equation (1.1), is referred as

Huber's equation.

$$D_x \frac{\partial^4 w}{\partial x^4} + 2H \frac{\partial^4 w}{\partial x^2 \partial y^2} + D_y \frac{\partial^4 w}{\partial y^4} = p(x, y) \tag{1.1}$$

Where w is the lateral deflection of the middle surface of the plate at point (x, y) as shown in Figure 1-7. The parameters D_x, D_y and H are rigidity coefficients, and $p(x, y)$ is the load density at any point expressed as a function of the coordinate x and y.

The basic assumption proposed by Huber for estimating the overall bending deflections and bending stresses in a stiffened plate, is to replace it by an equivalent orthotropic plate of constant thickness having the same orthogonal stiffness characteristics. This is called the Method of Elastic Equivalence (MEE).

Guyon (1946) used the method to analyze a deck without torsional stiffness of the rib. Massonnet (1950) extended the method to include the torsional stiffness. This work was further developed by Morice, Little and Rowe (1956). Rowe (1962) summarized the design technique based on a series solution of the governing partial differential equation at a stage before the widespread availability of the electronic digital computer.

The governing differential equations for large deflection orthotropic plate theory are the equilibrium equation and the compatibility equation. Considering the idealized initial imperfection, boundary conditions and load application, Paik and Thayamballi (2003) solved the governing differential equations. “Collapse” was assumed to occur when the Hencky-von Mises stress on the outer surface of the orthotropic plate reached the yield stress. However, it was found that “collapse” of the panel might not always be associated with the first yield on the outer surface of the orthotropic plate. As long as it was possible to redistribute the applied loads to the boundaries by membrane action, “collapse” would occur when the most stressed boundary location yielded.

For the purpose of design, various methods have been developed:

1. The Equivalent-orthotropic slab method in the AISC manual (Wolchuk, 1963) and James F. Lincoln Electric manual (Troitsky, 1967) simulates the deck by a continuous two-dimensional slab of uniform thickness with different stiffness in the longitudinal and transverse directions. Both manuals give design charts for approximation of stresses in the equivalent plate.
2. The Equivalent grid method (Bouwkamp, 1967; Bouwkamp and Powell, 1967; Erzurumlu and Toprac, 1970; Heins and Looney, 1966, 1968) simulates the deck

by a grid of one-dimensional beams. The deck plate is assumed slit between the longitudinal ribs, which are treated as individual beams between panel points of the grid system, with the deck plate strips acting as upper flanges. The effect of the deck plate rigidity perpendicular to the ribs is disregarded. In both methods the stiffness properties of the equivalent structure must be chosen to approximate adequately the behavior of the actual deck.

3. The Method of thin-walled-beam (Vlasov, 1967) accounts for the torsional distortional effects in an elastic analysis of box girders with an orthotropic deck.
4. The Ordinary folded-plate theory (De Fries-Suene and Scordelis, 1964) makes the following assumptions in analyzing box girder with an orthotropic deck.
   (a) The membrane (in plane) stresses produced in each plate element by longitudinal bending can be calculated by elementary beam theory applied to each element.

   (b) Transverse plate bending stresses can be calculated assuming the plate elements act as one-way slabs spanning longitudinal joints. The thin-walled-beam method accounts for the effects of torsional distortions of the cross-sectional shape.

More information for design of trapezoidal shaped stiffener can be found in the *Handbook of Structural Stability* (CRCJ, 1971) and in the book by Troitsky (1976).

1.2.2 Experimental and Analytical Studies on Open Rib Deck

In the evaluation of elastic behavior and strength of orthotropic deck, the lateral torsional buckling (tripping) of stiffeners must be considered. The ribs may buckle with the deck plate in a mode of overall buckling of the deck, or the ribs may buckle first and induce distorsion of deck plate and failure of the deck. Timoshenko has given solution for buckling of compression plates with various boundary conditions. Klitchieff (1951) provided a general solution for the critical compression force of a plate stiffened with open ribs.

Tests of steel plate panels stiffened with open ribs have been conducted primarily on components or relatively small scale model panels. Horne (1976) carried out compression tests of thirty four model stiffened plates with open ribs for compression flange of box girders.

The ultimate strength testing of model deck panels with open rib and under combined axial compression and lateral load was performed by Rutledge and

Ostapenko (1969). The analytical work was on the buckling strength of an isolated beam-column consisting of an open rib and an associated width of the deck plate. No post-buckling behavior was analyzed.

Murray (1973) tested thirteen thin steel plates with flat stiffeners in axial compression, bending and the combination. A set of simple design rules was derived for the case of axial load only.

Ueda (1984) carried out a study on the buckling and ultimate strength of plates and stiffened panels under combined in-plane biaxial and shearing forces. Grondin et al (2003) investigated the stability of steel plates stiffened with T-stiffeners subjected to uniaxial compression using a single stiffener half bay finite element model. It was found that the panels suffered an abrupt drop in load carrying capacity in the post-buckling range and referred to this behavior as the interaction failure mode.

1.2.3 Experimental and Analytical Studies on Closed Rib Deck

There were only limited analytical studies on the strength of deck panels stiffened by closed ribs. Pelican-Esslinger (1957) simplified Huber's equation for approximate evaluation of global forces of an equivalent orthotropic deck. The Pelican-Esslinger method assumes that the deck system is a continuous orthotropic plate, rigidly supported by longitudinal main girders and elastically supported by the floor beams. This method is considered practical and relatively simple for design evaluation. However, the parameters expressing certain rigidities of the orthotropic deck are disregarded in the method, as the parameters are considered of little importance in design. The method does not provide information on the load carrying strength of the deck panel.

Experimental tests of closed rib deck panels were performed by Dowling (1966). The specimen was 12 feet wide and 10 feet high with six closed ribs. Tests under lateral wheel loading or combination of in-plane and lateral loading were carried out in the elastic range of behavior. The ultimate strength test in tension was carried to the yield stress. No ultimate strength test in compression has performed.

Furuta and Kitada (1988) conducted tests on one-third scale, longitudinally stiffened plates with closed or open ribs and subjected to biaxial in plane forces. A method was proposed for predicting the maximum stresses of un-stiffened plates and stiffened plates. There was no ultimate strength test for closed rib deck panel.

Uang and Chou (2002) performed testing of two one-third scale steel orthotropic bridge deck panels, one stiffened with three closed ribs and the other with four open ribs. The specimens reached yielding before local buckling occurred.

Stub column tests on closed rib orthotropic deck stiffeners were done by Chen and Yang (2001). The study checked the buckling strength of components of trapezoidal shaped stiffeners against existing specifications.

From the above brief review of literature, it is concluded that there have been numerous studies and there are current design rules with respect to the local buckling of components of trapezoidal shaped stiffening ribs of orthotropic decks. There are also many studies on the equivalent orthotropic plate for deck panels. Forces in, and the buckling of the equivalent plate can be estimated. Based on this concept of orthotropic plate, provisions have been given in design specifications to prevent overall buckling. Yet, there is very little information on the post buckling behavior of the component plates of the ribs, or of the stiffened deck panel. The ultimate or load carrying strength and behavior of these decks are not known.

1.3 Objectives and Approach

The objectives of the study, herein reported, is to evaluated the load carrying behavior and ultimate strength of steel bridge orthotropic deck panels with trapezoidal shaped stiffening ribs. The study began with experimental work. The evaluation of local effects of wheel loads on local stresses in the ribs of deck panels was first made. The flexural behavior of ribs under wheel loads was then examined, followed by the evaluation of behavior and strength of ribs tested as column and beam-column. Analysis of the column and beam-columns were conducted by following the traditional theory of component plate buckling and by finite element analysis. From the results, a procedure for estimating the ultimate load carrying capacity of ribs acting as beam-columns was developed. This procedure was extended for the estimation of deck panel strength, with confirmation by a finite element analysis.

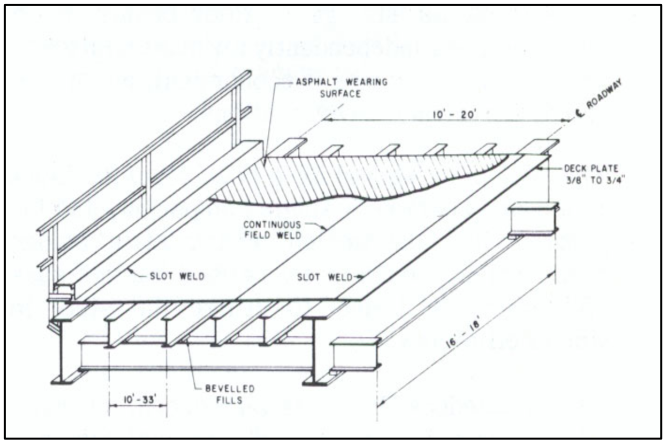

Figure 1-1 Battledeck Floor

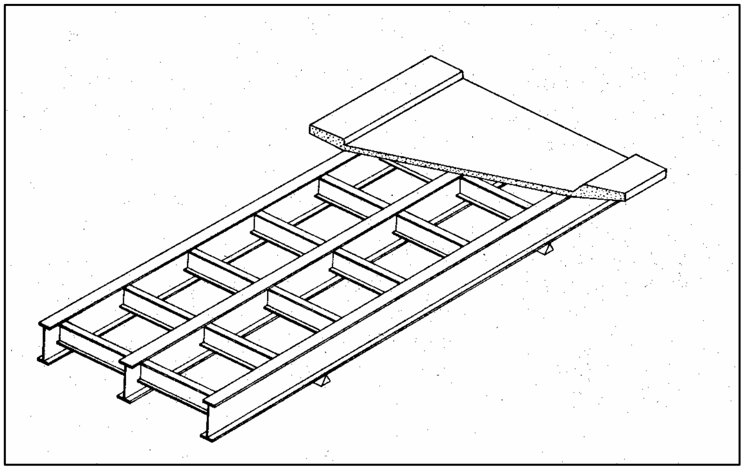

Figure 1-2 Gridworks Type Bridge

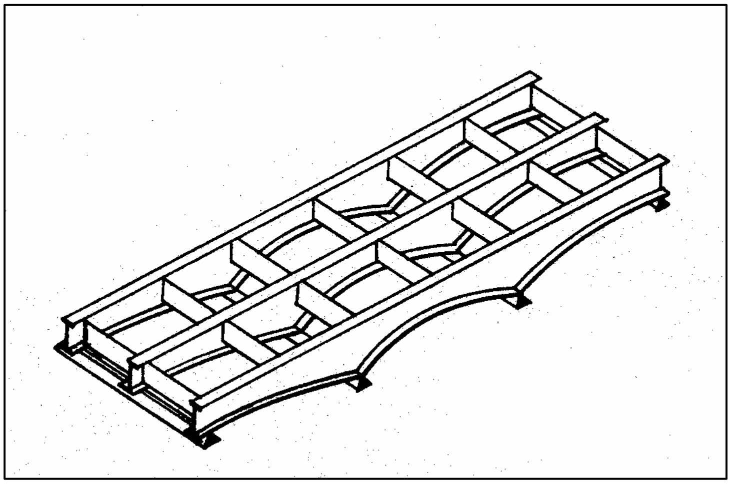

Figure 1-3 A Continuous Gridworks System

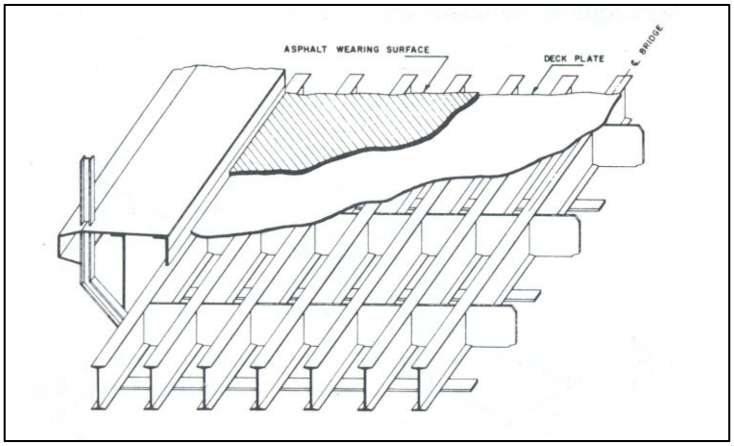

Figure 1-4 Cellular Type Bridge

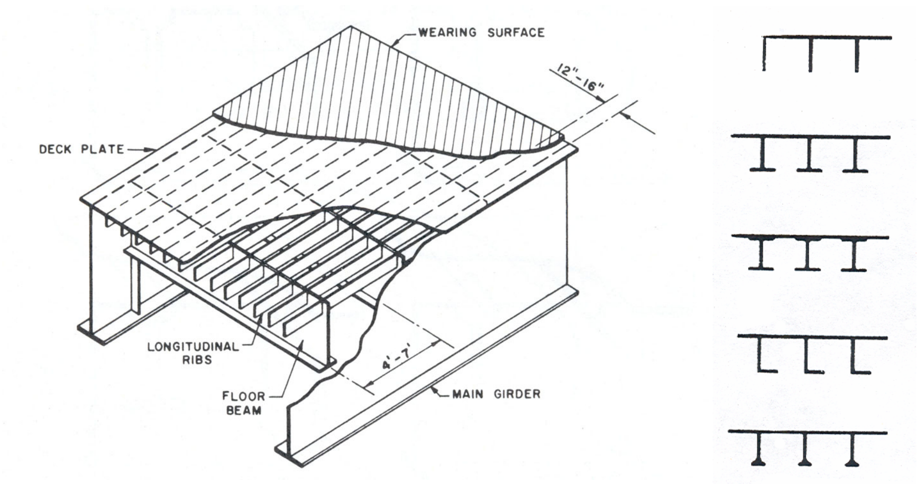

Figure 1-5 Orthotropic Deck System with Open Ribs

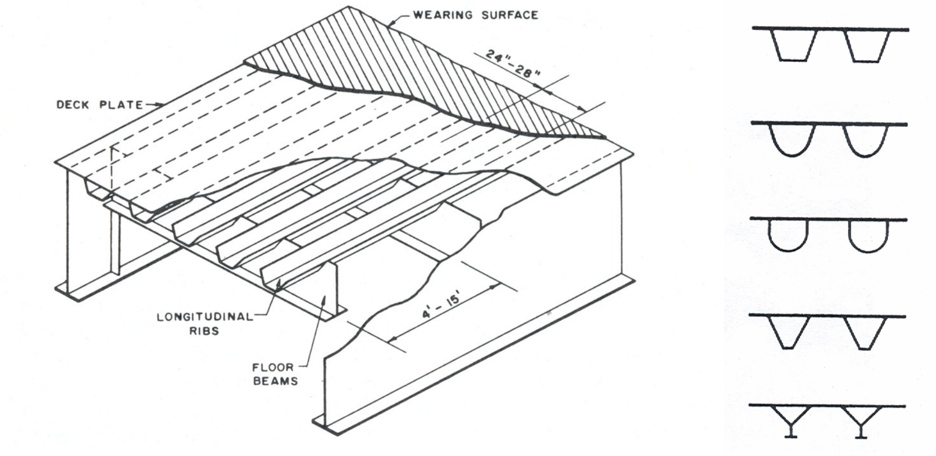

Figure 1-6 Orthotropic Deck System with Closed Ribs

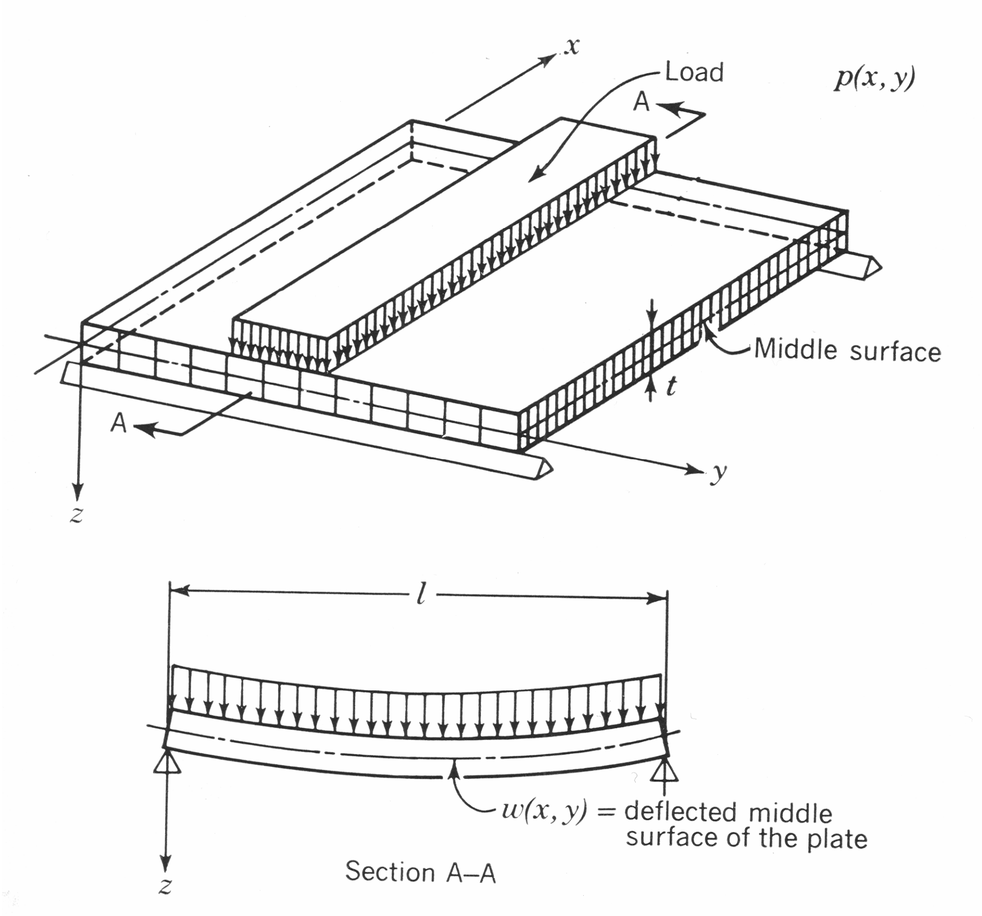

Figure 1-7 Orthotropic plate as an anisotropic system

Chapter 2 LOCAL STRESSES IN DECK COMPONENTS DUE TO VEHICULAR LOADS

2.1 Introduction

Steel orthotropic bridge deck with longitudinal, closed rib stiffeners under the deck plate serve the dual function of being the upper flange of the box girder, real or equivalent, and being the member to transfer vehicular loads to other parts of the bridges. The global stresses in these decks are primarily governed by the deck geometry, deck location relative to other parts of the bridge and by the dead weight of the bridge. The local stresses in the components of such decks are essentially produced by the vehicular loads directly on the deck. The combinations of the global and local stresses determine the safety margin against the load carrying strength of the deck components of longitudinal stiffeners and the deck plate. Stresses induced by vehicular loads are the primary subjected of many resent analytical and experimental studies for the examination of fatigue cracking at the connection between longitudinal ribs and transverse diaphragms (Connor 2001, Tsakopoulos 2002, Connor 2004, Ye 2004). The distribution of local stresses due to vehicular loads and their effects on the static strength of the deck components have not been systematically studied.

The evaluation of local stresses in deck components due to vehicular loads for examining the static strength of the deck is the topic of this chapter. Both experimental and analytical examinations have been conducted, and are presented below.

2.2 Experimental Program

The primary focus of this experimental program was to produce and document stresses in the components of a full-scale deck under various vehicular loadings. The full scale model deck of the Bronx-Whitestone Bridge (BWB) in New York City was constructed in the laboratory for fatigue testing (Tsakopoulos 2005). After the fatigue tests, two stages of static tests were executed. The first stage consisted of applying simulated wheel loads on the deck. The second stage was conducted after a portion of the deck was cut off.

2.2.1 Test Specimen and Instrumentation

The model deck of Bronx-Whitestone Bridge (BWB) was 48 ft. (14.63 m) long and 37 ft. (11.28 m) wide. It consisted of 2 panels of continuous deck supported by three diaphragm / floorbeams as shown in Figure 2-1 and Figure 2-2. The floorbeams were each supported by a wall column, and by a stiffening girder at the other end. Half way between the diaphragm / floorbeam, there were intermediate diaphragms (A1 and B1 in Figure 2-1). These diaphragms supported the deck but were not connected to a wall column or to the stiffening girder.

There were fourteen closed, trapezoidal stiffeners (or ribs) and two open, plate stiffeners near the stiffening girder. The trapezoidal ribs were 13 in. (330 mm) wide at the top and 5 in. (127 mm) wide at the bottom. The depth was 13.5 in. (343 mm) with the inclined rib wall being 14.1 in. (257 mm) deep. The spacing between ribs was also 13 in. (330 mm) so the deck plate was supported at equal spacing, except near the stiffening girder. Figure 2-3 shows the geometry of a trapezoidal rib at a diaphragm connection. The cutout at these connections was the main feature of the fatigue study (Tsakopoulos 2005). The thickness of the deck plate was 5/8 in. (16 mm), of the rib walls was 5/16 in. (8 mm) and of the diaphragm web was ½ in. (13 mm). All components were made from ASTM 709 Grade 50 structural steel.

A large number of strain gages and displacement transducers (LVDTs) were placed between Diaphragm A1 and B1. The emphasis was on measuring strains in the deck components at Floorbeam / Diaphragm B. The instrumentation plan is shown schematically in Figure 2-4 and Figure 2-5, for the two stages of testing, respectively. Figure 2-6 shows schematically the strain gage locations around Rib 6 at Diaphragm B.

The strain and LVDT readings were expected to confirm the overall linear elastic behavior of the deck. The strains at the component details were to provide information for examination of load behavior at the details. The numbers of strain gages on various components are listed in Table 2-1.

2.2.2 Loading Procedure

Hydraulic actuators applied vertical loads on the deck. Each load was applied through a 21 in. by 11 in. (53.3 mm by 27.9 mm) rubber pad (footprint) to simulate the rear wheels of a HS 25 truck, as shown in Figure 2-7. When linear behavior was confirmed from strain readings, the applied load was increased from 20 kips (88.96

kN) to 110 kips (489.3 kN) to exaggerate the strains in the components for easy comparison.

The loads were applied individually along six lines at four positions, as depicted in Figure 2-8. Loading line locations simulate the condition of truck wheels directly over the connection of rib walls to the deck plate, and in between. Figure 2-6 shows the location of these lines. The load positions were: above Diaphragm A1, halfway between A1 and B, above Diaphragm B and halfway between B and B1. These positions are indicated in Figure 2-8, and Figure 2-9.

2.3 Experimental Results

2.3.1 Linear Elastic Behavior

The model deck behaved linear elastically under the applied loads as expected. This was true even up to a simulated wheel load of 110 kips (498.3 kN) which is five and half times that of a HS 25 truck. The load-deflection and load-strain diagrams from the strain and deflection gages show the linearity.

Figure 2-10 shows as an example the load versus deflection relationship at nine LVDTs throughout the test deck. The applied load was on Line 1 at Position 2.

Figure 2-11 shows the load versus strain relationship of four strain gages at Diaphragm B1. In all cases, the deflection and strain increase linearly with the applied load, and returned to the same original value when the loads were removed.

2.3.2 Strains in the Deck Plate

The strain distributions on the bottom of deck plate along Diaphragm A1 when the simulated load was at different position on Line 6 are plotted in Figure 2-12. Line 6 was along the midwidth of Rib 8. With 80 kips (489.3 kN) applied at Position 1 directly over Diaphragm A1, the maximum stress on the bottom of the deck at Rib 8 was not the highest. The highest stress of about 7 ksi (48 MPa at 230 μin./in. strain) occurred when the load was at Position 2 between Diaphragm A1 and B. When the 80 kips (489.3 kN) load was at Position 3 over Diaphragm B, the stresses at the strain gages were practically zero. When the load was at Position 4 between two Diaphragms, the bottom of the deck plate was in low tension at the junction with the rib wall at Ribs 8, 9 and 10. With all the actuators at fixed location, it was possible to applied loads simultaneously. This was done with actuators at Positions 3 and 4, and 2, 3, and 4. The strain distribution under these load combinations are also given in Figure 2-12. The elastic behavior of the deck and the capability of strain (stress) superposition were confirmed.

Figure 2-13 shows the strain distribution on the bottom of the deck plate along diaphragm B under the same loading positions of Figure 2-12. All stresses were low under an 80 kips load over the adjacent diaphragm. The maximum of about 10 ksi (69 MPa; 320 μin/in strain) occurred when the applied load was between Diaphragms A1 and B. Under a wheel load of 20 kips (89 kN) for a HS 25 truck, the maximum live load stress under the deck would be less than 2.5 ksi (80 μin/in strain). Once more, the linear elastic behavior was confirmed by the superposition of response to loads at different position.

The strain distributions along Diaphragm B1 in Figure 2-14, and those in Figure 2-12 and Figure 2-13, indicate that the regional influence of a wheel load on deck plate stresses is confined to only the rib under load and at most partially to the adjacent one.

2.3.3 Strains in Diaphragm at Cutout

The longitudinal stiffening ribs pass though a diaphragm web with a cutout, as shown in Figures 2-2, and 2-3. The geometry of the cutout was determined by analysis and was one of the main features of fatigue testing of the model deck (Tsakopoulos and Fisher 2002; Ye and Fanjian, 2004). In the static testing of the deck model to examine the regional effects of loads, strains on diaphragm web at cutouts were measured when loads were applied at various loading positions. Example results are presented in Figures 2-15 to 2-16.

In Figure 2-15, the strains on Diaphragm B at the top of the cutout for Ribs 6, 7, 8, and 9 are presented. The loads were applied along Line 3 over the connection between the deck plate and a web of Rib 6. When the 80 kips (489.3 kN) load was at Position 2 between diaphragms, the highest strain of about 380 μin./in. was induced at the cutout for Rib 6. That is corresponding to less than 3 ksi (21 MPa; 100 μin./in.) under the 20 kips wheel load of a HS 25 truck.

Again, the influence of a wheel load on local stresses is mainly limited to one rib only, as depicted by the strains in Figure 2-15.

The variation of stresses on Diaphragm B at cutouts of Rib 6 to 9 for loading Position 2 of Loading Line 1 to 5, are presented in Figure 2-16. Position 2 is between diaphragms. As the loading line moved away from Rib 6 (from 1, 2, 3 to 4 and 5), the strains at the cutout of Rib 6 decreased. The region of effect of basically only one rib is again obvious. When the applied load was on Line 5 over Rib 8, relatively high strains developed in that rib. There was a splice of the diaphragm between Rib 8 and Rib 9 (as shown in Figure 2-2), which slightly affected the behavior of Rib 8.

2.3.4 Strains on Walls and Bottom of Ribs

The strain gages were mounted on the walls of Ribs 6, 7 and 8 near the Diaphragms B and B1 and at the midspan, as shown in Figure 2-4. At each cross section, there was one rosette on each rib wall and one rosette or two uniaxial gages on the bottom of the rib. The measured longitudinal strains in Ribs 6 and 7 are summarized in Tables 2-2 and 2-3. The maximum response is at the midspan of the ribs. Under a wheel load four times that of a HS 25 truck, the maximum compression strain was about 740 μin./in. (22 ksi, 152 MPa) on a rib wall and the tension strain was about 980 μin./in. (28.4 ksi, 196 MPa) on the bottom of the rib. When this very high magnitude load was moved in the longitudinal direction from Position 1 to Position 4, the maximum strain range on the bottom of the rib was about 1250 μin./in. This corresponds to about 310 μin./in. or 9.5 ksi (65 MPa) for a wheel load of a HS 25 truck.

Some examples of distribution of longitudinal strains in Ribs 6, 7 and 8 are presented in Figures 2-17 to 2-20. Figures 2-17 and 2-18 show the magnitude of strains on the surface of walls and bottom flange of these ribs at midspan when the 80 kips load was directly over the cross section. From Figure 2-17, it is obvious that the longitudinal stresses of the rib walls close to the deck plate were very low even under the 80 kips of simulated wheel load. Directly under the load on Line 3, the effect of wheel contact was observed. The bottom of Rib 6 was subjected to relatively high stresses when the wheel load was directly above on Lines 1, 2 and 3, while the bottom of Rib 7 also sustained some stresses. This condition implies, again, that a wheel load is primarily carried by one rib with some participation of the immediately adjacent ribs. When a wheel is between two ribs (Line 4) both ribs carry the load.

Figure 2-18 for strains in Ribs 6, 7 and 8 at midspan of A1-B shows the distribution of strains at the bottom of the ribs. The same conclusion may be drawn that a wheel load is primarily carried by the rib beneath the wheel.

The distribution of strains in rib walls when the wheel loads were in the next deck span is given in Figure 2-19 for the cross section between Diaphragms B and B1, and in Figure 2-20 for cross section at A1-B. Once again, the condition that a wheel load is primarily carried by one rib is revealed,

2.3.5 Deflection of Deck Due to Simulated Wheel Load

The vertical deflection of various points of the test deck obviously depended on the location of the wheel load with respect to the points. Directly under the wheel load, relatively high magnitude of deflection was expected. The “composite” deflection shape of the transverse cross section of the deck between Diaphragm B and B1 when the applied loads were directly over the cross section is shown in Figure 2-21. Plotted are the deflection of the bottom of the rib and the deck plate between ribs. The curves represent a “composite” shape of the deck under load. Little difference exists among the shapes for the different loading lines. Figure 2-22 shows, in different scale, the shape of the same cross section when the loads were in the adjacent span. The deflection shapes are in the opposite direction to that of Figure 2-21. This indicates the stronger effect of loads in spans (in the longitudinal direction) than in different lines (in the transverse direction). Whether the wheel load is directly over a rib or in between did not cause much difference in the deflection shape.

Overall, the magnitude of vertical deflection of the deck plate between ribs and rib walls was small. The maximum value was less than 0.2 in. (5 mm) downward when the 80 kips load was in the span. It was 0.025 in. (0.6 mm) upward when the load was in the adjacent span. These were linear elastic deflections, as has been shown by Figure2-10.

2.4 Influence Lines of Strains

2.4.1 Influence Line of Strains from Experimental Data

The strain diagrams presented so far, Figure 2-12 to 2-20, provide information on the distribution of stresses in deck components near the point of loading. The subsequent diagrams show the magnitude of strain at specific points as a load was applied at different locations nearby. These diagrams are the “Influence Lines” of strains.

Figure 2-23 shows the horizontal and vertical strains on the web of Diaphragm

B at the connection of deck plate and Rib 6. The strain gage locations are given in Figure 2-6. Both the horizontal and vertical strains at gage 10(x) and 12(y) were highest when the 80K load was directly above. The magnitude of strains at these gages decreased as the load was placed away. Similarly, the horizontal and vertical strains at gage 20(x) and 22(y) were the highest when the load was directly above. When the load was at Line 5 over Rib 8, the strain at all four gages at Rib 6 were practically zero.

On Diaphragm B at the cutout of Rib 6, strains on the South surface of the diaphragm web at the top of cutout (Figure 2-24) were slightly higher when the load was at Line 2 between the rib walls than when the load was directly over the walls. The difference in strains at the back to back strain gages (128/129,134/135) indicates that the diaphragm web was subjected to local bending. In this case, the local bending of web was about the same on the two sides of Rib 6. On the other hand, the diaphragm web plate local bending at the lower corners of the cutout was not prominently affected by the loading line, as the strains at the back to back strain gages (130/131 and 132/133 in Figure 2-25) increase or decrease similarly. All four gages had the highest strain when the applied load was directly above and had almost no strain when the load was one rib away.

The rib walls were also subjected to local bending when the applied load was nearby. The “Influence Lines” for strain gage pairs on the walls of Rib 6 at Diaphragm B are given in Figure 2-26. The difference in strain between the gages of each pair (137/138, 139/140) signifies local plate bending. The maximum difference was about 350 μin/in (10.2 ksi) in the 5/16 in. (8 mm) thick rib wall, comparing to about 400 μin/in (11.6 ksi) in the 1/2 in. (12.7 mm) web plate of Diaphragm B in Figure 2-24.

Figure 2-27 shows the “Influence Line” of strain on the wall of Rib 6 between Diaphragm B and B1. When the applied load was at Position 4 directly over the cross section of the rib, the bottom of the rib had the highest strain regardless whether the load was over the rib wall or in between. The shape of the “Influence Line” is typical for a continuous beam. The strains on the web of the rib about an inch from the deck and directly below the applied load, however, increased without changing sign when the load was moved from Position 1 to 4. There were practically no local strains at the point on the opposite web of the rib.

2.4.2 Influence Surface from the Measured Strains

The influence lines of strains can be summarized into influence surface of strains for specific points of deck components. Figure 2-28 shows the influence surface of strain on the web of Diaphragm B at the top of cutout for Rib 6. The highest compression stress happened when the load was at the midpoint between Diaphragm B and B1 and directly over Rib 6. In the transverse direction, the effect of wheel load was confined to the rib and one adjacent rib. At the bottom of this cutout on the web of Diaphragm B, as shown in Figure 2-29, the relatively high compressive strain occurred only when the load was on Rib 6. When the load was away from Rib 6, the strains was reduced to zero and then changed to low tension. The effect of the wheel load was primarily confined to only one rib.

The influence surfaces for strains on the wall of Rib 6 inside the cutout at Diaphragm B are presented in Figures 2-30 to 2-33. The highest stresses occur not when the wheel load was over the diaphragm but between diaphragms. The back-to-back strain gages on the rib walls, Gages 137 and 138 in Figures 2-30 and 2-31 and Gages 139 and 140 in Figures 2-32 and 2-33, do not have an identical shape of influence surface. This condition indicates that the stresses on the surfaces of the rib wall are the combination of membrane (in plane) and plate (out of plane) bending stresses. The important phenomenon is that the wheel load affects primarily only the rib directly under the wheel, and only slightly the adjacent rib.

2.5 Results of Finite Element Analysis

To confirm analytically the participation of ribs under wheel loads, a finite element analysis was conducted. Figure 2-34 shows the three-dimensional finite element model of the full-scale laboratory specimen with two continuous panels supported on three transverse floor beams. The model was developed and analyzed using the commercial software ABAQUS (2004). All steel plates were modeled using four-node S4R shell elements which consider both the membrane and plate bending behavior. The stress-strain relationship was from tensile coupon tests.

The finite element analysis results of strains in Rib 6 at Diaphragm B when the simulated wheel load is directly above are shown in Figure 2-35. The corresponding load case in the experimental phase is Loading Line 2 and Position 3. The computed and measured strains in the webs and the bottom flange of the rib agree quite well respectively. Figure 2-36 shows the strains contour of the deck plate under the same loading conditions. The 80 kips (489 kN) load only affect the deck plate locally around the footprint. Under the deck plate, the analytical results show that the load causes moderate strains on the top and bottom of cutout on the diaphragm web as shown in Figure 2-37. Figure 2-38 shows the strain contour in Rib 6 between Diaphragm A1 and B under the same loading condition. The stresses of moderate magnitude are concentrated within one rib.

2.6 Discussion and Conclusions

The measured and computed stresses in the model orthotropic deck of the BWB indicate that in the transverse direction of the deck, primarily only one rib carries the simulated wheel load of a truck. By considering that the transverse distance between wheels of the same axle of a AASHTO truck (72 in., 1829 mm) or parallel trucks is more than the width of two ribs of the BWB deck panel (2 × 26 = 52 in., 1321 mm), it can be concluded that only wheel loads need to be considered in the evaluation of stresses and strength of ribs.

From the experimental results with an applied load of 80 kips (356 kN) which is four times the HS 25 wheel load, all response of stresses are in the linear elastic range. This indicates the adequacy of superposition of multiple wheel loads in the longitudinal direction and the utilization of influence line for beams. In the subsequent chapters on the strength of ribs, it is conservative to assume that wheel loads are supported transversely by only one rib. In the longitudinal direction, multiple simulated wheel loads were applied during testing. Because of the difference in stiffness of the diaphragms with or without floorbeams, the effect of longitudinal load position was strong on the local stresses of the diaphragms and adjacent rib walls.

Table 2-1 Strain Gages on Component Details

	Stage I		Stage II	
Gages	Rosette	Uniaxial	Rosette	Uniaxial
on diaphragm	21	29	12	50
on ribs	20	20	62	33
on deck plate	4	0	4	0
on the rib splices	0	12	0	16
Total	45	61	78	99

Table 2-2 Longitudinal Strains on Wall and Bottom of Rib 6 (μin/in)

P=80 kips at		Near B1			Mid-span			Near B		
Position	Line	East Wall	Bottom	West Wall	East Wall	Bottom	West Wall	East Wall	Bottom	West Wall
1	1	10.34	17.38	11.44	18.43	-107.84	12.33	47.80	39.19	16.36
	2	13.88	17.82	12.34	25.24	-260.70	16.37	175.09	144.79	33.67
	3	2.94	4.42	-1.70	2.74	3.18	0.18	48.33	-70.46	-269.30
	4	-26.89	-4.17	-59.14	-97.02	905.31	-17.83	75.15	46.29	-27.90
	5	-22.69	1.23	-59.26	-99.14	925.03	-20.08	96.67	5.05	-262.57
	6	-17.84	18.76	-43.11	-73.24	672.67	-5.08	219.91	145.76	-220.41
2	1	11.46	17.93	9.28	16.26	-89.26	14.92	37.20	56.05	27.33
	2	19.42	19.82	16.85	20.92	-273.37	24.39	159.65	197.05	67.61
	3	-2.07	6.08	-0.49	1.49	10.40	-4.53	-17.91	-46.05	-214.45
	4	-52.93	-11.58	-42.32	-59.11	969.18	-48.10	77.17	72.35	-0.79
	5	-55.59	-19.66	-45.08	-36.69	980.64	-	-14.66	28.27	-255.60
	6	-43.77	-4.80	-31.62	-32.10	681.25	471.20	105.29	210.05	-188.35
3	1	7.35	8.31	4.07	16.39	-87.05	-23.06	29.60	48.11	28.03
	2	13.57	16.24	6.13	18.95	-239.75	-387.40	112.07	170.78	69.39
	3	-4.99	-3.92	-4.98	-4.40	24.95	-502.14	-42.53	-55.95	-294.53
	4	-37.51	-24.11	-17.83	-50.40	803.67	-640.68	65.82	54.17	-2.02
	5	-63.94	-24.32	-14.80	-50.58	835.14	-740.08	15.53	14.55	-285.34
	6	-54.86	-10.69	-7.65	-39.17	597.47	-624.52	95.84	156.25	-233.42
4	1	12.39	10.97	1.01	21.89	-100.96	17.16	24.78	62.45	22.94
	2	18.71	11.36	2.85	32.25	-210.20	31.42	66.84	147.61	59.42
	3	-2.55	-1.43	6.27	6.04	31.98	-19.86	-3.46	-32.83	-66.28
	4	-53.99	-30.25	14.14	-56.52	493.71	-153.76	37.41	61.98	26.86
	5	-57.53	-30.66	23.88	-55.64	516.40	-123.58	36.28	9.67	-112.42
	6	-47.86	-13.25	29.82	-26.90	-350.11	812.13	101.85	139.88	-70.29

Table 2-3 Longitudinal Strains on Wall and Bottom of Rib 7 (μin/in)

P=80 kips at		Near B1			Mid-span			Near B		
Position	Line	East Wall	Bottom	West Wall	East Wall	Bottom	West Wall	East Wall	Bottom	West Wall
1	1	9.17	-56.19	16.10	15.34	-76.49	9.46	20.73	-26.61	29.91
	2	0.28	-83.62	21.62	36.03	-104.63	26.39	23.89	14.24	19.53
	3	4.93	10.35	0.00	-3.64	-20.57	0.40	-6.62	12.32	-6.94
	4	40.00	194.30	-44.76	-67.30	50.34	-29.52	39.60	-68.76	12.73
	5	41.85	206.90	-44.36	-72.64	62.90	-28.43	40.43	-60.49	-0.40
	6	43.45	127.14	-25.65	-33.61	-14.43	3.11	68.61	-47.74	20.68
2	1	5.16	-55.26	8.32	23.47	-60.09	14.42	25.43	-35.06	23.30
	2	0.43	-80.81	12.32	43.98	-85.29	28.23	42.65	3.21	25.46
	3	1.28	15.29	-1.19	1.77	13.99	-1.17	-0.37	13.34	-14.58
	4	42.68	175.07	-42.42	-87.00	126.83	-36.68	52.44	-105.42	13.85
	5	45.57	186.60	-46.38	226.78	58.66	-664.69	50.58	-91.91	1.63
	6	41.35	107.95	-31.16	-44.67	49.49	-15.51	82.15	-95.98	17.60
3	1	7.16	-48.54	3.69	21.16	-63.05	14.42	28.66	-36.72	25.00
	2	0.81	-76.44	9.34	37.64	-102.71	23.46	48.02	-22.92	29.32
	3	1.41	5.72	-4.64	-0.57	14.36	4.62	-1.45	19.30	-10.25
	4	25.51	136.19	-49.37	-132.47	219.97	-47.61	52.69	-156.17	15.99
	5	22.96	141.01	-53.74	-137.83	241.13	-51.72	49.37	-139.37	2.88
	6	24.43	69.77	-37.66	-103.40	131.76	-24.49	96.25	-166.92	33.44
4	1	12.09	-46.68	10.85	24.65	-71.07	11.21	24.82	-36.15	20.40
	2	9.65	-59.44	18.25	38.67	-147.36	17.70	71.11	-81.61	43.08
	3	3.01	4.97	-0.24	0.78	12.52	-1.37	-83.68	33.20	-36.69
	4	-2.61	72.47	-59.69	-125.00	403.65	-53.37	46.22	-193.18	11.75
	5	-0.60	79.14	-57.93	-113.13	422.13	-54.70	-52.38	-167.56	-4.88
	6	4.26	7.09	-40.50	-84.32	283.51	-26.57	16.21	-267.73	44.11

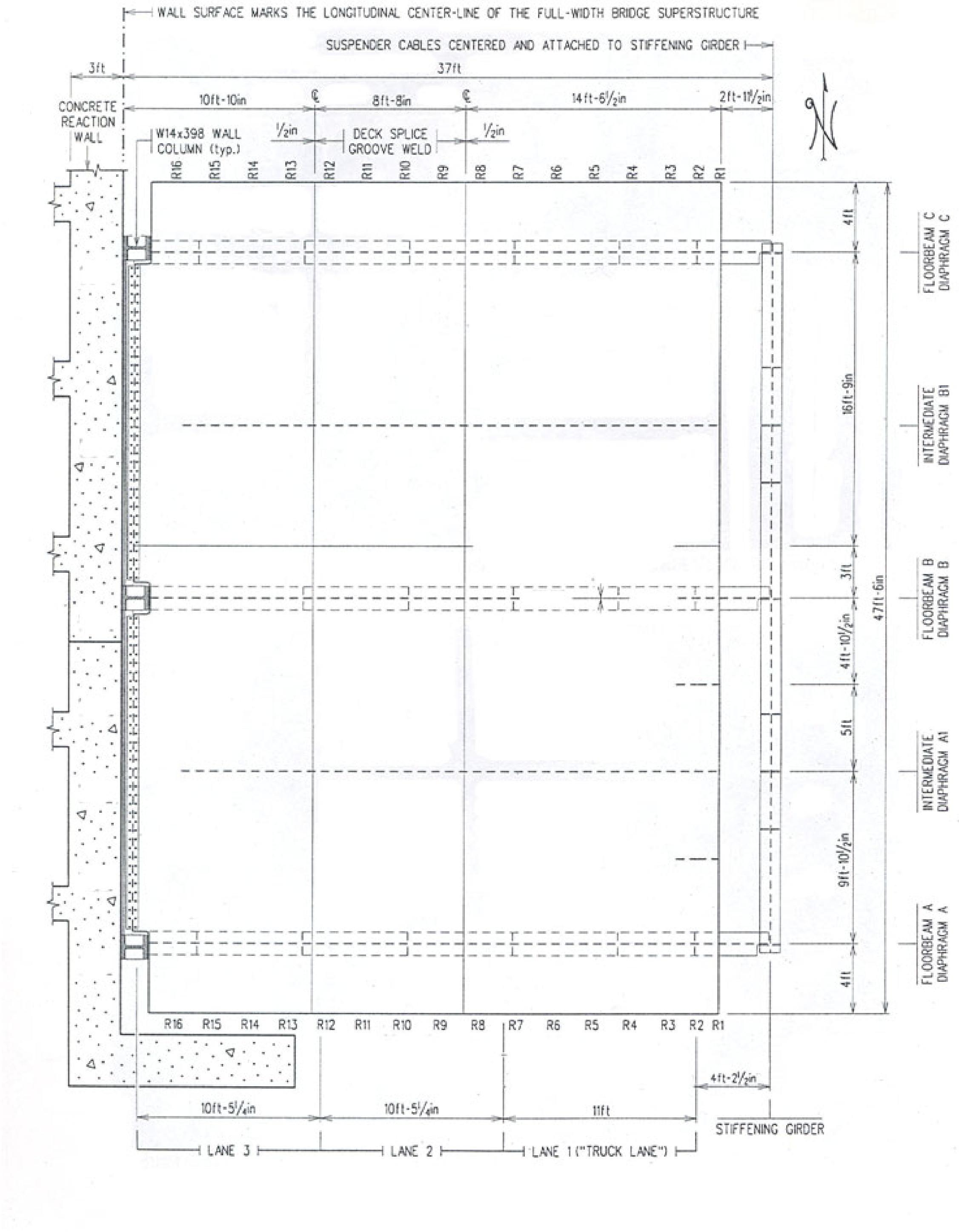

Figure 2-1 Plane of Specimen

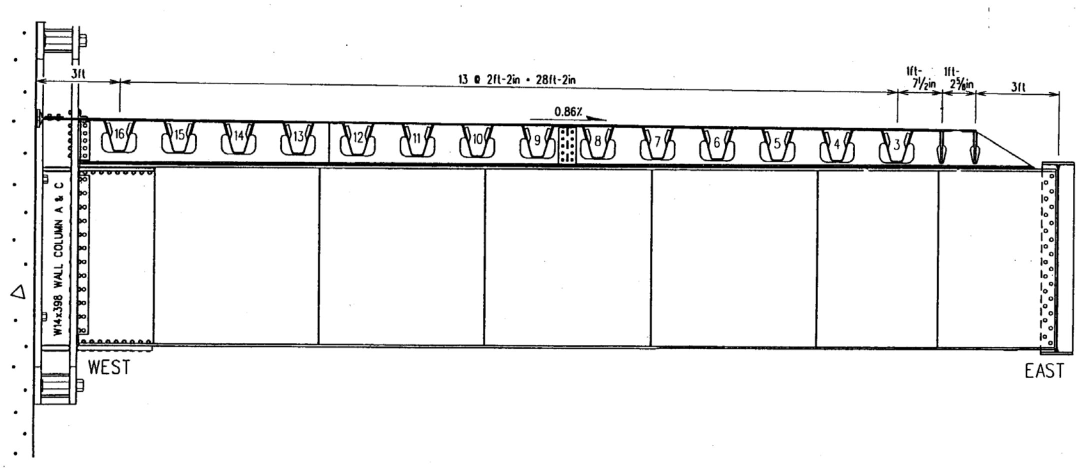

Figure 2-2 Elevation of Specimen

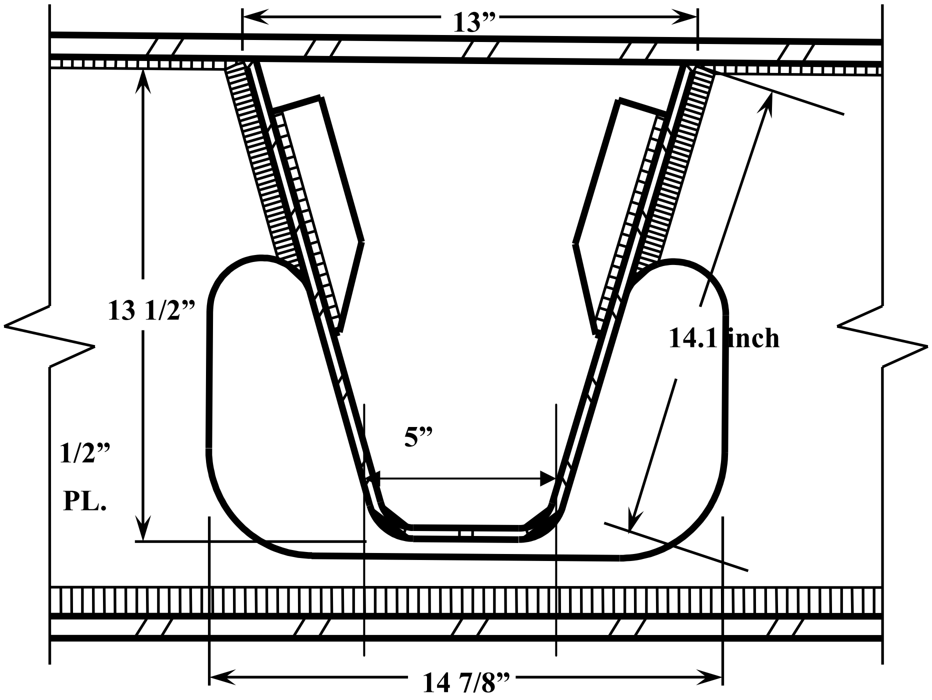

Figure 2-3 Geometry of Trapezoidal Stiffener

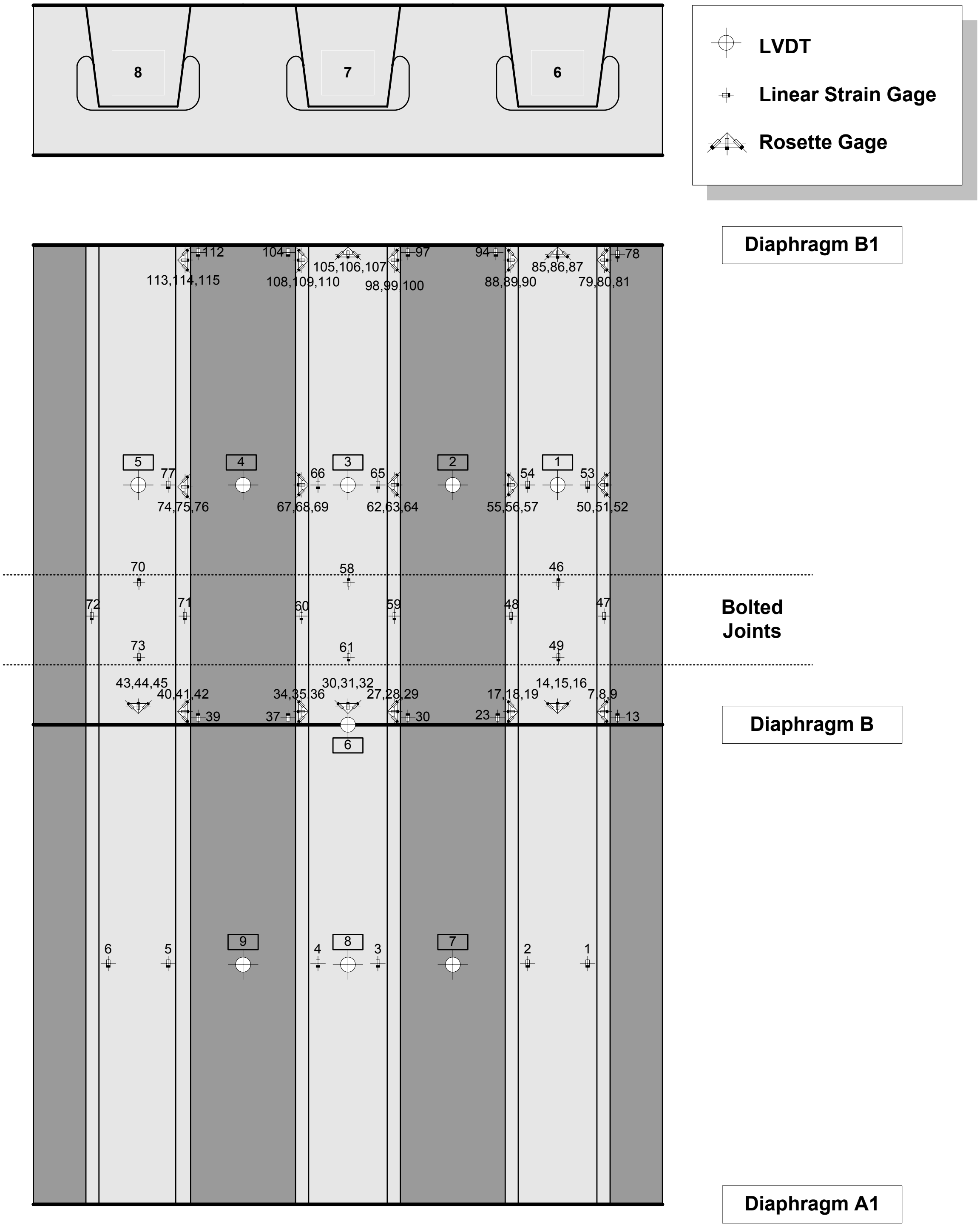

Figure 2-4 Instrumentation Plan (Stage I)

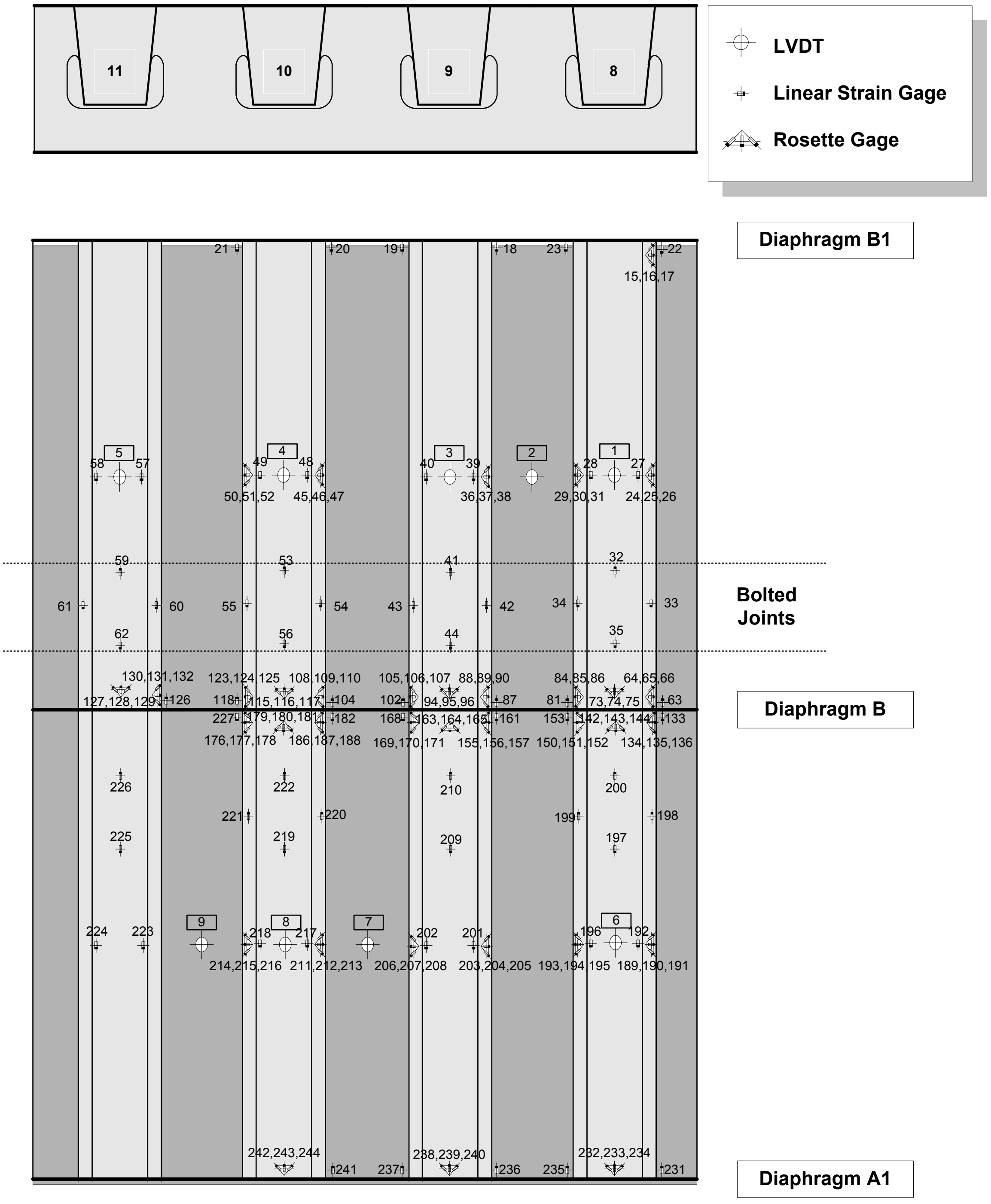

Figure 2-5 Instrumentation Plan (Stage II)

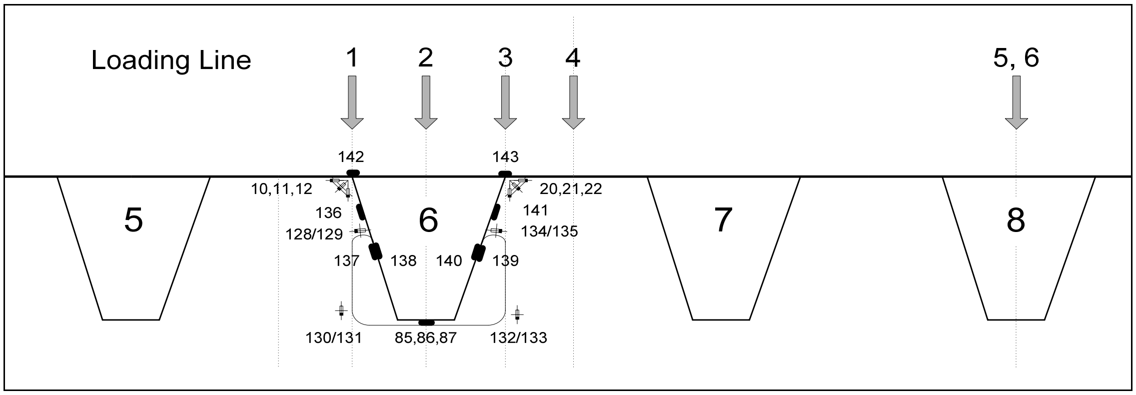

Figure 2-6 Gage Location and Loading Lines, Rib 6 at Diaphragm B

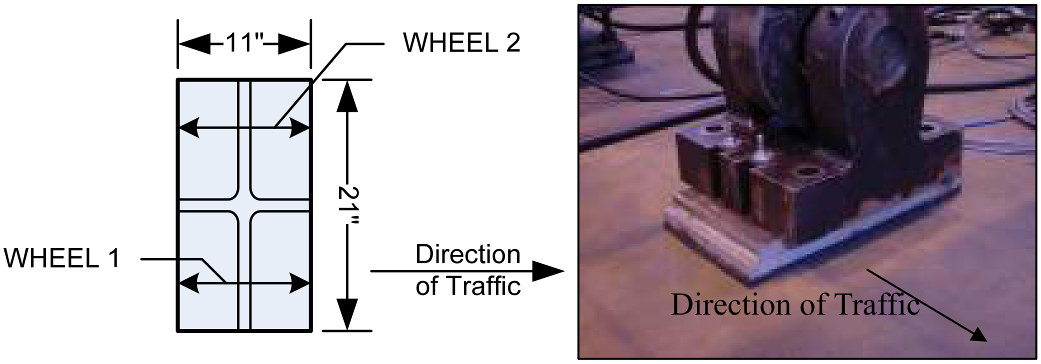

Figure 2-7 Footprint

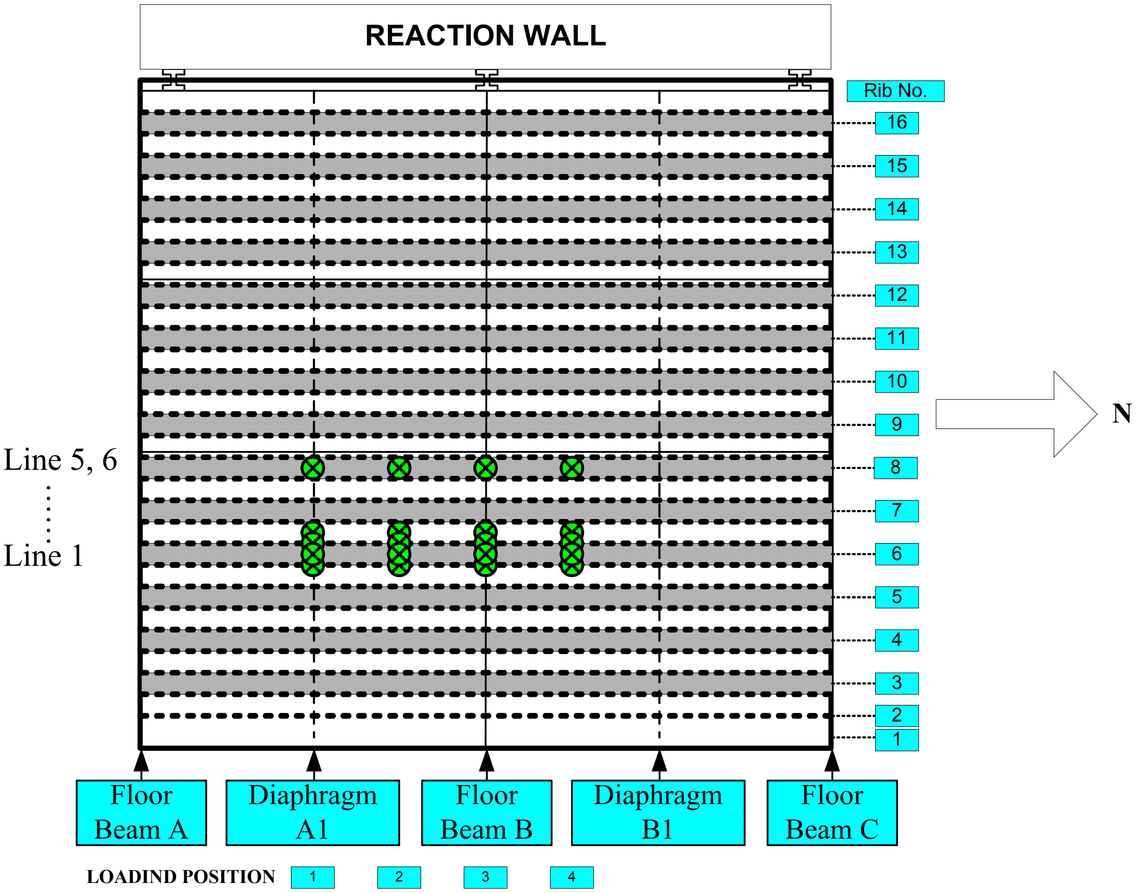

Figure 2-8 Loading Lines and Positions

For Stage I For Stage II

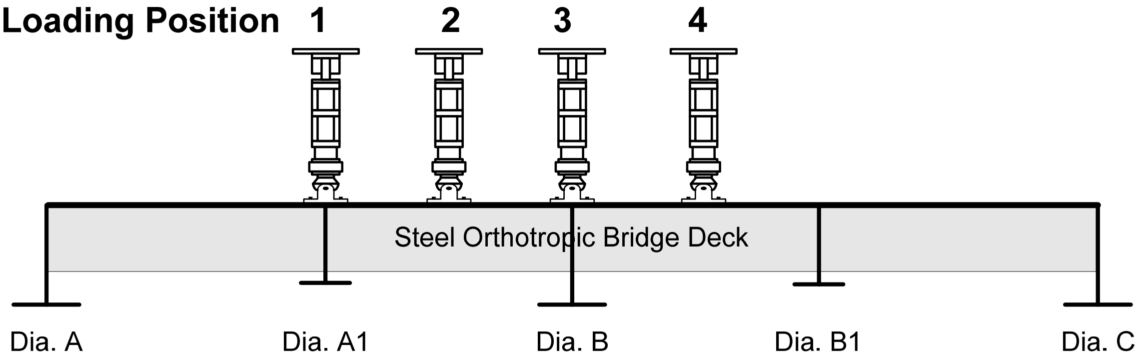

Figure 2-9 Load Positions

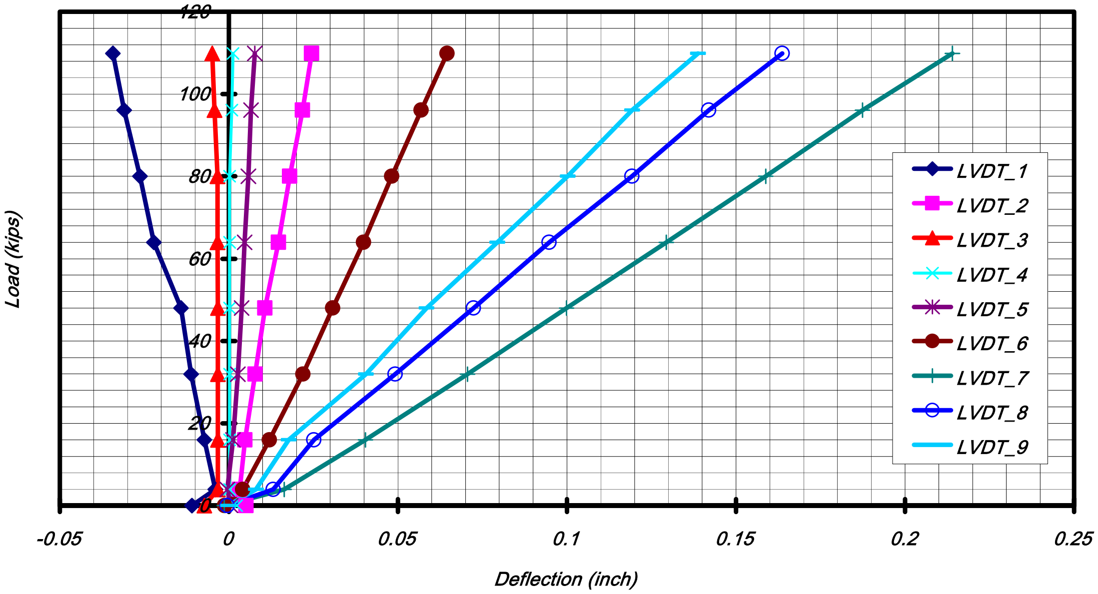

Figure 2-10 Load vs. deflection at various locations of deck (Line 1, Position 2)

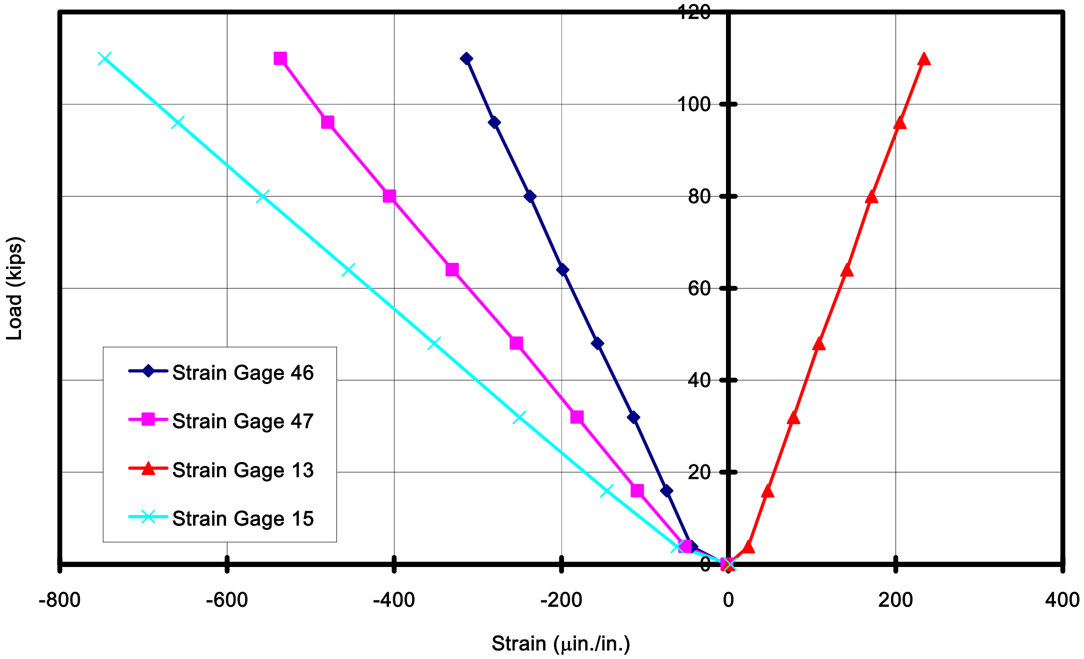

Figure 2-11 Load vs. strain at Diaphragm B1 (Line 1, Loading Position 2)

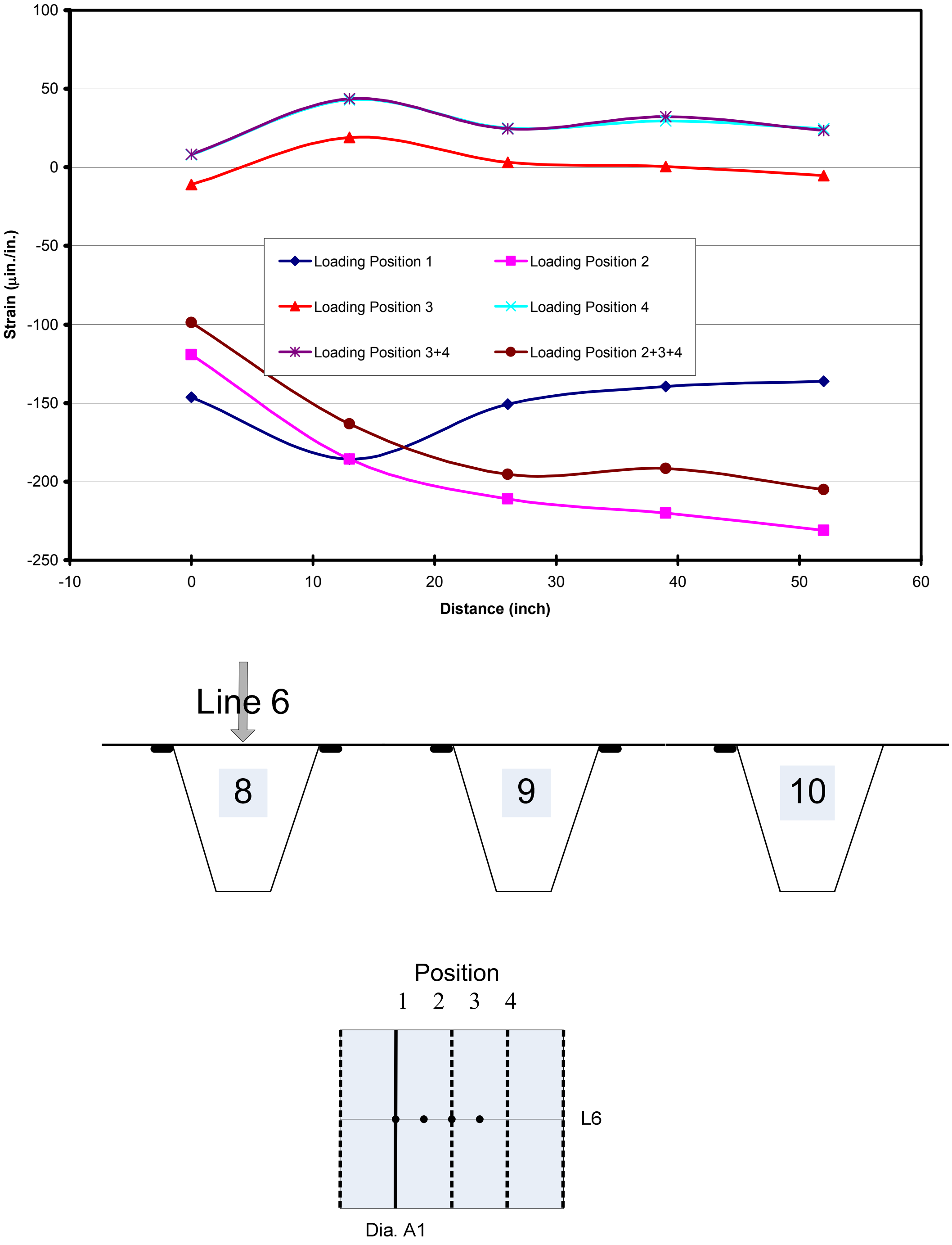

Figure 2-12 Strains on the bottom of deck plate along Diaphragm A1 (loads on Line 6)

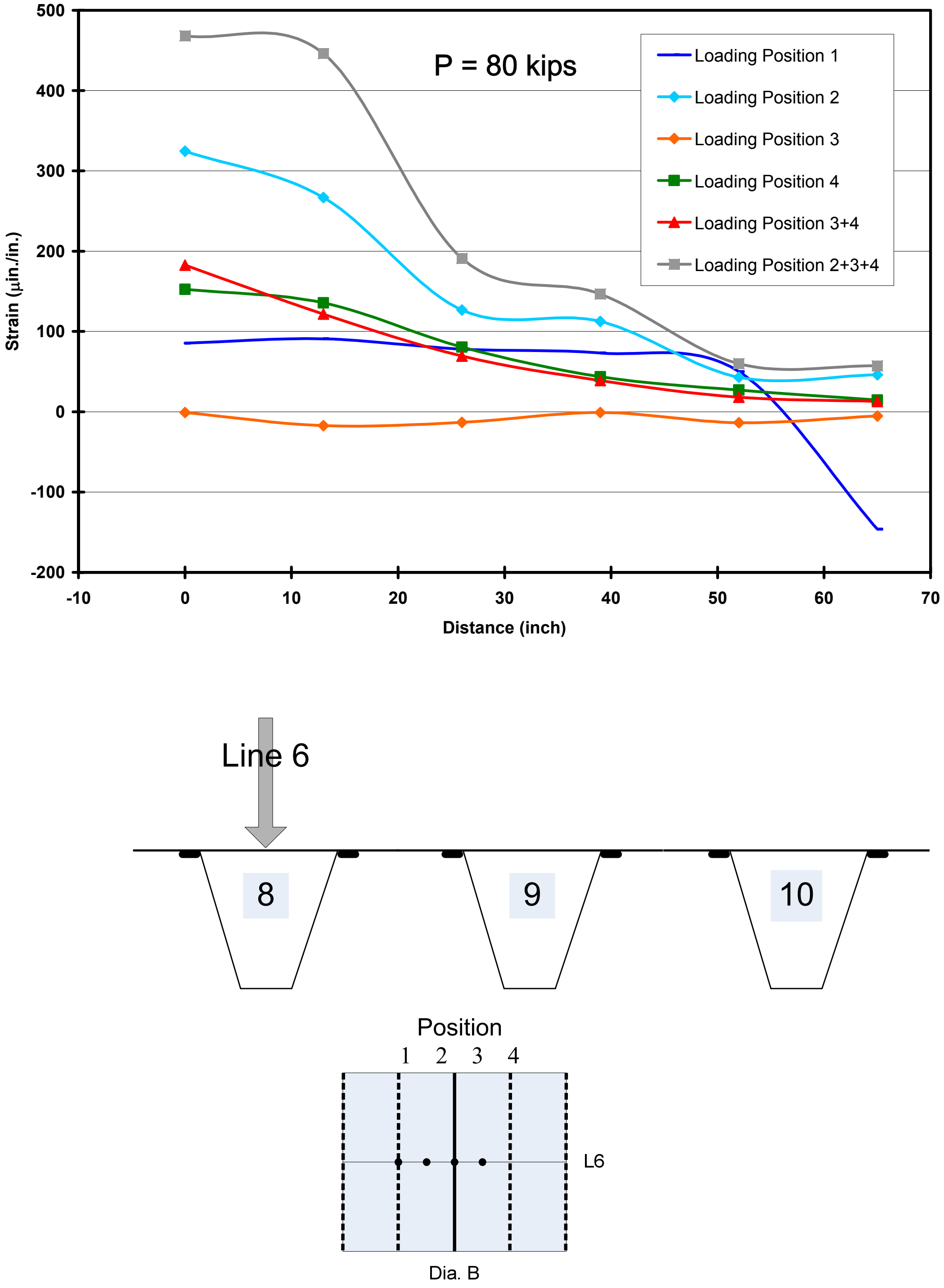

Figure 2-13 Strains on bottom of deck plate along Diaphragm B (loads on Line 6)

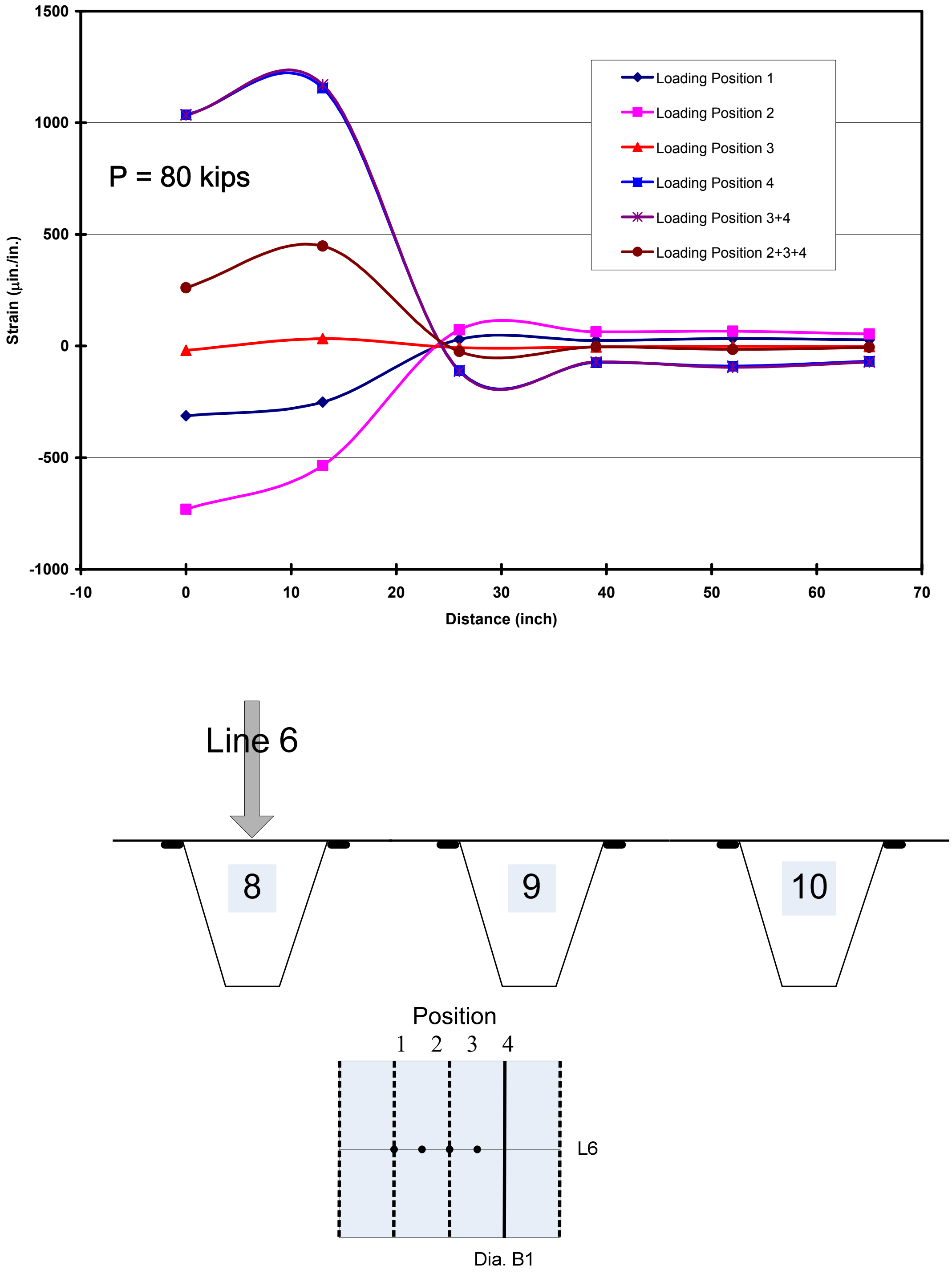

Figure 2-14 Strains on the bottom of deck plate along Diaphragm B1 (loads on Line 6)

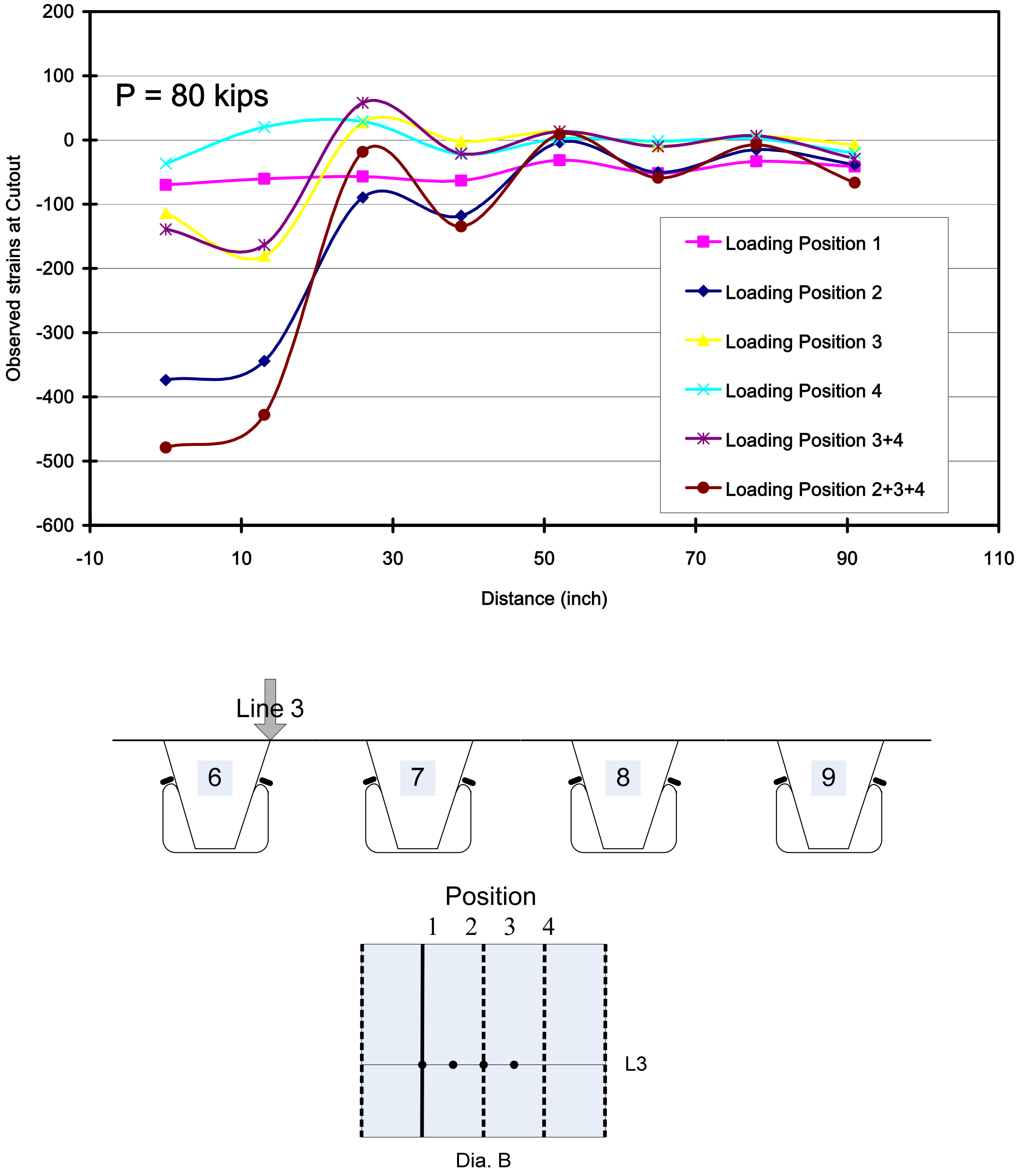

Figure 2-15 Strains at cutout on South face of Diaphragm B (Loads on Line 3)

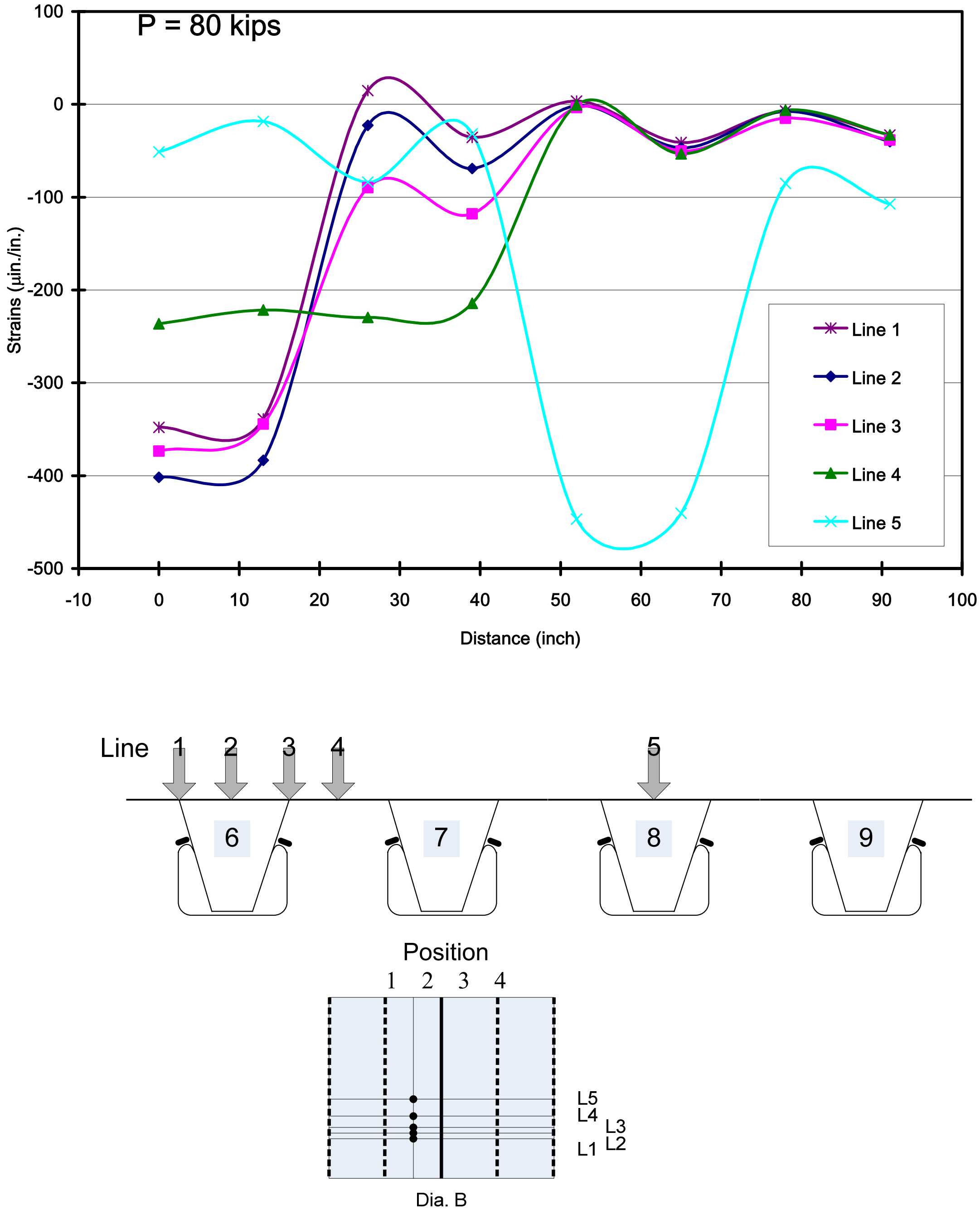

Figure 2-16 Strains at cutout on the South face of Diaphragm B (Loading Position 2)

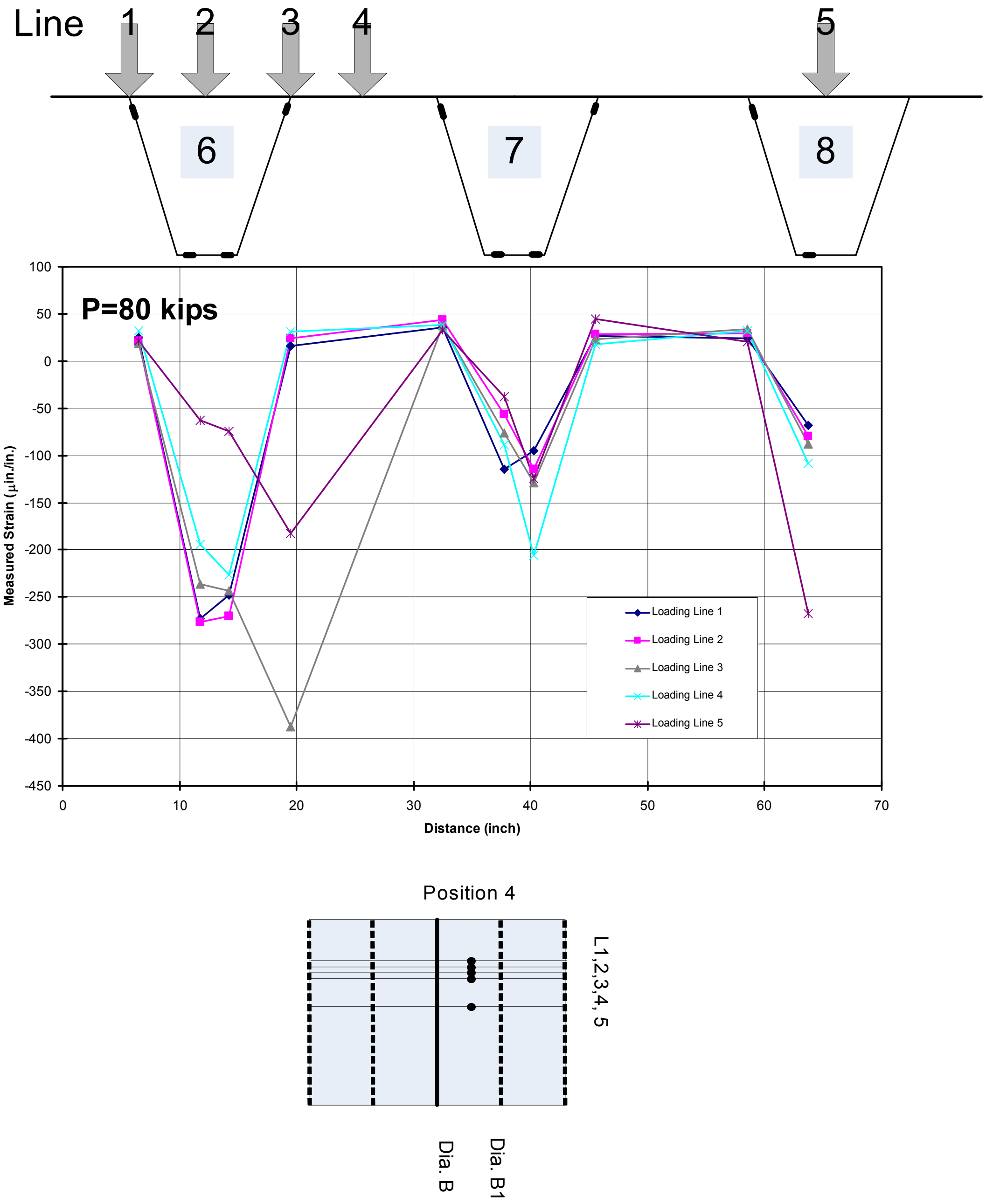

Figure 2-17 Strains on Rib Walls between Diaphragm B and B1, loads over Cross Section (Position 4)

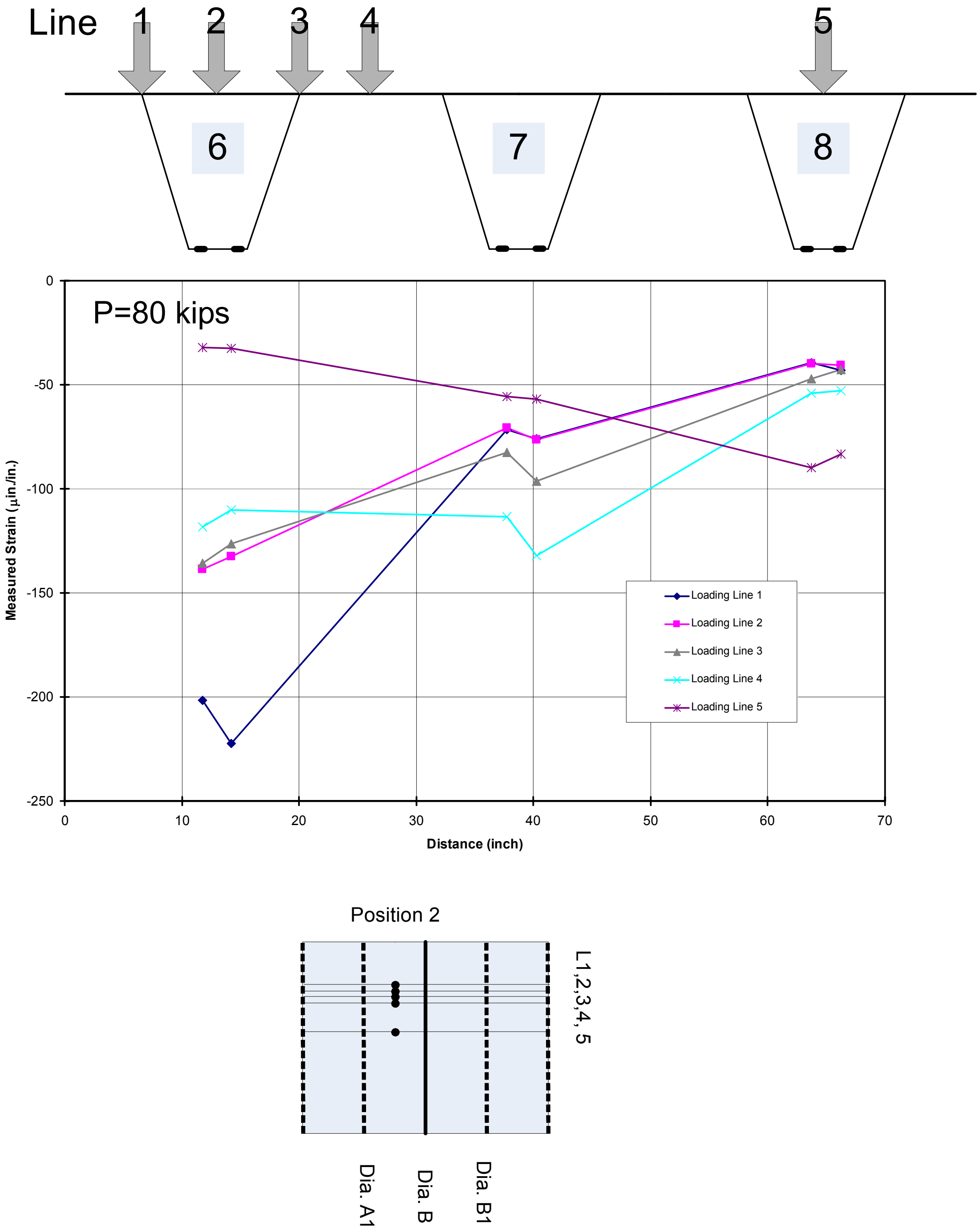

Figure 2-18 Strains on Rib Walls between Diaphragm A1 and B, loads over Cross Section (Position 2)

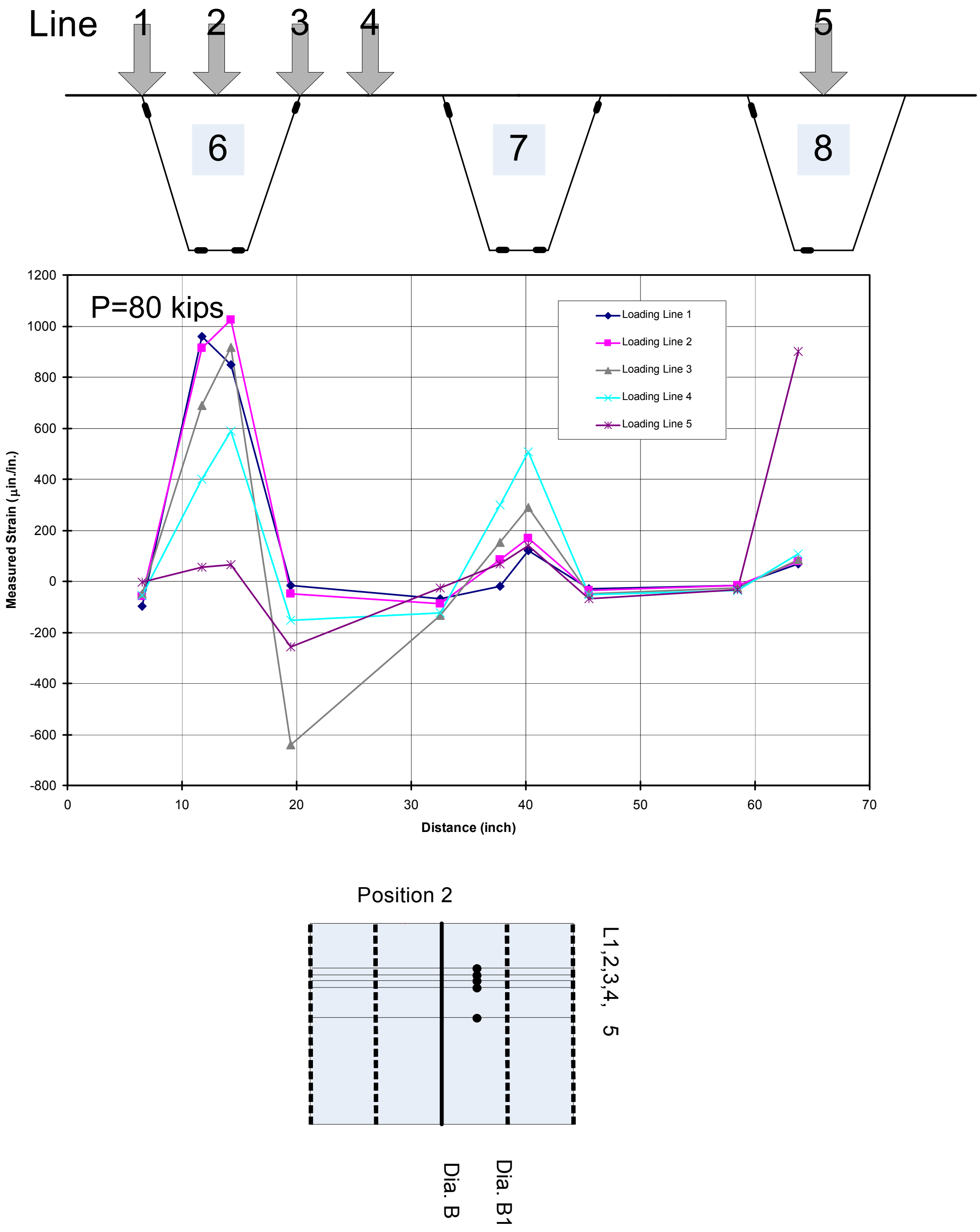

Figure 2-19 Strains on Rib Walls between Diaphragm B and B1, loads in Next Span (Position 2)

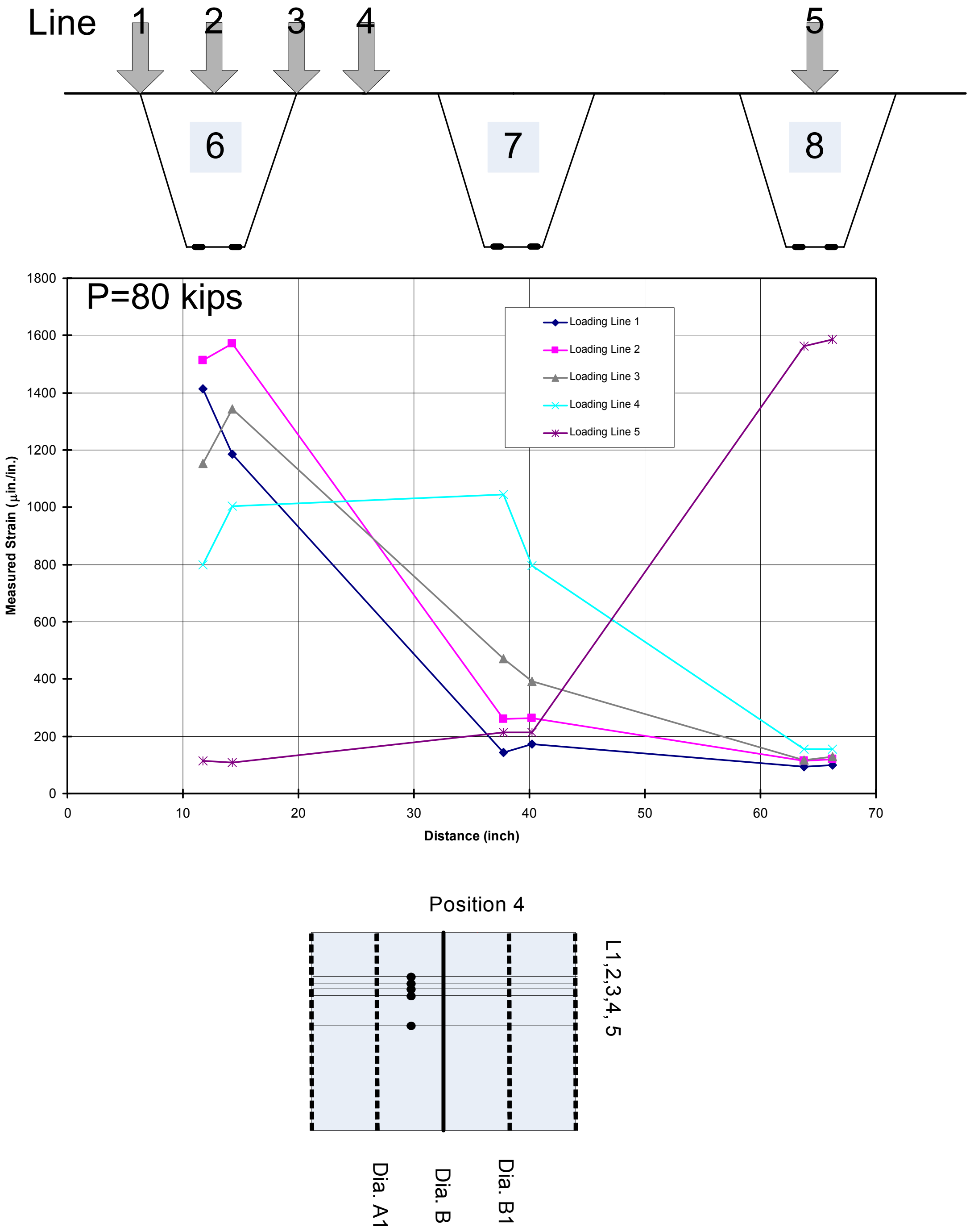

Figure 2-20 Strains on Rib Walls between Diaphragm A1 and B, loads in Next Span (Position 4)

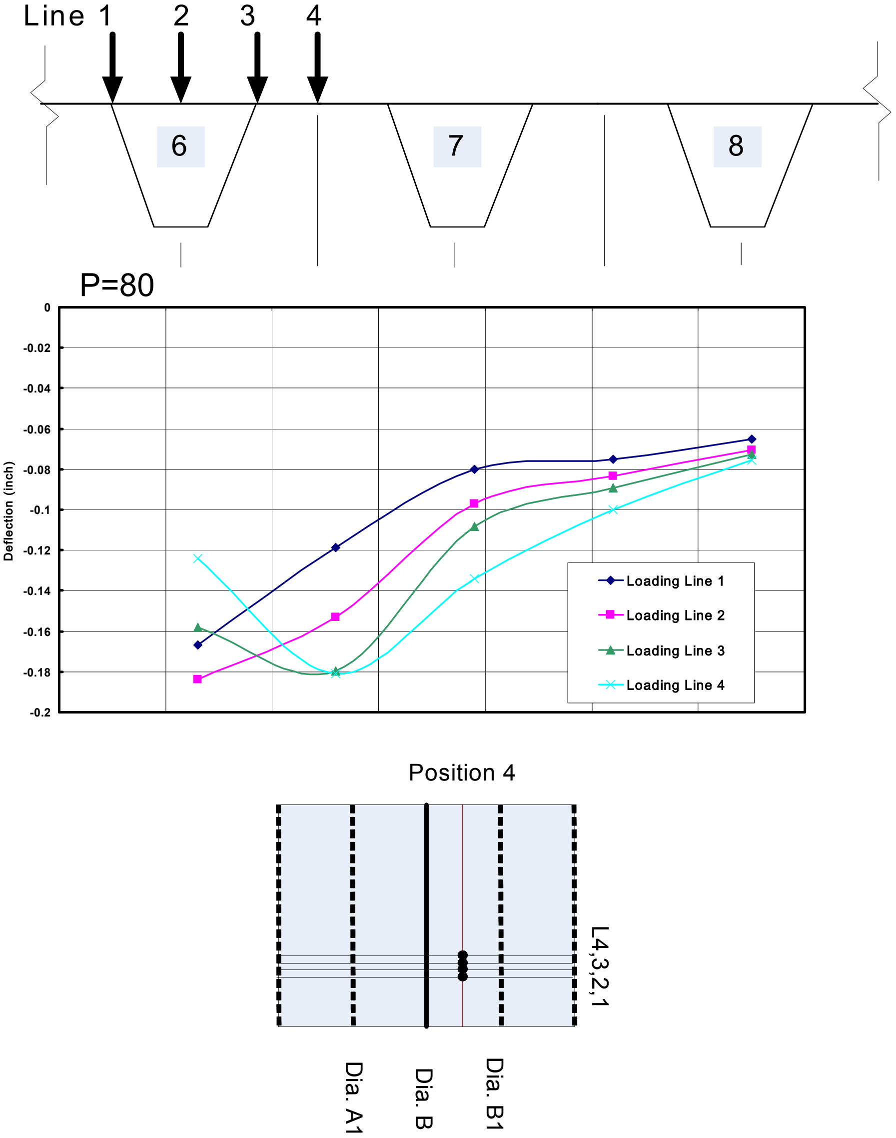

Figure 2-21 Deflection of Deck between Diaphragm B and B1, loads on Position 4

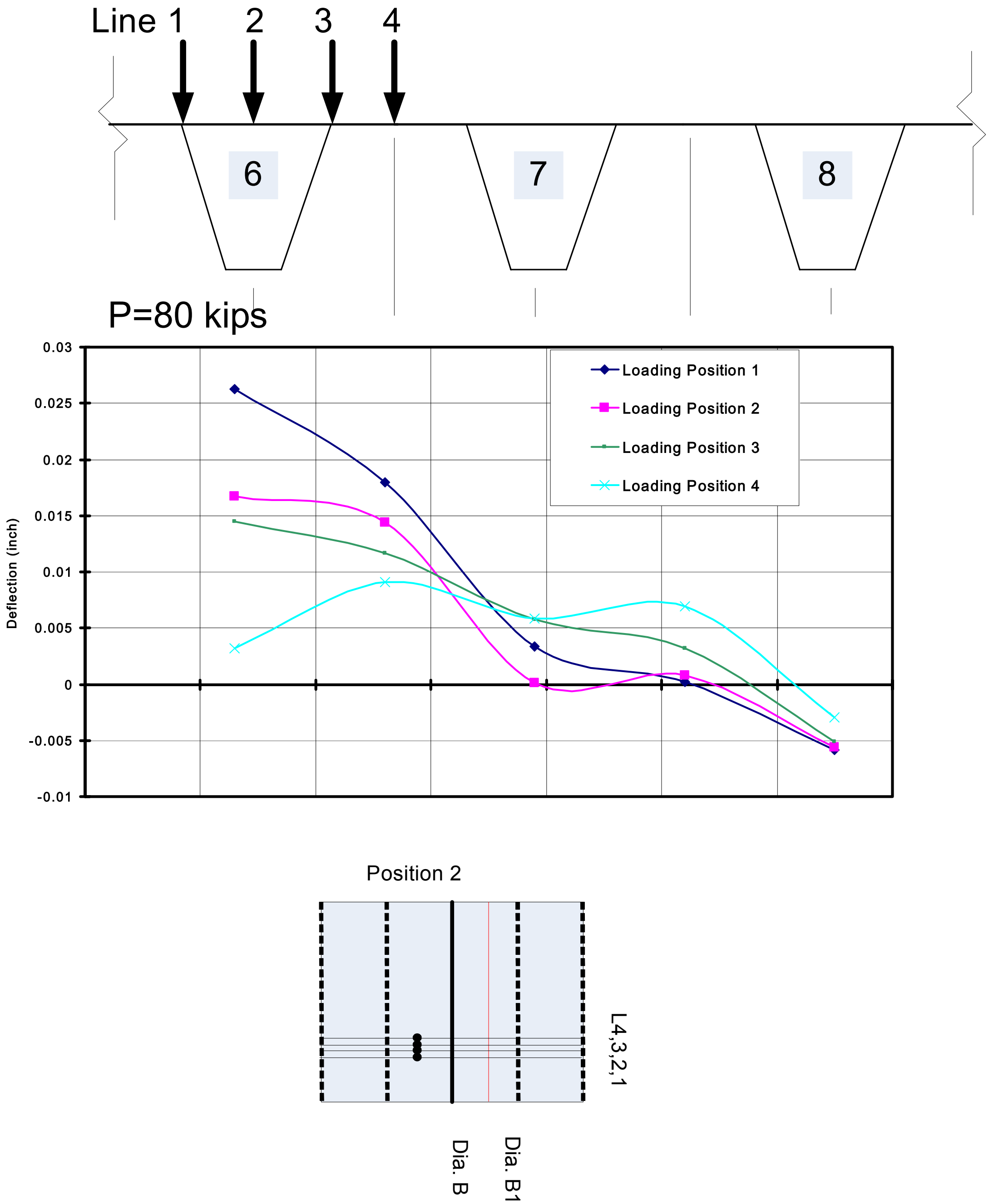

Figure 2-22 Deflection of Deck between Diaphragm B and B1, loads on Position 2

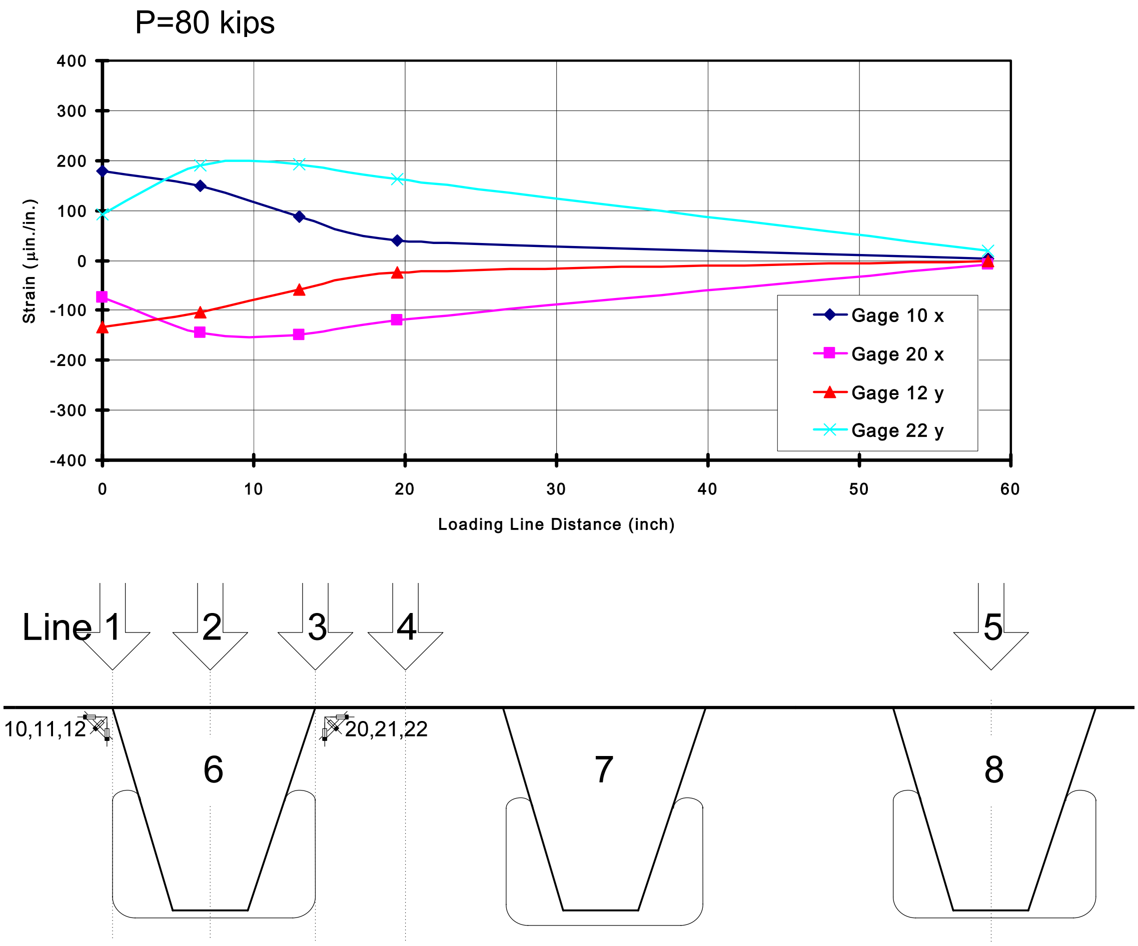

Figure 2-23 Influence lines of Horizontal (x) and vertical (y) strains on Diaphragm B at connection of deck and Rib 6

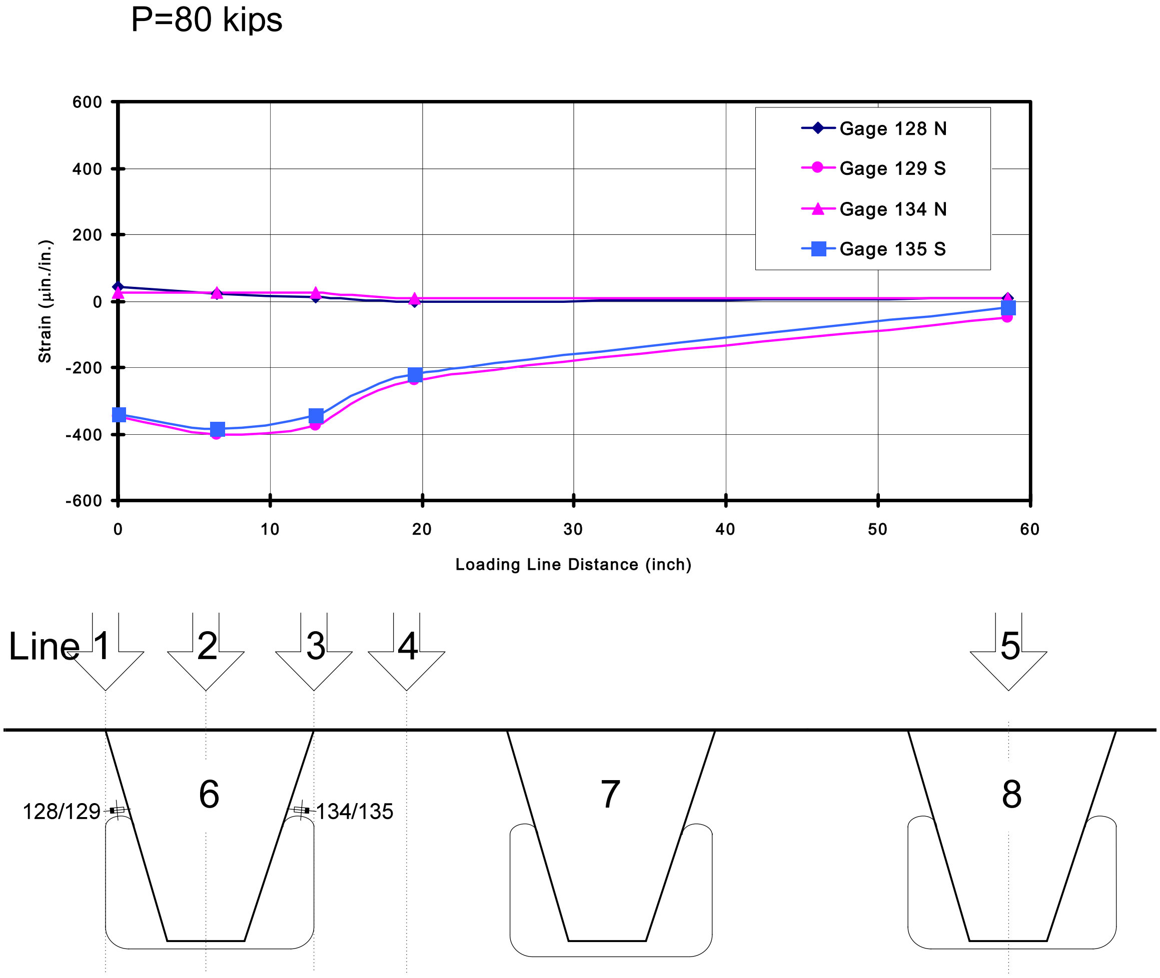

Figure 2-24 Influence lines of strains on North and South faces of Diaphragm B at top of cutout, Rib 6

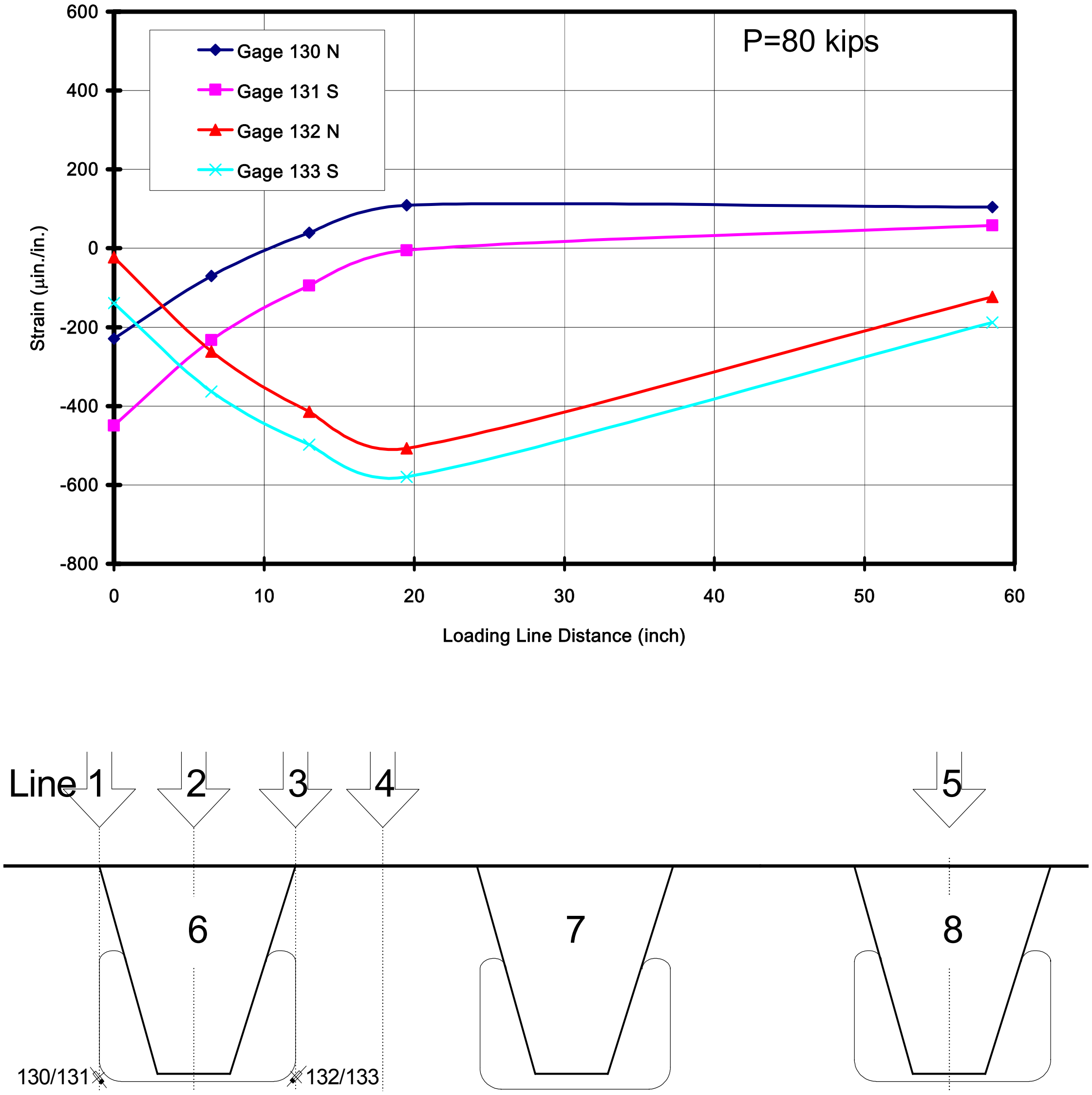

Figure 2-25 Influence lines of strains on Diaphragm B at lower corner of cutout, Rib 6

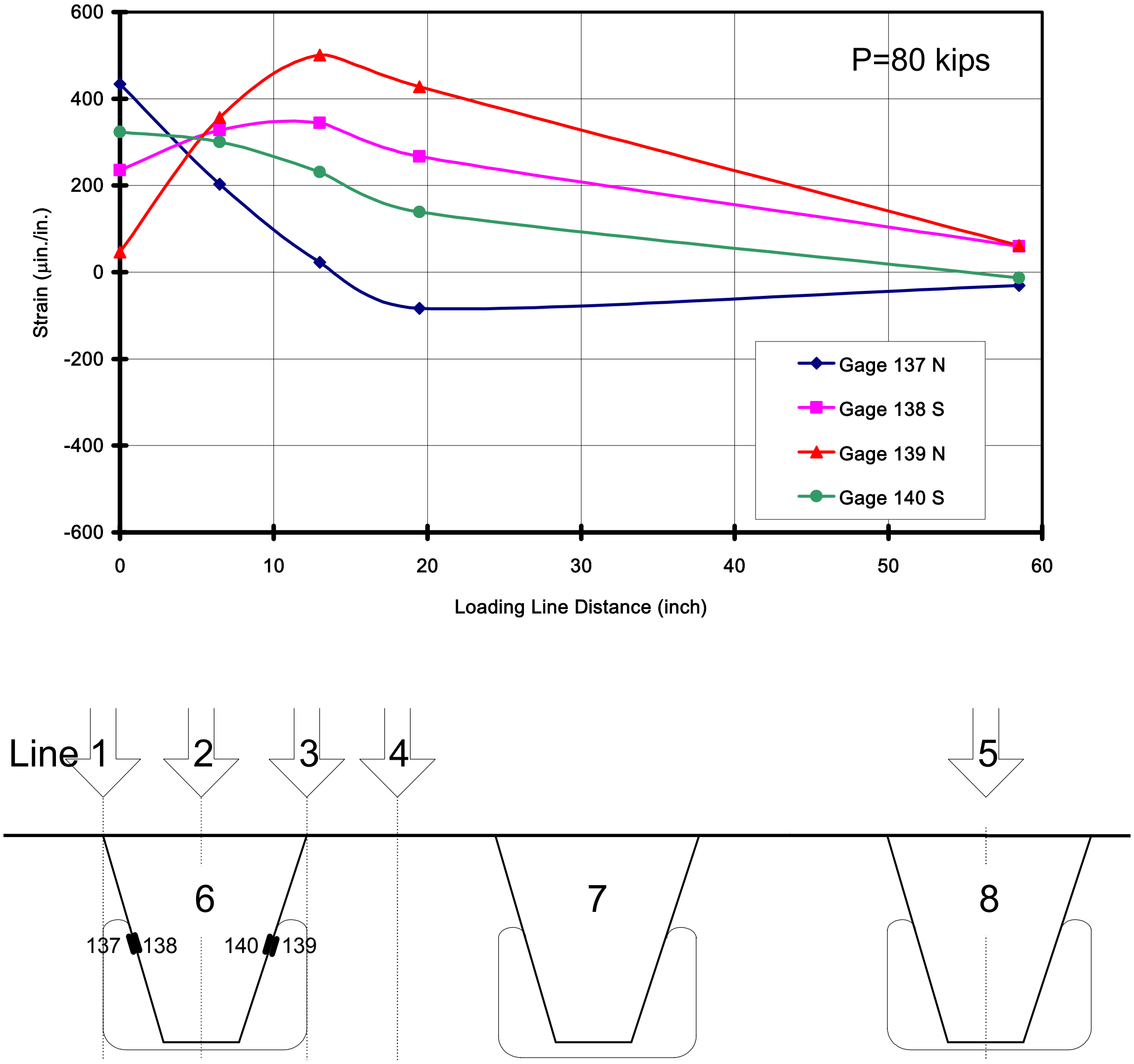

Figure 2-26 Influence lines of strains on web of Rib 6 at Diaphragm B

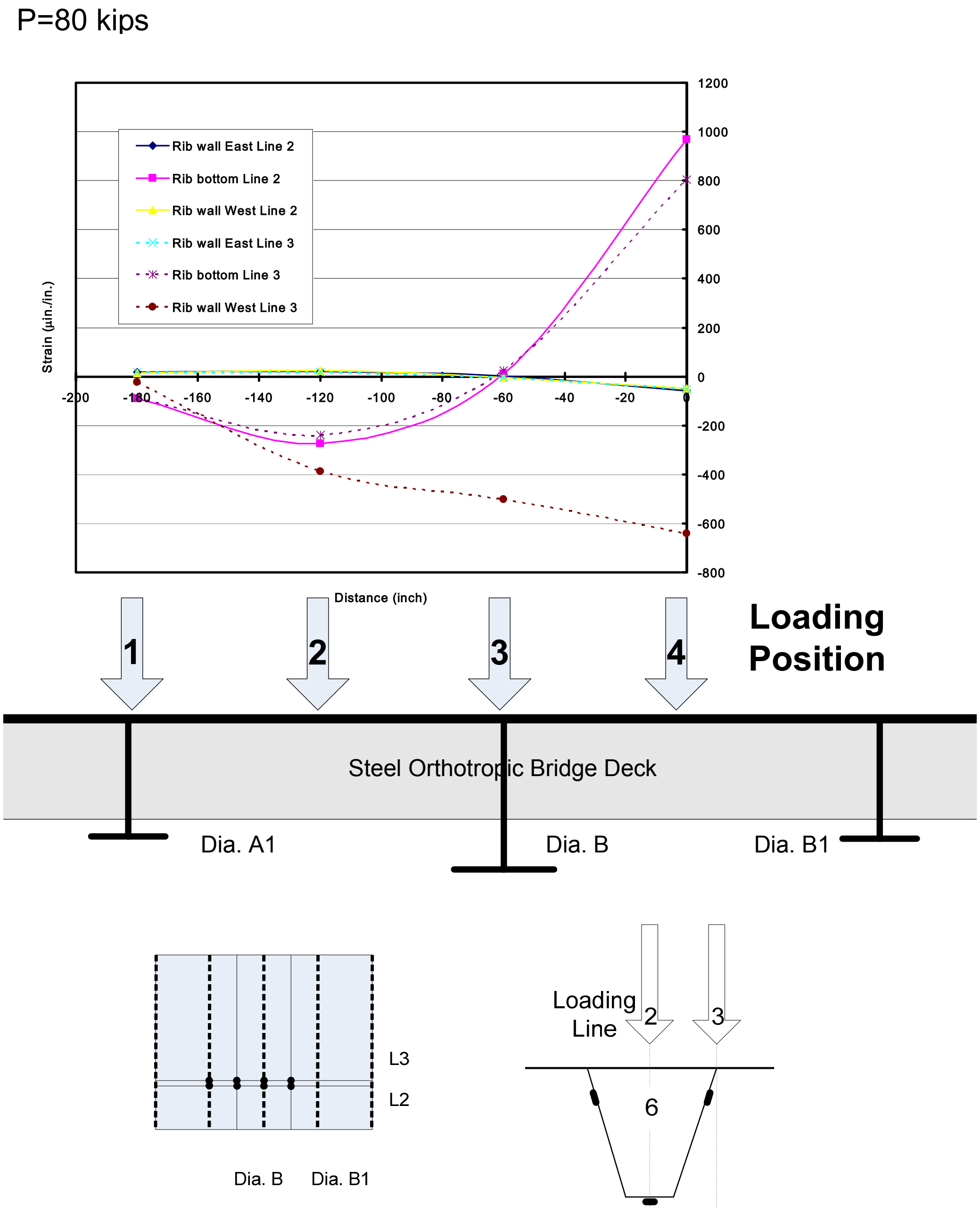

Figure 2-27 Influence Line of strain on Rib 6 between Diaphragm B and B1

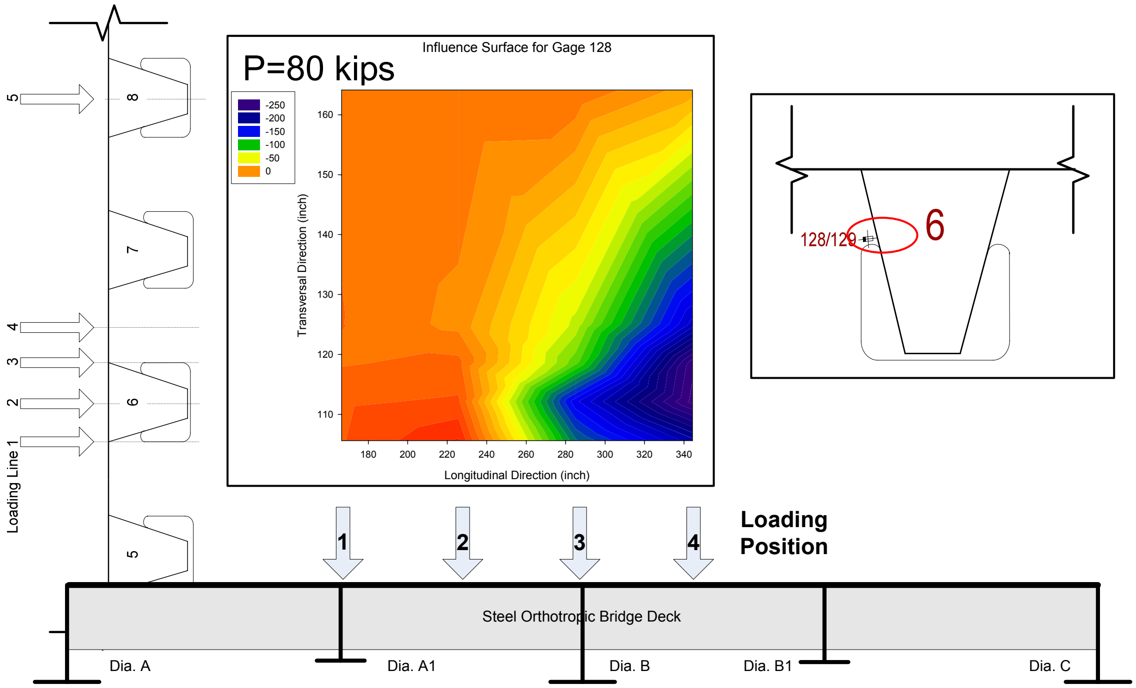

Figure 2-28 Influence Surface of Strain at top of cutout on Diaphragm B

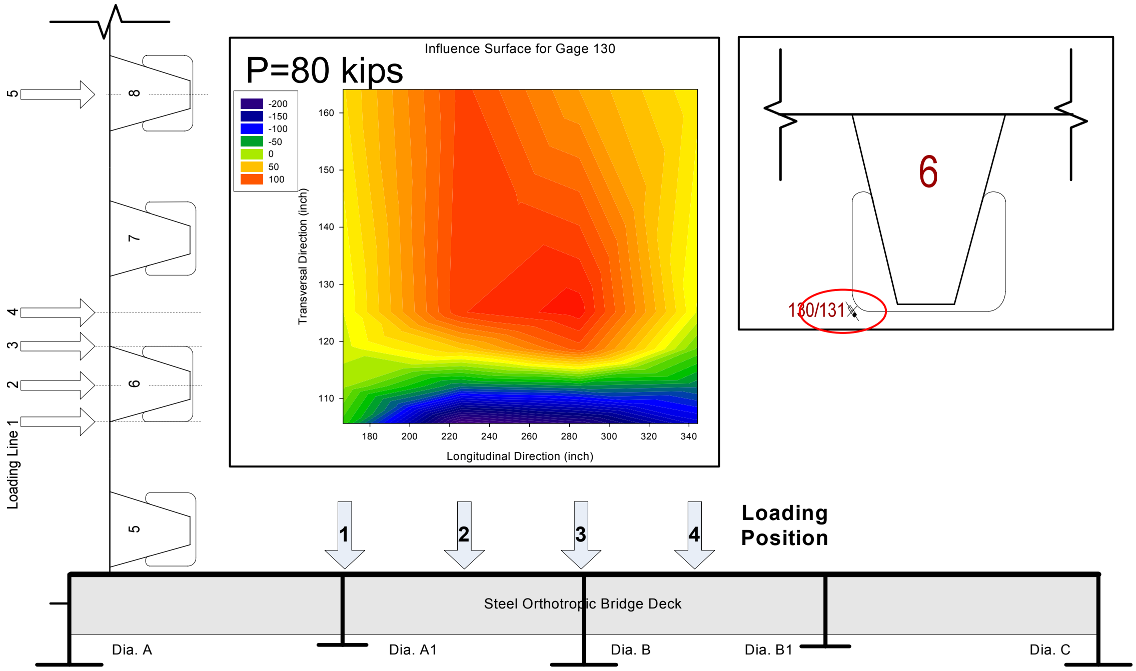

Figure 2-29 Influence Surface of Strain at bottom of cutout on Diaphragm B

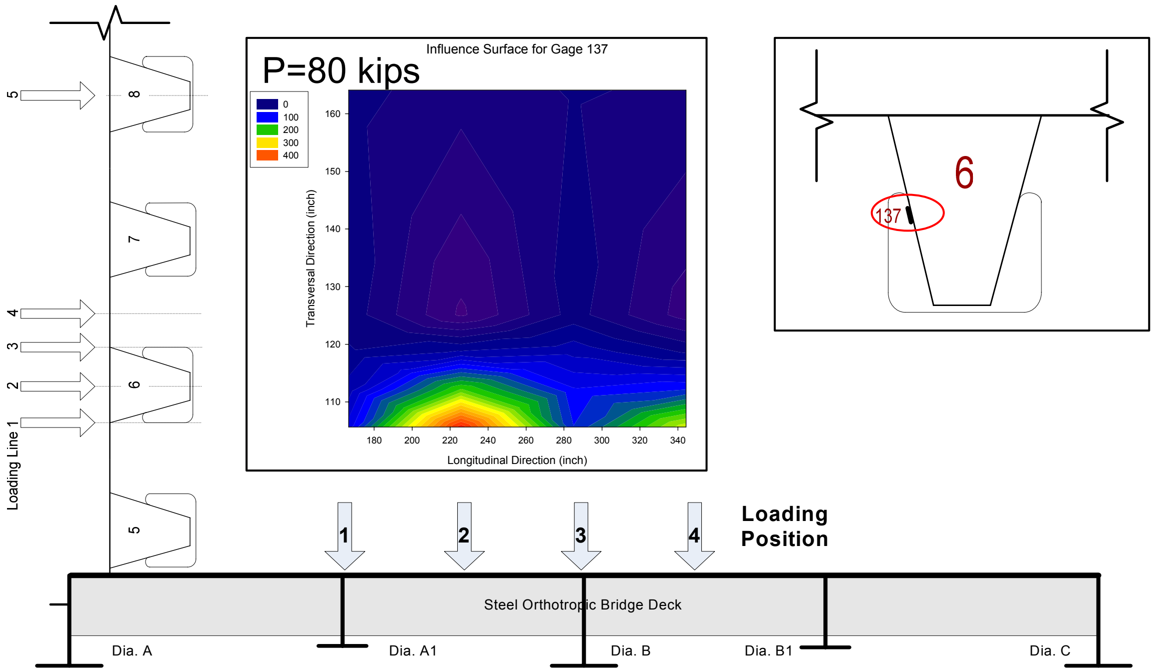

Figure 2-30 Influence Surface of Strain of Rib Wall Exterior Face at Diaphragm B

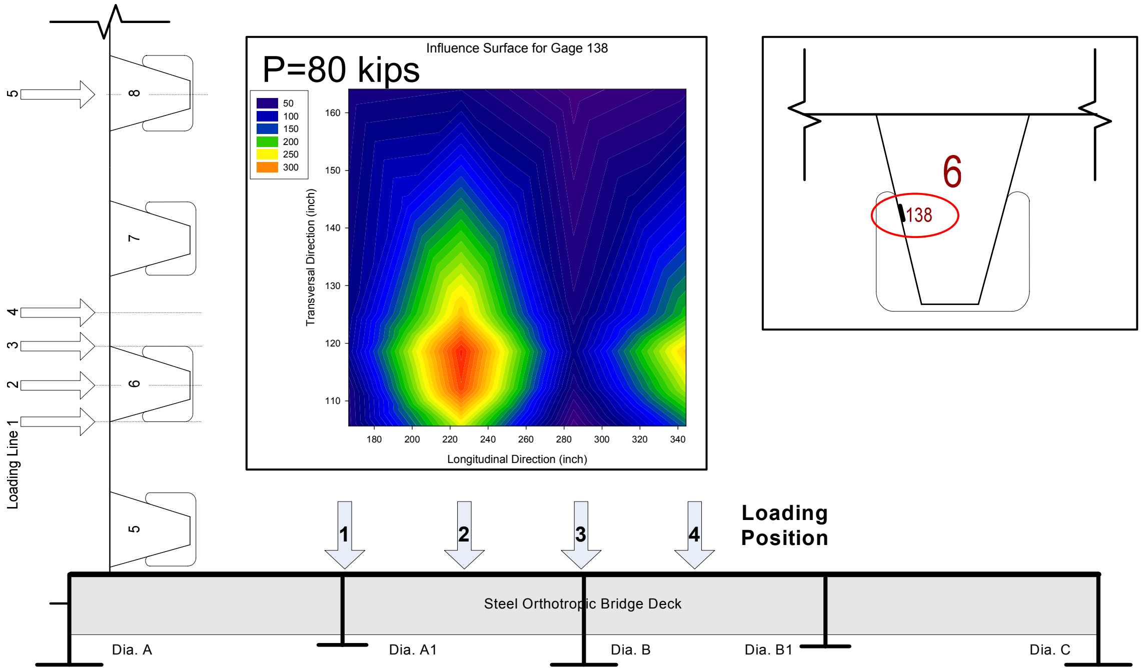

Figure 2-31 Influence Surface of Strain on Rib Wall Interior Face at Diaphragm B

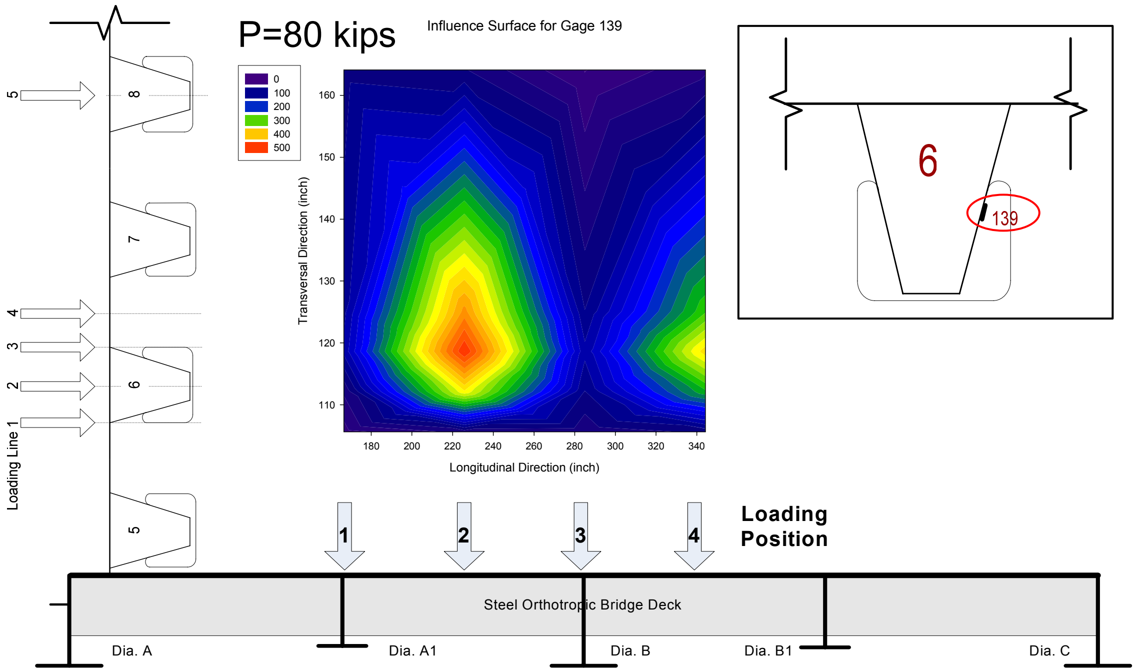

Figure 2-32 Influence Surface of Strain on Rib Wall Exterior Face at Diaphragm B

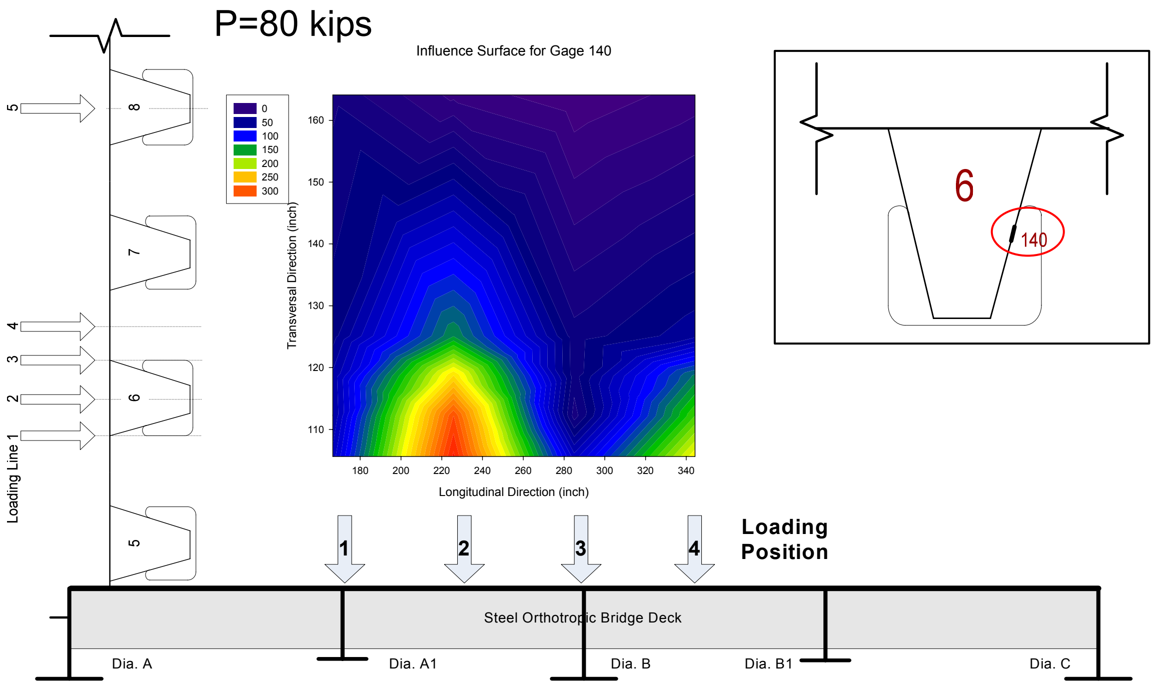

Figure 2-33 Influence Surface of Strain on Rib Wall Interior Face at Diaphragm B

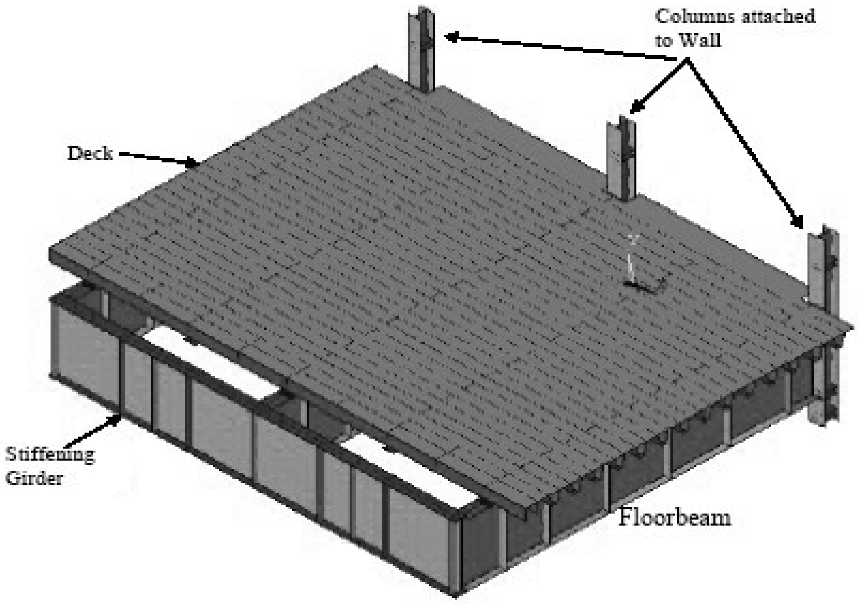

Figure 2-34 Finite Element Model of Deck Specimen

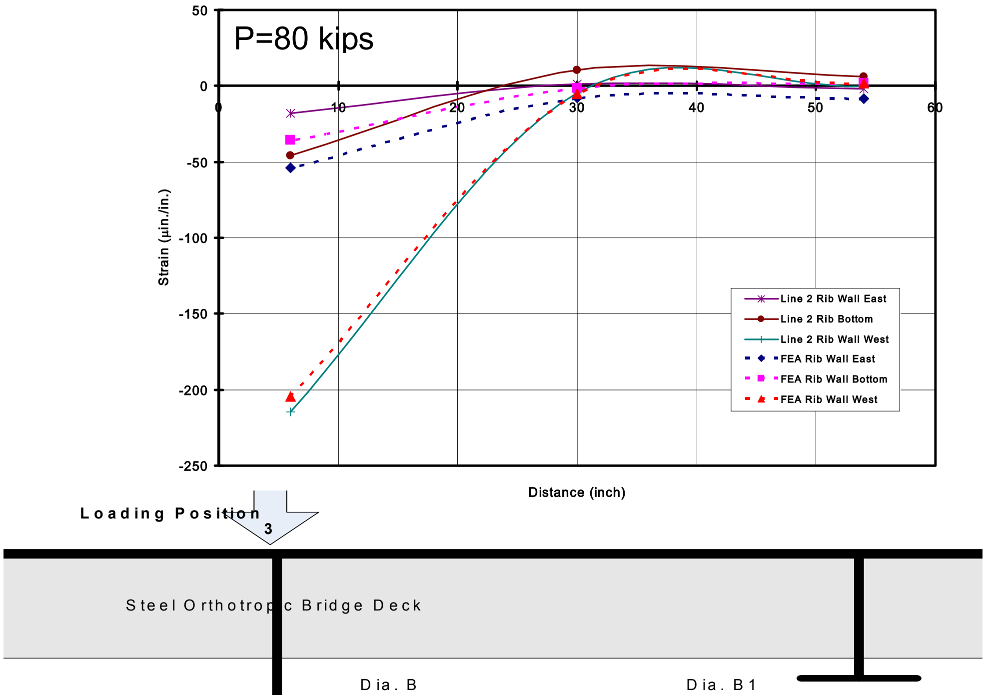

Figure 2-35 Strains in Rib 6, Load at Position 3 on Line 2

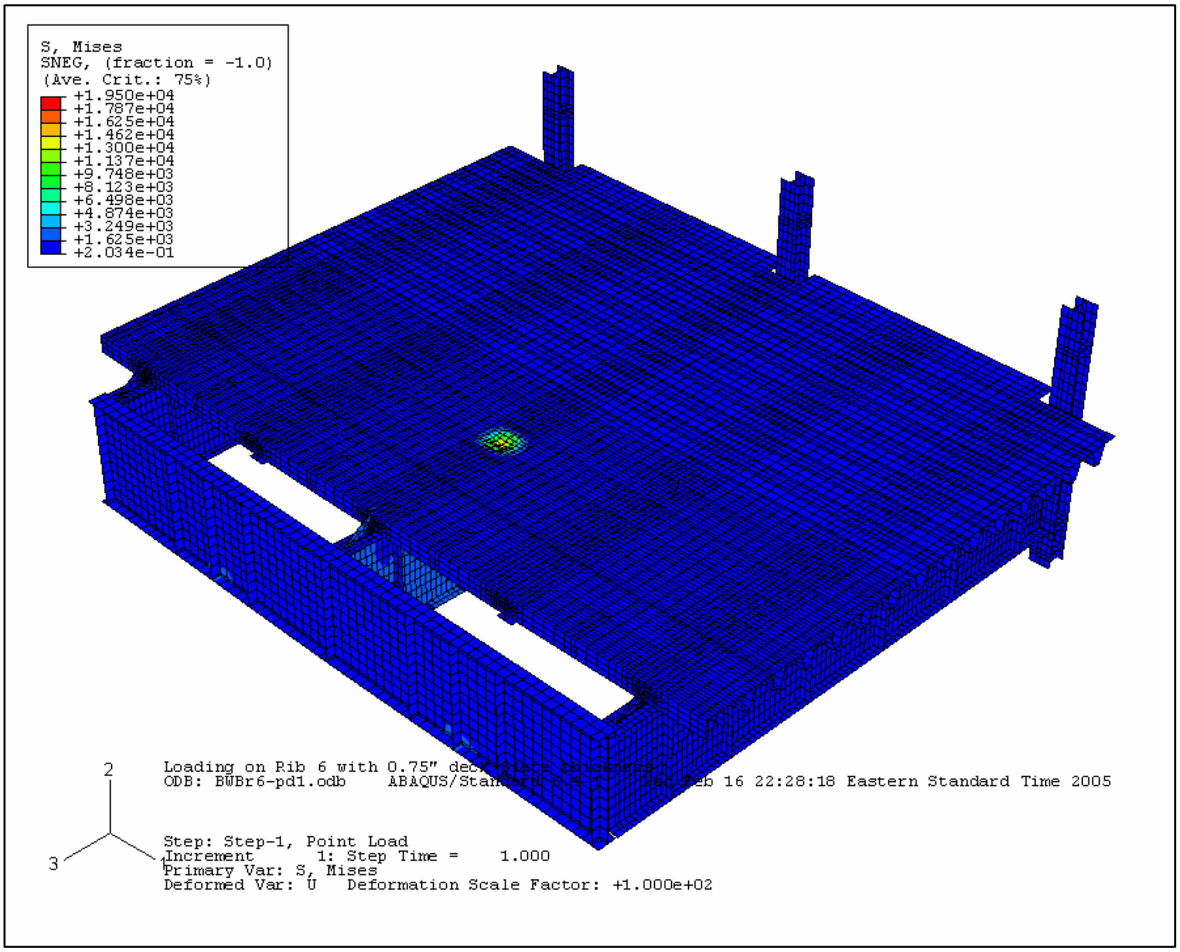

Figure 2-36 Contour of Strain in Deck Plate, Load above Rib 6 at Diaphragm B

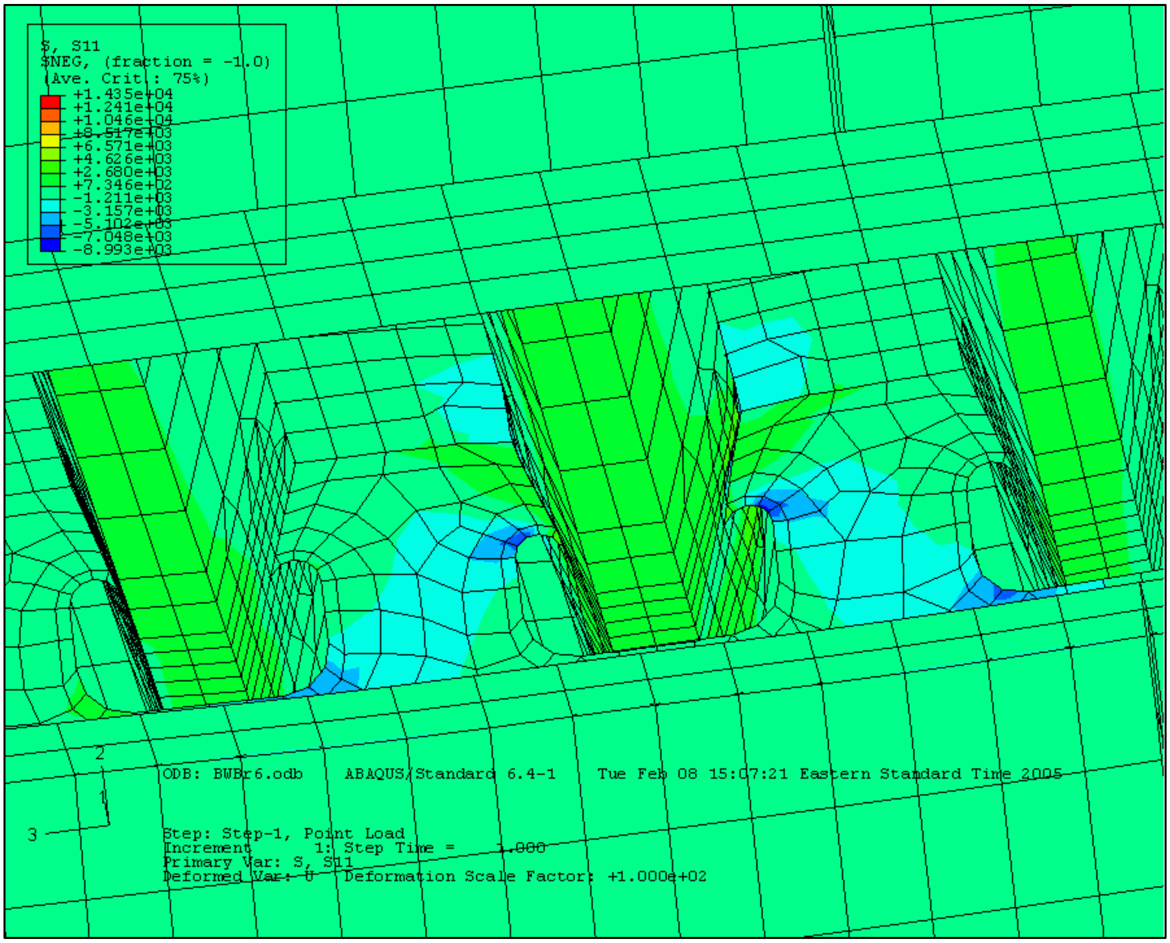

Figure 2-37 Strains in Rib 6 and Diaphragm B, Load on Deck Directly above Rib

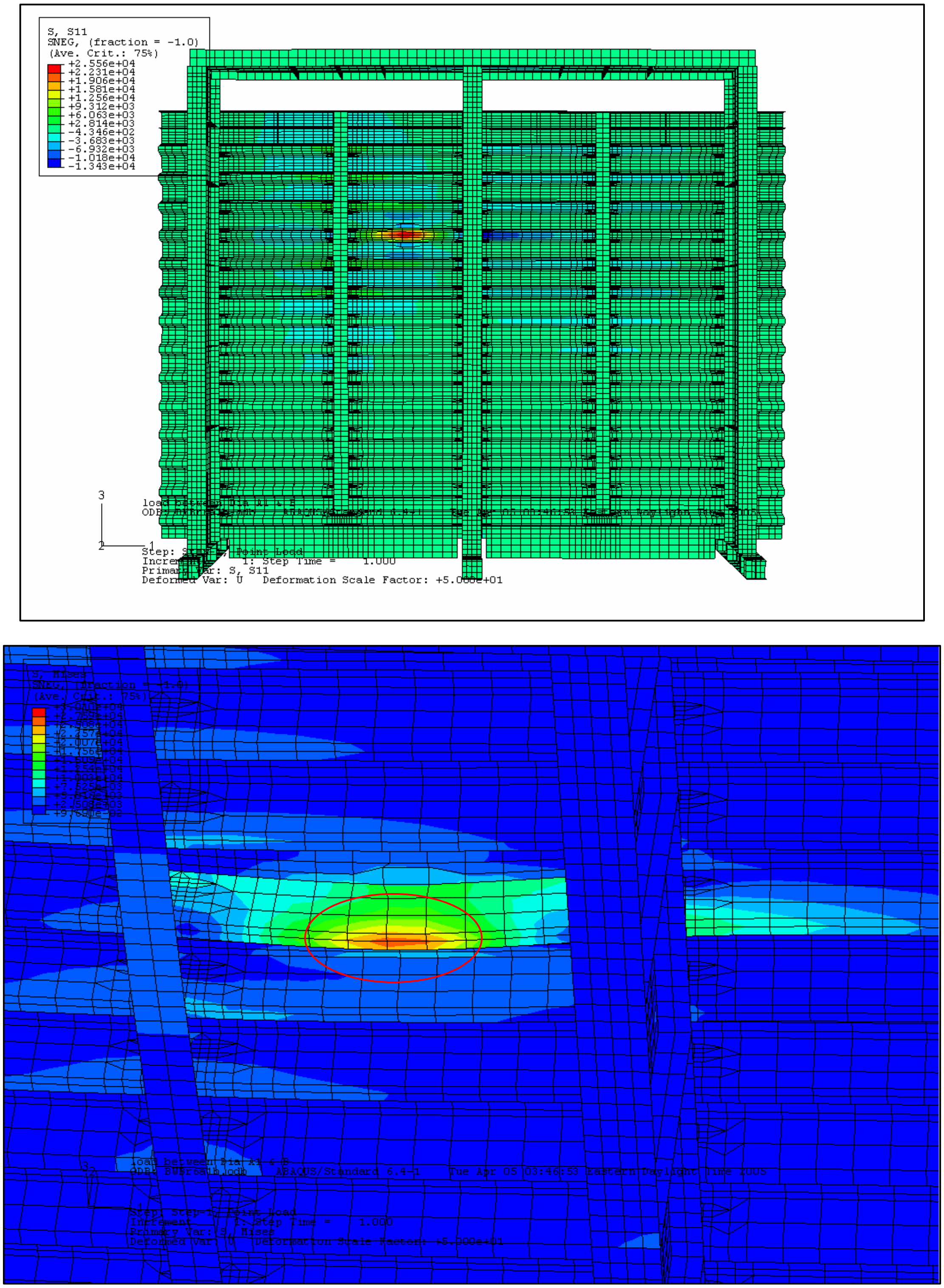

Figure 2-38 Strain Contour in Rib 6 between Diaphragm A1 and B

Chapter 3 Flexural Strength of Trapezoidal Shaped Stiffeners in Steel Orthotropic Deck

3.1 Introduction

The results of strain measurement, reported in the last chapter, indicate that a wheel load of a truck on an orthotropic deck with trapezoidal-shaped stiffening ribs is primarily carried by one rib. This condition could provide a basis for deck strength evaluation. Because a rib in an orthotropic deck resists both flexural loads from trucks and axial compression from global forces, it is necessary that the flexural, compression and “beam-column” strength of a stiffening rib is known.

Much has been done in the evaluation of local buckling of component plates of trapezoidal-shaped ribs (Wolchuk 1963) and of the overall strength of such rib in compression (Chen and Yang 2001). The behavior and strength of ribs under flexural loading is the subject of the brief examination in this chapter. Longitudinal ribs of the model test deck of the BWB were used for the bending tests.

Each bending specimen were 47.5 ft. (14.5 m) long, supported by floor beam diaphragms at mid length and at the ends, with intermediate diaphragm at the quarter points. All structural elements were made of ASTM A709 Grade 50 steel (345 MPa). The deck plate was 5/8 in. (16 mm) and the rib walls were 5/16 in. (8 mm) thick. The deck portion of each rib section was 26 in. (660 mm) wide. The ribs contained a longitudinal connection by continuity plates of the web in one span. The plane and end view of the bending test specimens are shown in Fig. 3-1(a).

3.2 Experimental Program

The program had four phases, Phase I to IV. In Phase I, individual static loads were imposed along Rib 10 of the partial deck, as shown in Figure 3-1. The longitudinal stiffening ribs 1 to 7 had been removed (for examination of possible fatigue damages) after the measurement of local stresses, which are reported in Chapter 2. The partial deck had nine trapezoidal shaped stiffeners (Rib 8-16). The partial deck is shown in Figure 3-2. The purpose of Phase I with loads on Rib 10 was to reconfirm the linear elastic behavior of the deck and to examine the local stress distribution among ribs of the partial deck without support on one edge. After Phase I testing, the partial deck was cut longitudinally to create two bending specimens. One consisted of Rib 8 alone. The other had triple ribs, Ribs 9, 10 and 11.

These two specimens can be seen in Figure 3-2.

In Phase II, the triple rib beam with Ribs 9, 10 and 11 was subjected to the same loads as in Phase I. The goal of this phase was to examine further the distribution of stresses among the ribs.

Phase III and Phase IV were the ultimate strength testing of the single rib and the triple-rib specimens, respectively. The test program is summarized in Table 3-1. The sketches of test setup are given in Figure 3-3. In Phase I and II, the load at midpoint between Diaphragms A1 and B (A1-B) was first applied and released, then the load at midspan of Diaphragms B and B1 (B-B1). And then both loads were applied simultaneously. In Phase IV, for the triple rib specimen, two actuators spaced one foot apart and centered to the midspan were needed for the ultimate load testing.

The vertical loads simulating vehicular wheels were applied though a 21 in. by 11 in. (533 mm by 279 mm) loading pad, shown in Fig. 2-7. The maximum load of Phase I and II was 300 kips (1335 kN) which is 15 times that of the wheel load of the HS 25 truck.

Nine displacement transducers (LVDTs) were used to measure the vertical deflections of the bottom of the partial deck specimen and bending specimens. The arrangement of the transducers is indicated in Figures 3-4 and 3-5. Also shown are the locations of the linear uniaxial and rosette strain gages.

3.3 Test Observation and Results

3.3.1 Observation

The test results are listed in Table 3-2. In Phase I and II, all response appeared linear elastic. There was no observed damage or permanent deformation of the partial deck of nine ribs or the triple rib beam. In Phase III and IV, failure of both the single rib and the triple rib beam was by buckling of the webs of the trapezoidal-shaped stiffener(s). Buckling of the continuity plates of rib walls occurred prior to the final failure, transforming the continuous beams into single span beams with an overhang and constraint at the failed continuity plates.

The buckled splice plates of the single rib beam and of the triple rib beam as viewed from below are shown in Figures 3-6 and 3-7. A buckled wall of a rib of the triple-rib beam at Diaphragm B is shown in Figures 3-8 and 3-9. The appearance of the beams after testing is revealed in Figure 3-10. The permanent deflection of the beam is revealed by the gap between the beam and the remaining part of the partial deck. The permanent deflection can also be seen vaguely in the top view of the partial deck in Figure 3-2, which was a photograph taken after the strength testing of the triple-rib beam.

3.3.2 Results of Phase I and II

The behavior of the partial deck in Phase I was linear when the 300 kips (1335 kN) load was applied between Diaphragm A1 and B (Point A1-B). This is depicted by the straight lines of the load-displacement relationship in Figure 3-11(a) for all nine displacement transducers. The maximum deflection of the partial deck under load was 0.738 in. (19.3 mm) by LVDT8. At 80 kips, (489.3 kN), the deflection was 0.2 in. (5 mm). This is comparable but slightly higher than the 0.18 in. (4.6 mm) of Rib 6 of the full deck when the load was directly above (see Figure 2-21). Obviously, the partial deck without support on one edge was less rigid than the full deck with support on all edges.

When the load was at midspan between Diaphragm B and B1 (Point B-B1), the vertical deflection at the measurement points are shown in Figure 3-11(b). The maximum deflection of the rib directly under load was 0.78 in. (19.8 mm), which is slightly higher than the maximum value of 0.738 in. (19.3 mm) in Figure 3-11(a). This is attributed to the onset of nonlinear behavior of the rib connections in the span. The load-deflection lines in Figure 3-11(b) deviate from being straight lines at about 200 kips (890 kN). However, when the applied load was removed, there was little residual deflection at the measurement points.

With both loads at the Points A1-B and B-B1 applied simultaneously up to 300 kips (1335 kN) each, the magnitudes of vertical deflection were reduced because of the load in the neighboring span. The load-deflection behavior is shown in Figure 3-11(c). The maximum deflection was 0.68 in. (17.3mm) and 0.66 in. (16.8mm) at Points B-B1 and A1-B respectively. The slight nonlinear behavior started at about 160 kips (712 kN).

In Phase II, testing of the triple-rib beam was made under the same loading condition as in Phase I for the partial deck. The load-deflection diagrams are presented in Figures 3-12 (a, b and c). Again, the behavior of the specimen was linear under the 300 kips (1335 kN) load at Point A1-B (Figure 3-12(a)) and slightly nonlinear when the load was at Point B-B1 (Figure 3-12(b)) and at both Points (Figure 3-12(c)). This phenomenon is consistent between Phase I and II. When both loads were applied simultaneously in Phase II, LVDT4 under the load point of Rib 10 at B-B1 revealed relatively higher nonlinear behavior in that region. However, no local damage or unusual occurrence was observed or detected from strain readings.

The magnitude of the maximum vertical deflection during Phase I and Phase II testing are listed in Table 3-3. In Phase II, there were only three ribs to resist the same magnitude of applied loads in comparison to nine ribs for Phase I. The magnitudes of vertical deflection were higher in Phase II.

3.3.3 Results of Phase III, Single-rib Beam Test

Phase III was the flexural strength testing of Rib 8 to failure. The loading scheme is shown in Figure 3-3(b), with the simulated wheel load applied at the midpoint between Diaphragm A1 and B. The load-displacement relationships at this point (LVDT6) and at the middle of the next span (LVDT1) are plotted in Figure 3-13. The relationship was linear up to the buckling (out-of-plane bending) of the splice plates of the rib walls between Diaphragm B and B1, at about 160 kips (712 kN). The calculated yield load at first yielding of the rib bottom without considering residual stresses was about 100 kips (445 kN).

At bending of the splice plate, the actuator load dropped. The load was reduced to zero and then reapplied. The single rib beam specimen was now a single span beam with an overhang from Diaphragm B to the rib splice, which provided constrain to the beam. This “new” beam of a single rib could sustain an ultimate load slightly less than 160 kips (712 kN). The failure mode was the buckling of the rib wall near Diaphragm B.

The measured strains at some gage locations in Phase III are shown in Fig. 3-14 to 3-18 for the rib bottom, the rib wall, the top and bottom of deck plate and the spliced connection. The strains increased proportionally with the applied load at almost all locations in compliance with the bending moment diagram of Figure 3-19. The stresses at the bottom of the rib at the loading point (Figure 3-14) started to deviate from being linear at about 80 kips (356 kN). This corresponded to the beginning of nonlinear behavior of a rib splice plate in the adjacent span, as depicted by the strains at Gages 33 and 34 in Figure 3-18. When the strain at Gage 35 on the bottom of the rib at the connection reached about 1500 με (43.5 ksi, 300 MPa), the splice plate buckled outward. The strains on the outer surface of the splice plates became tensile.

Figure 3-20 presents the stresses in the beam cross section under the load (A1-B) and at Diaphragm B before failure of the single rib beam. The distribution was slightly unsymmetrical with respect to the vertical axis of the beam. The onset of rib connection failure in the adjacent span obviously had strong influence on the stress distribution at the cross section. The ability of the trapezoidal-shaped rib to endue torsion associated with the unsymmetrical stress distribution is evident from these results.

3.3.4 Results of Triple-rib Beam Test, Phase IV

The loading scheme is shown in Figure 3-3(c). Two actuators spaced one foot apart applied loads on Rib 10 at the midpoint between Diaphragm A1 and B. Two actuators were needed for the high magnitude of expected failure load of the specimen. The load-displacement curves in Figure 3-21 are for the loading cross section (LVDT8) and the midspan cross section of the adjacent span (LVDT4). The vertical downward displacement under load was higher than the uplift of the adjacent span. The onset of nonlinear behavior began around 370 kips (1647 kN), above the computed yield load of 300 kips (1335 kN). The failure of the beam was at 591 kips (2630 kN) due to buckling of the rib connection splice plates (Figure 3-7).

The increases of strains at strain gages on the splice plates (SG 54, SG 55) and on the bottom of Rib 10 (SG 53, SG 56) are plotted in Figure 3-22. Also included are the increase of strain at gages (SG 220, SG 221) on the walls and at gages (SG 219-SG 222) at the bottom of the rib between the loading point and Diaphragm B (see Figure 3-3 (b) for gage location). Around 370 kips (1647 kN), the strains deviated from linear, changed more pronouncedly with the increased load. Around 500 kips (2225 kN) the strains on the splice plate surface changed from compression to tension. This signified the large out of plane deflection of these plates. The bottom of Rib 10 near the load point (SG 219) was subjected to very high strain before failure of the connection of all ribs (Figure 3-7). At the failure load, the walls of the ribs at Diaphragm B started to buckled (Figure 3-8 and 3-9).

Strains increased linearly with load at other points on the bottom and the webs of Rib 10, as shown in Figure 3-23 and 3-24. All exhibited changes around 370 kips (1647 kN) and at higher load magnitudes. Figure 3-25 shows the strains on the rib walls at two cross sections of the specimen at 370 kips (1647 kN) and 500 kips

(2225 kN) of load on Rib 10. The participation of all rib in carrying the applied load is evident.

By assuming that the three ribs took equal shares in carrying the applied load, the load-deflection curves of Figure 3-21 for the triple-rib beam are converted to average curves for each rib. These are shown in Figure 3-26 to compare with those of the single rib beam from Phase III. It reveals that the behavior of the specimens are quite similar. The average strength of the triple-rib beam is higher. This is expected because of the constraint provided by the adjacent ribs of the triple-rib beam.

3.4 Finite Element Analysis

Finite element models (FEM) for the analysis of the single and triple-rib specimens were developed. As in modeling the deck in Chapter 2, the nonlinear finite element software ABAQUS (2004) was selected. The models are shown in Fig. 3-27 and 3-28. ABAQUS S4R elements were selected to model the test specimen. Because the major concerned of this study was the strength of the orthotropic deck, not the connection of individual ribs, the splice plate connections was ignored.

The failed shape of the finite element models are shown in Figure 3-29 and 3-30, with a large scale for deflection. The shapes are in full agreement with the experimental results. The load deflection curves from the FEM for the single rib and triple-rib bending specimens are shown in Figures 3-31 and 3-32 for comparison with the experimental results. The analytical and experimental curves agree fairly well before failure of the beams at the rib connection. Without failure of the connections, the single rib beam would be able to resist a 300 kips (1335 kN) downward load. The triple-rib beam had a strength of more than 900 kips (4005 kN), or 300 kips for each rib.

3.5 Discussions and Conclusions

The examination reported in this chapter on flexural loads on partial deck panels and on single rib and triple-rib beams lead to the following conclusions.

First, the partial deck panels which were supported on three sides and free on the fourth, behaved linearly under a simulated wheel load up to 300 kips (1335 kN) in the panel. The behavior was slightly nonlinear when the load was in the partial panel with the rib connections, and when two simultaneous loads were in the two adjacent panels. Second, one or two 300 kips (1335 kN) loads applied on a triple-rib continuous beam, which was isolated from the partial deck, induced similar behavior as that of the partial deck panel.

A single rib continuous beam sustained a maximum vehicular wheel load of 162 kips (720 kN) in one span with failure located at the rib connection in the other span. A similar triple-rib beam sustained 591 kips (2631 kN), being slightly higher than three times the single-rib beam strength. This condition indicates the participation of all ribs of the triple-rib beam in carrying loads placed on one rib. Analysis by finite element models indicates that the strength of each rib without a connection would be 300 kips (1335 kN) or higher.

The magnitude of 300 kips (1335 kN), being the maximum applied load on the partial deck panels as well as the flexural load strength of each rib, is 15 times the HS 25 wheel load of 20 kips (89 kN). With the conclusion from Chapter 2 that wheel loads affect primarily only one rib (or at most also the adjacent rib), and that wheel loads of the same axle are two or more ribs apart, it can be concluded that axle loads of HS 25 trucks do not cause problem with respect to static flexural strength of the ribs of the model deck.

Table 3-1 Test Program

Phase	Specimen	Loads on
I	Nine ribs, (8-16)	Rib 10
II	Triple-rib, (9-11)	Rib 10
III	Single-rib, (8)	Rib 8
IV	Triple-rib, (9-11)	Rib 10

Table 3-2 Test Results

Test Phase	Specimen	Load on	Max. Load (kips)	Deflection (inch)	Failure Mode
I	Nine-ribs (8-16)	Rib 10	300.00	0.738	NA
II	Triple-rib, (9-11)	Rib 10	300.00	0.931	NA
III	Single-rib, (8)	Rib 8	162.12	1.143	Buckling of rib connection plate
IV	Triple-rib (9-11)	Rib 10	591.36	3.720	Buckling of rib connection plate

Table 3-3 Maximum Vertical Deflection Phase I and II

Test Phase	**Specimen**	**Load on**		**Deflection (inch)**	**At**
		Rib	**Point**		
I	Nine Ribs (8-16)	10	A1-B	0.738	A1-B
			B-B1	0.780	B-B1
			A1-B and B-B1	0.680	A1-B
II	Triple-rib (9-11)	10	A1-B	0.930	A1-B
			B-B1	0.900	B-B1
			A1-B and B-B1	0.720	A1-B

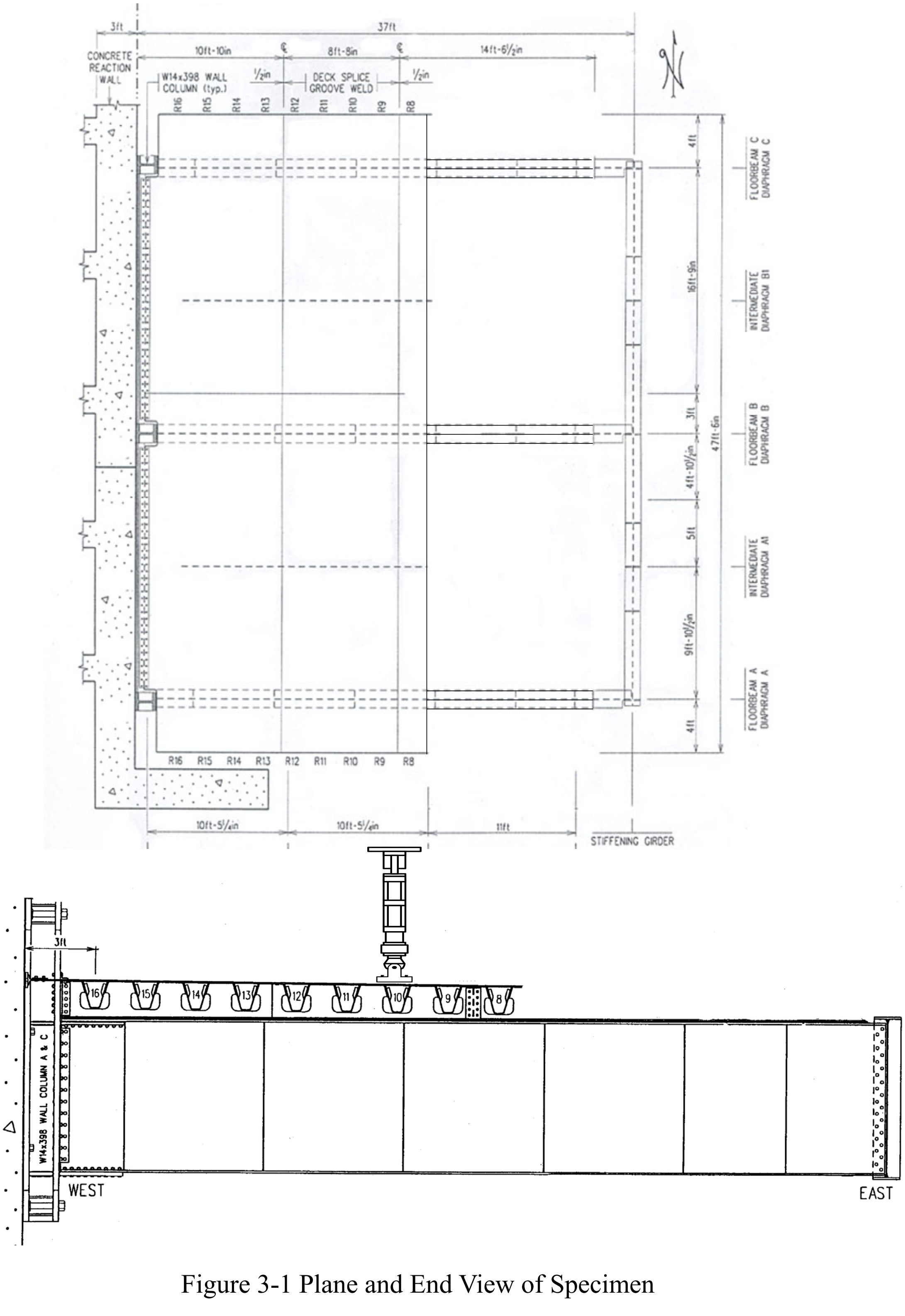

Figure 3-1 Plane and End View of Specimen

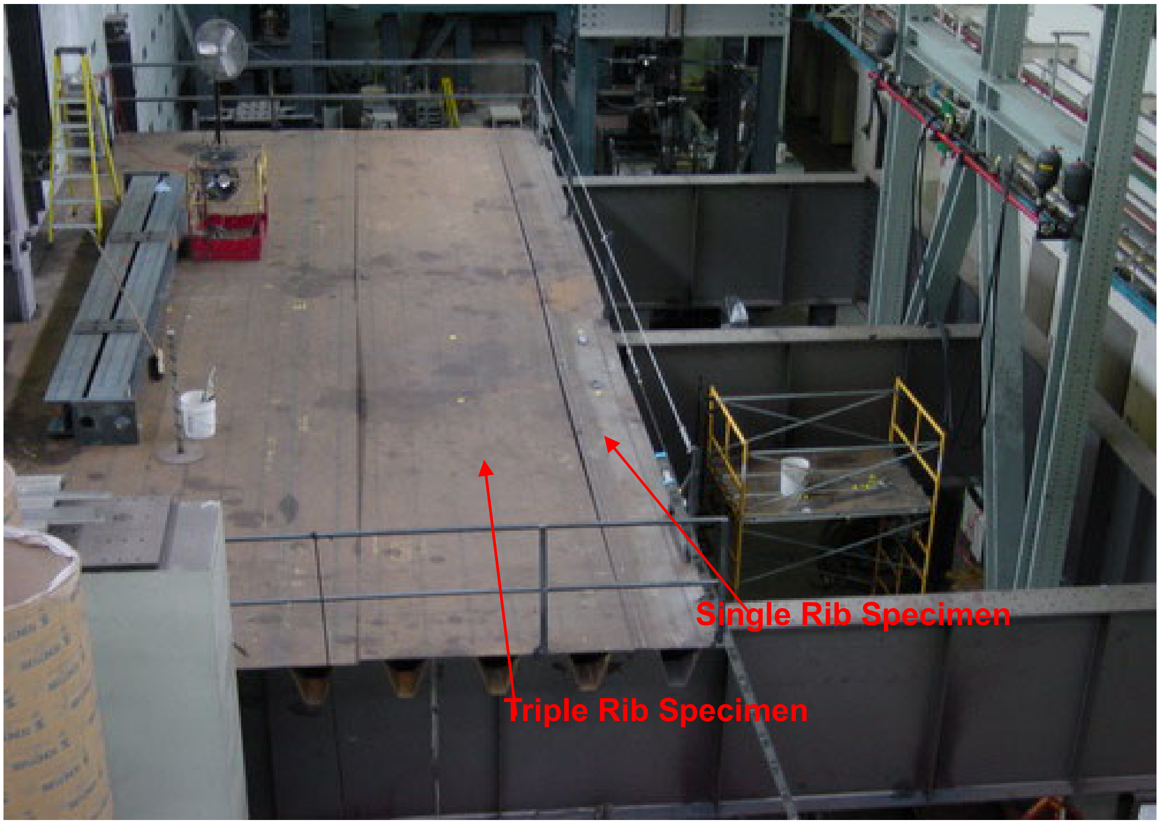

Figure 3-2 Partial Deck, Rib 1 to 7 Removed

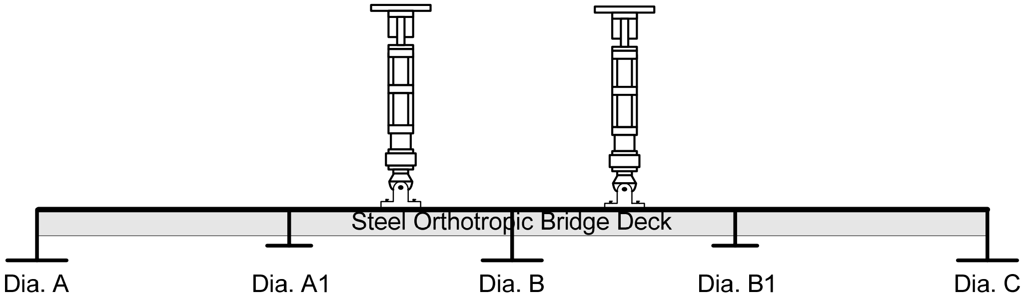

(a) Phase I and II tests

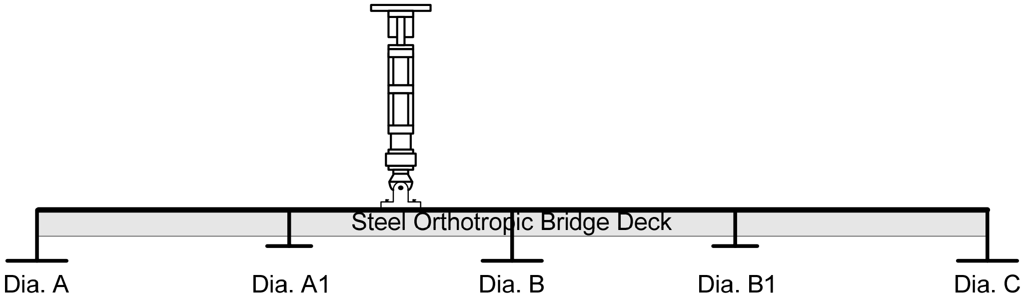

(b) Phase III test

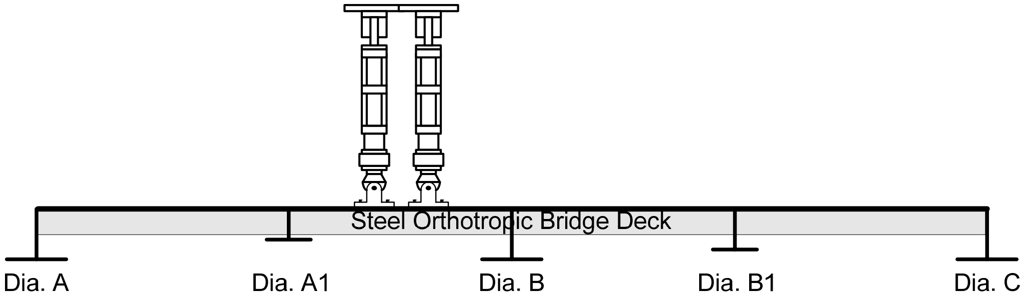

(c) Phase IV test

Figure 3-3 Sketches of Test Setup

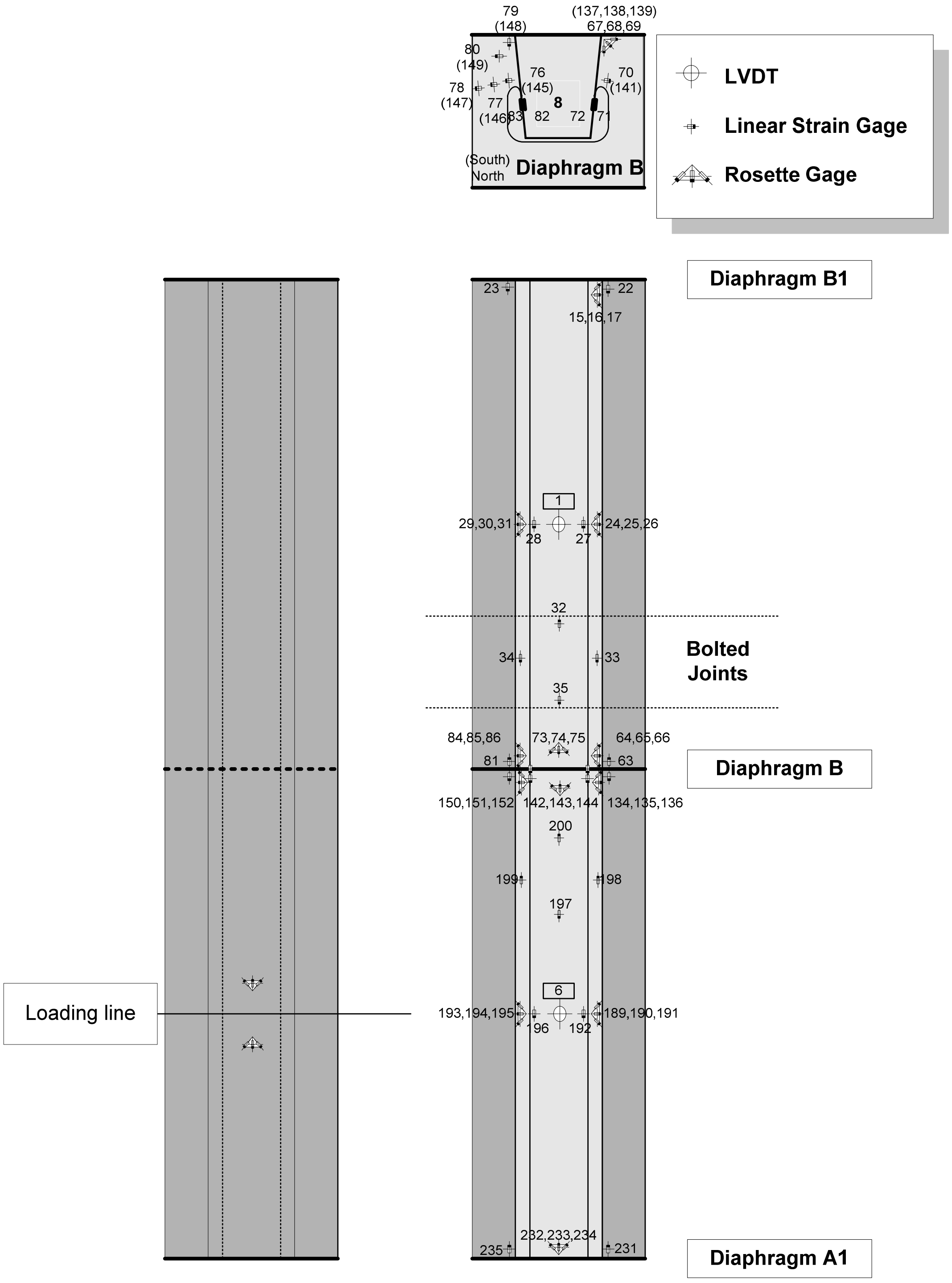

(a) Top of Deck Plate (b) Bottom of Deck Plate and Rib Walls

Figure 3-4 Arrangement of the displacement transducers and strain gages, Phases I and III

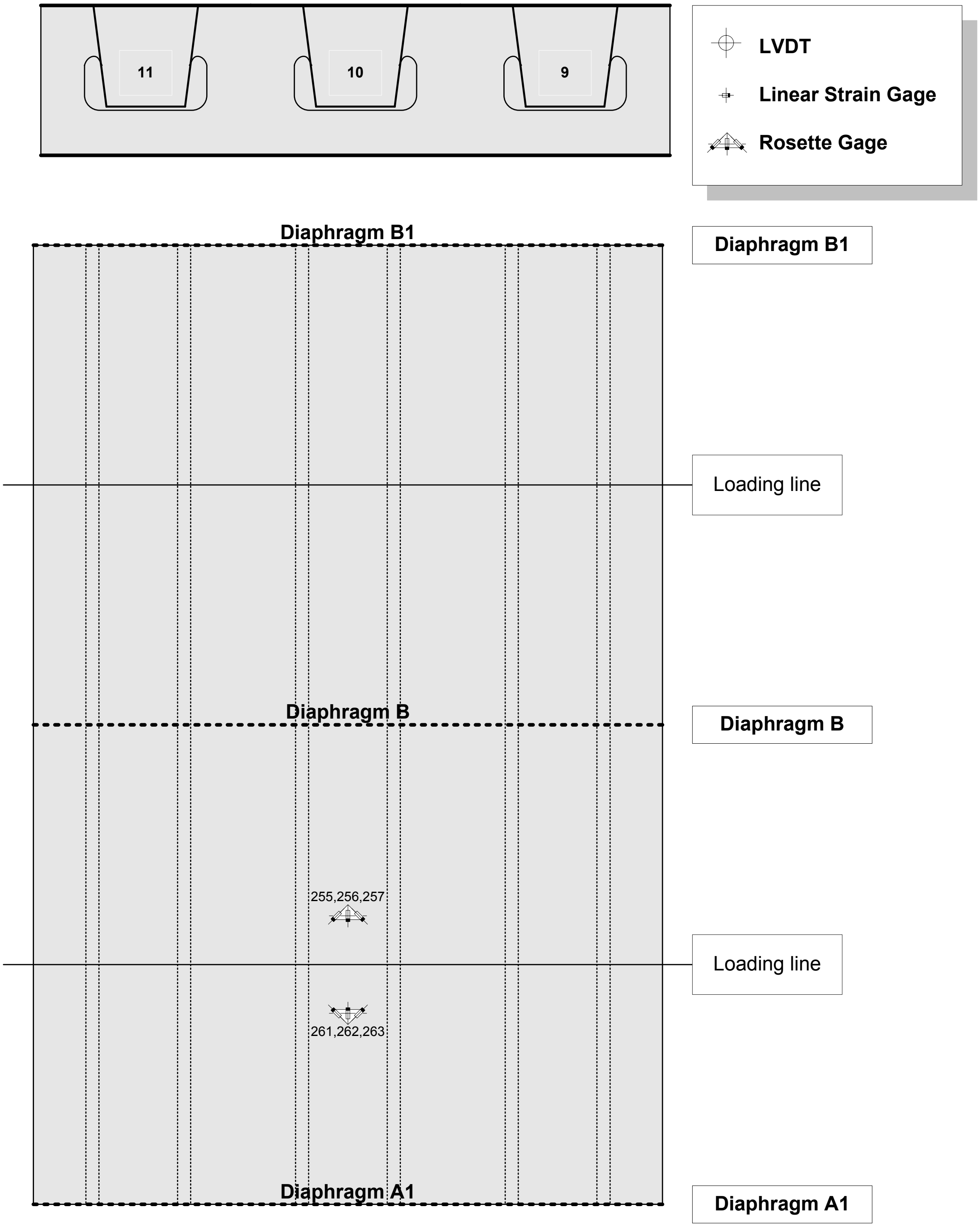

Figure 3-5 (a) Top of Deck Plate

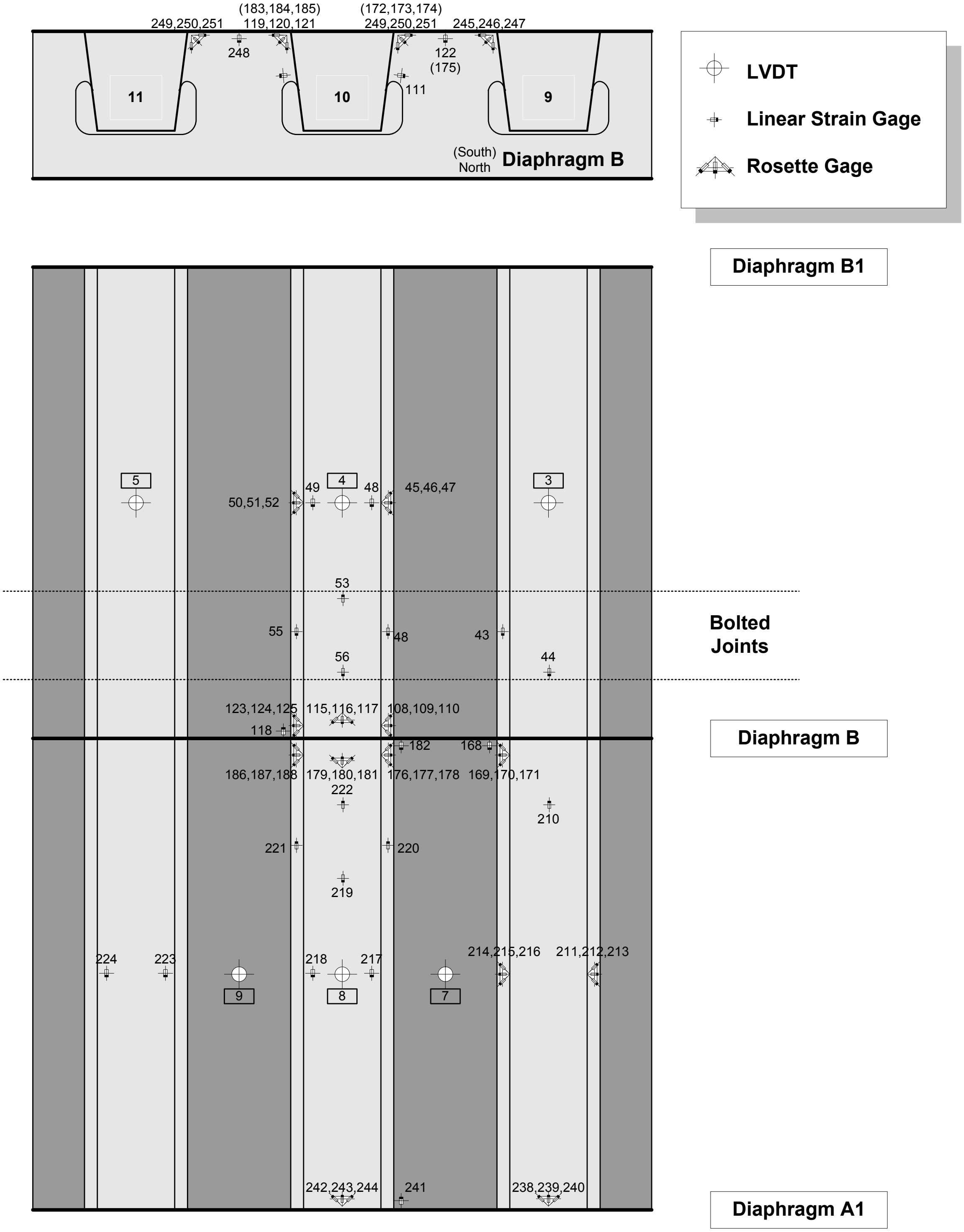

(b) Bottom of Deck Plate and Rib Walls

Figure 3-5 Arrangement of the displacement transducers and strain gages, Phase I, II and IV

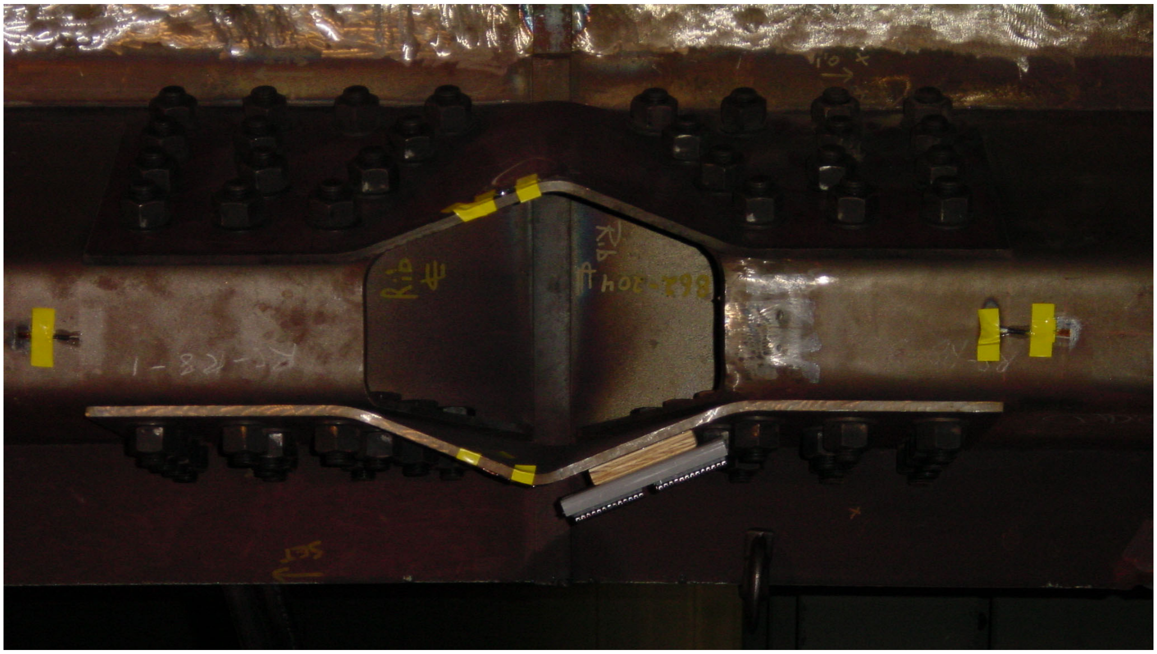

Figure 3-6 Buckled Splice Plates, Single-rib Beam

Figure 3-7 Buckled Splice Plates, Triple-rib Beam

Figure 3-8 Buckled rib wall, Triple-rib Beam

Figure 3-9 Closed Up View of Buckled Rib Wall of Triple-rib Beam

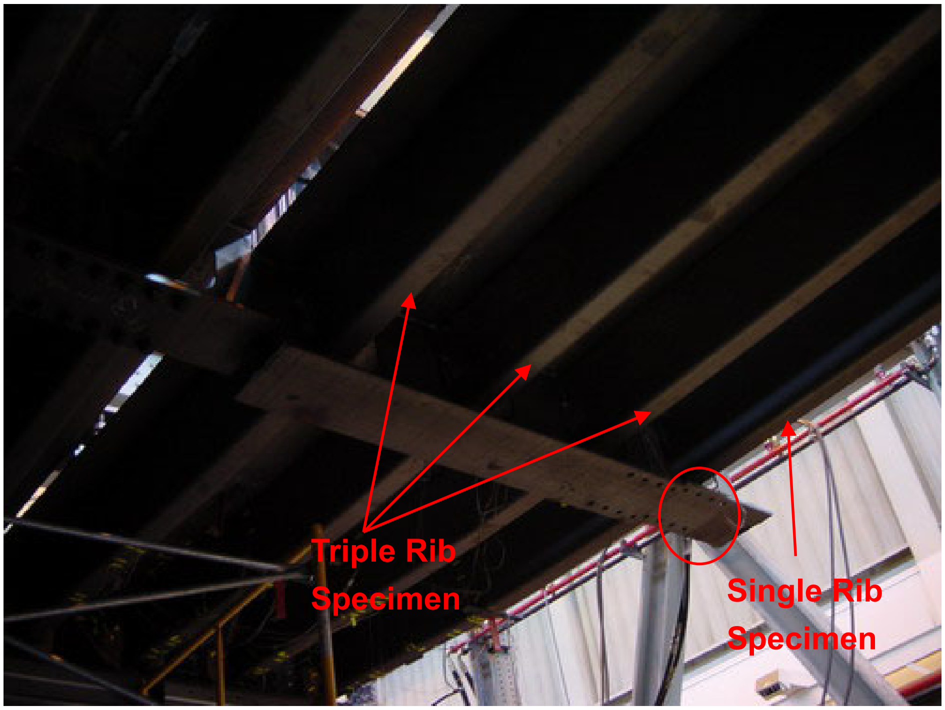

Figure 3-10 Appearance of Single and Triple-rib Beams after Testing Viewed from Below

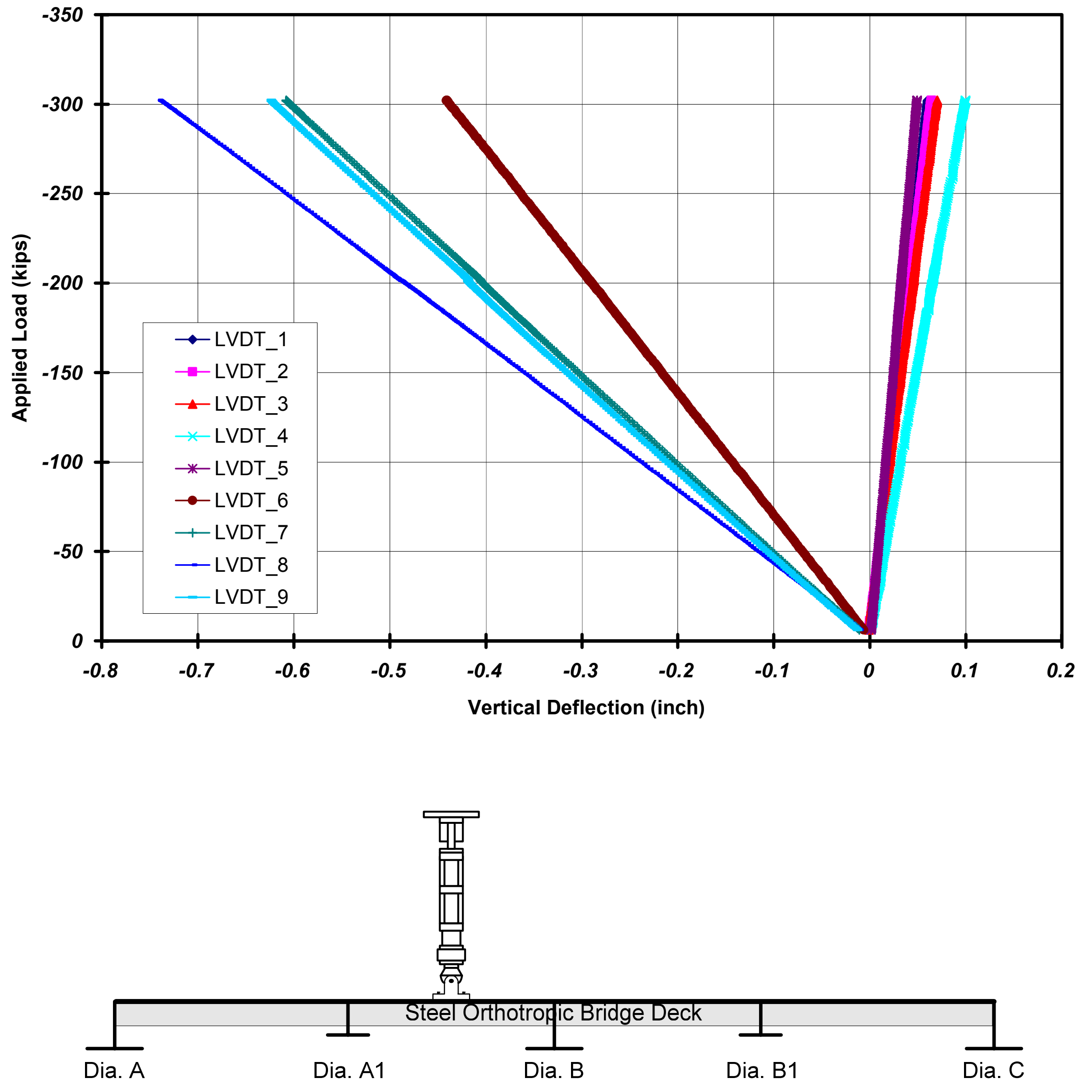
Applied Load (kips)
-350
-300
-250
-200
-150
-100
-50
0
-0.8
-0.7
-0.6
-0.5
-0.4
-0.3
-0.2
-0.1
0
0.1
0.2
Vertical Deflection (inch)
LVDT_1
LVDT_2
LVDT_3
LVDT_4
LVDT_5
LVDT_6
LVDT_7
LVDT_8
LVDT_9
Steel Orthotropic Bridge Deck
Dia. A
Dia. A1
Dia. B
Dia. B1
Dia. C

Figure 3-11 (a)

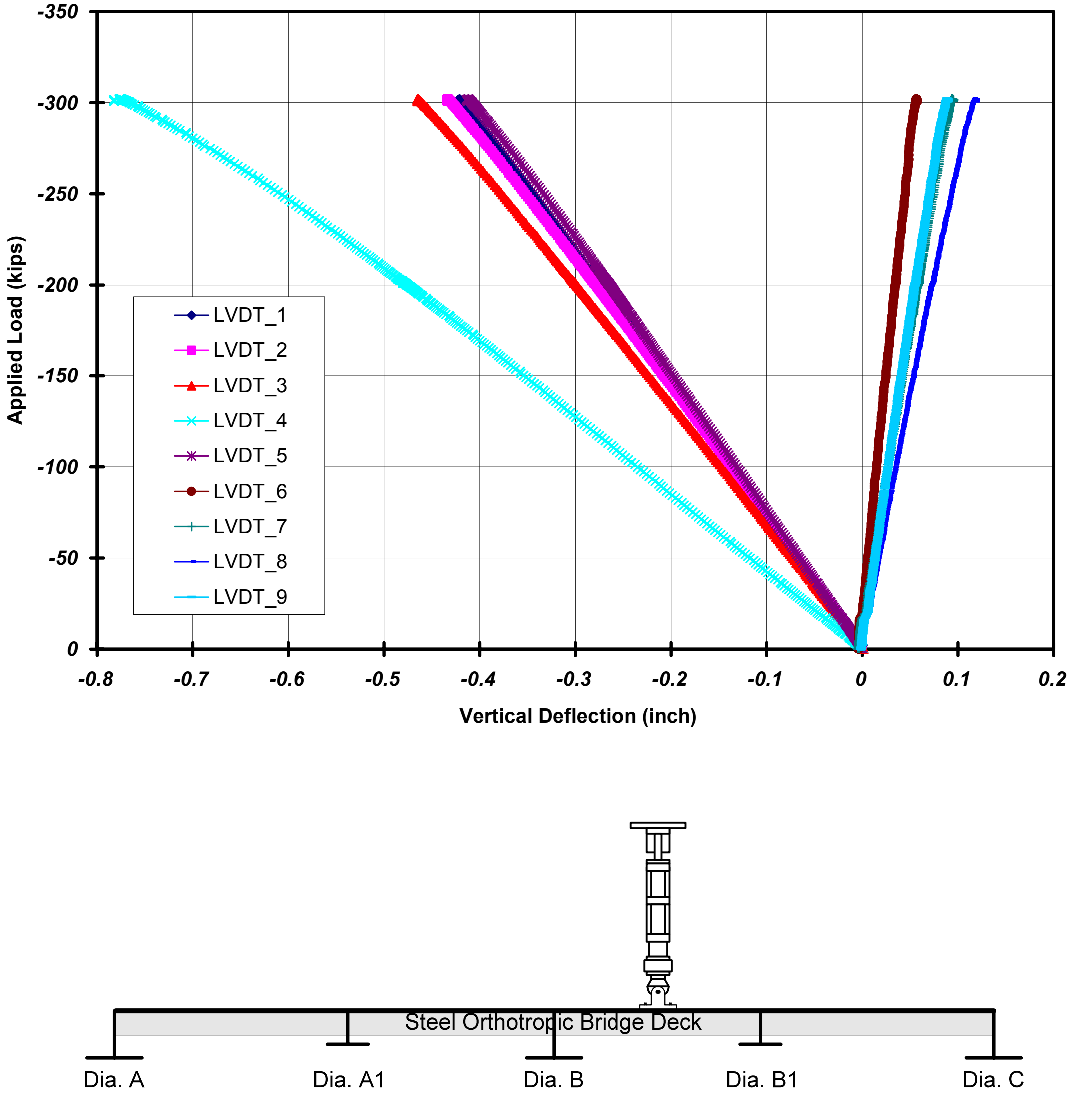
-350
-300
-250
-200
-150
-100
-50
0
Applied Load (kips)
-0.8
-0.7
-0.6
-0.5
-0.4
-0.3
-0.2
-0.1
0
0.1
0.2
Vertical Deflection (inch)
LVDT_1
LVDT_2
LVDT_3
LVDT_4
LVDT_5
LVDT_6
LVDT_7
LVDT_8
LVDT_9
Steel Orthotropic Bridge Deck
Dia. A
Dia. A1
Dia. B
Dia. B1
Dia. C

Figure 3-11 (b)

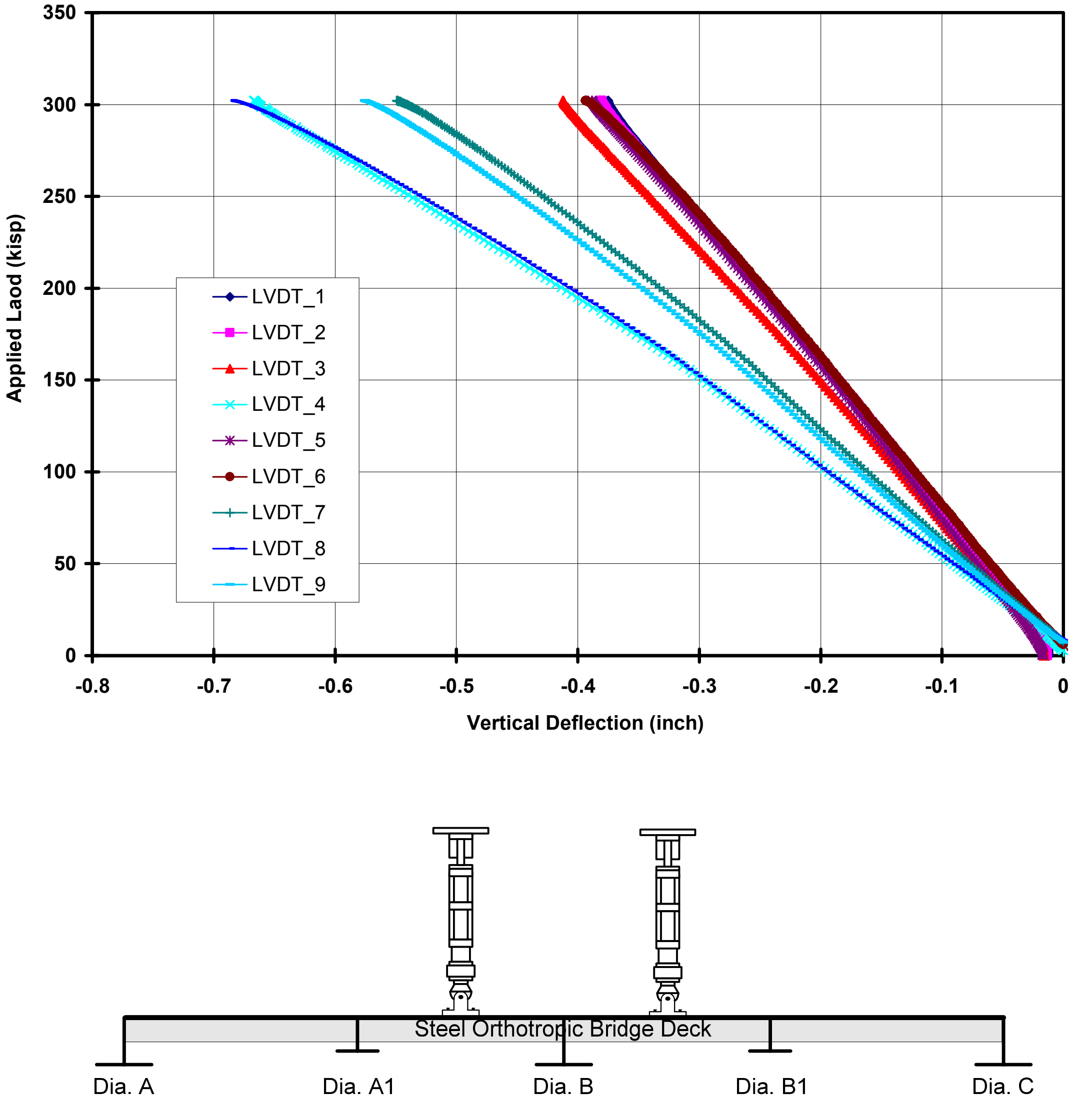

Figure 3-11 (c) Measured Vertical Displacement of Deck, Phase I

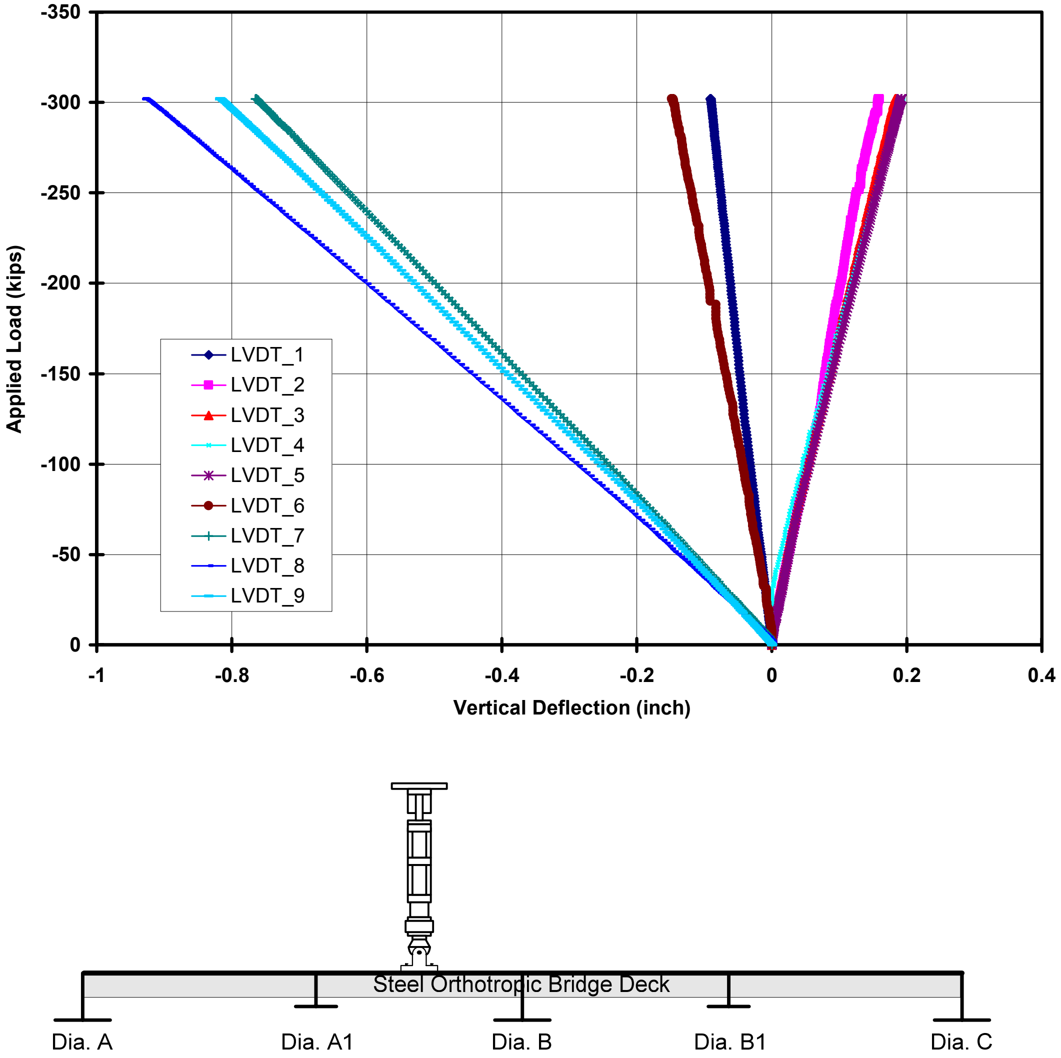
-350
-300
-250
-200
-150
-100
-50
0
Applied Load (kips)
-1
-0.8
-0.6
-0.4
-0.2
0
0.2
0.4
Vertical Deflection (inch)
LVDT_1
LVDT_2
LVDT_3
LVDT_4
LVDT_5
LVDT_6
LVDT_7
LVDT_8
LVDT_9
Steel Orthotropic Bridge Deck
Dia. A
Dia. A1
Dia. B
Dia. B1
Dia. C

Figure 3-12 (a)

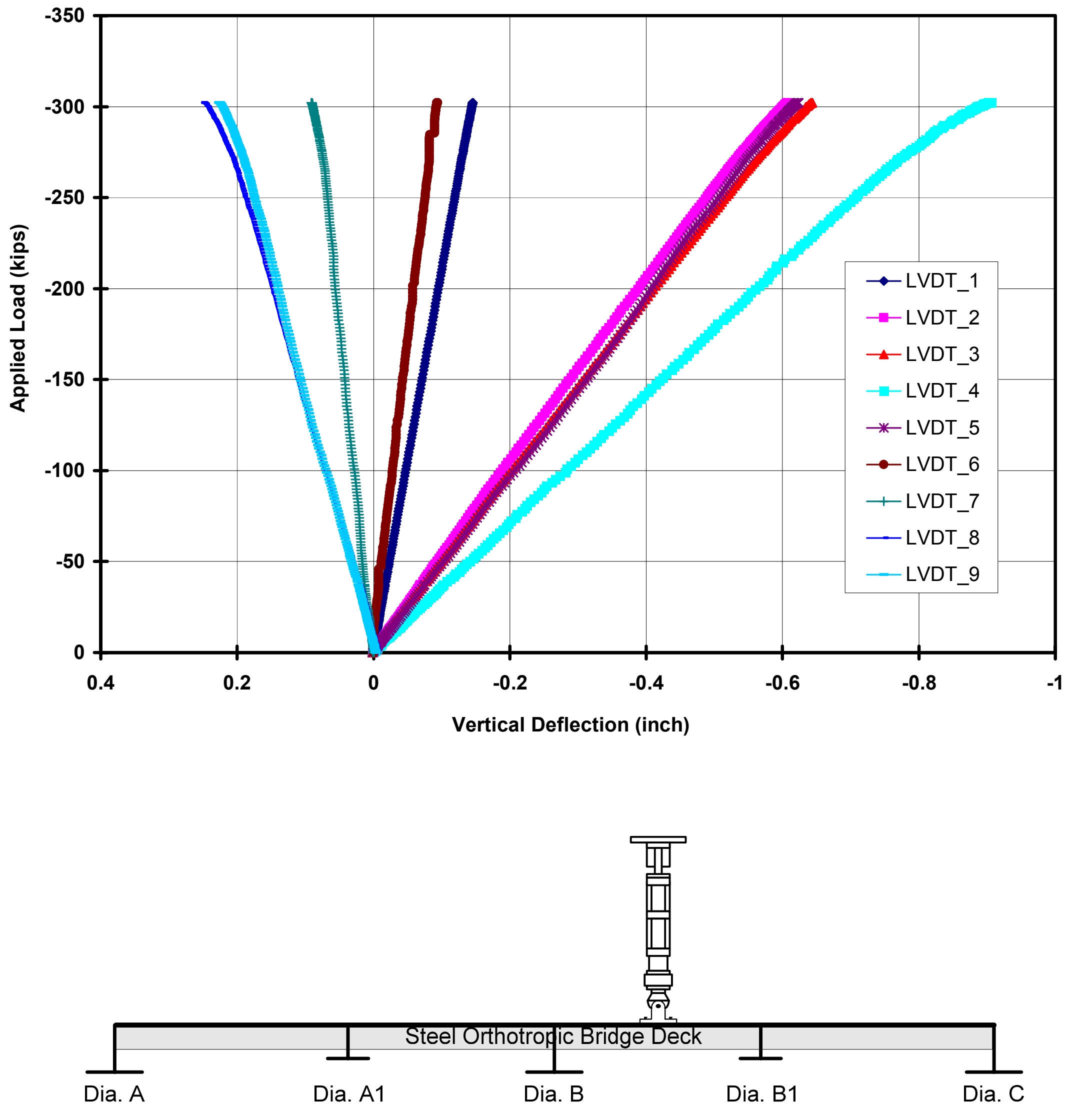
-350
-300
-250
-200
-150
-100
-50
0
Applied Load (kips)
0.4
0.2
0
-0.2
-0.4
-0.6
-0.8
-1
Vertical Deflection (inch)
LVDT_1
LVDT_2
LVDT_3
LVDT_4
LVDT_5
LVDT_6
LVDT_7
LVDT_8
LVDT_9
Steel Orthotropic Bridge Deck
Dia. A
Dia. A1
Dia. B
Dia. B1
Dia. C

Figure 3-12 (b)

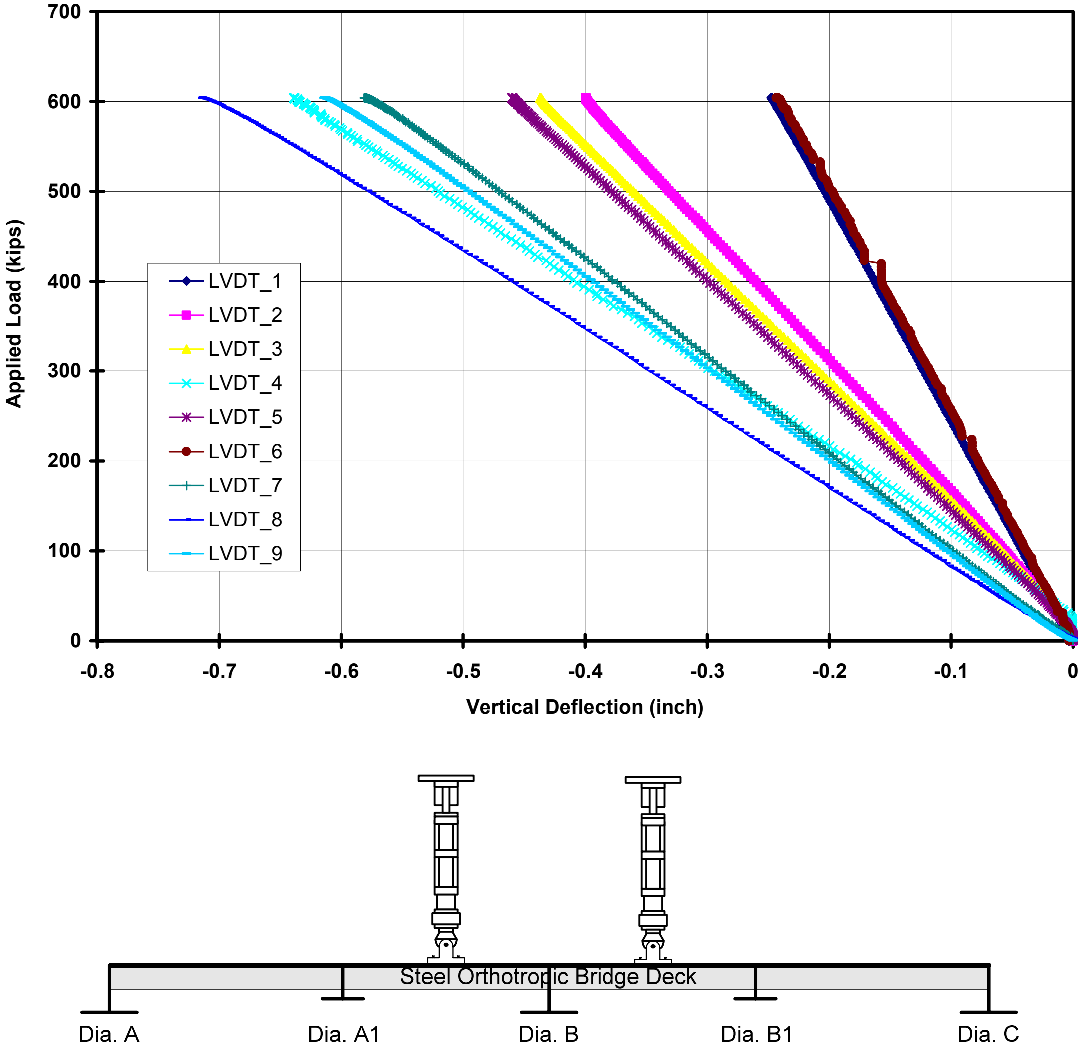

Figure 3-12 (c) Measured Vertical Displacement of Deck, Phase II

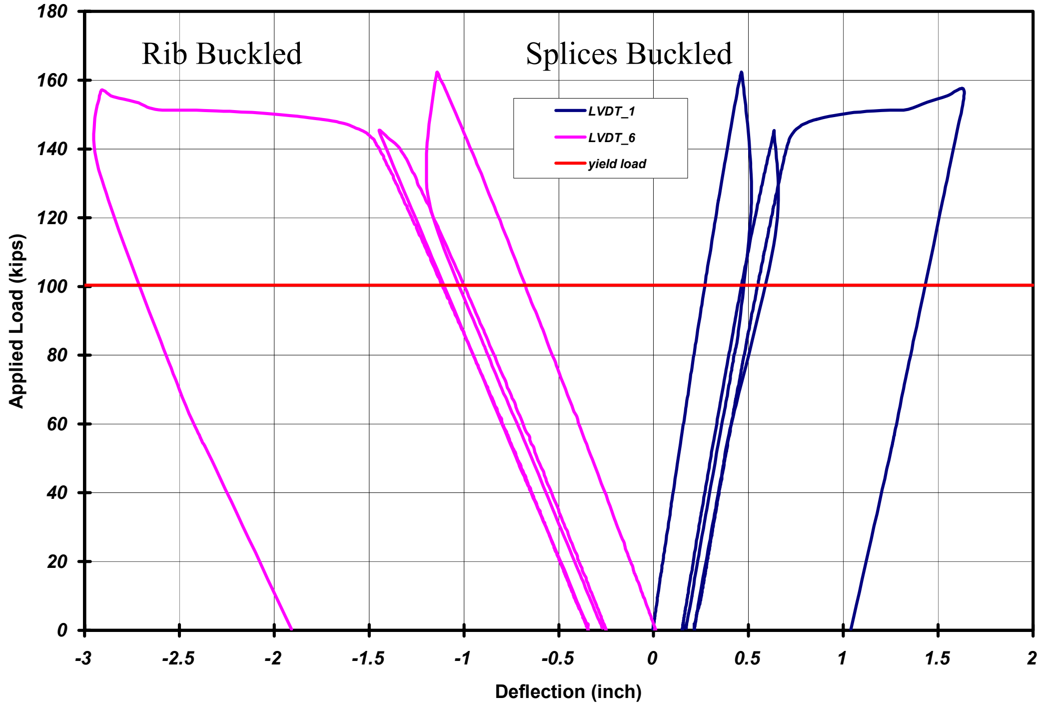

Figure 3-13 Measured Vertical Displacement of Rib, Phase III

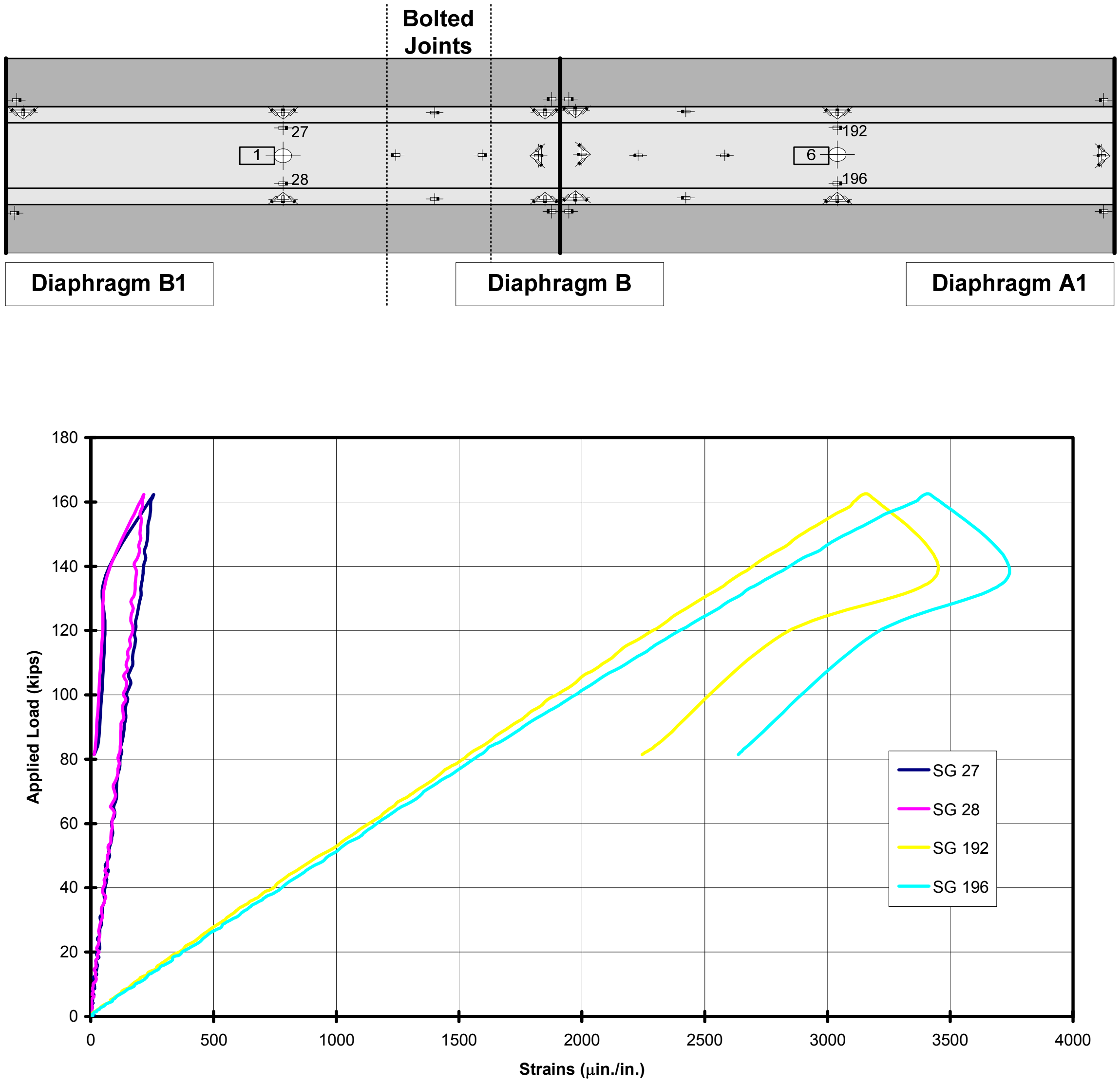

Figure 3-14 Strains on Bottom of Rib, Single Rib Bending Test, Phase III

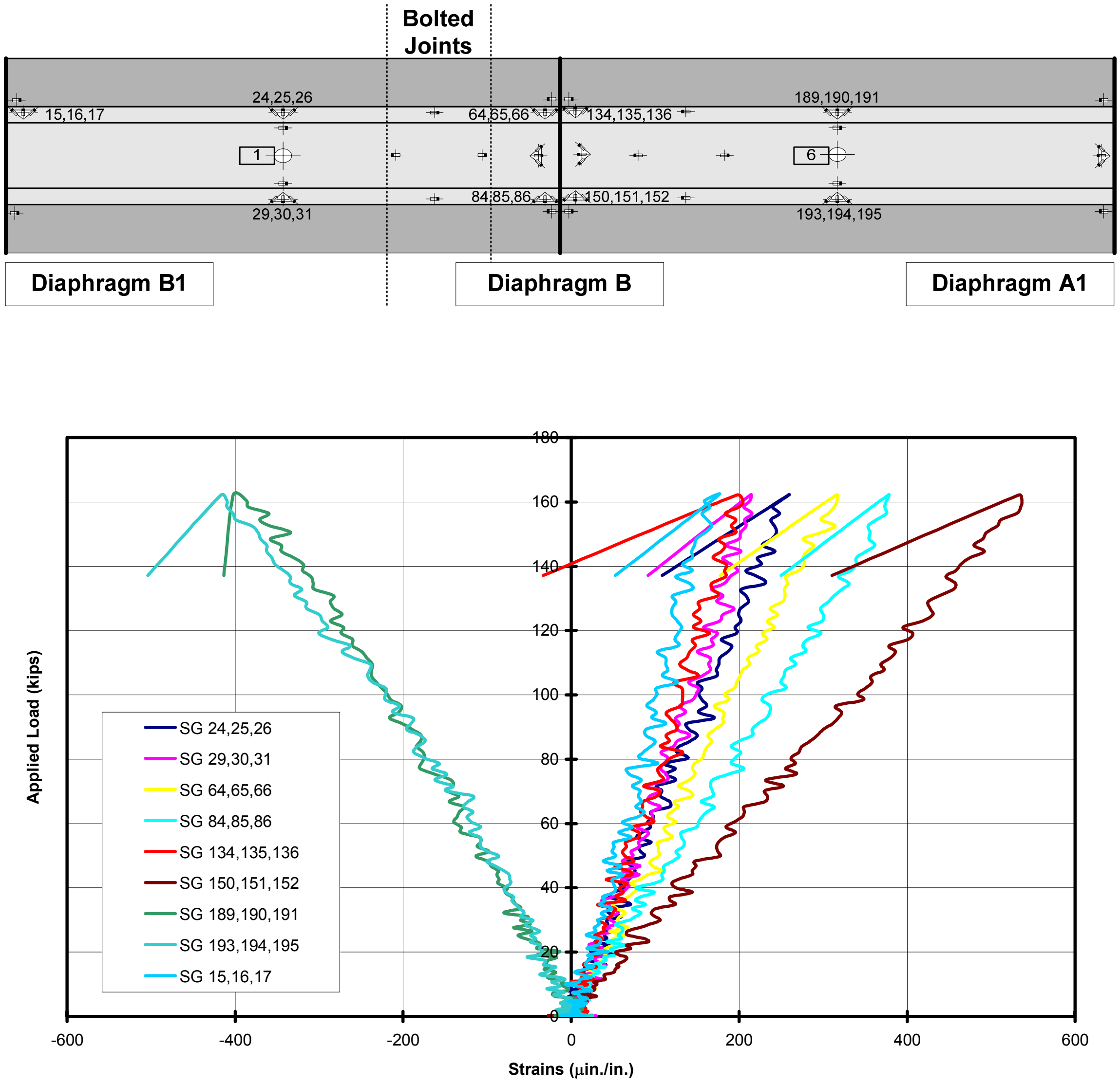

Figure 3-15 Longitudinal Strains on Rib Wall, Single Rib Bending Test, Phase III

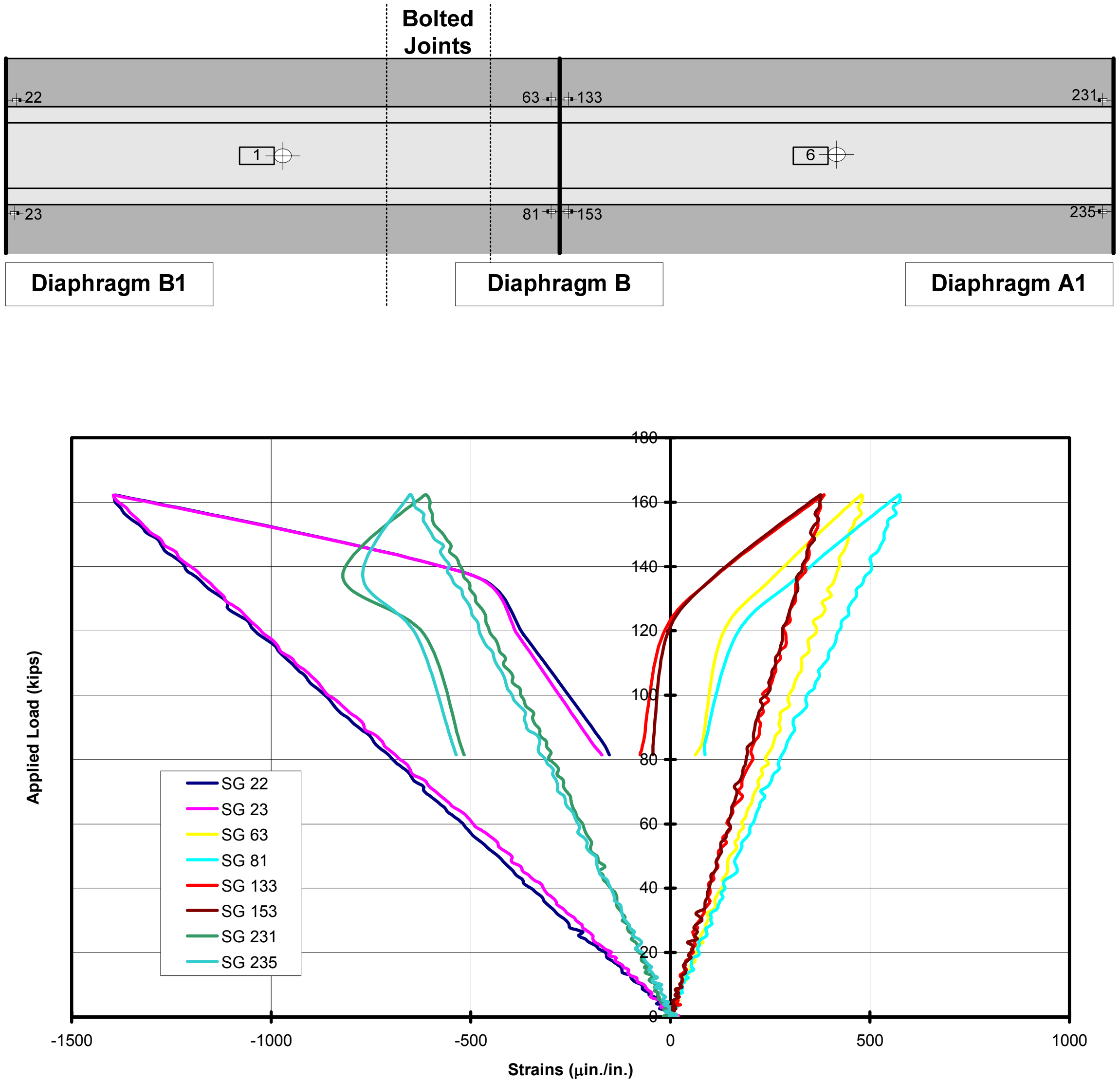

Figure 3-16 Longitudinal Strains on Bottom of Deck Plate, Single Rib Bending Test, Phase III

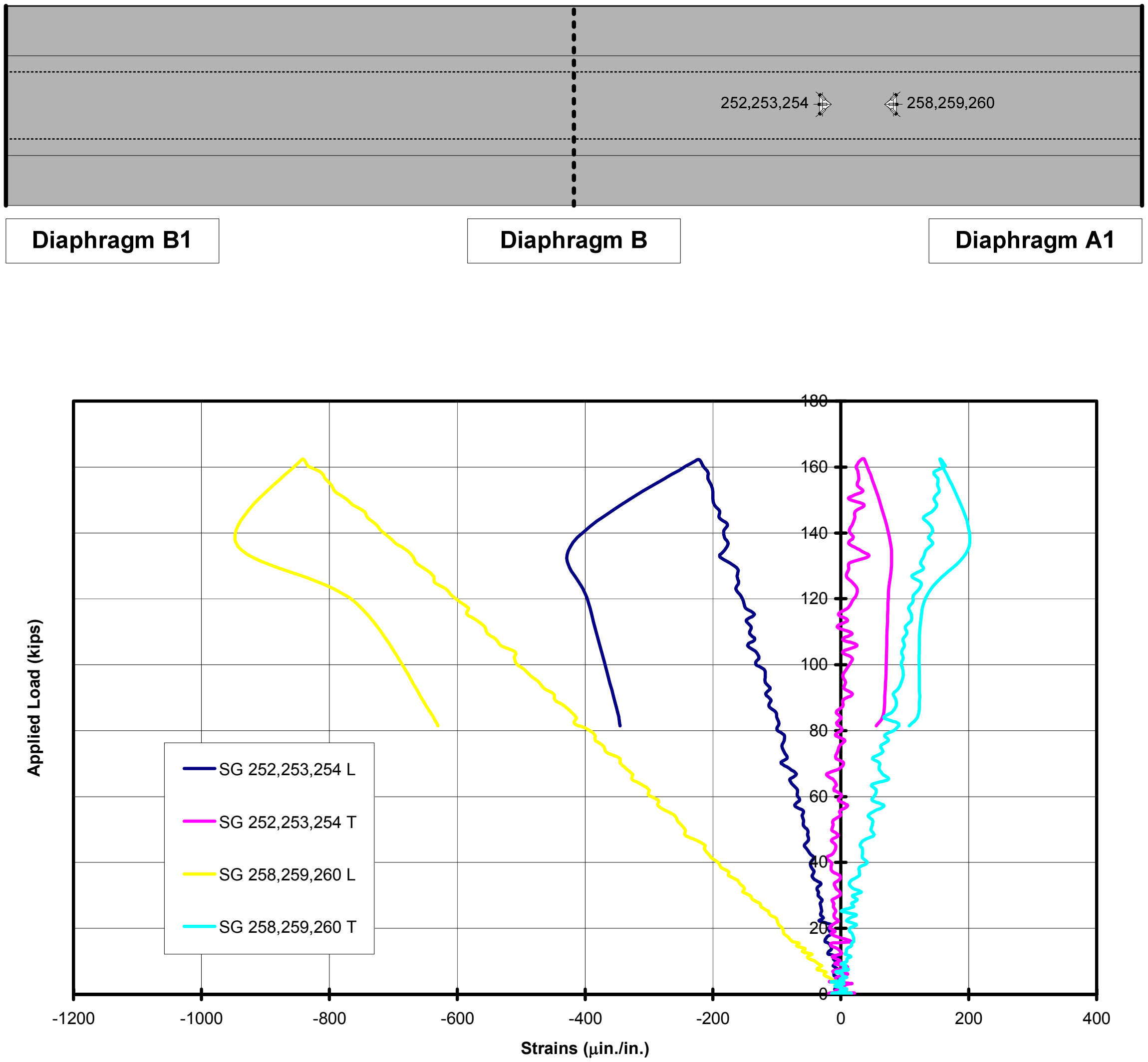

Figure 3-17 Longitudinal Strains on Top of Deck Plate, Single Rib Bending Test, Phase III

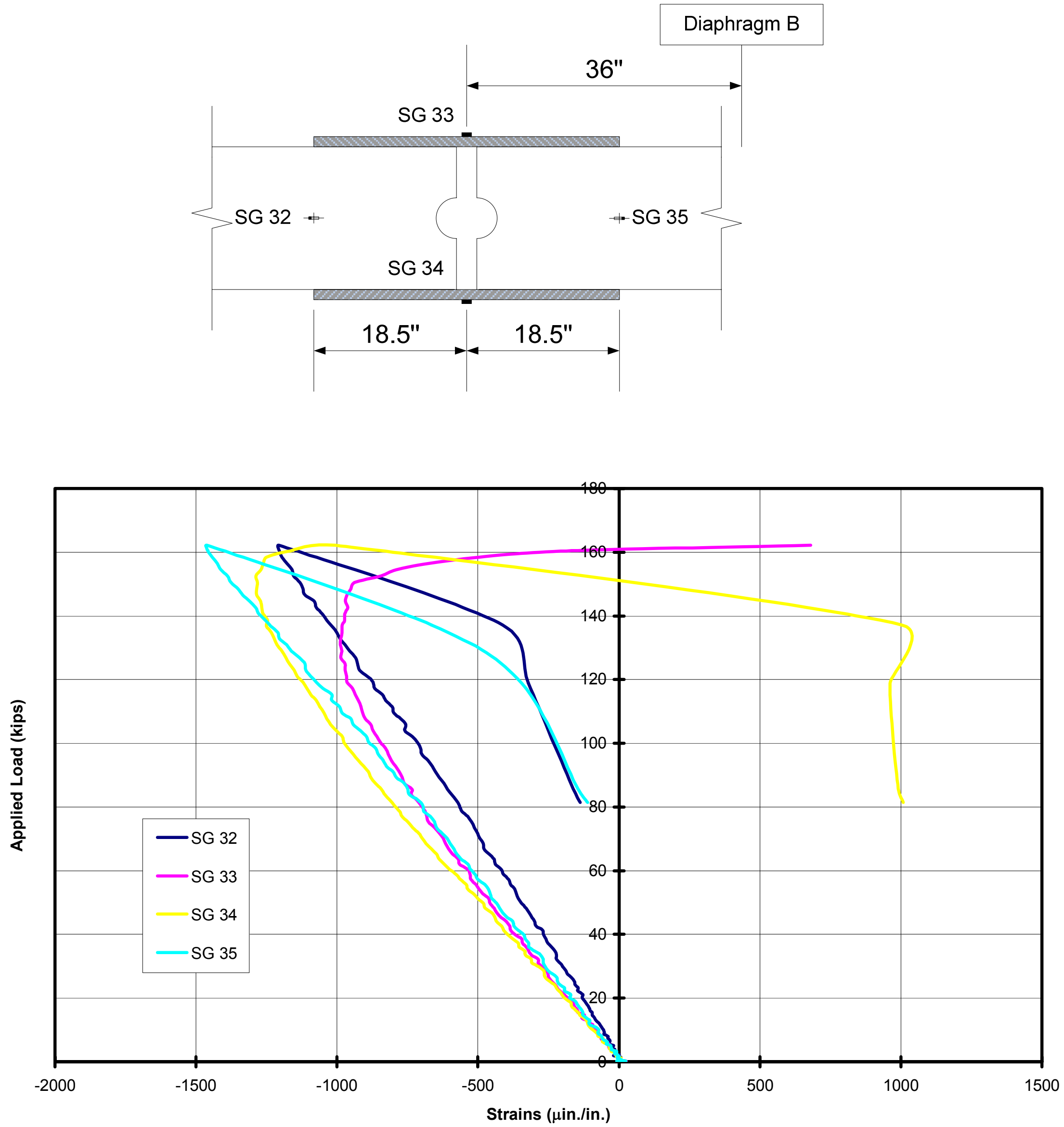

Figure 3-18 Strains at Splice of Rib, Single Rib Bending Test, Phase III

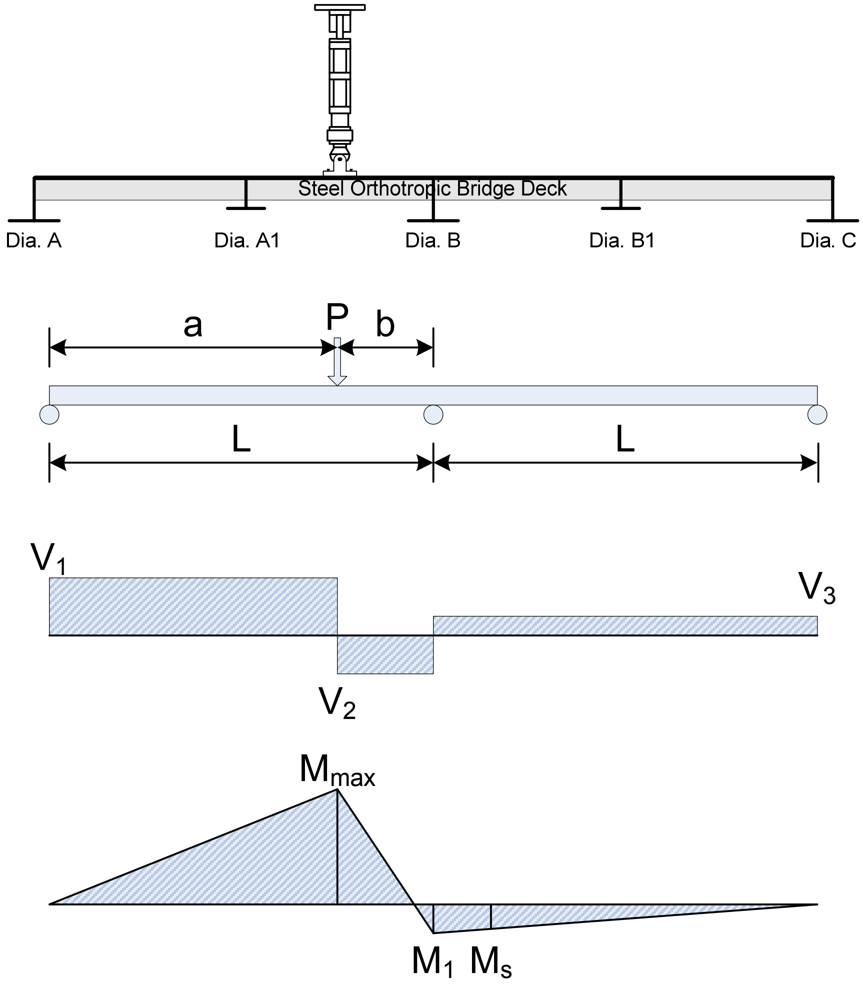

Figure 3-19 Beam Moment Diagram for Phase III and Phase IV

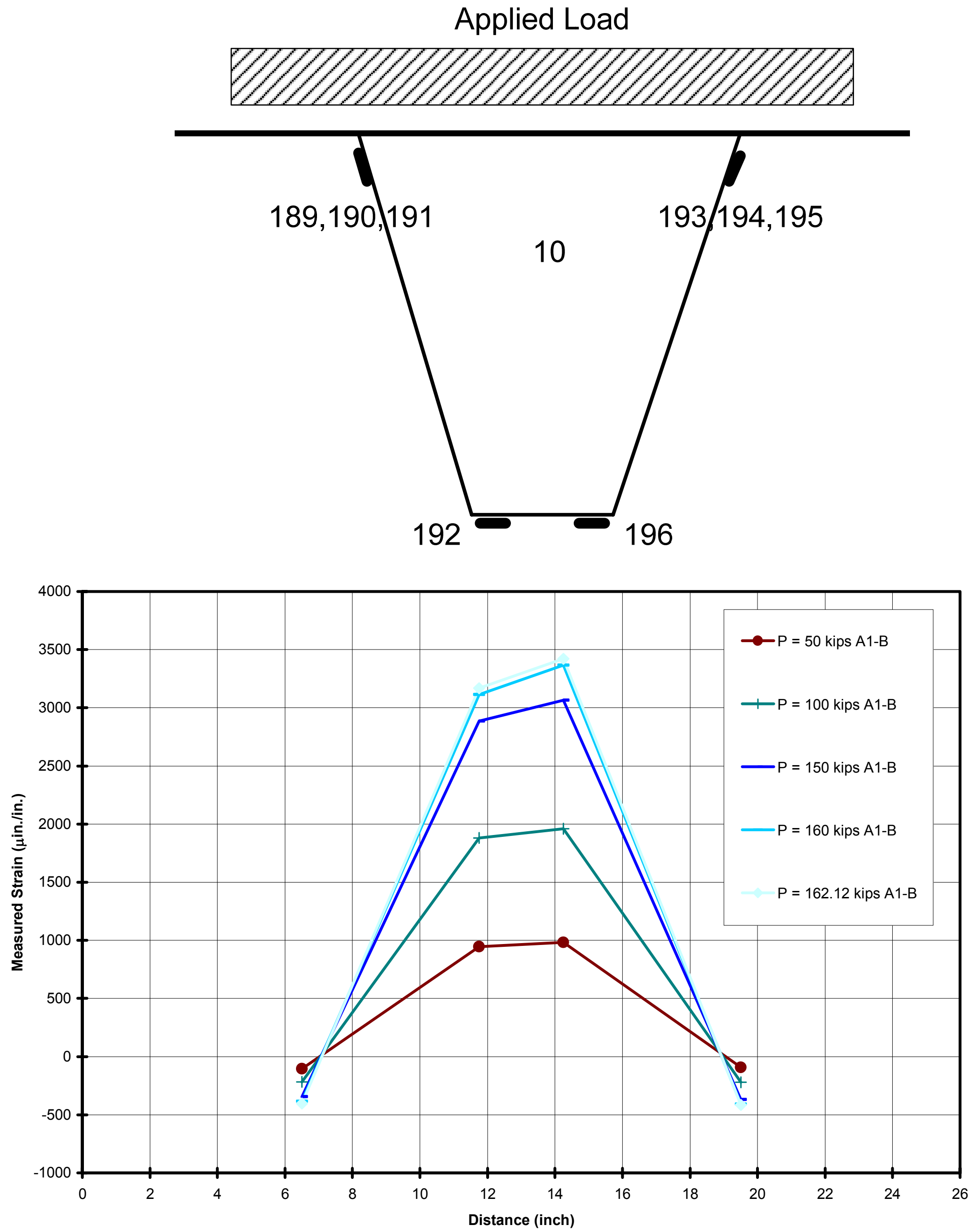

Figure 3-20 (a) Point A1-B

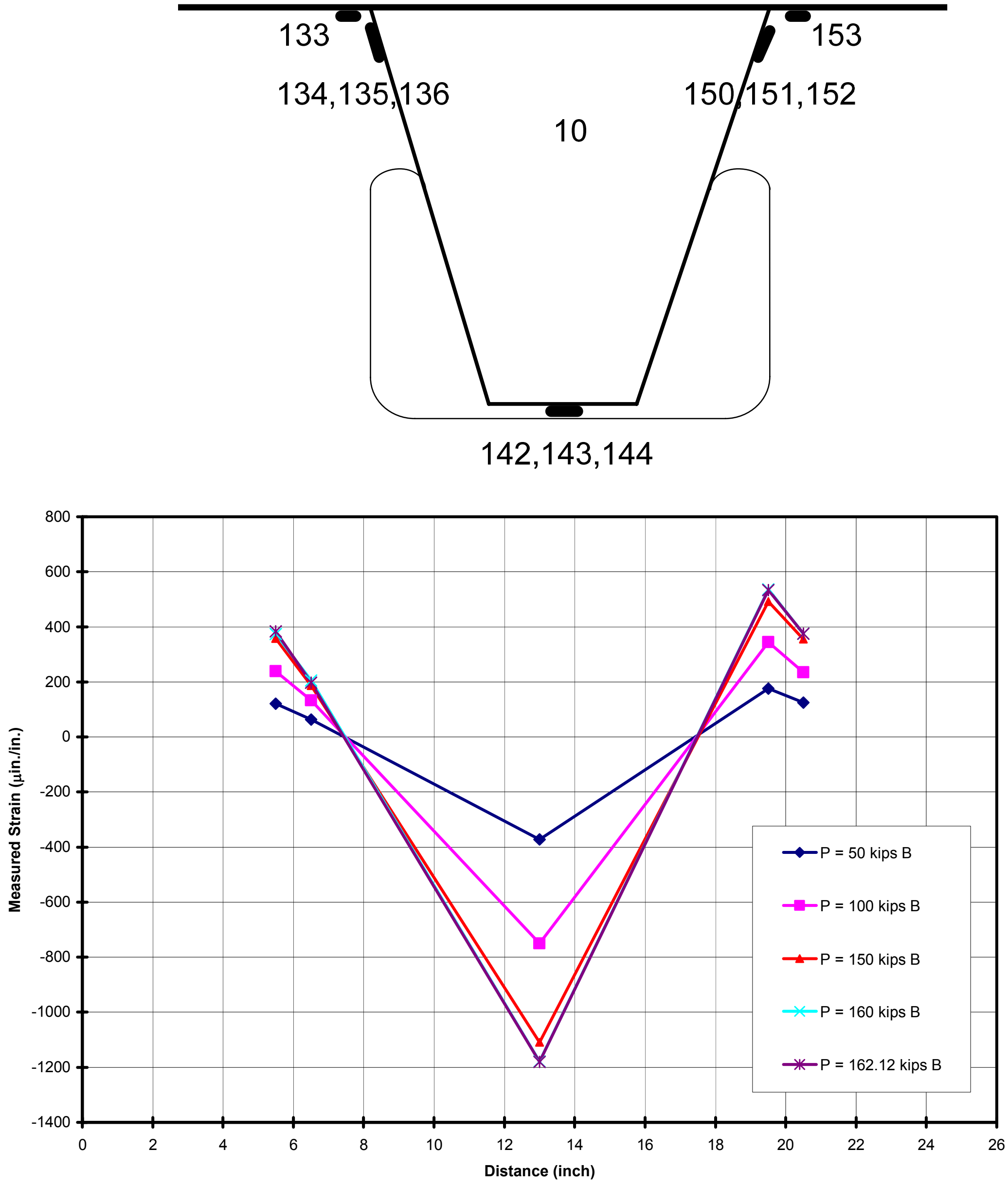

(b) Diaphragm B

Figure 3-20 Strains of Rib and Deck at Diaphragm B and Point A1-B, Single Rib Bending Test, Phase III

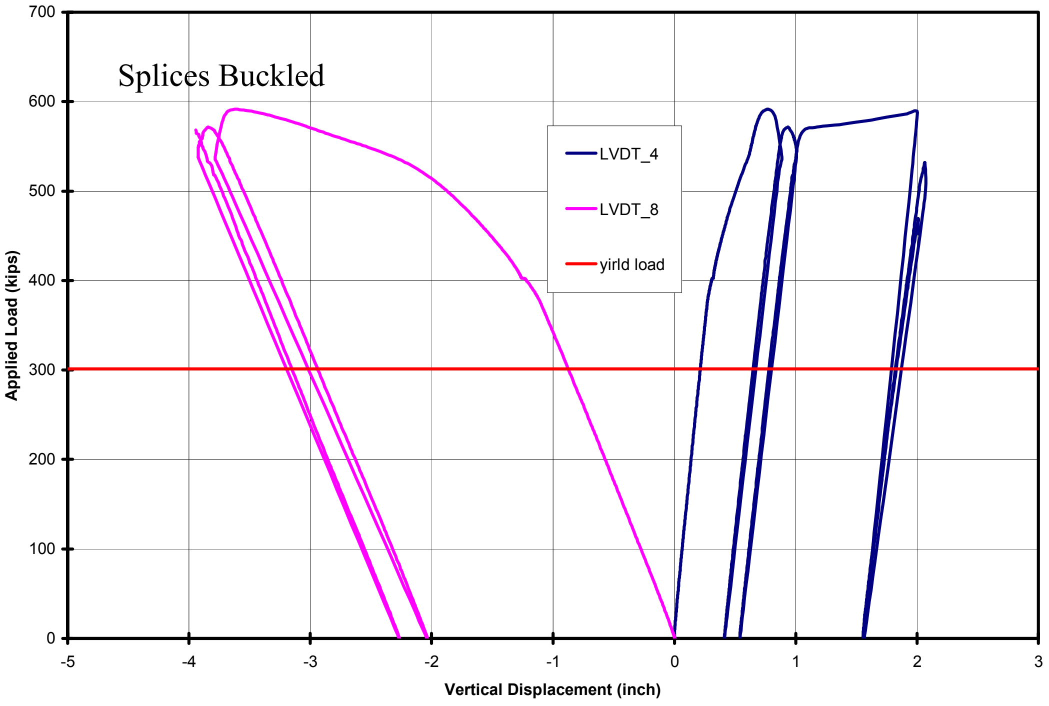

Figure 3-21 Measured Vertical Displacement of Rib 10, Phase IV

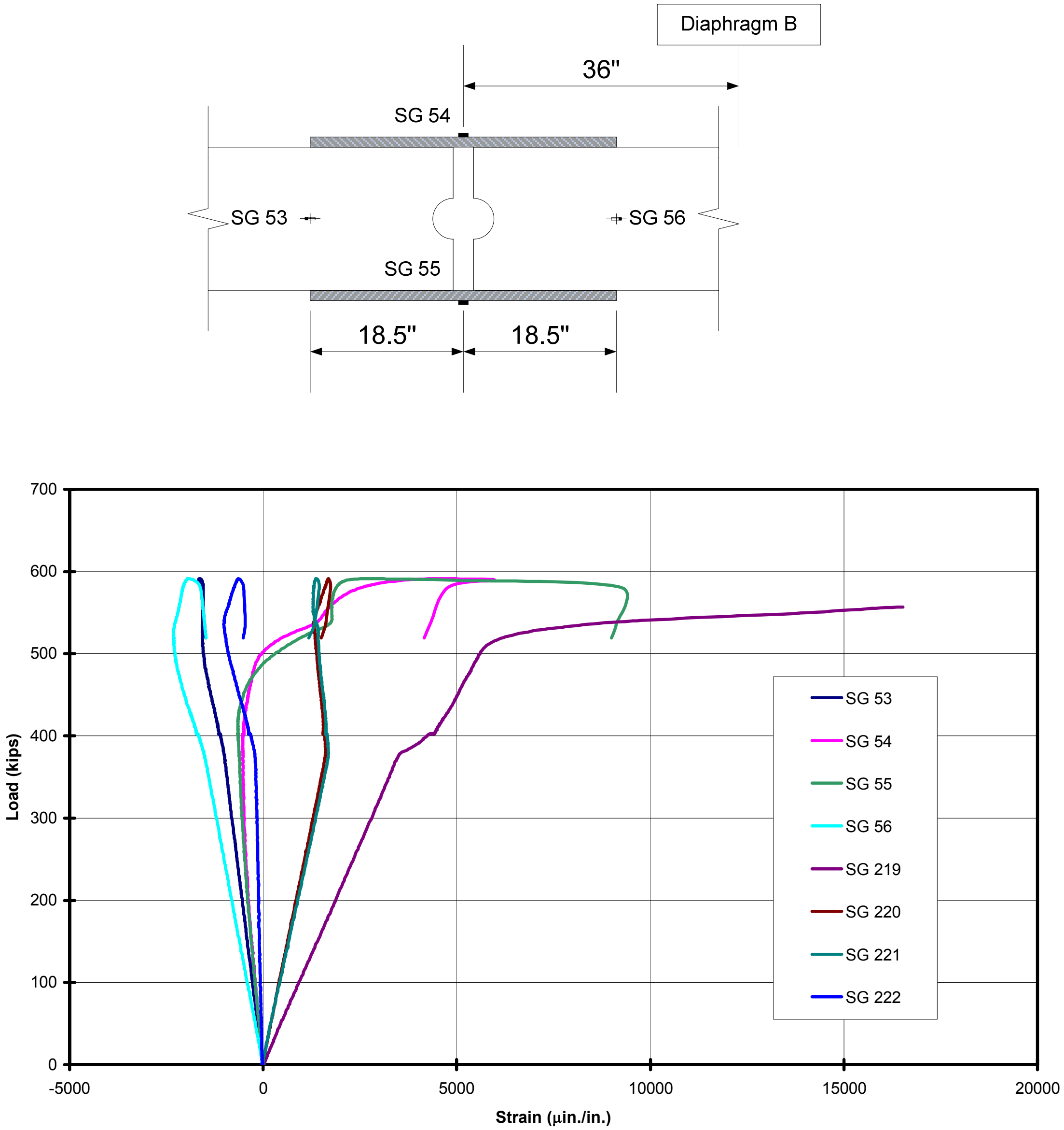

Figure 3-22 Strains on Splice Plate and Bottom of Rib 10, Triple Rib Bending Test, Phase IV

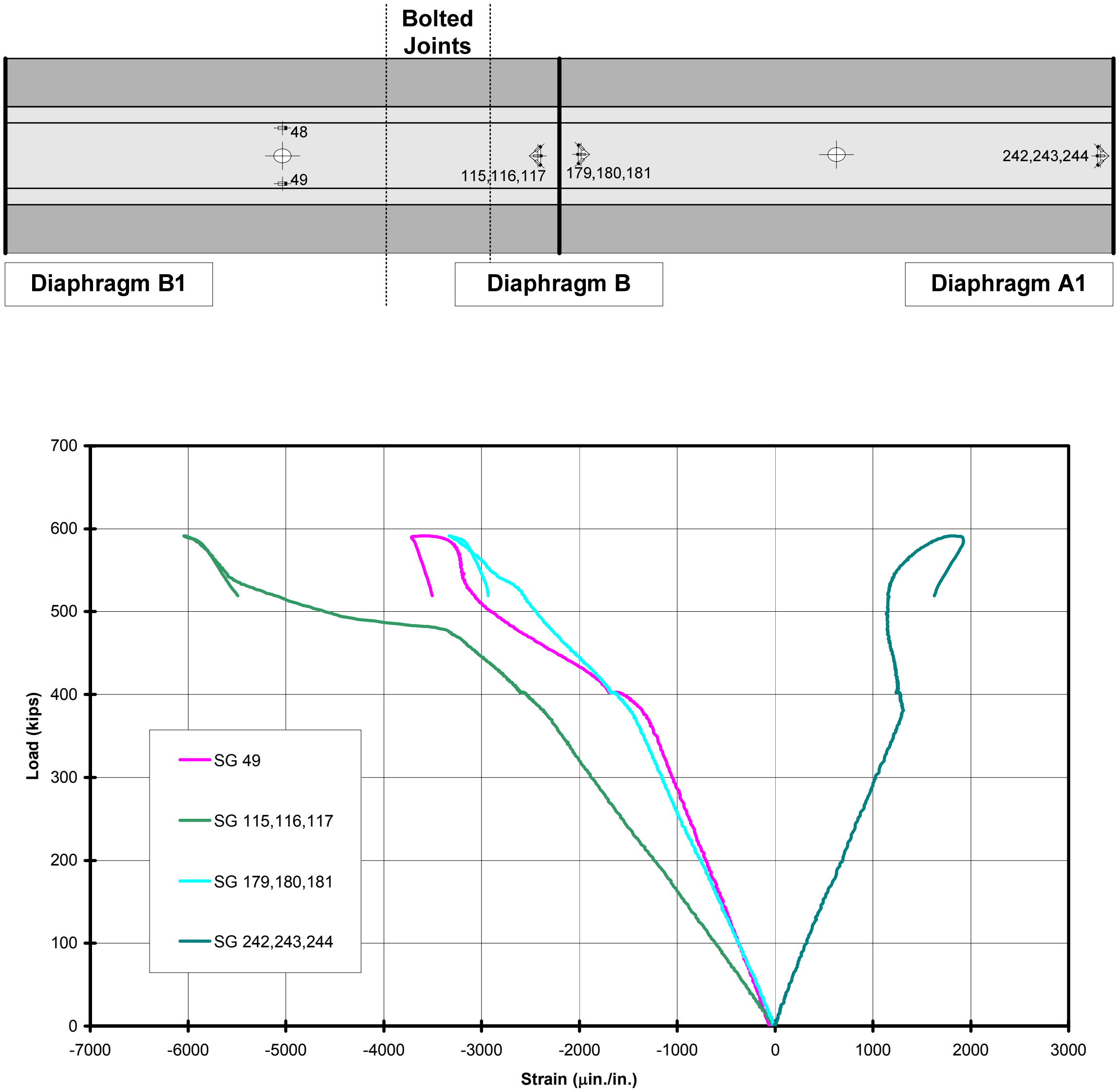

Figure 3-23 Responses of Strain on the Bottom of Rib, Triple Rib Bending Test, Phase IV

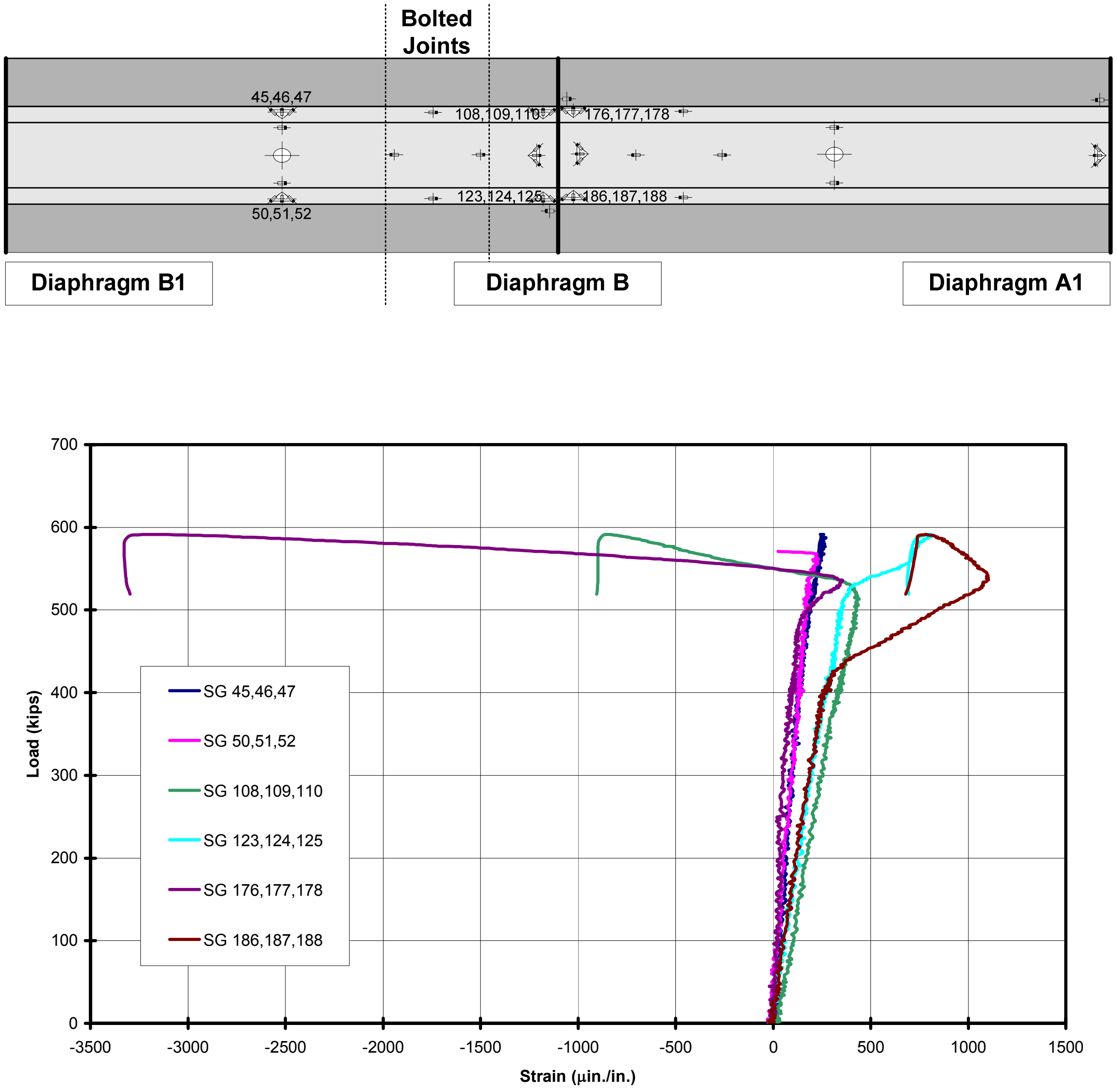

Figure 3-24 Responses of Strain on Rib Walls, Triple Rib Bending Test, Phase IV

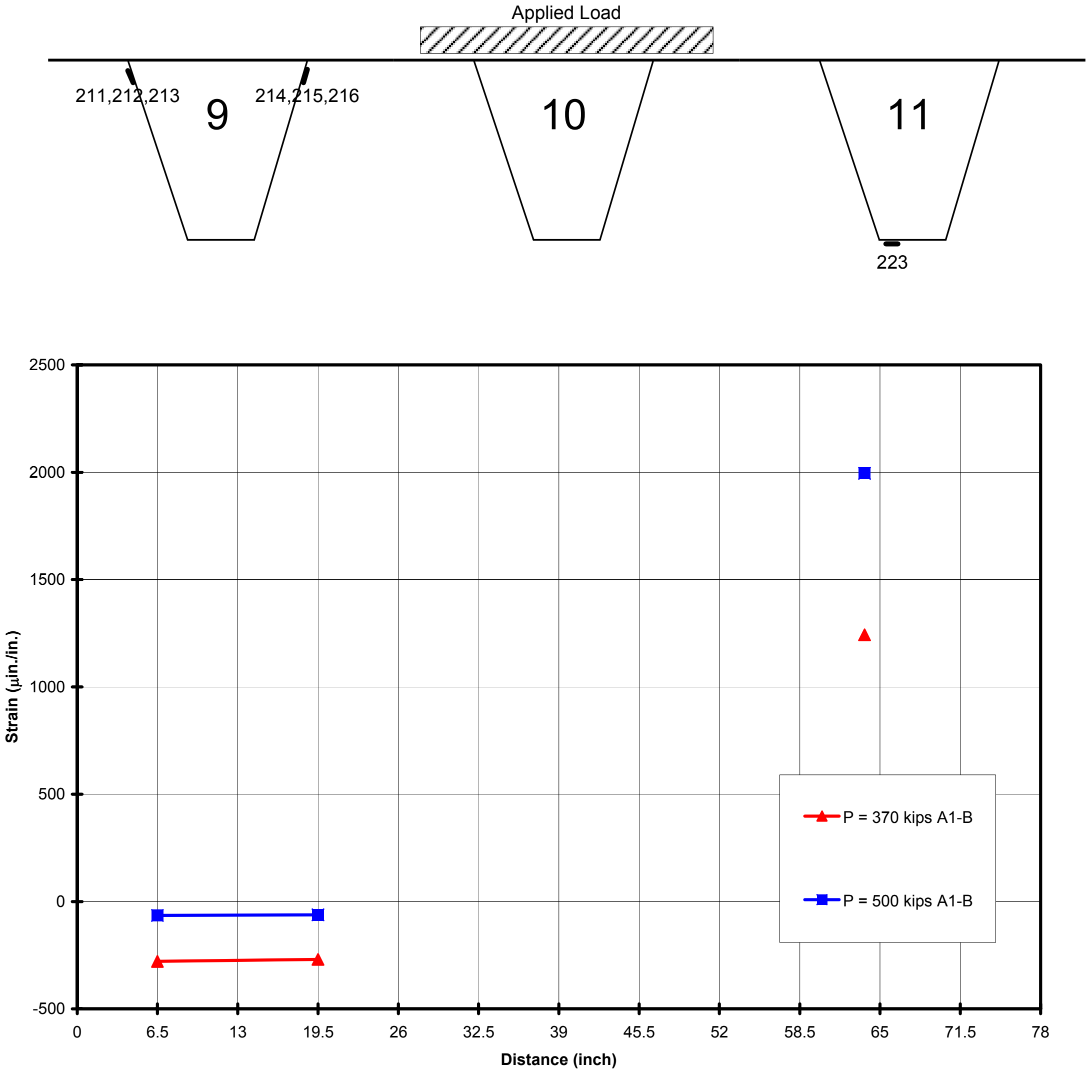

Figure 3-25 (a) Point A1-B

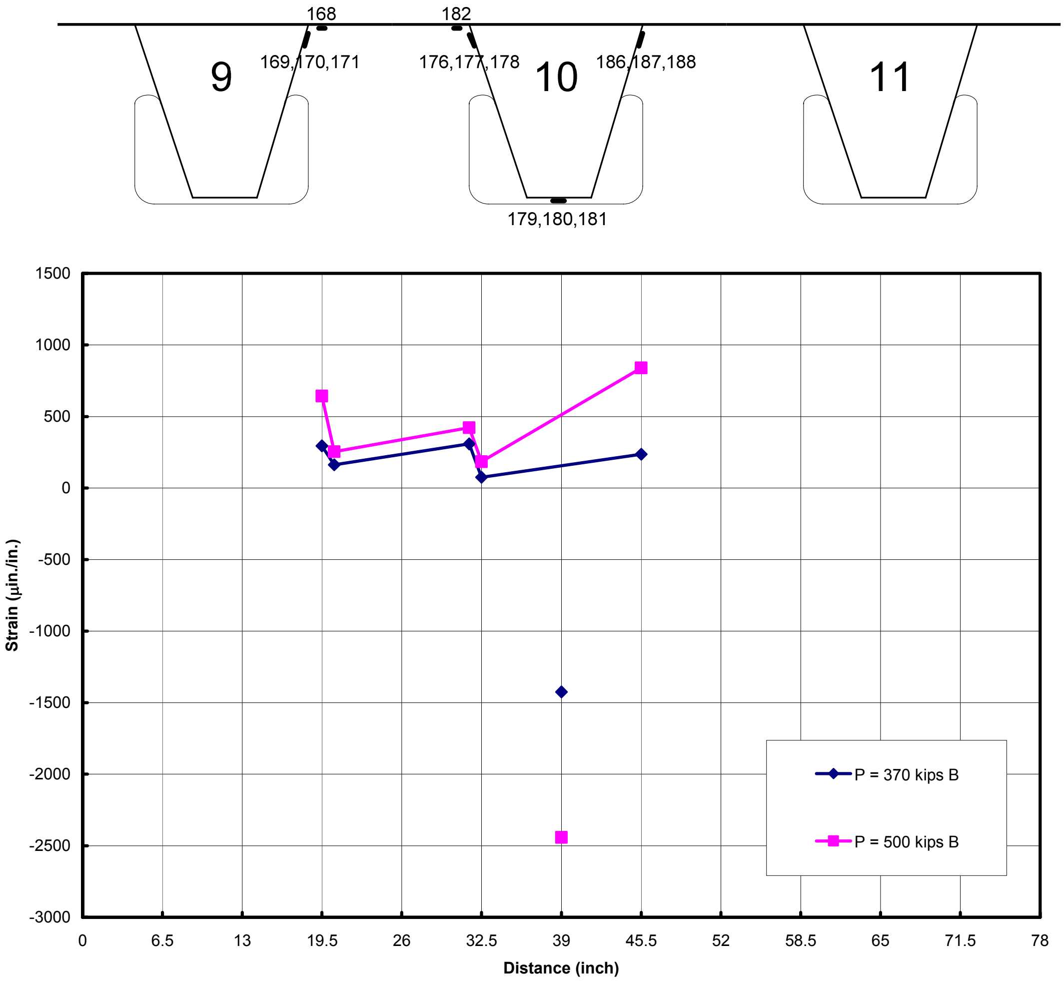

(b) Diaphragm B

Figure 3-25 Strains on Bottom of Deck plate and Rib, Triple Rib Bending Test, Phase IV

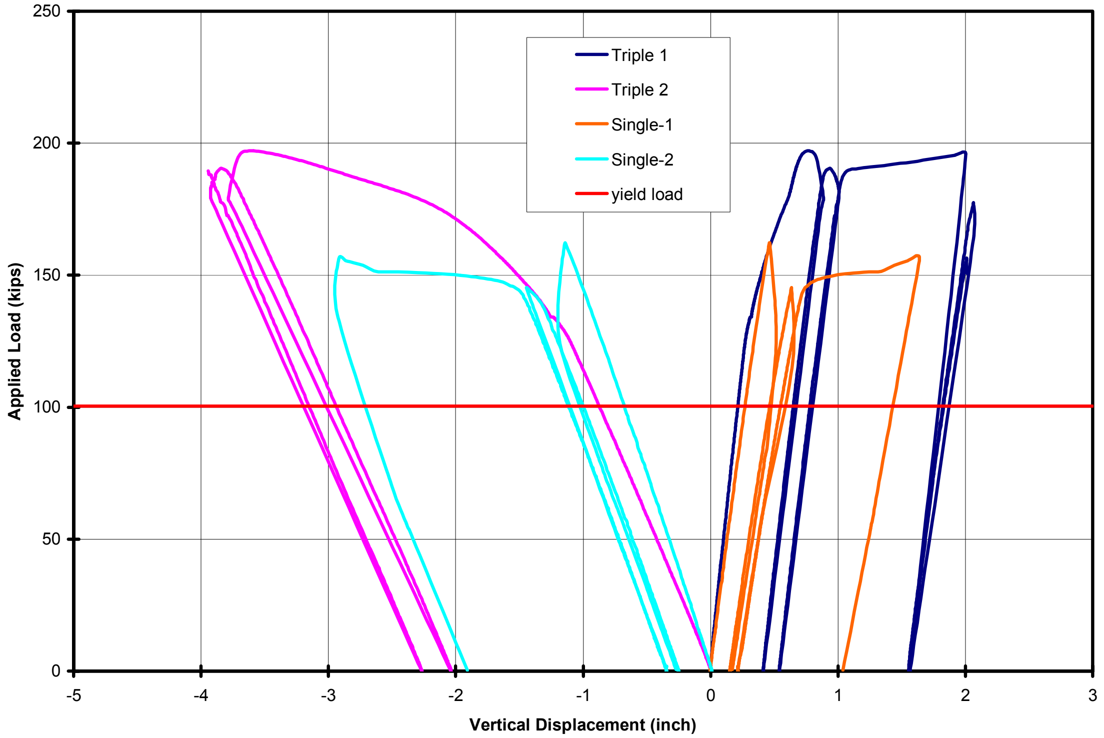

Figure 3-26 Comparison of Phase III and IV Measured Vertical Displacement, Triple and Single Rib Beams

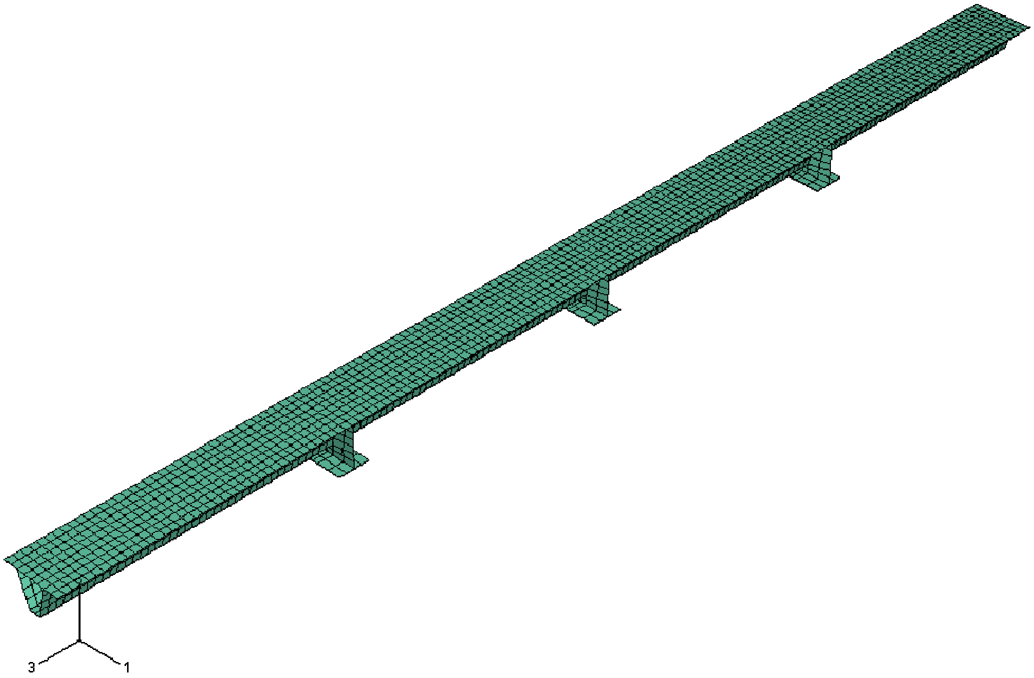

Figure 3-27 FEM for Single Rib Specimen

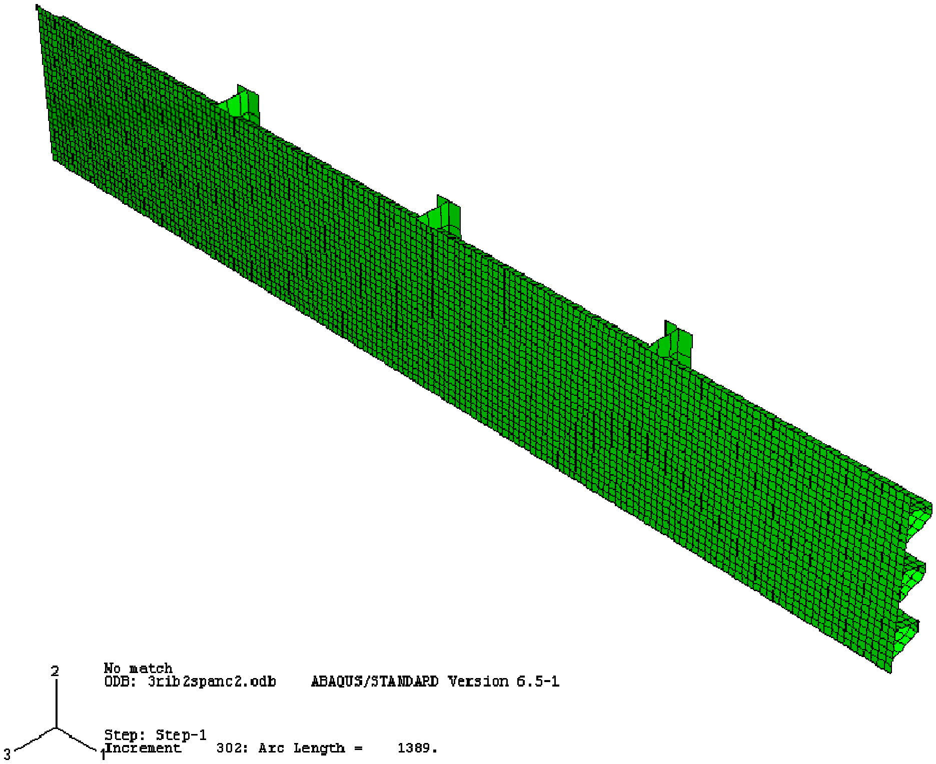

Figure 3-28 FEM for Triple Rib Specimen

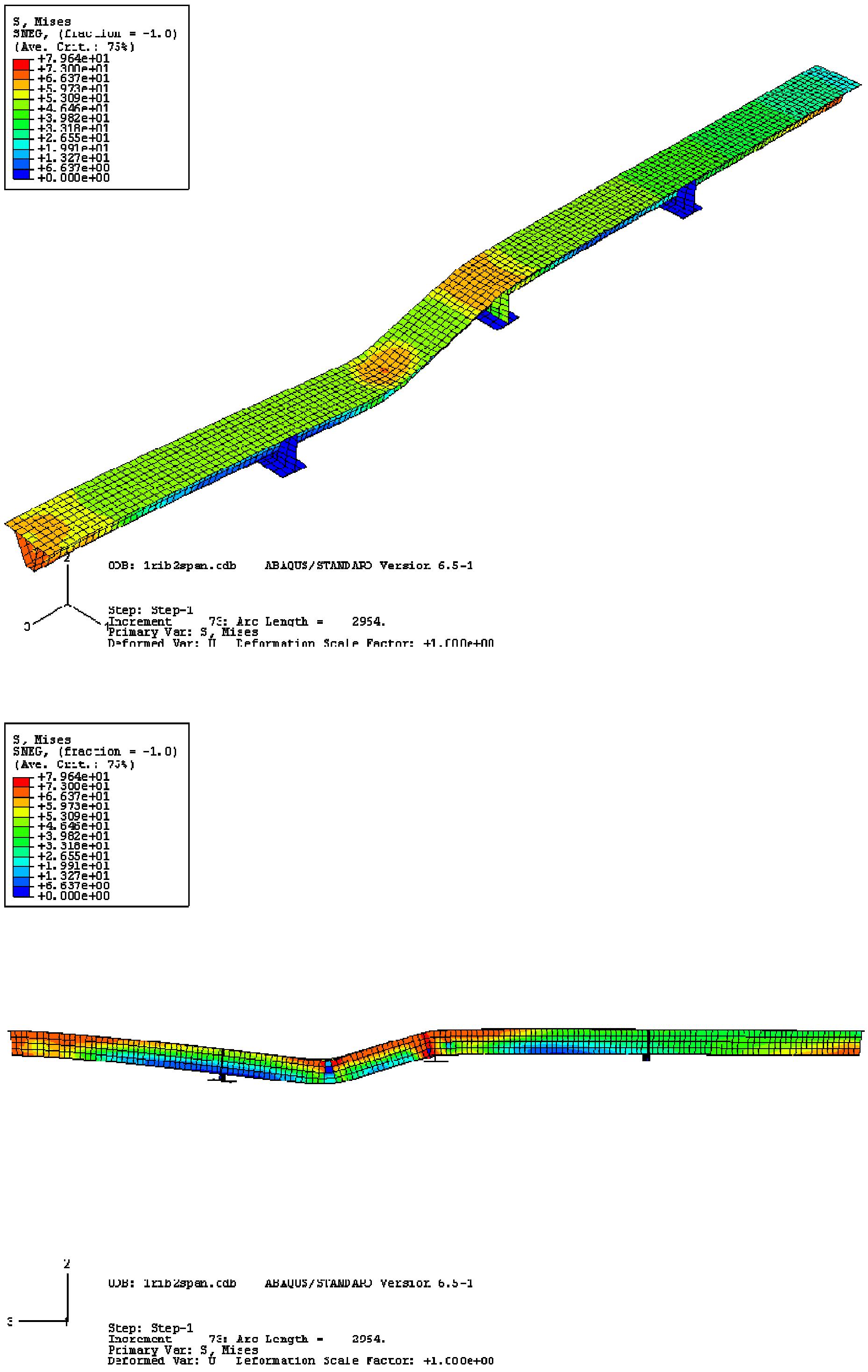

Figure 3-29 Shape of Failed FEM for Single Rib Specimen

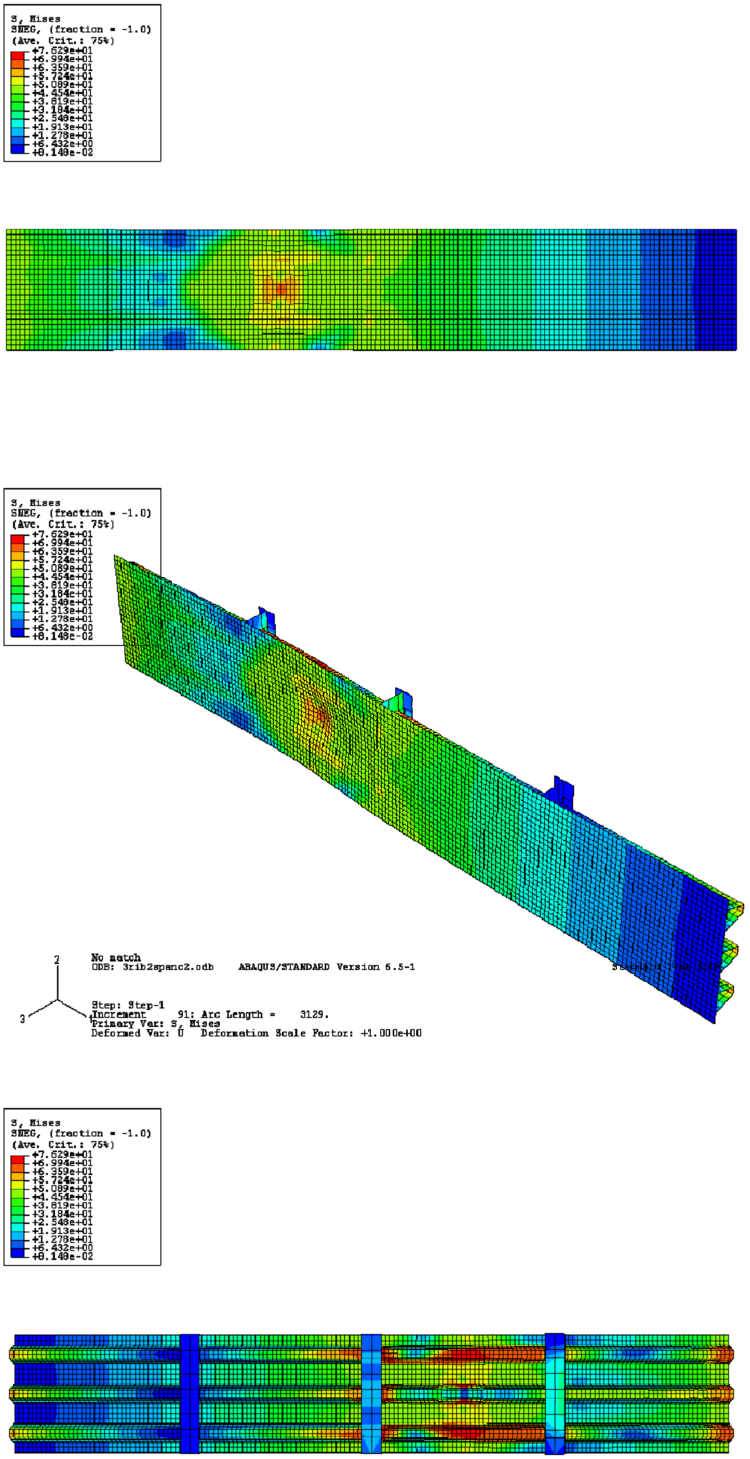

Figure 3-30 Shape of Failed FEM for Triple Rib Specimen

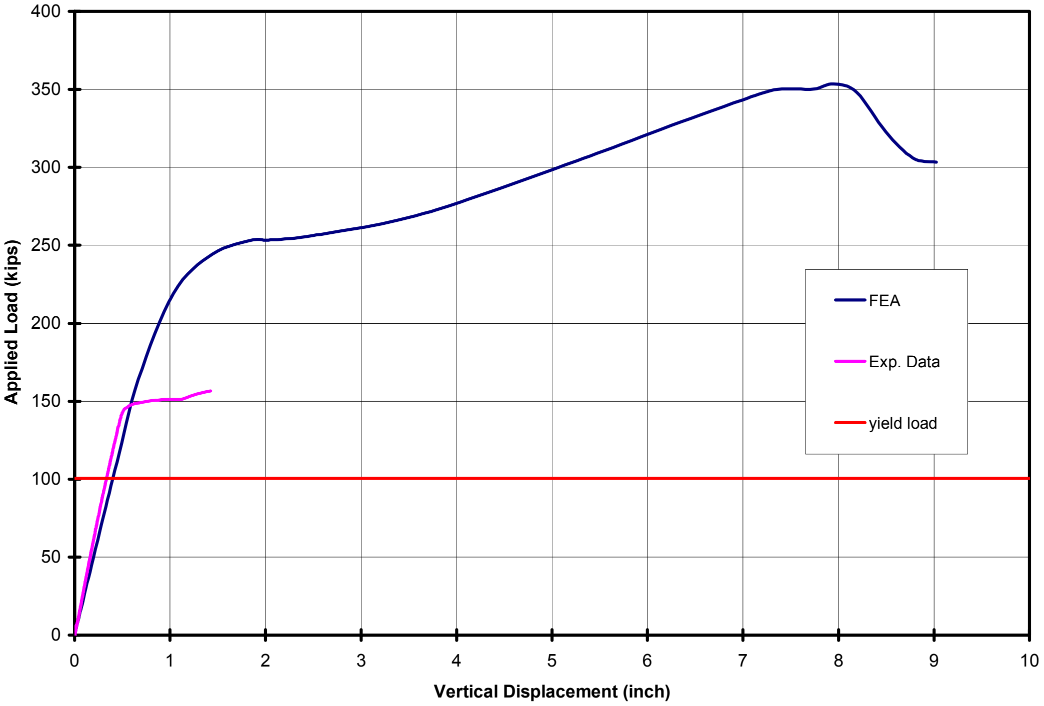

Figure 3-31 Comparison of FEM results with single rib experimental data

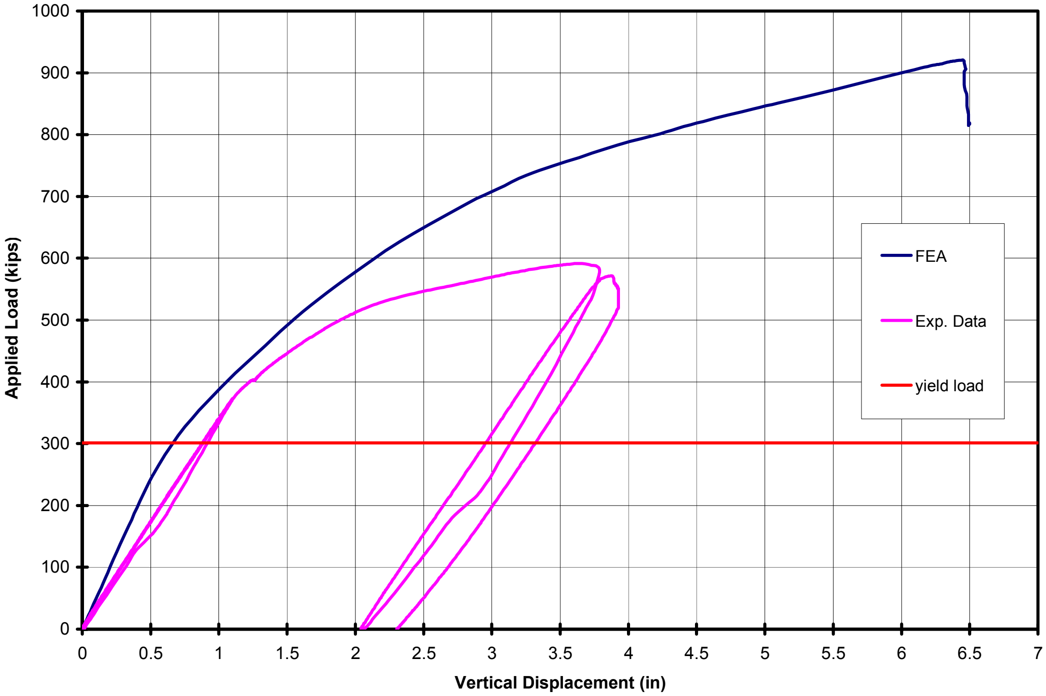

Figure 3-32 Comparison of FEM results with triple rib experimental data

Chapter 4 **Compressive and Beam-Column Strength of Trapezoidal-Shaped Ribs**

4.1 Introduction

Orthotropic steel plate panels with trapezoidal-shaped longitudinal stiffeners (ribs) are primarily compression members. Most often the stiffened panels serve as roadway decks thus are also subjected to vertical loads transverse to the deck. Therefore, when examining the load carrying behavior and strength of trapezoidal-shaped ribs, both compressive and transverse forces need to be considered.

To evaluate the compressive strength of the stiffening ribs of the BWB model deck under load was the main task of this part of the study. Both experimental and analytical examinations were made.

The results from Chapter 2 indicate that wheel loads affect the local stresses of deck components primarily in the rib directly under the loads, and the results from Chapter 3 showed that the flexural strength of a single-rib beam and of each rib of a triple-rib beam are essentially the same. Consequently, the experimental and analytical examination of rib column strength and rib beam-column strength can be conducted on specimens of a single rib or of multiple ribs.

4.2 Experimental Programs

4.2.1 Test Specimens and Properties

Four test specimens were cut from the BWB model deck for study. All were 18 ft. (5.5 m) long with two diaphragms 10 ft. (3 m) apart, each being 4 ft. (1.2 m) from the end. The four specimens were a single rib column (SC), two single rib beam-columns (SBC1 and SBC2) and a triple rib beam-column (TBC).

The dimensions of the component plates of a single rib are listed in Table 4-1. The sectional properties are shown in Table 4-2. The yield strength of 50 ksi (345 MPa) for the deck plate and 70 ksi (483 MPa) for the rib walls and bottom flanges were obtained by testing coupons (ASTM A370) with an 8-inch gage length. The stress-strain curves from the coupon tests are shown as Figure 4-1 and 4-2. The results are listed in Table 4-3.

The computed reference loads for the specimens, including the component buckling loads of the deck plate ($P_{cr,d}$) and of the rib wall ($P_{cr,r}$), are listed in Table

4-4. The condition of simply supported plates was adopted. The computation is given in the Appendix. For the study of compressive strength of structural members, the initial imperfection of components is important. The out of flatness of the deck plate and the rib walls and the out of straightness of each specimen were measured. Figure 4-3 shows a single rib specimen with a 2 in. by 6 in. (51 mm by 152 mm) marking for measurement of the deck plate surface. The results are shown in Figure 4-4. The maximum relative deflections of all four specimens are listed in Table 4-5. The maximum absolute imperfection of the deck plate of the four specimens was 0.525 in. (13 mm) and of the ribs, 0.017 in. (0.4 mm).

4.2.2 Test Setup, Instrumentation and Test Procedure

The specimens were tested vertically in the 5 Million Pound Universal Test Machine in Fritz Engineering Laboratory. A single-rib beam-column specimen in the test machine is shown in Figure 4-5. The ends of each single-rib specimens had a 2 in. (51 mm) thick end plate attached for a “flat-ended” condition. A 3 in. (76 mm) thick plate was used for each end of the triple-rib specimen. For beam-column specimens, the horizontal force simulating a wheel load on the deck was introduced by a hydraulic jack at mid height. This is also shown in Figure 4-5.

Strain gages were placed on the deck plate and the rib wall. Some of these gages are visible in Figure 4-5. Most of the LVDTs for measuring displacement of the specimens in the direction of the simulated wheel load were placed against the rib bottom. The locations of strain gages and of LVDTs for the specimens are given in Figures 4-6 to 4-11.

Axial compressive force of the column specimen (SC) was applied monotonically to failure of the column. For the beam-column specimens (SBC1, SBC2 and TBC) an axial force of 300 kips (1335 kN) was first applied, then the simulated wheel load of 40 kips (178 kN) and then the additional axial compression to failure.

4.3 Test Observations and Results

4.3.1 Strength of Specimens and Failure Modes

The results of specimen ultimate loads and failure modes are summarized in Table 4-6.

The single-rib column specimen, SC, sustained an ultimate axial compression of 1385 kips (6162 kN), which was practically the computed deck plate buckling load. The final appearance of the column is shown in Figure 4-12. Failure was due to inelastic buckling of the rib wall near the ends. Closed up views of the buckled rib wall near the lower end of the deck plate are given in Figure 4-13. Local buckling of the deck plate at mid height occurred after the ultimate load. The buckle can be seen in Figure 4-12 and is shown in a closer view in Figure 4-14.

The strength of the single-rib beam-columns, SBC1 and SBC2, was 1358 kips (6045 kN) and 1412 kips (6284 kN), respectively, being slightly different from the computed buckling load of the deck plate. The appearances of the failed specimens are shown in Figure 4-15 and 4-16. Yielding of the deck plate occurred before the ultimate load. The yield lines were observed near the mid height of the beam-column where the bending moment was the highest. The yield lines can be seen in Figure 4-17. At the maximum load, local buckling of the rib wall developed near the ends, Figure 4-18. The deck plate and rib wall near the simulated wheel load also buckled, as shown in Figures 4-19 and 4-20.

The final appearance of the triple-rib beam-column specimen, TBC, is shown in Figure 4-21. Yielding of the deck plate was observed before local buckling of the ribs near the ends. The ultimate load was 4422 kips (19680 kN), being about 30 percent higher than the computed load of 3402 kips (15140 kN) at first yield. The yield lines along a diaphragm can be seen in the photograph, Figure 4-22, which was taken after the specimen was removed from the test machine. One of the buckled rib walls is shown in Figure 4-23.

4.3.2 Load-Displacement Behavior

The four specimens had similar load-displacement behavior. The applied load versus axial shortening relationship of the specimens is plotted in Figure 4-24. The load for the triple-rib beam-column, TBC, was the average value of each rib. That is the applied load divided by three. The testing of this specimen was not carried through a large amount of displacement as did the other two beam-columns for reasons of safety at high loads. In Figure 4-24, all the curves for the beam-columns are quite close to each other, indicating similarity in behavior and strength. Nonlinear behavior was noticeable beyond about 1200 kips (5340 kN) per rib. It is to be noted that the column specimen SC under went more shortening than the beam-columns. That the column specimen was cut from Rib 8 which was along the longitudinal welded joint of the deck plate, might have some effect in addition to those by residual stresses in the cross section.

The lateral displacements of the mid point of the specimens are presented in Figure 4-25. The single rib column SC began to displace laterally above 1300 kips (5785 kN) at the onset of failure by local buckling. The beam-columns were subjected to a 300 kips (1335 kN) axial compression before the application of the 40 kips (178 kN) lateral force of simulated wheel load. Lateral displacement occurred accordingly. Upon the continuation of application of the axial load, the single rib specimens SBC1 and SBC2 deflected slightly more whereas the triple-rib specimen did not. This implies the constraint of the two outer rib to the lateral displacement of the middle rib under the lateral load. Beyond 1200 kips (5340 kN) local nonlinear behavior started and the lateral displacement increased at a higher rate. After the attainment of the maximum load, the lateral deflection increased with a decreasing ability of the specimens to carry axial load. As indicated earlier, the testing of specimen TBC was terminated shortly after reaching the maximum load, not allowing a large magnitude of lateral displacement.

Figures 4-26, 4-27, and 4-28 depict the laterally deflected longitudinal profile of the rib bottom of the specimens. Measurements were made in the mid length region of the specimens. The displacement of the single-rib column changed from slightly towards the deck plate at low axial load to the opposite direction at failure of the column. The beam-columns, due to the lateral load at 108 in. (2.74 m) from the bottom, gradually increased the magnitude of lateral deflection with the load and increased much more at failure load.

In all cases, the lateral displacement was steady and stable without instability.

4.3.3 Measured Strains

The load-strain relationship of specific points of the column and beam-column specimens provide more detailed information on the load behavior of the specimen components which contain those points. Figures 4-29 and 4-30 are load-strain plots of strains at a few points on the deck plate and on the rib wall of the single-rib column, SC. (The strain gage locations and numbers are given in Figures 4-6 and 4-7.) Noticeably large deviation from linear behavior started around 900 kips (4000 kN) in the deck plate and about 1000 kips (4450 kN) in the rib. This deviation from linearity at loads lower than that of the global behavior (Figure 4-24) indicates the influence of local initial out of flatness of plates.

Similar results of better indication of local behavior by local strains can be drawn from the load-strain plots of the single-rib beam columns and the triple-rib beam-column. Representative load-strain plots are presented as Figures 4-31 to 4-39. The main observation from these plots is that all changes of strains with load were linear and gradual under load until near or at the maximum load of the members.

Of interest to this study of orthotropic deck panel strength is the distribution of strains in the triple-rib beam-column specimen, TBC. Figure 4-40 shows the distribution of strain on top of the deck plate, and Figure 4-41 shows that of the lower face of the deck and the outer surface of the rib walls on the respective projected points on the deck. The uniformity of the compressive strains on the top surface of the deck before and after the application of the simulated wheel load indicates that it had little effects on the deck strains in comparison to the effects of axial loads. The 40 kips (178 kN) transverse load was much less than the magnitude of 4000 kips (17800 kN) axial forces applied to the specimen. On the lower side of the deck, the 40 kips (178 kN) simulated wheel load induced flexural bending of the loaded rib and changed the compressive strains to tensile strains at the bottom of the rib. This effect was local, as was discussed in Chapter 3. When the axial load was increased, the overall compressive strain increased accordingly. Only at high compressive loads near the ultimate strength of the triple-rib specimen did the strain distribution become irregular due to local behavior of the component plates.

4.4 Analytical Evaluation

4.4.1 Local Buckling of Component Plates

To analyze the test specimens as a column or a beam-column, it is essential to evaluate the buckling strength of the compressive components. Following the provisions of AISC / AASHTO as listed in Appendix A, the elastic and inelastic buckling strength of the deck and wall plate of a rib are computed. The results are presented in Table 4-7 and 4-8. The lowest buckling strength of the component plate is for the rib wall, being 52.1 ksi (359 MPa) which is higher than the yield strength of the deck plate. This indicates that the column and beam-column specimens would fail in the inelastic range, as observed during the experiment.

4.4.2 Column / Beam-column Strength

Without component buckling and overall member buckling, the onset of yielding of the deck plate with σ_y = 50 ksi (345 MPa) would be the reference strength of a specimen. For a single rib:

Column Yielding	$P_y = P_p$ = 1368 kips (6088 kN)
Beam-column Yielding	P_y = 1134 kips (5046 kN)
Corresponding Moment	M_y = 1174 kips-in. (133 kN-m)

The reference strength for a single rib column as computed using the provision in Appendix A are the following:

Column Elastic Buckling σ_{cr} = 339 ksi (2336 MPa)

P_{cr} =9272 kips (41260 kN)

Column Inelastic Buckling with uniform yield stress of σ_y = 50 ksi (345 MPa)

σ_{cr} = 48.6 ksi (335 MPa)

P_{cr} =1329 kips (5914 kN)

With a weighted yield stress of f_y = 57.64 ksi (397 MPa)

σ_{cr} = 55.8 ksi (384 MPa)

P_{cr} =1526 kips (6791 kN)

Because the single rib column failed by the inelastic buckling of the rib walls, not by the overall buckling of the specimen, the provisions of Appendix A are not directly applicable. The procedure as developed by Usami and Fukumoto (1982) in conjunction with the AISC *Q*-factor method was adopted. The strength reduction factor, *Q*, accounts for the buckling of the rib wall in the evaluation. The strength of the column is assumed as the sum of the component strength. The relevant equations and the results of computation are presented in Appendix B. the results are summarized in Table 4-9. The computed column strength of specimen SC is 1372 kips (6105 kN).

The procedure for computation of beam-column strength at first yield is summarized in Appendix C. There is no simple, comprehensive equation for the evaluation of load carrying strength of beam-column in the inelastic range of behavior. Based on the observed condition that the single rib and triple rib beam-columns behaved practically the same as the single rib column, the procedure of Appendix B was utilized for the beam-columns. These results are discussed later with those from the finite element analysis.

4.5 Finite Element Analysis

4.5.1 Structural Modeling

For the estimation of the load carrying capacity of the beam-column specimens, the finite element method was adopted. The nonlinear software ABAQUS was again selected. The finite element models of the single-rib and triple-rib specimens are shown in Figure 4-42 and 4-43. Shell elements (S4R) of about 3 × 3 in. (76 × 76 mm) were used.

The models had flat ends with one end being fixed and the other allowed to move with the shortening of the specimen, simulating the test setup. The edges of the models were free to displace in any direction. The global initial out of straightness of a specimen from measurement was idealized as a half sine curve and incorporated.

Residual stresses in the rib specimens were also incorporated in the analysis. The magnitude and distribution of residual stresses in the deck plate and rib walls were assessed based on previous studies (Chen and Yang 2002), and are shown in Figure 4-44. At the welds, the magnitude of the tensile residual stress was the respective yield stress of the plate. In the rib walls, the compressive residual stress was assumed to be 0.1 of the material yield stress, or 7 ksi (48 MPa). The material properties of the deck plate and the rib wall were modeled as elastic-perfectly plastic.

In order to model the full range of behavior of the specimens, including the pre-buckling, post-buckling, yielding and post ultimate load stages, a solution strategy utilizing a modified Riks method was adopted.

4.5.2 Results of Analysis

The results of computed ultimate loads by the finite element analysis are listed with the experimental results in Table 4-10. The finite element analysis (FEA) included two cases: a) incorporated only the overall initial out of straightness of the specimens with no consideration of residual stresses and b) included both. For all four specimens the inclusion of residual stresses resulted in only a slightly lower computed strength. The highest deviation is about 4%. This indicates that the presence of residual stress has only minor effect on the load carrying capacity of the column and beam-columns. In comparison with the experimental results, the computed strength with consideration of residual stresses are generally closer to the recorded ultimate loads of testing, with an overestimate of the column strength and slight underestimate of the beam-column strength.

Single Rib Column

The load deflection curves of the column specimen from the finite element analysis are compared with that from experimental results in Figure 4-45. The analytical curves with and without consideration of residual stresses are quite close to each other. The curve from test results, however, shows that the test specimen was less stiff and attained a lower ultimate load than computed. This could be due to the condition that the column specimen was Rib 8 along the deck plate welded connection of the model test deck of Chapter 2, and was a part of the two span continuous beam specimen of Stage III in Chapter 3 (Figure 3-2 and Table 3-2).

The appearance of the specimen with residual stresses and under 1385 kips (6163 kN) maximum load, and at computed axial shortening of 1.36 in. (35 mm), are shown in Figures 4-46 and 4-47 respectively. At the ultimate load, hardly any local deformation of the component plates is visible from Figure 4-46. This is in full agreement with the test results. Figure 4-47 shows the local buckling of the rib wall near the ends, corresponding to the buckles of Figure 4-13. The local deflection of the deck plate in Figure 4-12 and 4-14, possibly due to local out of flatness, was not generated by the finite element analysis.

Single Rib Beam-column

The computed curves of load versus axial shortening of the single-rib beam-columns are presented in Figure 4-48. Three cases were examined: with a rigid load pad at mid height (FEA-1), no loading pad (FEA-2) and with residual stresses. Also plotted are the recorded load-shortening curves from the two beam-column specimens SBC1 and SBC2. The effect of the load pad on the ultimate strength is relatively minor, whereas the effects of the residual stresses are noticeable. The difference is about 4%. The curves from the test specimens fall between the computed curves. Figure 4-49 and 4-50 are the computed appearance of the beam-columns with and without a load pad after the attainment of the ultimate load. The axial shortening is about 1in. (25 mm). It is obvious from these figures that the load pad which simulates the wheels of a truck presents the unrealistic “punching” of the deck plate after reaching the ultimate load. At the peak load, even the relatively concentrated load without a load pad did not induce serious local deflection, as is shown by the computed deflection shaped in Figure 4-51. The computed local deflections at the ends and at mid height of the model in Figure 4-50 are of the same shape as that of the actual ones of the specimens, as shown in Figure 4-15, 4-18 and 4-19.

Triple Rib Beam-column

The results of finite element analysis of the triple-rib beam-column are essentially the same as those of the single-rib beam-columns. Figure 4-52 contains the load-deflection curves of the specimen by the finite element analysis and from testing. Again, the inclusions of residual stresses resulted in a slightly lower ultimate strength. Overall, the computed and measured load-deflection relationships agree well all the way up to the computed ultimate load.

At the ultimate load, the appearance of the specimen from finite element analysis is shown in Figure 4-53. Little local damage is visible in this figure, as is the situation in the photograph of Figure 4-21. Figure 4-54 shows the computer generated appearance of the specimen at an axial shortening of 1.8 in. (46 mm). Yielding and local buckling of the web wall near the ends was the cause of failure.

Figure 4-55 shows the strain distribution on the surface of the deck at the mid height of the triple-rib beam-column under increased axial loads. The strain distribution shapes are corresponding to those from the measured strains as shown in Figure 4-41, showing that the wheel load effect was confined to only one rib. This similarity of results between computed and experimental results confirms the validity of both.

4.6 Discussion and Recommendation

The experimental and analytical results of the single rib column and beam-columns were very similar. So were the results from single-rib and triple-rib beam-columns. Failure of the specimens at ultimate load was by local buckling of the rib walls and yielding of the deck plate. There was no overall buckling of the ribs.

The primary reason that the beam-column and column specimens of the rib behaved very similar is the insignificant magnitude of the lateral load. The applied lateral load of 40 kips (178 kN), even though it is twice that of the wheel load of a HS 25 truck, is very low in comparison to the maximum applied axial load of around 1400 kips (6230 kN) to each of the ribs of the specimens. The 40 kips load generated bending moments in the beam-columns, but the magnitudes of the moment were not high enough to induce overall beam-column action. Rather, failures was due to local buckling of the rib walls.

There is no existing procedure for computing the strength of beam-columns which failed by local buckling of the rib wall. The method of summation applied to columns (Usami and Fukumoto, 1982) is recommended, assuming that the buckled rib walls can continue to carry loads till buckling or yielding of all other components of the cross section. Thus, by using the component characters of Table 4.9, the estimate compressive strength of the single rib column and beam-column specimens is:

$$50 \times 8.45 + 50 \times 8.45 + 47.07 \times 8.93 + 70 \times 1.52 = 1372 kips (6105 kN)$$

The triple rib beam-column is estimated to have strength of three times this values, or 4116 kips (18315 kN). These values are listed in Table 4-11. The estimated strengths from the recommended procedure of summation are fairly close to the experimental results. The estimated strengths are higher than the reference values of the computed loads at global buckling of a rib column, and are on the conservative side when compared with the test results.

It is to be noted that local buckling of the ribs occurred near the ends of the specimens. These are locations with negative bending of the ribs in deck panels. There is a compress stress gradient in the ribs which was not considered in the recommended procedure. Refinement on the estimation of buckling strength of the rib wall should provide even better results then given in Table 4-11.

Table 4-1 Dimensions of Components of a Stiffening Rib (in.)

Component	**t**	**b**	**h'**	**A**	**y**	A_y	A_y^2	I_0
Deck Plate	0.650	26.00	-	16.90	0.33	5.49	1.79	0.60
Rib Walls	0.325	0.68	14.07	8.93	7.32	65.37	478.42	129.20
Rib flange	0.325	4.66	-	1.51	13.99	21.19	296.38	0.01
Σ				27.35		92.05	776.58	129.81
	y_bar=	3.37	**I =**	466.73				
	y(top)=	3.37	**S(top)=**	138.66				
	y(bot)=	10.76	**S(bot)=**	43.38				

Table 4-2 Sectional Properties of a Rib

A (in^2)	I (in^4)	r (in)	L (in)	L/r	b/t_d	h'/t_r
27.35	466.73	4.13	120	29.06	20.00	43.29

Table 4-3 Material Properties of Rib Components

Steel plates	**Yield Strength σ_Y (ksi)**	**Tensile Strength σ_u (ksi)**	**Elongation (%)**	**Grade**
Deck plate	50	67	23.75	A709
Rib plate	70	80	18.25	A709

Table 4-4 Reference Load

Sepcimen	P_y (kips)	P_p (kips)	M_p (kips-in.)	$P_{cr,d}$ (kips)	$P_{cr,r}$ (kips)
SC	-	1576	4409	1376	420
SBC1	1134	1576	4409	1376	420
SBC2					
TBC	3402*	4729	13227	4131	1261

* At first yield of deck plate with 40 kips simulated wheel load

Table 4-5 Maximum Relative Initial Deflection

Specimens **Initial deflection**	**Single Rib Column**	**Single Rib B-C 1**	**Single Rib B-C 2**	**Triple Rib B-C**
$\delta_{1,max} / b$	1/130	1/35	1/117	1/684
$\delta_{2,max} / h'$	1/824	1/875	1/933	1/933
$\delta_{3,max} / L$	1/320	1/563	1/1636	1/1674

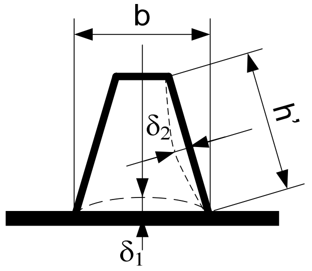

Initial deflection of deck plate and rib wall

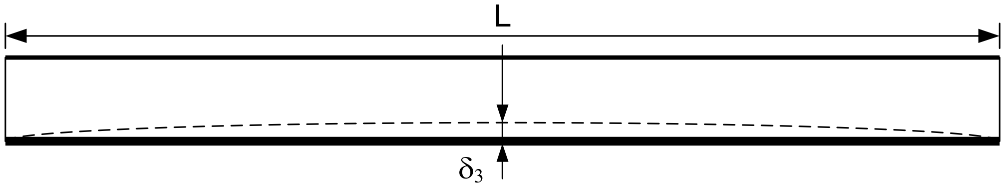

Initial deflection of stiffener

Table 4-6 Test Results

Specimen	**Ultimate Load (kips/kN)**	**Max. Axial Deflection (inch/mm)**	**Max. Lateral Deflection (inch/mm)**	**Failure Mode**
SC	1385 (6162)	1.048 (27)	1.980 (50)	local buckling of rib wall near ends
SBC1	1358 (6162)	0.877 (22)	2.570 (65)	yielding of deck plate at mid height then local buckling of rib wall near ends and at mid height
SBC2	1412 (6283)	0.904 (23)	2.549 (65)	yielding of deck plate at mid height then local buckling of rib wall near ends and at mid height
TBC	4422* (19678)	0.550 (14)	0.436 (11)	yielding of deck plate and local buckling of rib wall near ends

* Average per rib, 4422 / 3 = 1474 kips

Table 4-7 Computed Elastic Buckling Strength of Single Rib Components, (AISC)

Section	***b*** **(inch)**	***t*** **(inch)**	***b / t***	**Boundary Conditions**	**Buckling Strength (ksi)**
Deck Plate	26.00	0.650	40.00	S.S. – S.S.	242.33
Rib Walls	14.07	0.325	43.29	S.S. – S.S.	51.70
Rib Bottom	5.00	0.325	15.38	S.S. – S.S.	409.50

S.S.: Simply Supported

Table 4-8 Computed Inelastic Buckling Strength of Single Rib Components, (AISC)

Section	***b*** **(inch)**	***t*** **(inch)**	***b / t***	**Boundary Conditions**	**Buckling Strength (ksi)**
Deck Plate	26.00	0.650	40.00	S.S. – S.S.	49.60
Rib Walls	14.07	0.325	43.29	S.S. – S.S.	52.10
Rib Bottom	5.00	0.325	15.38	S.S. – S.S.	69.60

Table 4-9 Buckling Strength of Rib Components, AISC / Fukumoto (1985)

Section	***b*** **(inch)**	***t*** **(inch)**	***b / t***	**No.**	**Area (inch^2)**	**σ_y (ksi)**	**σ_{cr} (ksi)**	**P_u (kips)**
Deck Plate 1	13.00	0.650	20.00	1	8.45	50.0	81.5	422.5
Deck Plate 2	6.50	0.650	10.00	2	8.45	50.0	140.0	422.5
Rib Walls	14.07	0.325	43.29	2	8.93	70.0	47.1	420.4
Rib Bottom	5.00	0.325	15.38	1	1.51	70.0	94.2	106.0
								Σ = 1371.4

Table 4-10 Experimental and FEA Results

Specimen	**Ultimate Load (kips)**				**Max. Axial Deflection (inch)**		
	Exp.	FEA		Difference	Exp.	FEA	
		(a)	(b)	(b) (%)		(a)	(b)
SC	1385	1578	1546	11.6	0.542	0.512	0.519
SBC 1	1358	1441	1381	1.6	0.440	0.448	0.453
SBC 2	1412	1441	1381	-2.2	0.463	0.448	0.453
TBC	4422 (1474)	4198 (1399)	4041 (1374)	-8.6	0.503	0.481	0.464

(a) without consideration of residual stresses.

(b) with consideration of residual stresses.

Table 4-11 Strength of Specimens (kips)

Specimen	Experiment	FEA	$P_{estimate}$	Reference	
				$P_{cr,rib}A$	P_p or P_y
SC	1385	1546	1372	1293	$P_p = 1576$
SBC1	1358	1381	1372	1293	$P_y = 1134$
SBC2	1412				
TBC	4422 (1474)	4041 (1347)	4116 (1372)	3879 (1293)	$P_y = 3402$ (1134)

$P_{estimate}$: from summation of parts

$\sigma_{cr,rib} A_i$: from AISC column global elastic buckling stress calculation

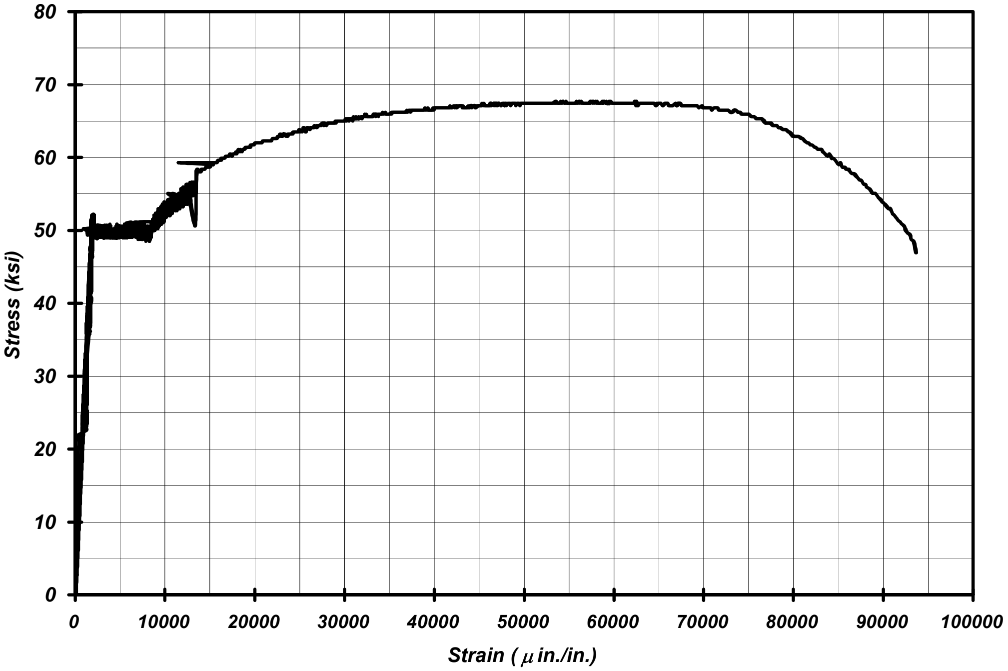

Figure 4-1 Deck Plate Coupon Test Results

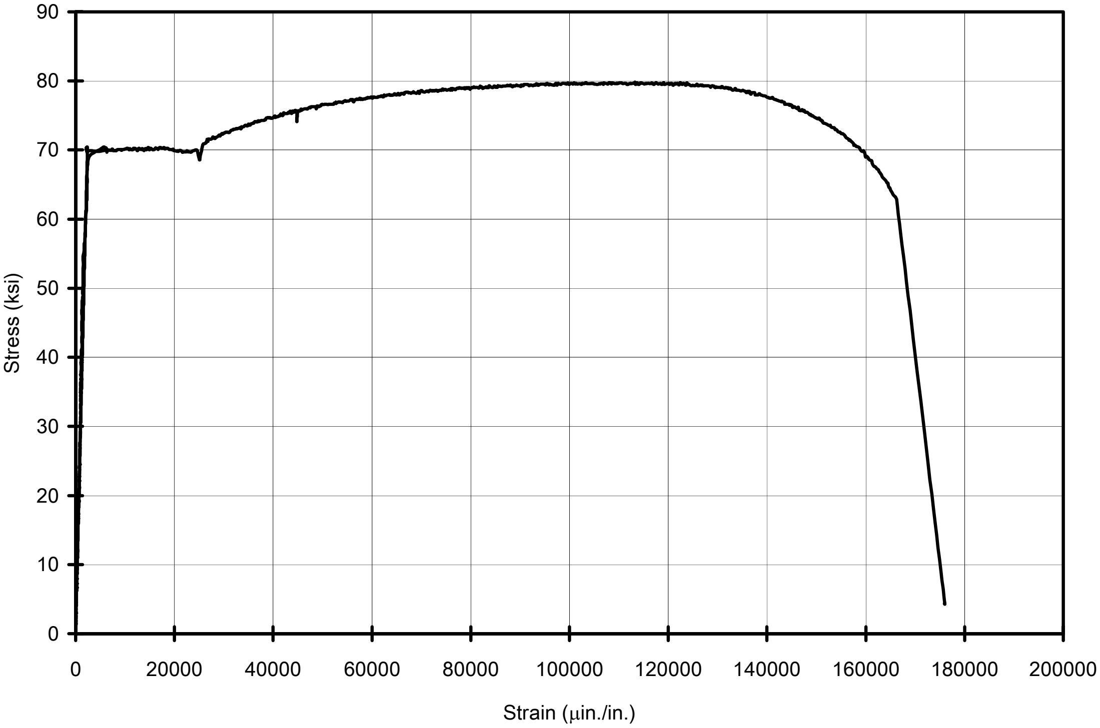

Figure 4-2 Rib Plate Coupon Test Results

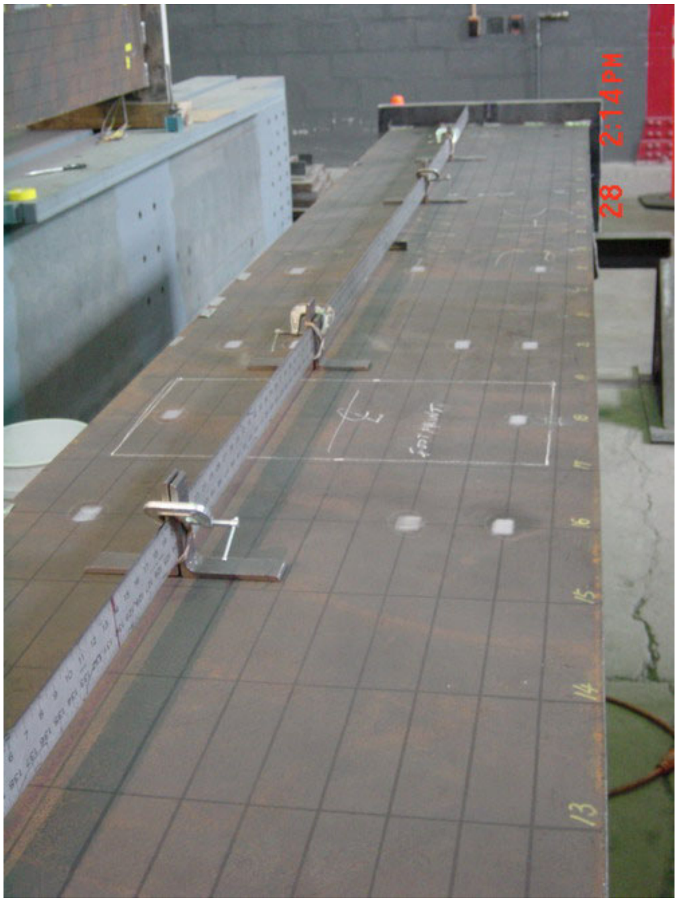

Figure 4-3 Measurement of Initial Imperfection

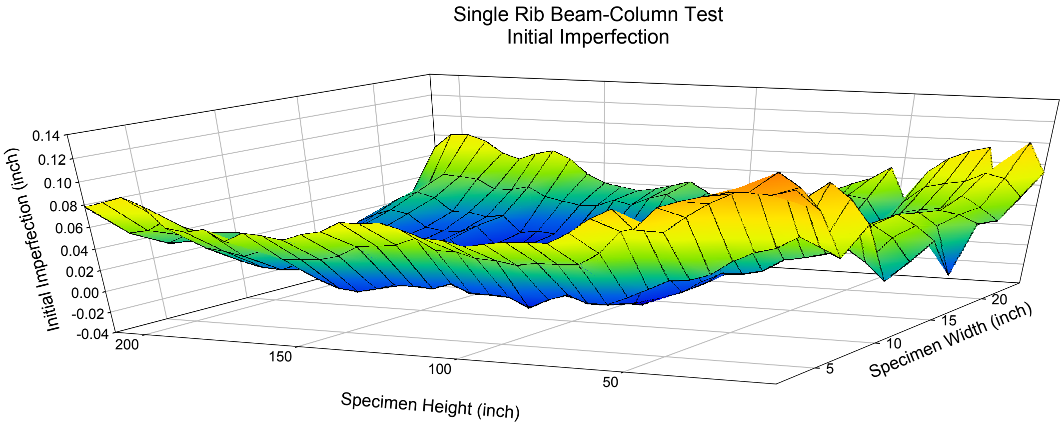

Figure 4-4 The Geometric Imperfection of Specimen, SBC1
(Note Different Scale)

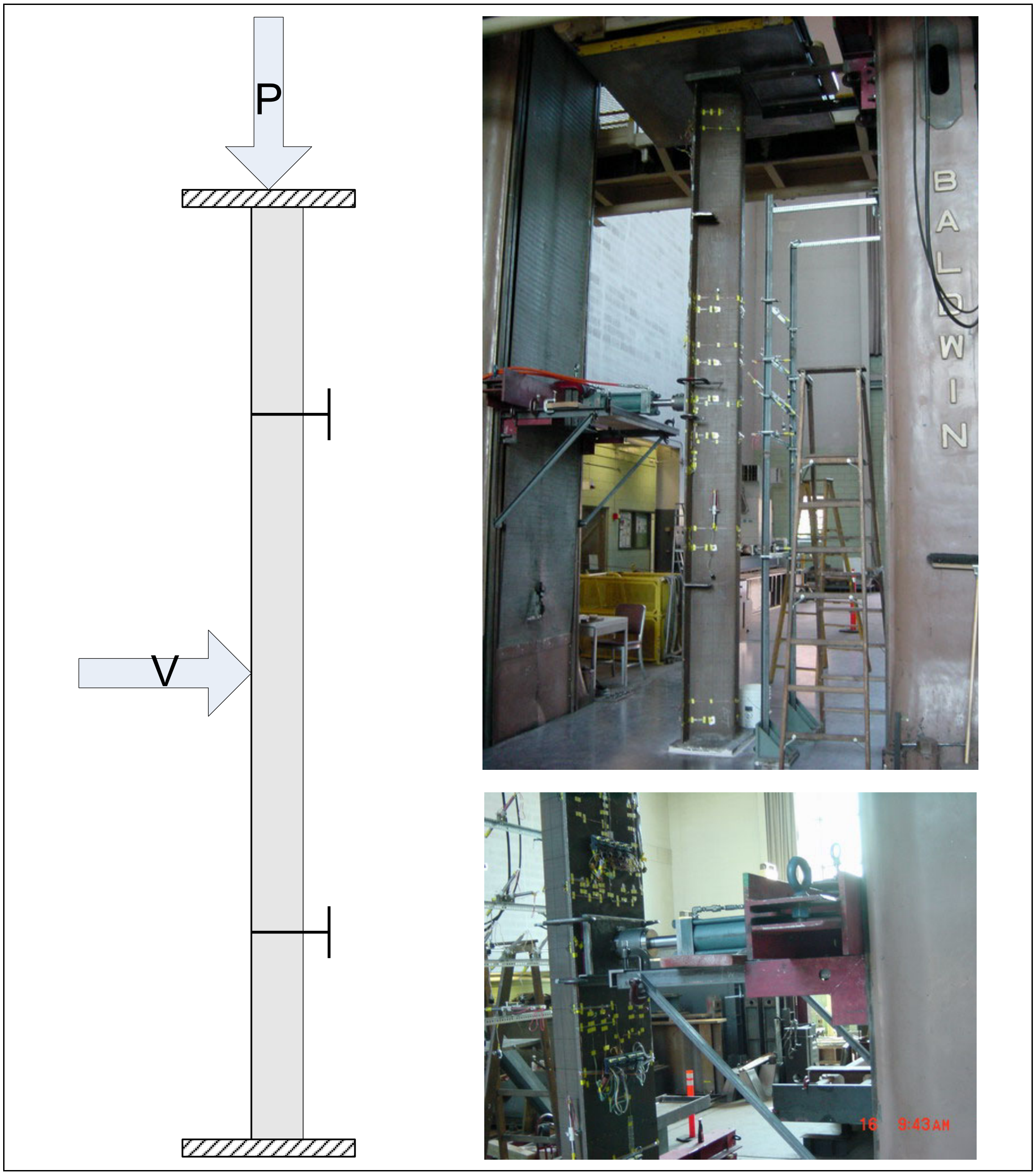

Figure 4-5 The Setup of Test Specimens

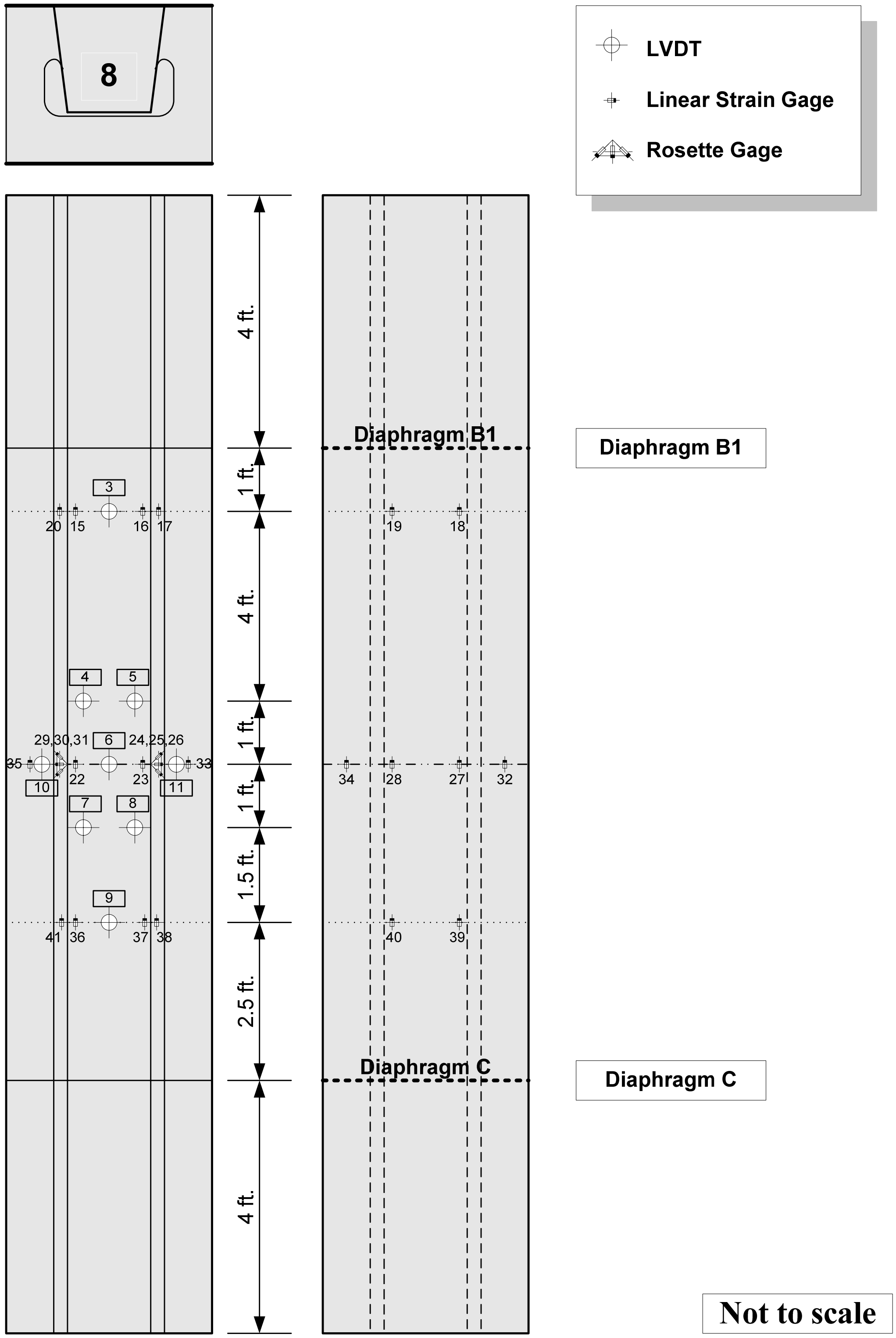

Figure 4-6 Instrumentation Plan for Single Rib Column, SC

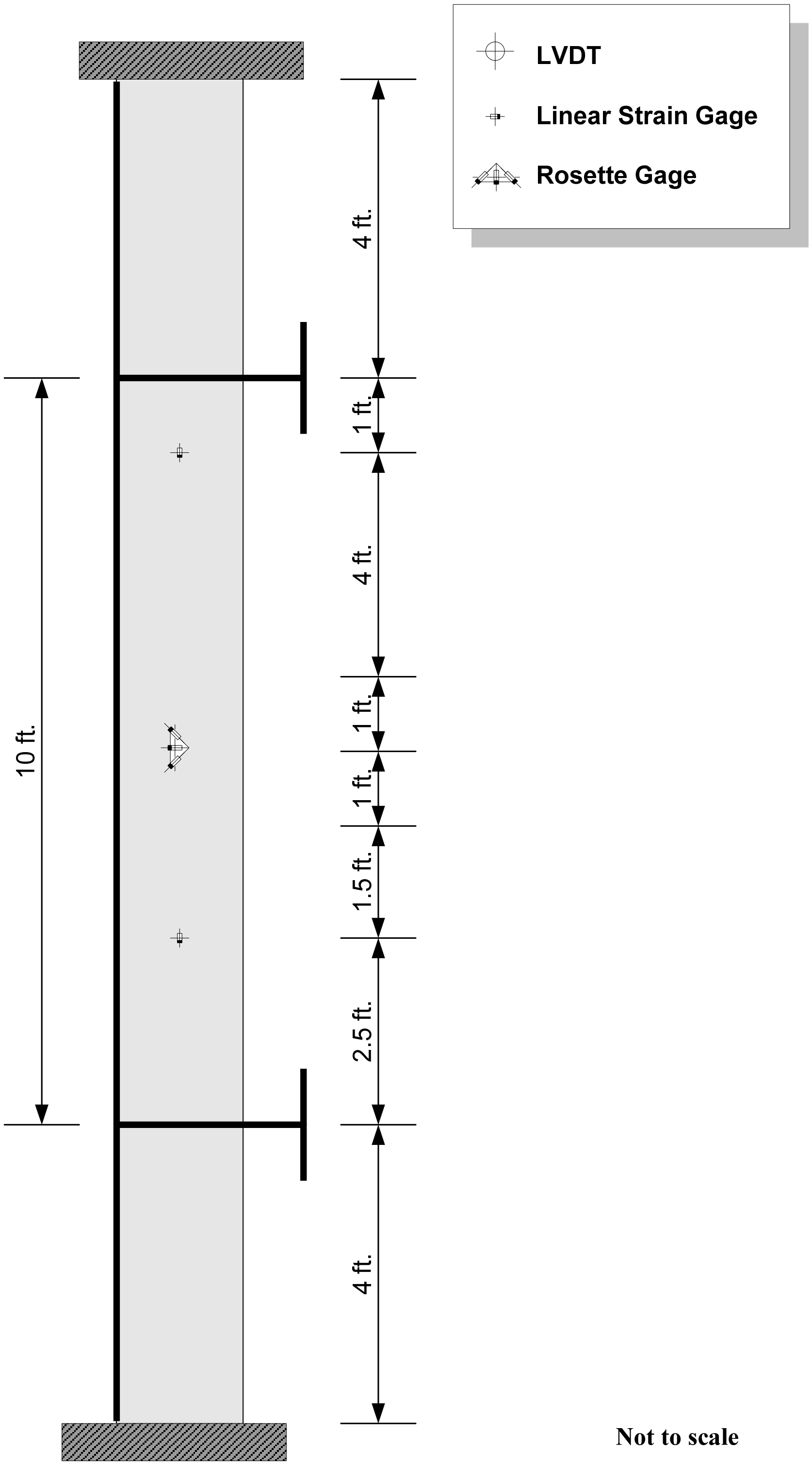

Figure 4-7 Instrumentation Plan for Single Rib Column, SC

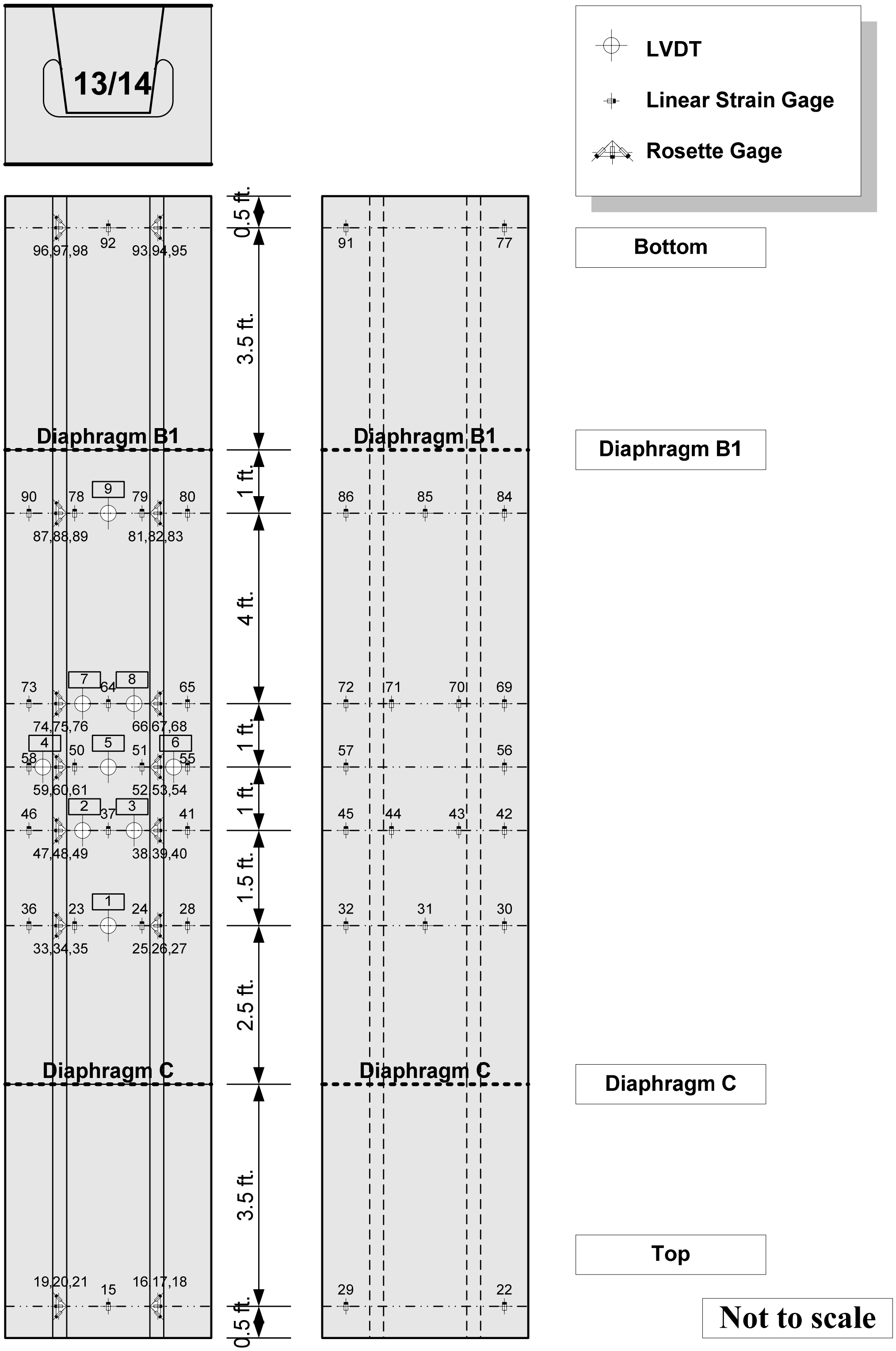

Figure 4-8 Instrumentation Plan for Single Rib Beam-column, SBC

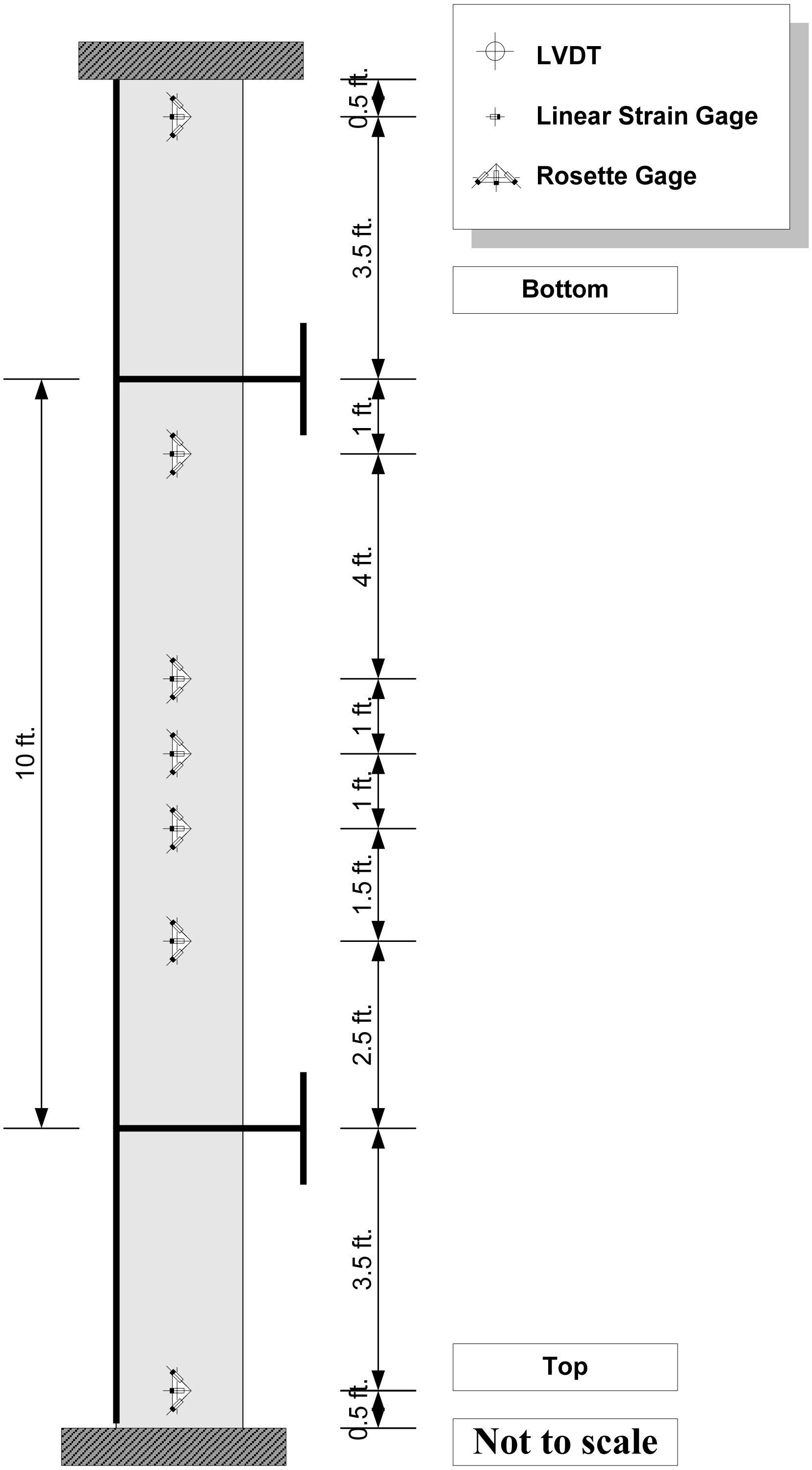

Figure 4-9 Instrumentation Plan for Single Rib Beam-column, SBC

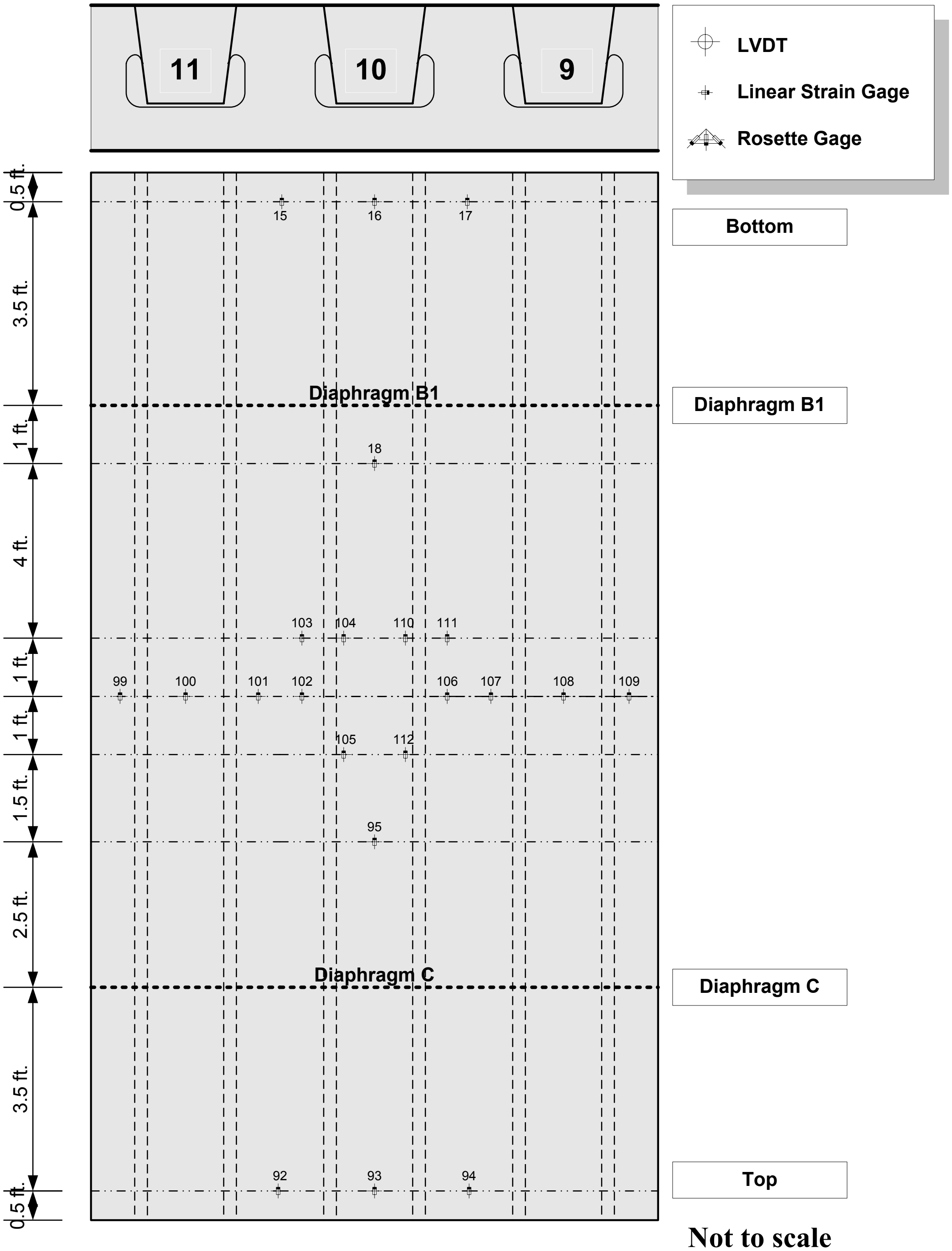

Figure 4-10 Instrumentation Plan for Triple Rib Beam-column, TBC

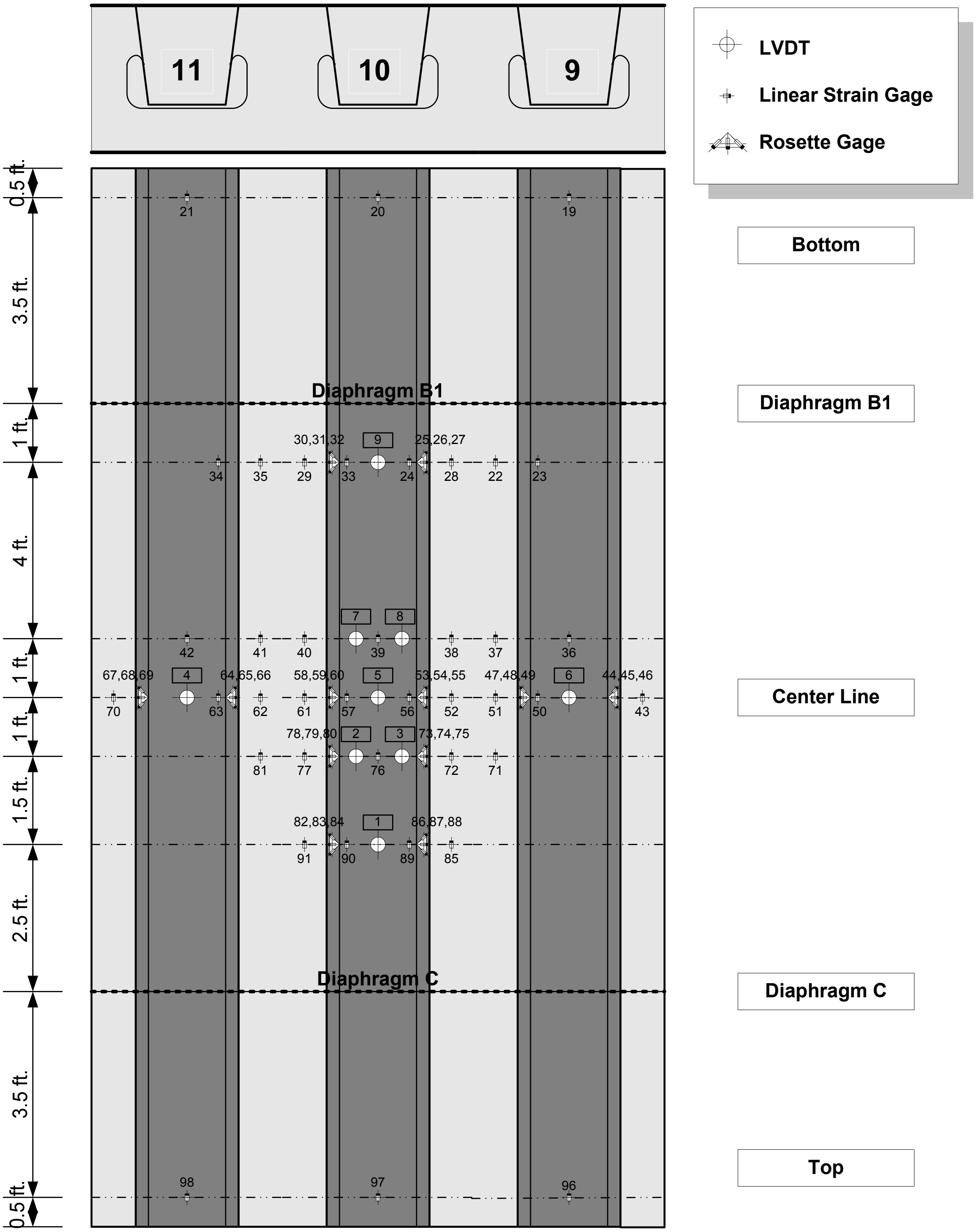

Not to scale

Figure 4-11 Instrumentation Plan for Triple Rib Beam-column, TBC

Figure 4-12 Final Appearance of Single Rib Column, SC

Figure 4-13 Local Buckling of Rib Wall near the Bottom of Column, Specimen SC

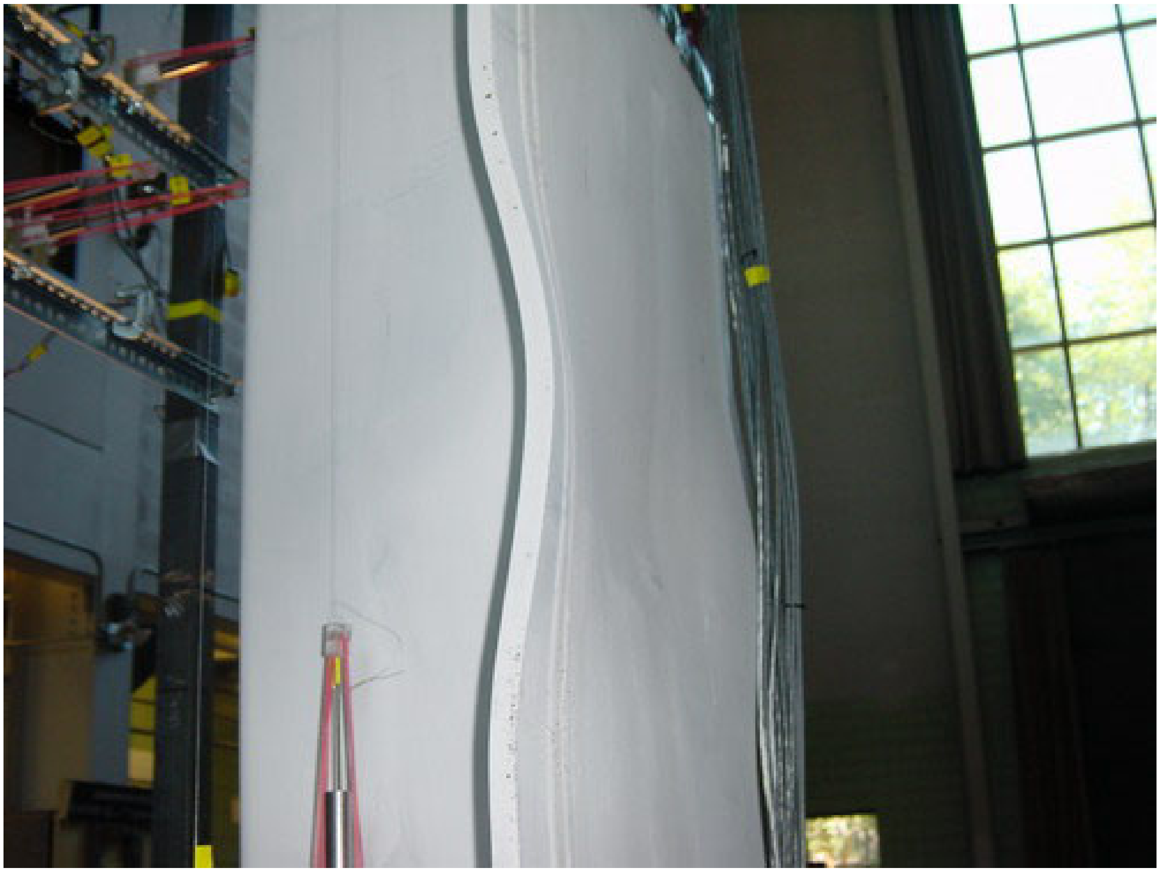

Figure 4-14 Local Buckling of Deck Plate near Mid-height of Single-rib Column, SC

Figure 4-15 Final Appearance of Single Rib Beam-column Specimen SBC1

Figure 4-16 Final Appearance of Single Rib Beam-column Specimen SBC2

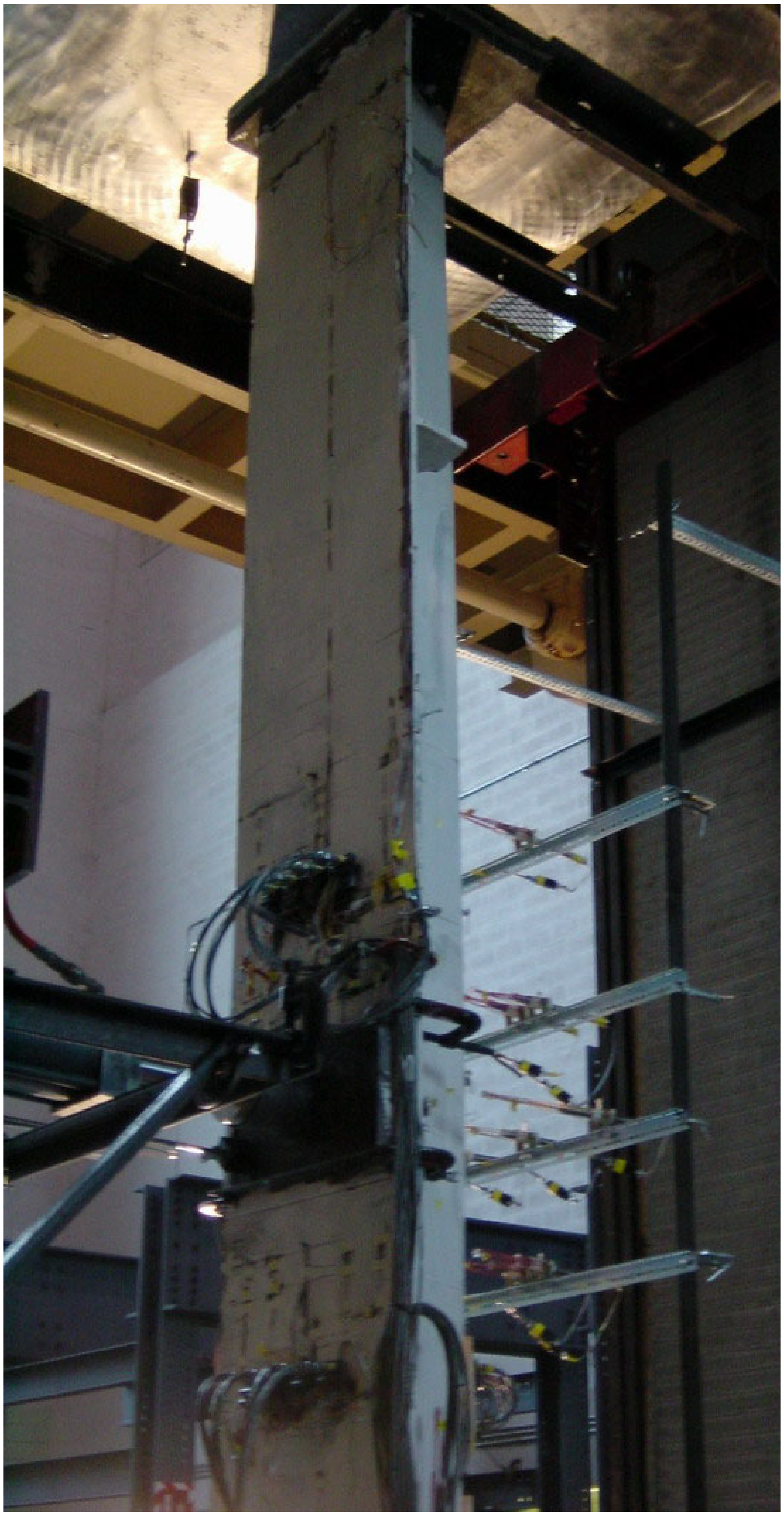

Figure 4-17 (a) SBC1

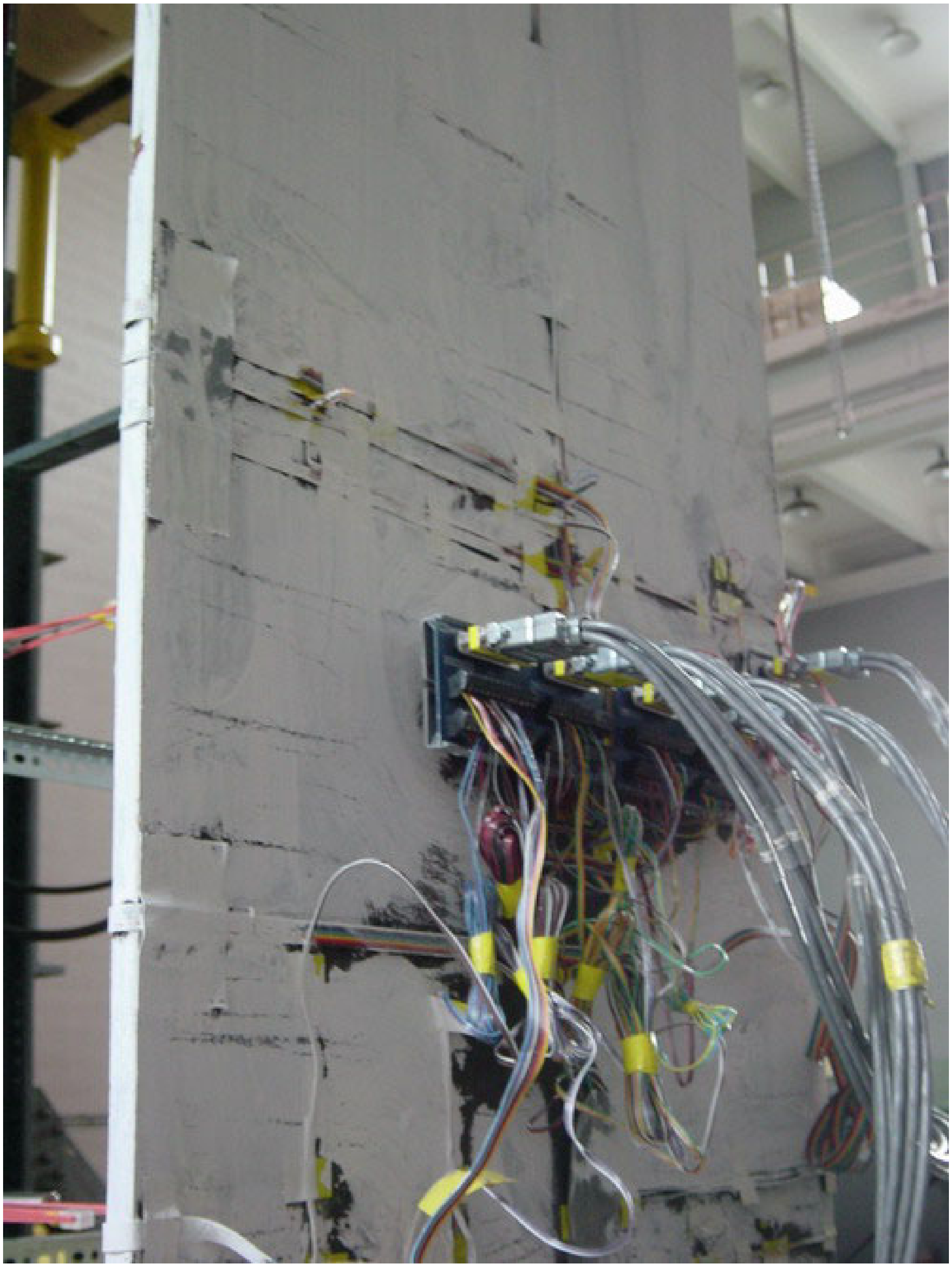

(b) SBC2

Figure 4-17 Yielding Line of Deck Plate near Mid-height, Single-rib Beam-column Specimens

Figure 4-18 Local Buckling of Rib Wall near the Ends of Beam-column, SBC1

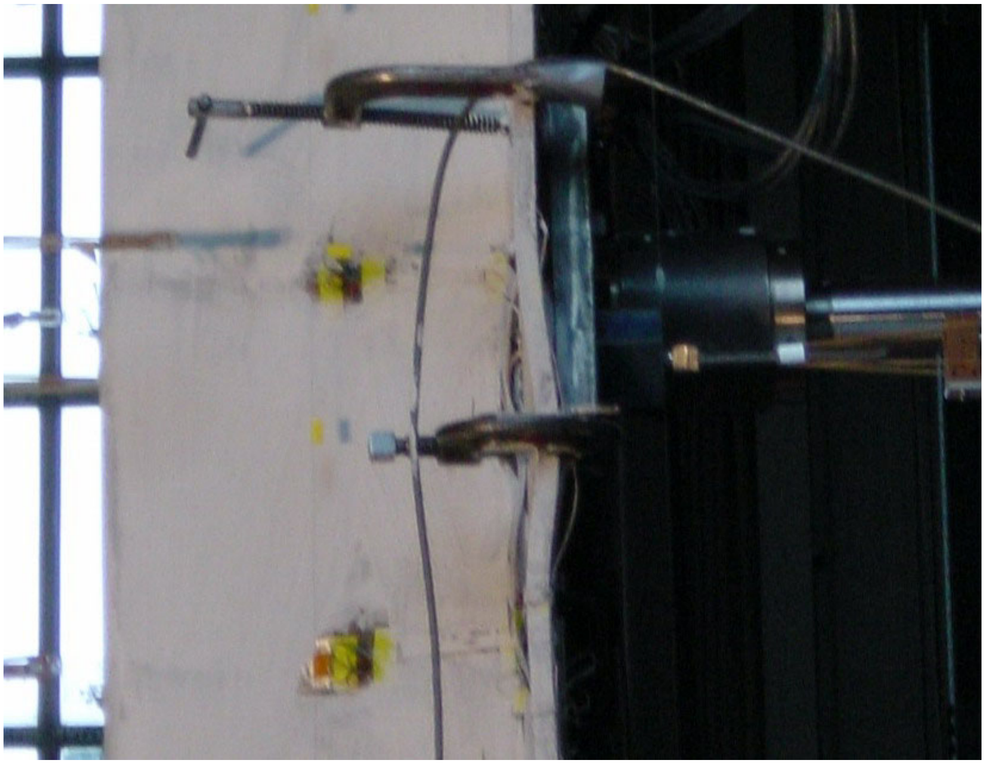

Figure 4-19 Deck Plate Local Buckling near the Simulated wheel Load

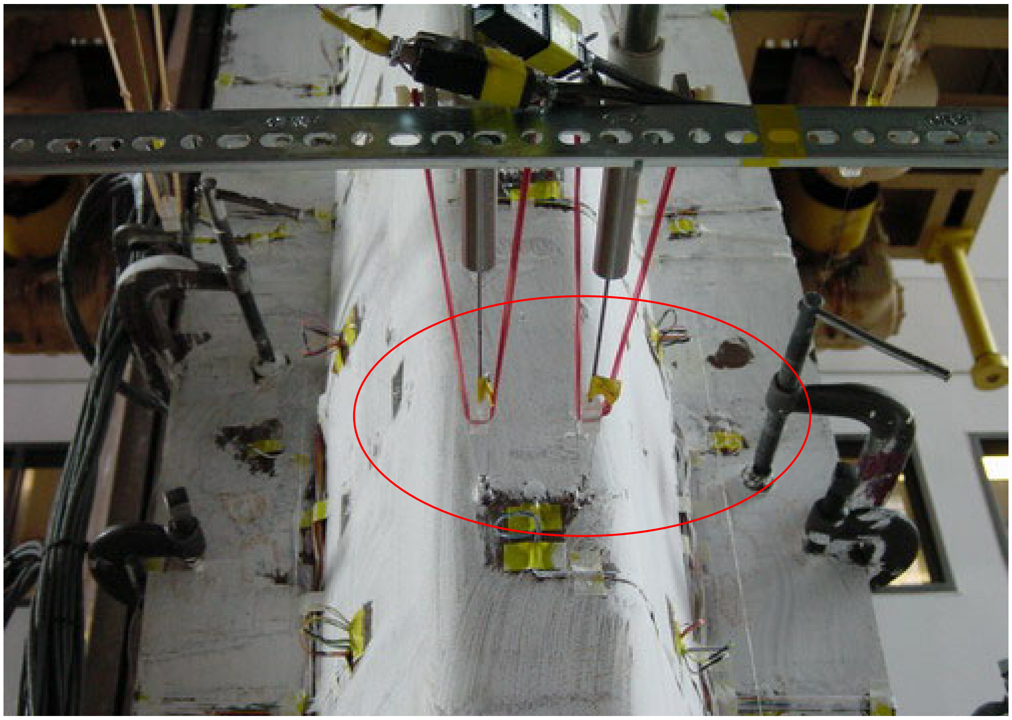

Figure 4-20 Rib Wall Local Buckling near the Simulated wheel Load

Figure 4-21 Final Appearance of Triple-rib Beam-column, TBC

Figure 4-22 Yielding Lines on Deck Plate of Triple-rib Beam-column, TBC

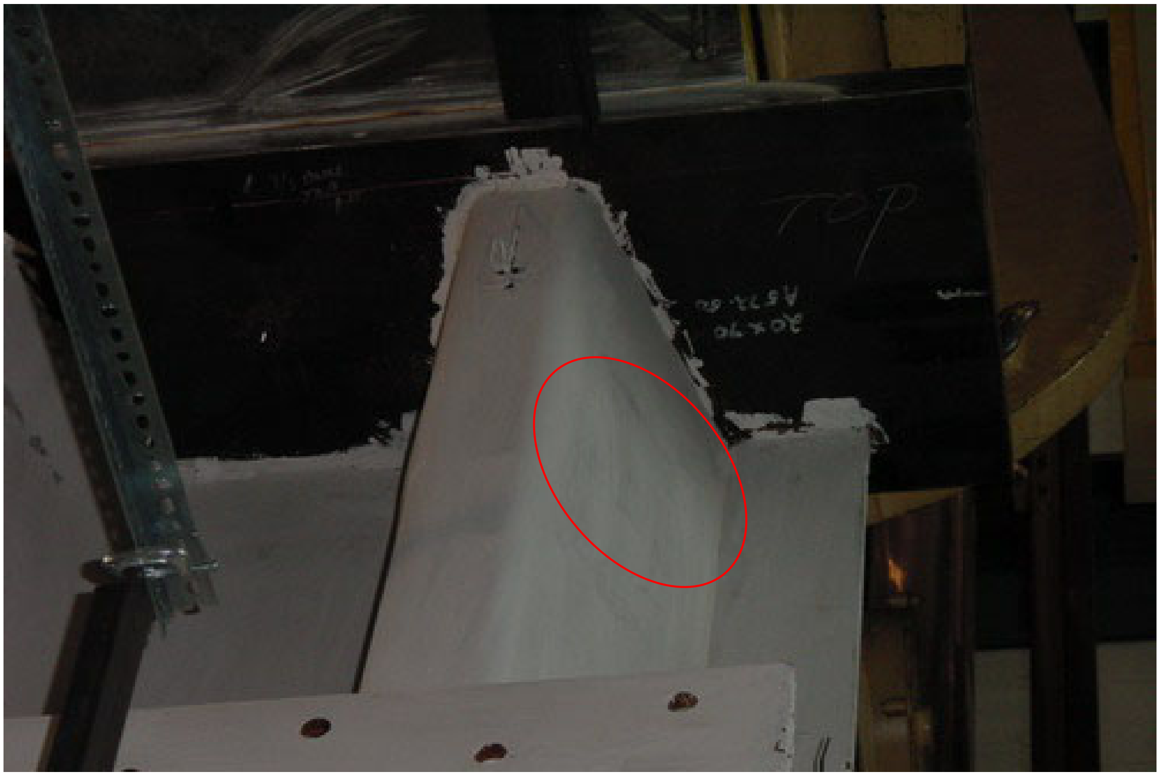

Figure 4-23 Local Buckling of Rib Wall of Triple-rib Beam-column, TBC

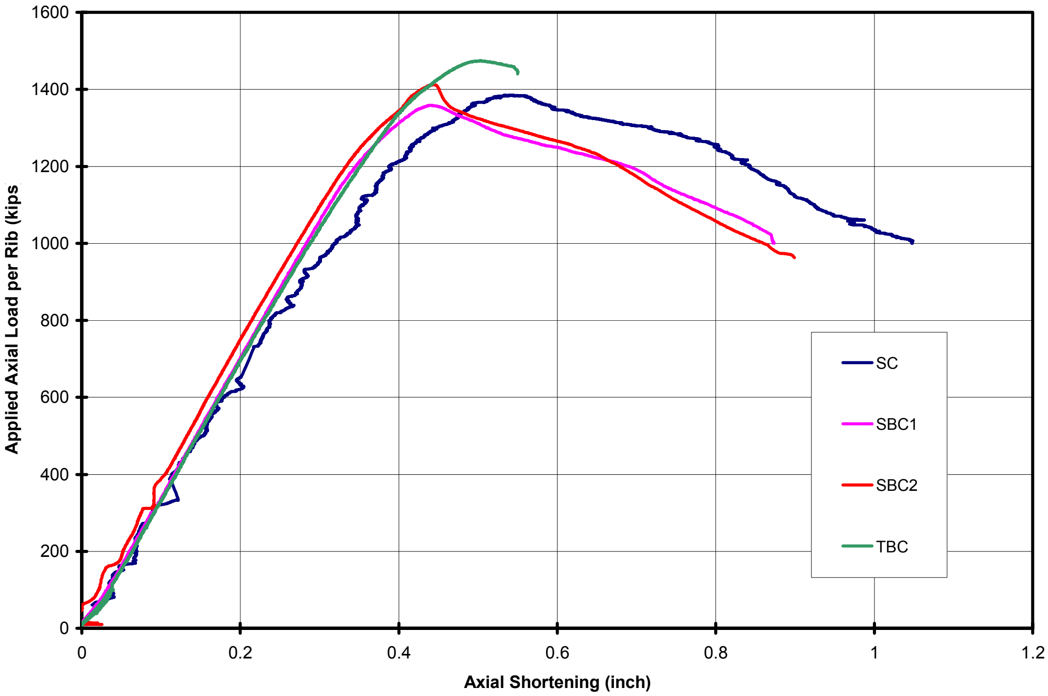

Figure 4-24 Axial Shortening of Specimens

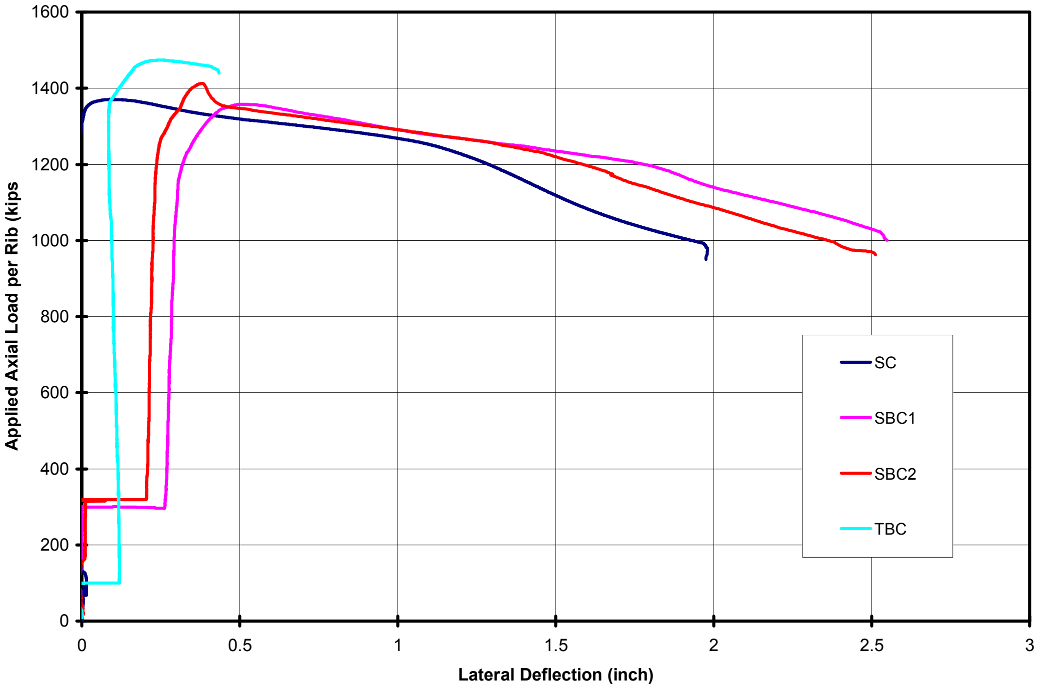

Figure 4-25 Lateral Displacement at Mid Point of Specimens

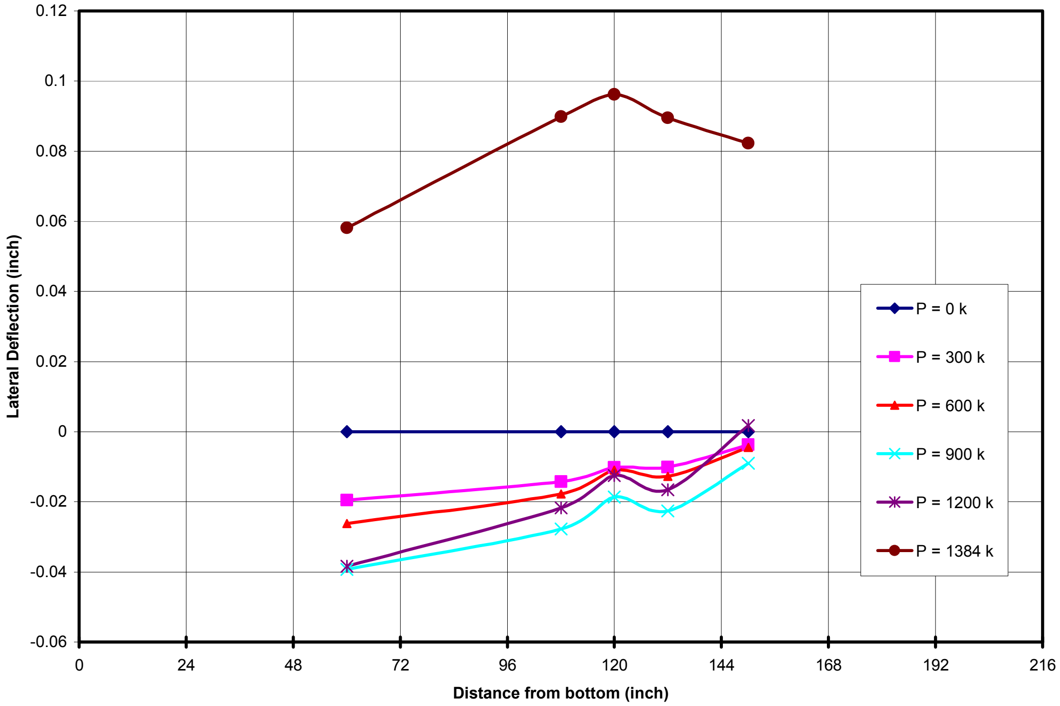

Figure 4-26 Lateral Deflection Profile of Rib, Single-rib Column, SC

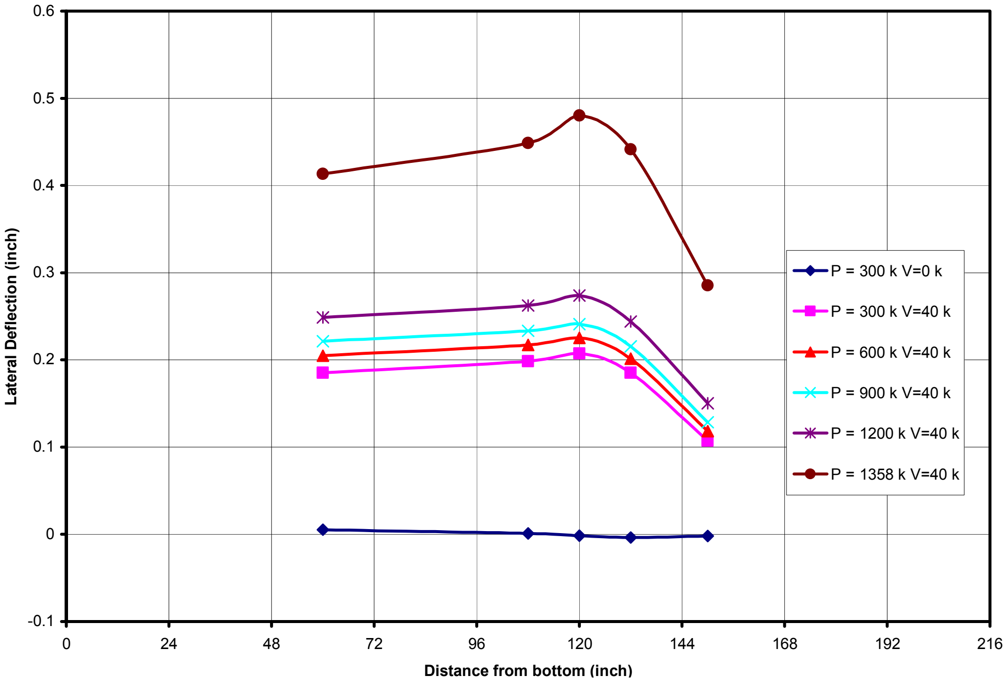

(a) Specimen SBC1

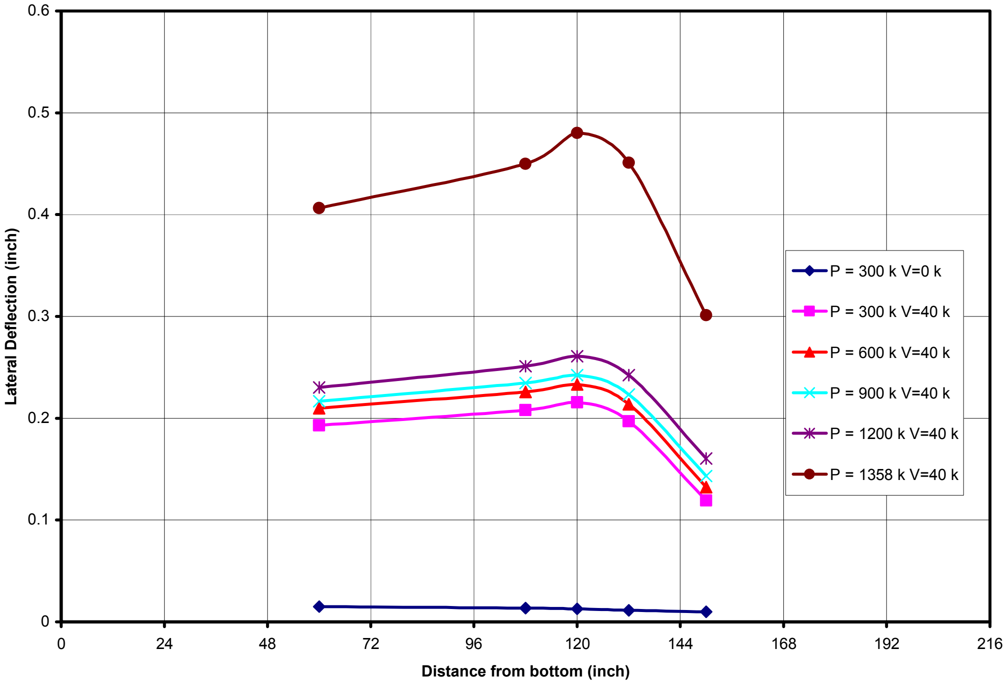

(b) Specimen SBC2

Figure 4-27 Lateral Deflection Profile of Rib, Single-rib Beam-columns

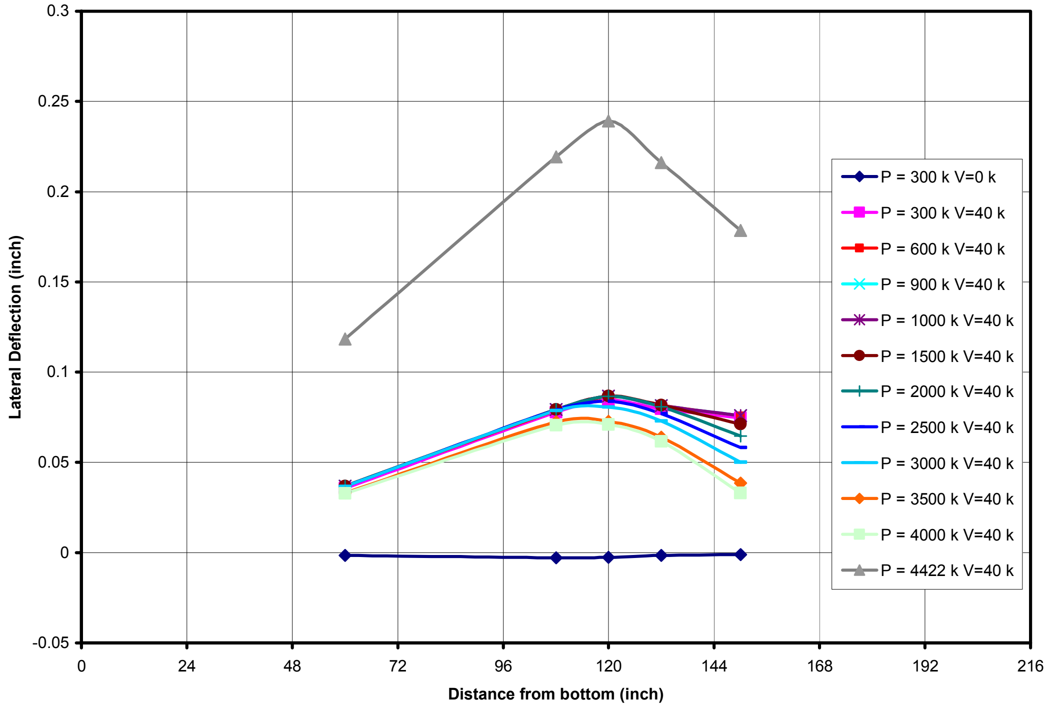

Figure 4-28 Lateral Deflection Profiles of Middle Rib, Triple-rib Beam-column, **TBC**

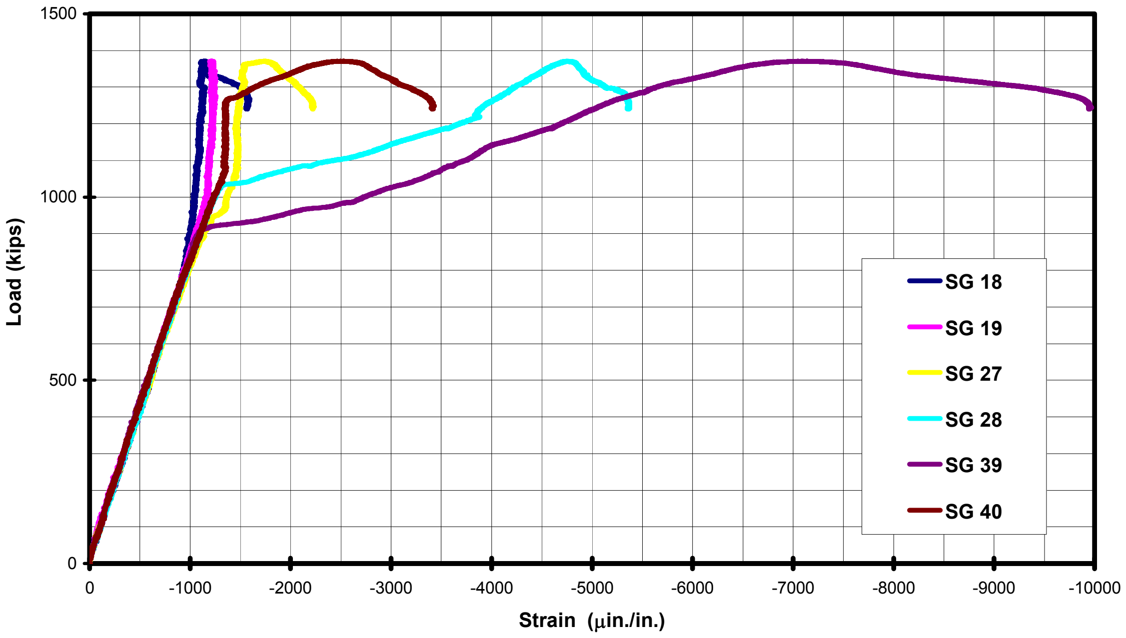

Figure 4-29 Strains on Deck Plate of Column, SC

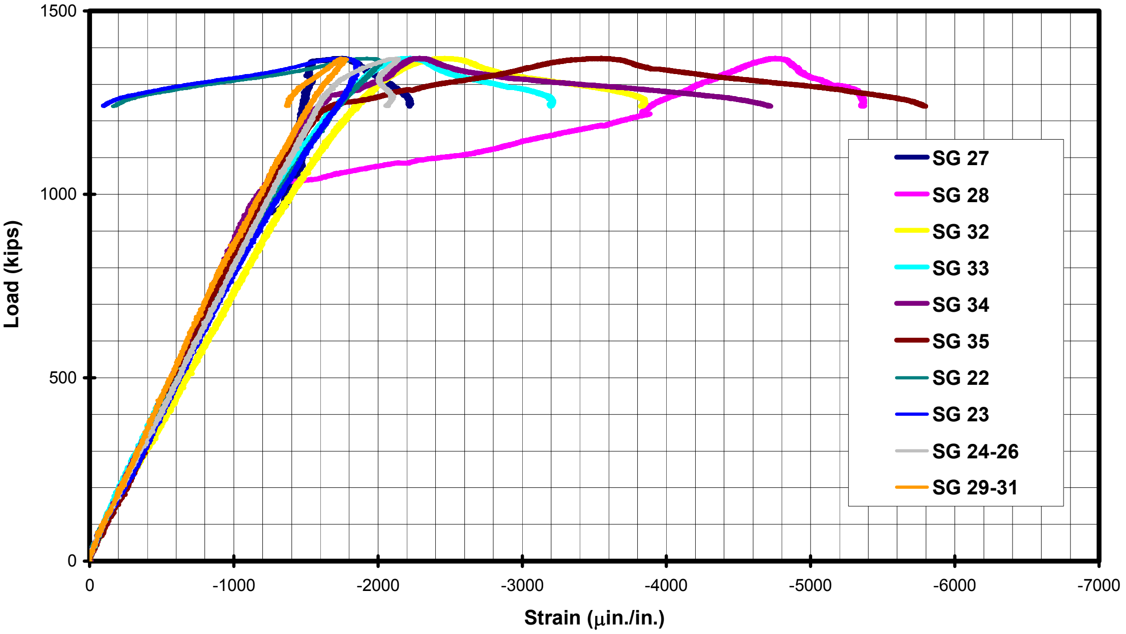

Figure 4-30 Strains on Rib at Mid-height of Single Rib Column, SC

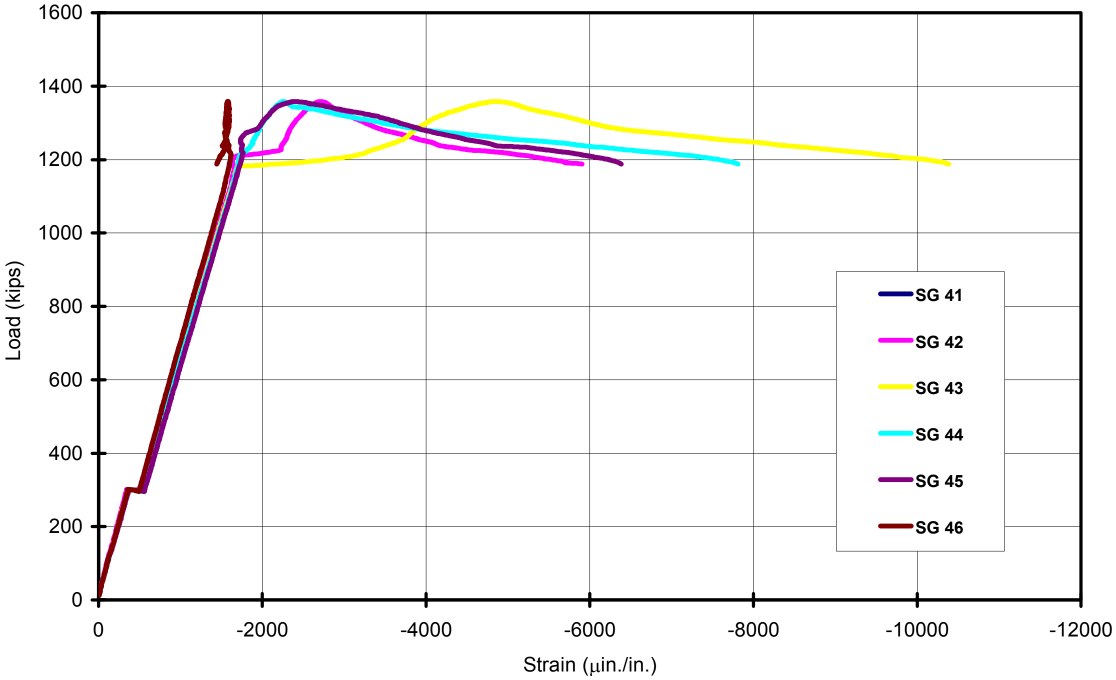

Figure 4-31 Load vs. strain on Deck Plate of Single-rib Beam-column, SBC1

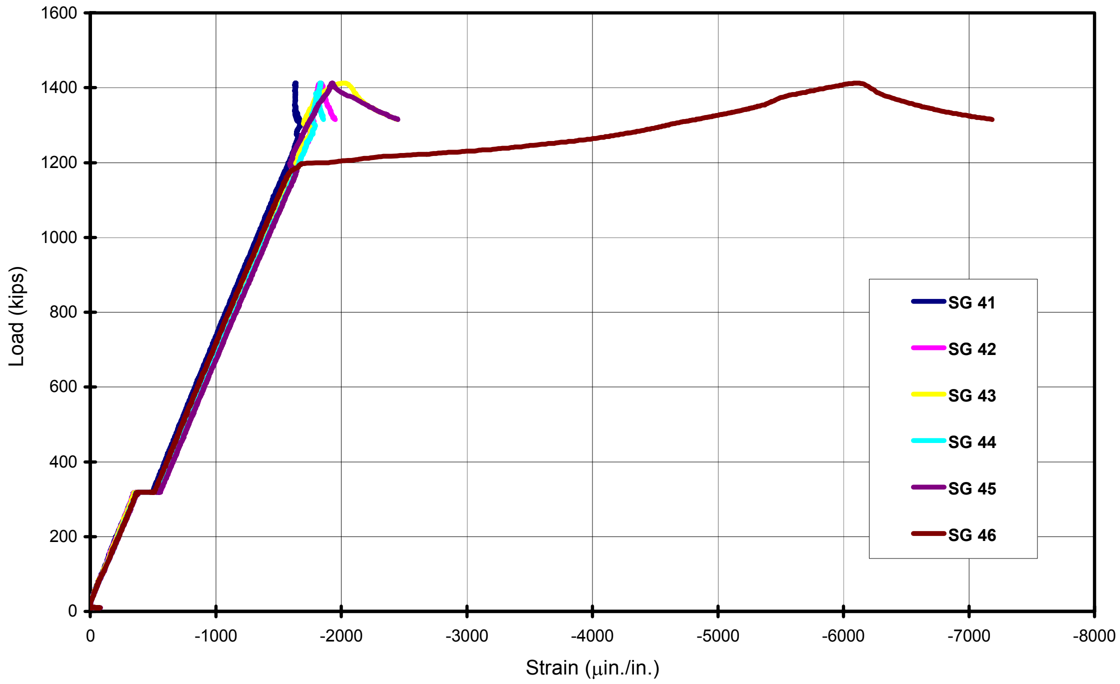

Figure 4-32 Load vs. strain on Deck Plate of Single-rib Beam-column, SBC2

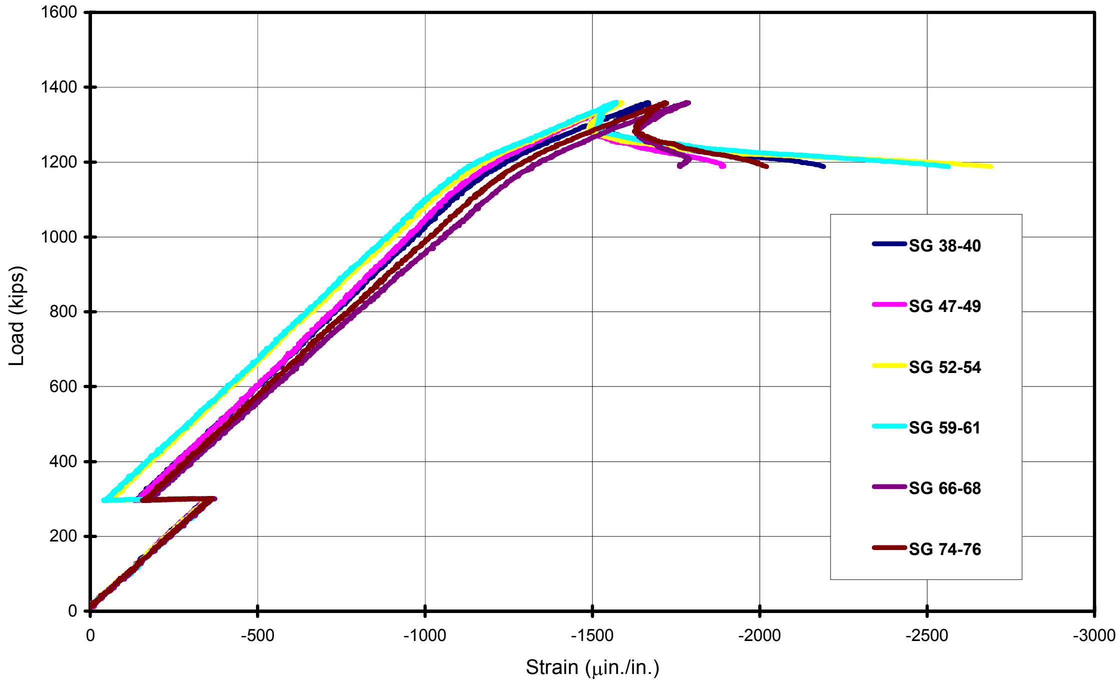

Figure 4-33 Strains on Rib Wall of Single-rib Beam-column, SBC1

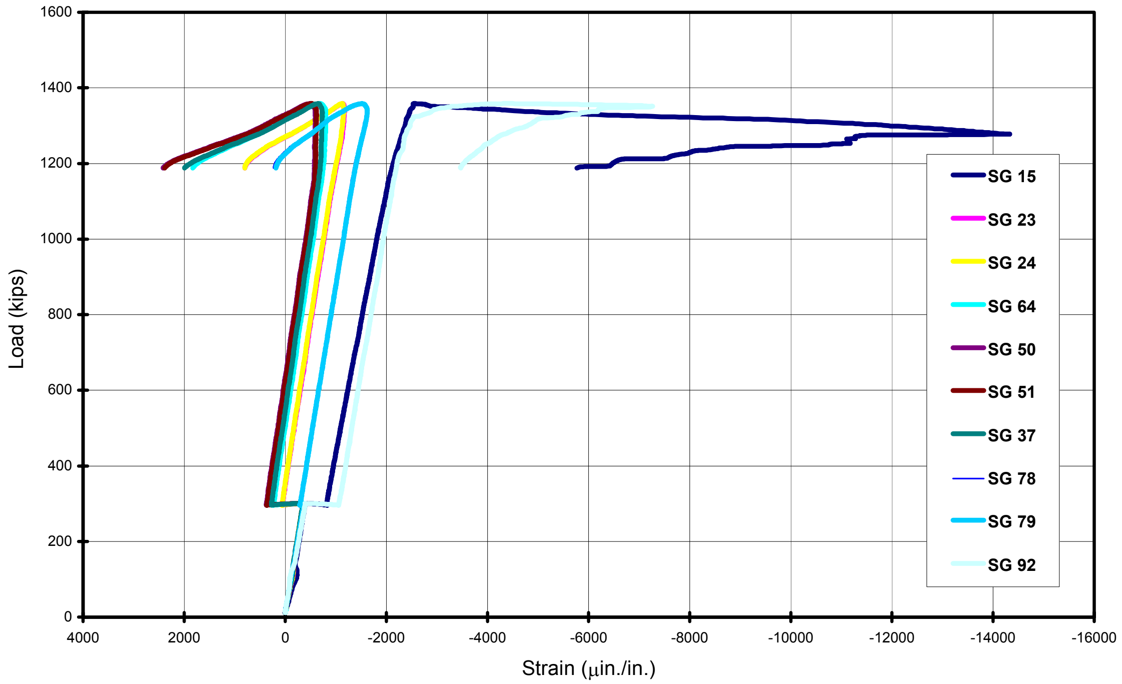

Figure 4-34 Strains on Bottom Flange of Rib, Single-rib Beam-column, SBC1

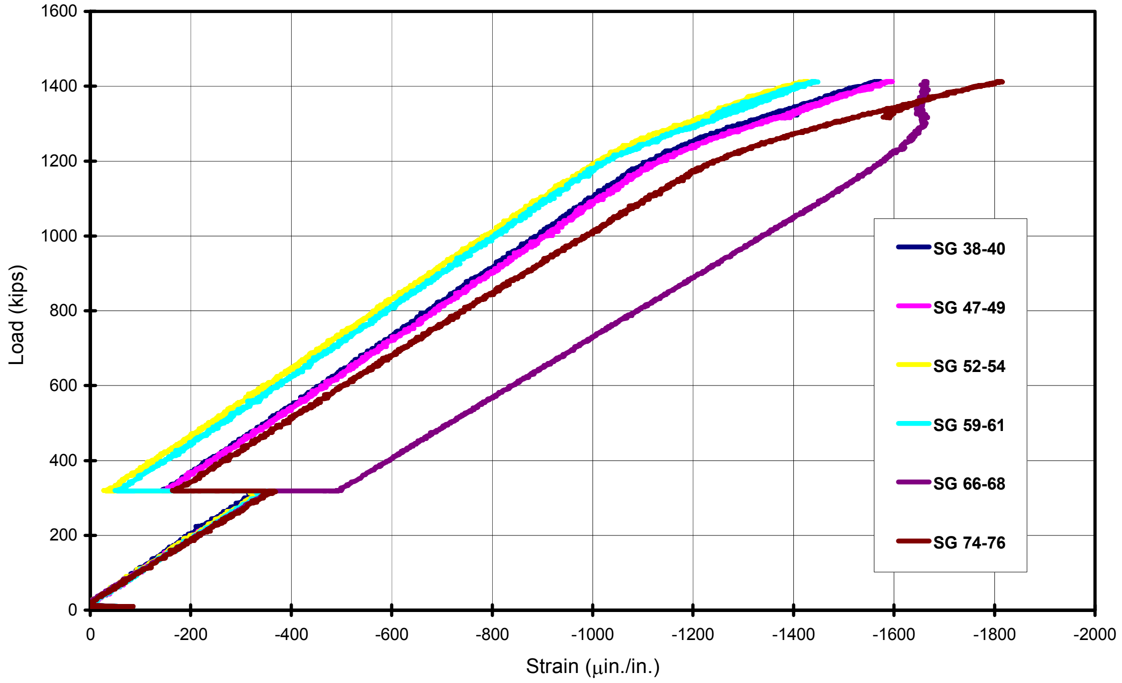

Figure 4-35 Strains on Rib Wall of Single-rib Beam-column, SBC2

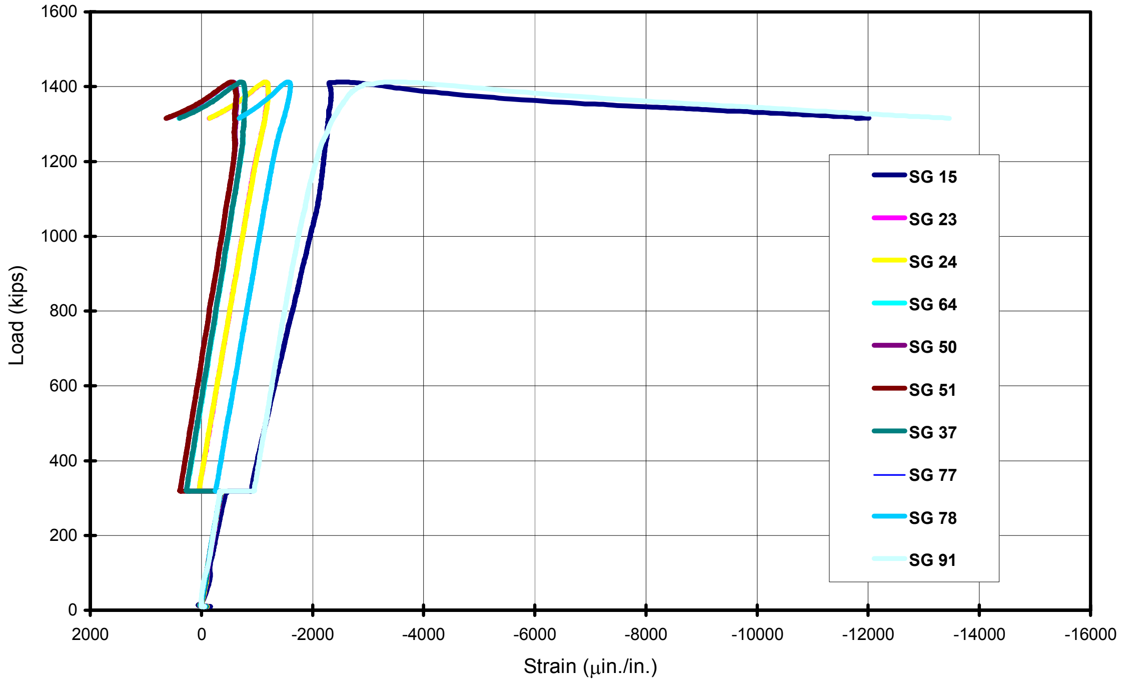

Figure 4-36 Strains on Bottom Flange of Rib, Single-rib Beam-column, SBC2

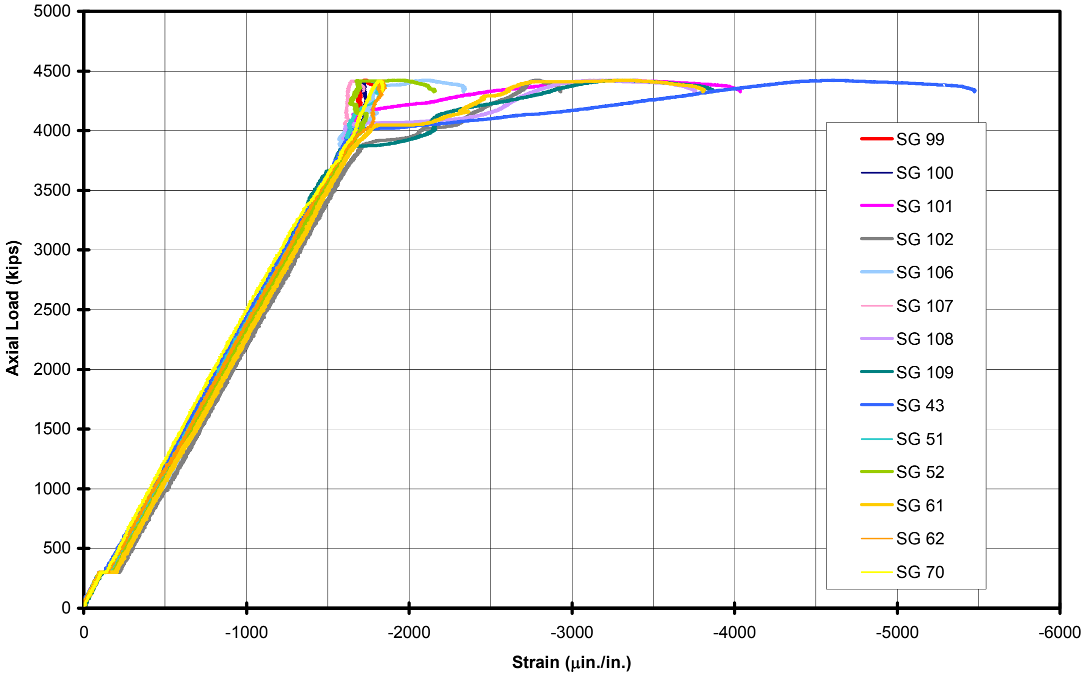

Figure 4-37 Load vs. strain on Deck Plate of Triple-rib Beam-column, TBC

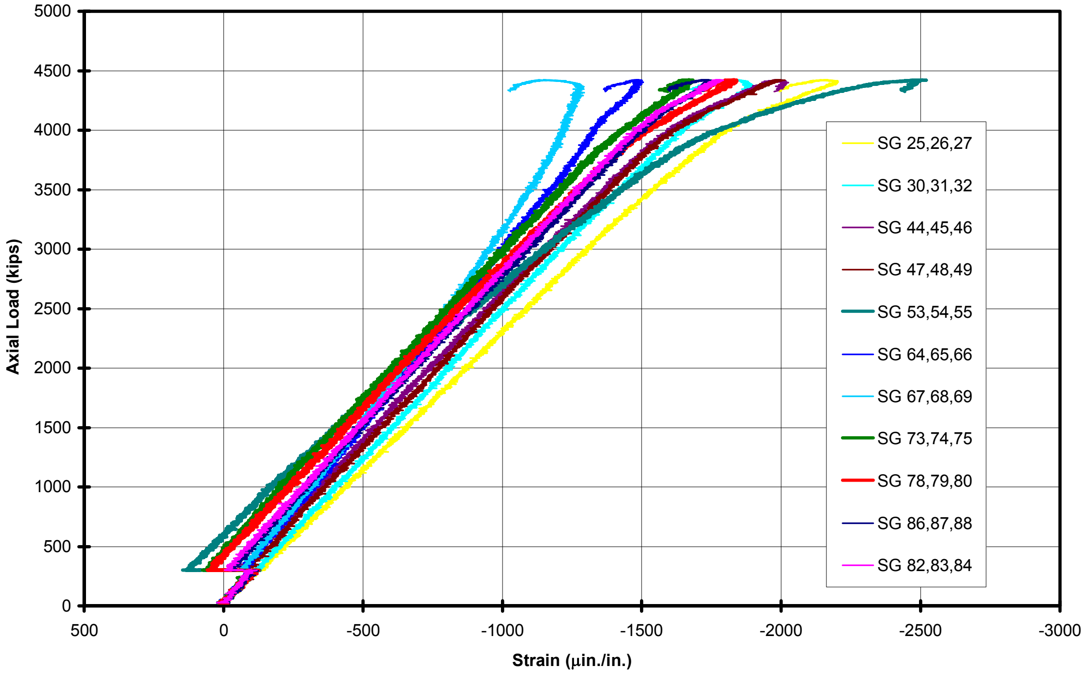

Figure 4-38 Strains on Rib Wall of Triple-rib Beam-column, TBC

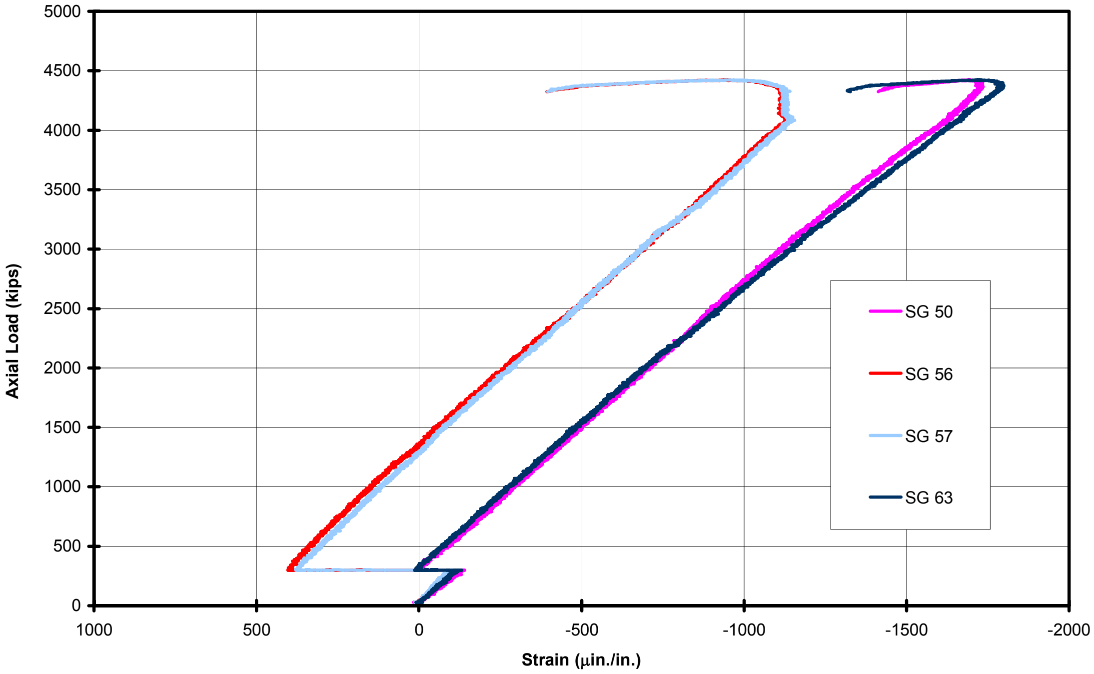

Figure 4-39 Strains on Bottom Flange of Rib, Triple-rib Beam-column, TBC

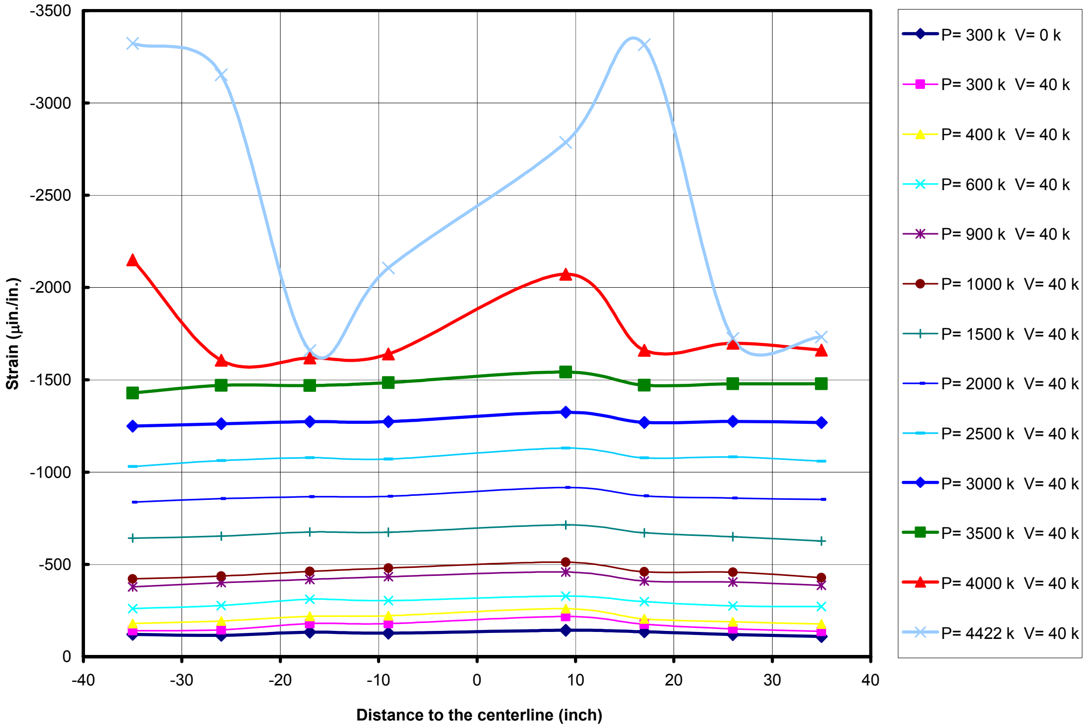

Figure 4-40 Strains Distribution on the Top of Deck Plate at Mid-height of Triple-rib Beam-column, TBC

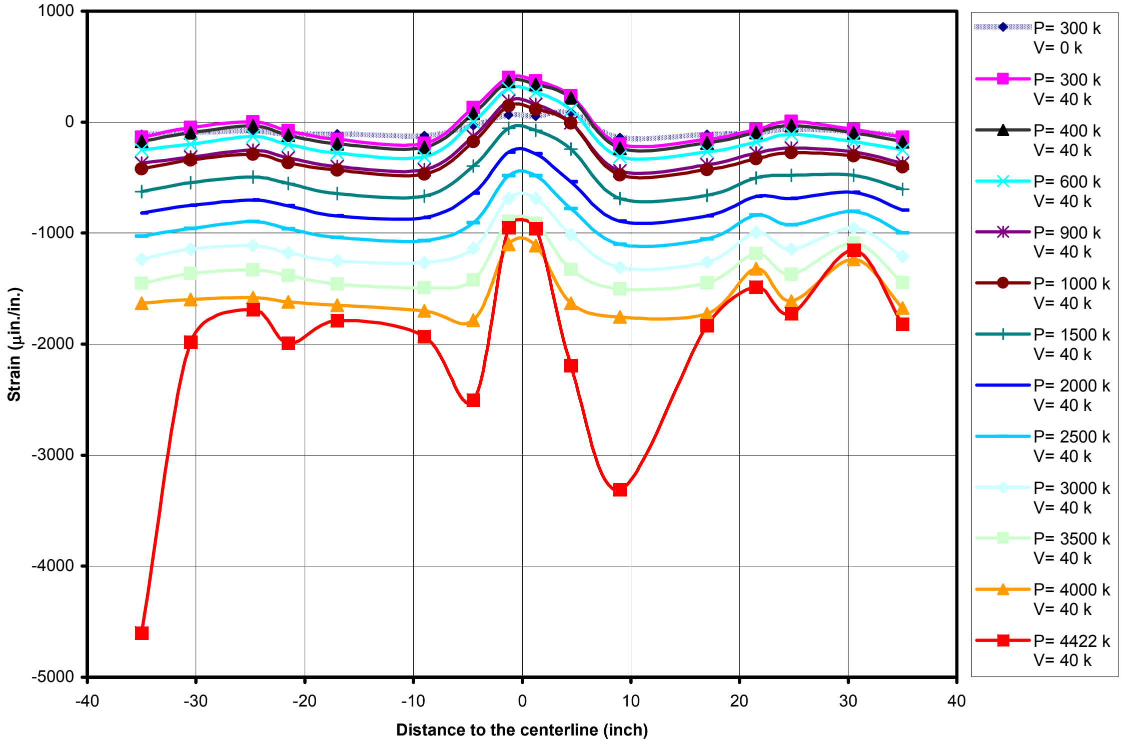

Figure 4-41 Strains Distribution on the Lower Surface of Deck Plate and on the Rib Wall at Mid-height of Triple-rib Beam-column, TBC

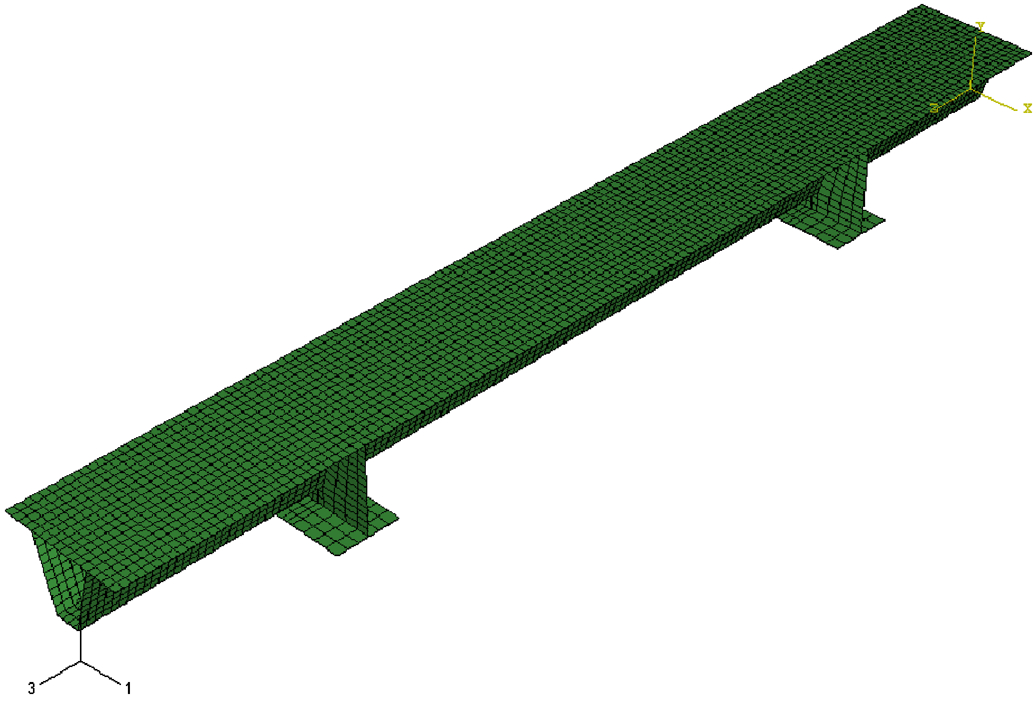

Figure 4-42 Finite Element Model of Single-rib Specimen

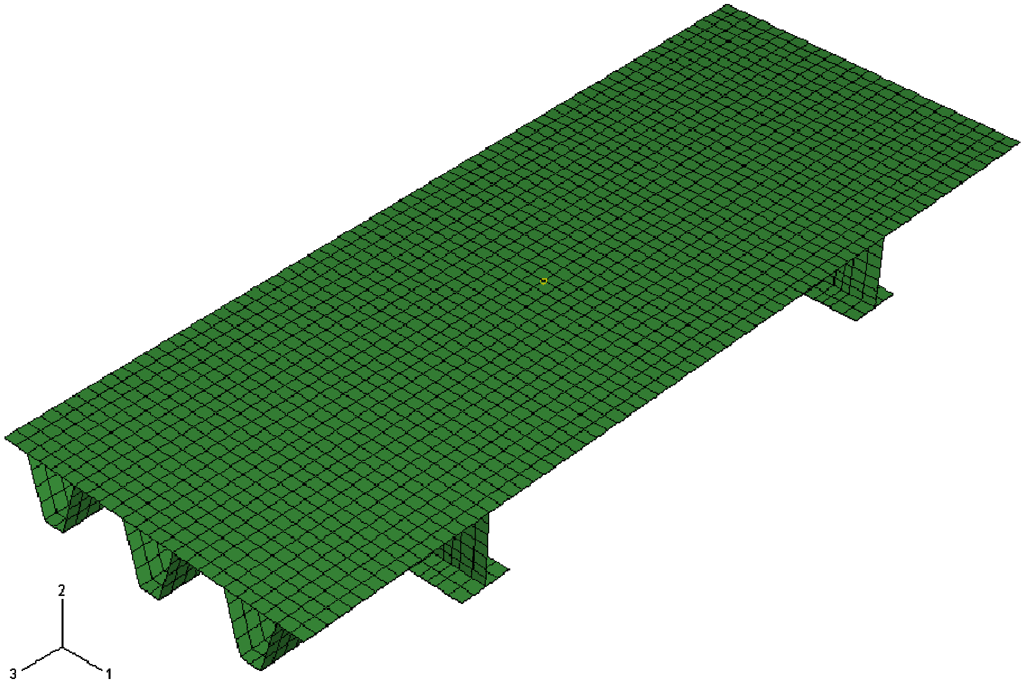

Figure 4-43 Finite Element Model of Triple-rib Specimen

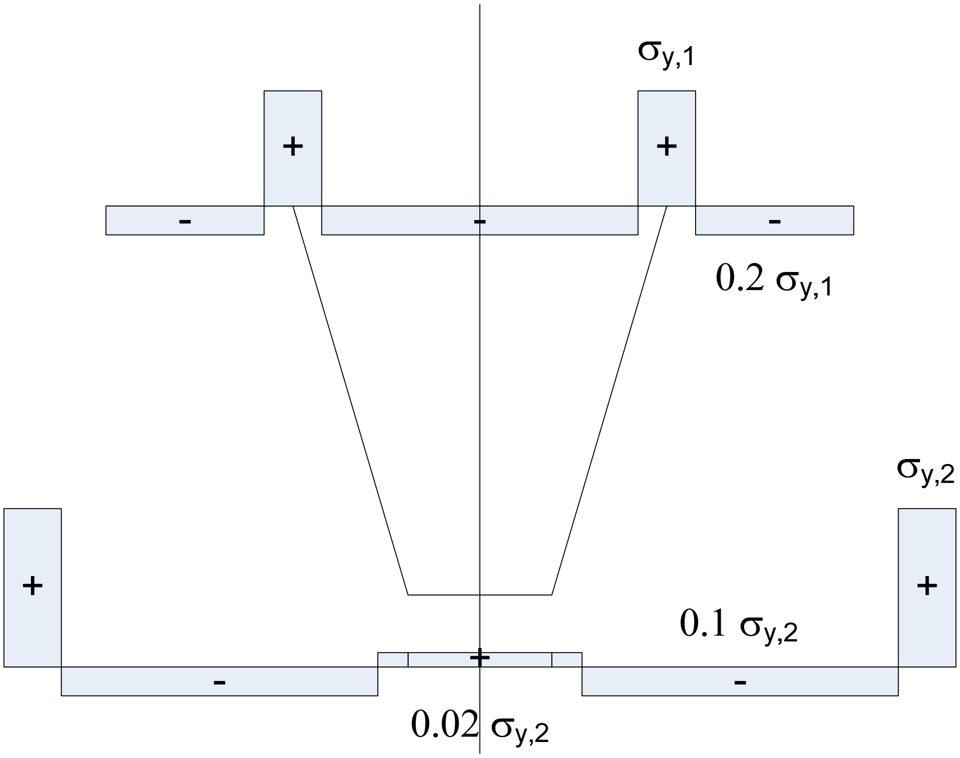

Figure 4-44 Magnitude and Distribution of Residual Stresses

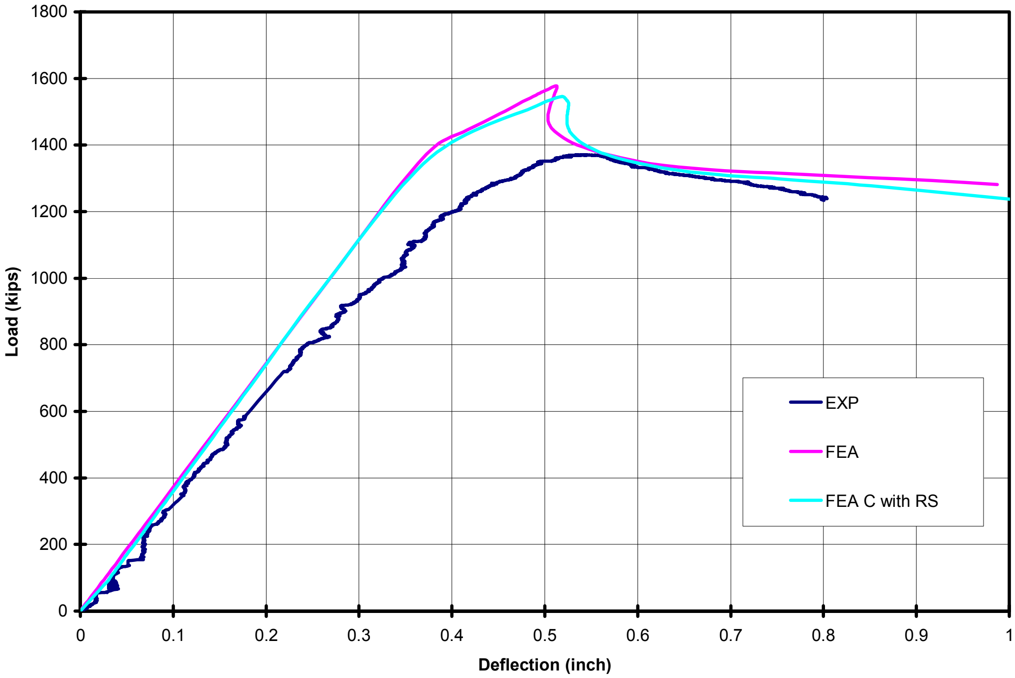

Figure 4-45 Load-Deflection Curves of Single-rib Column, SC

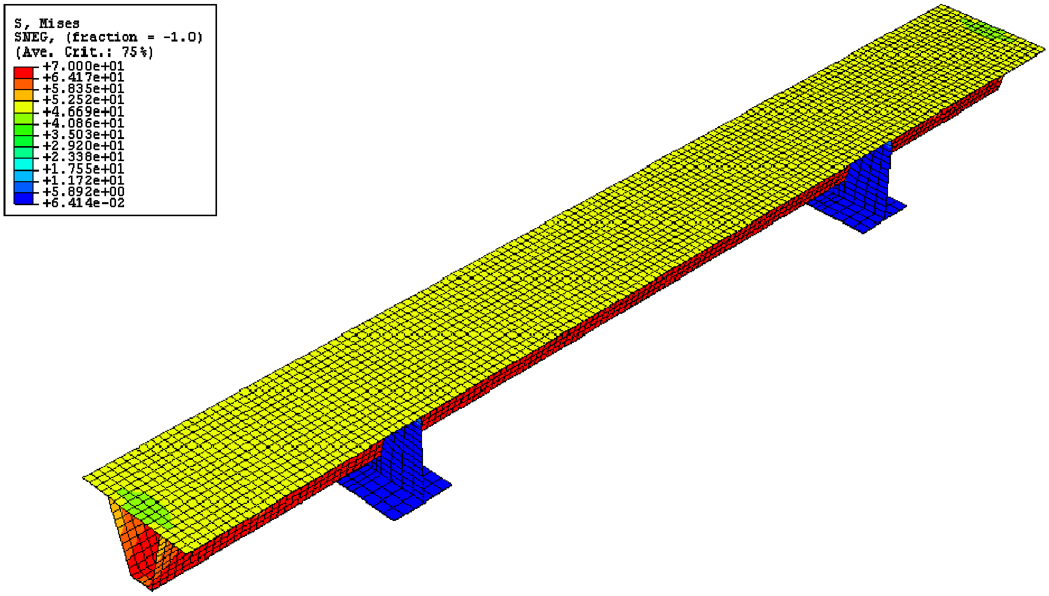

Figure 4-46 Appearance of Single-rib Column (SC) at Peak Load (1385 kips) by FEA

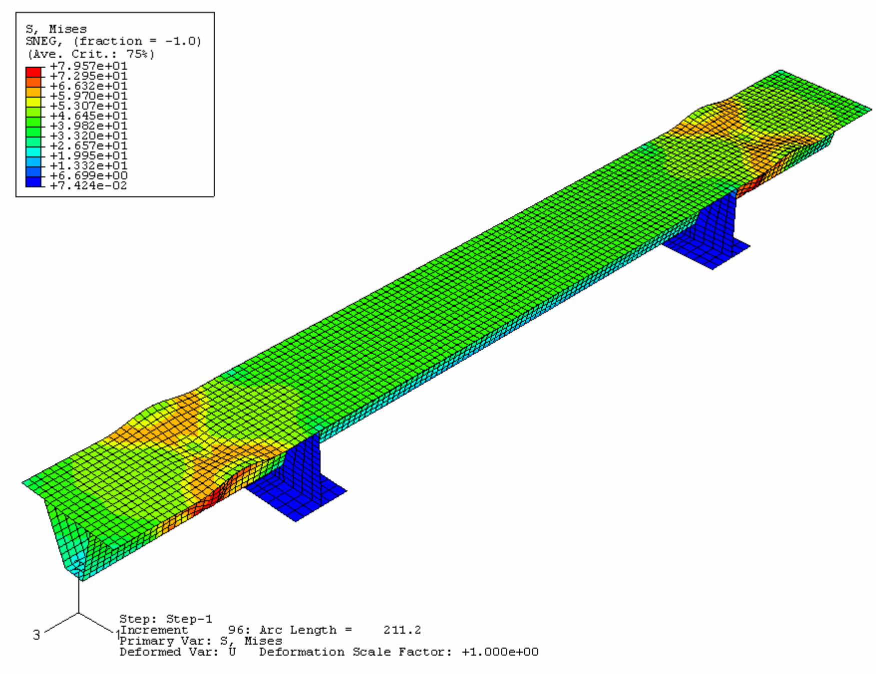

Figure 4-47 Final Appearance of Single-rib Column (SC) by FEA

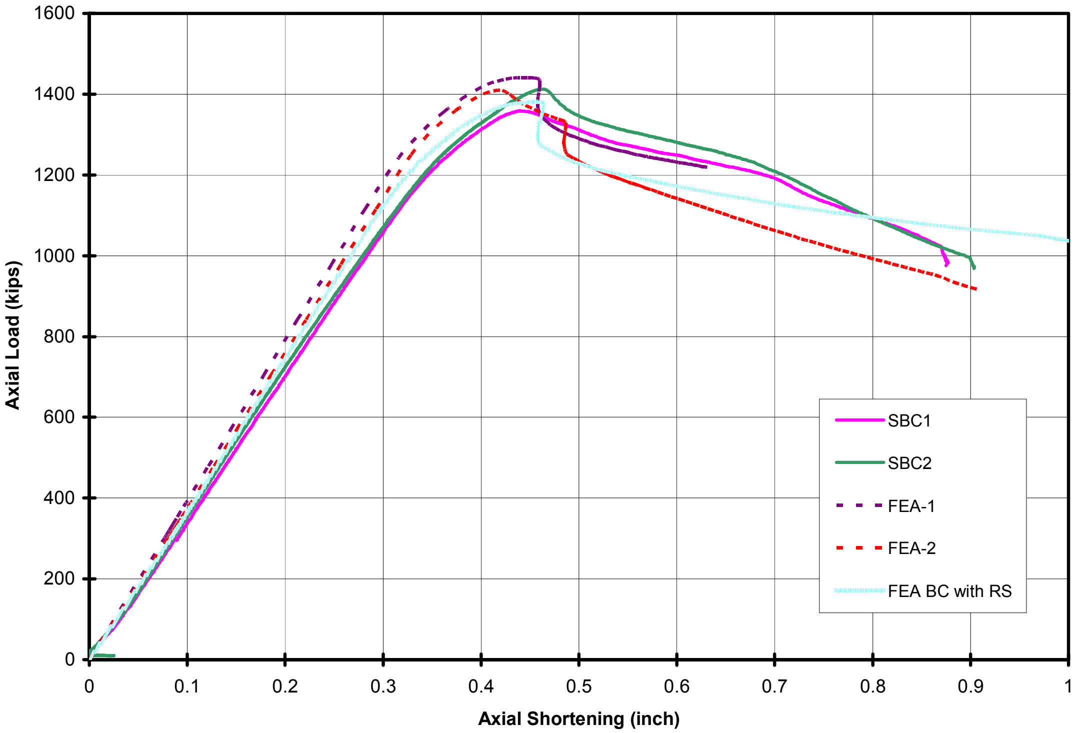

Figure 4-48 Load-Deflection Curves of Single-rib Beam-column, SBC

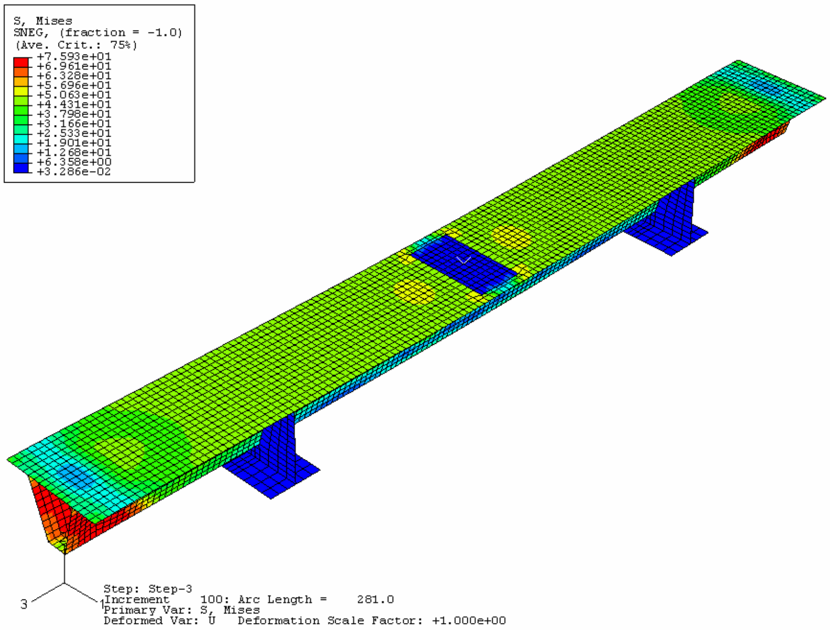

Figure 4-49 Appearance of Single-rib Beam-column with Rigid Loading Pad, by FEA

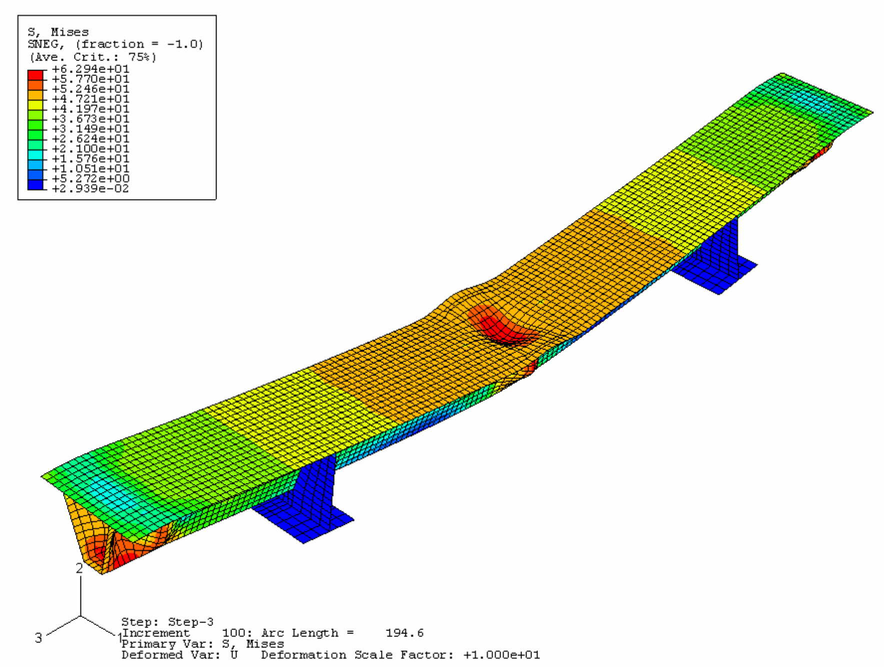

Figure 4-50 Final Appearance of Single-rib Beam-column (SBC) by FEA

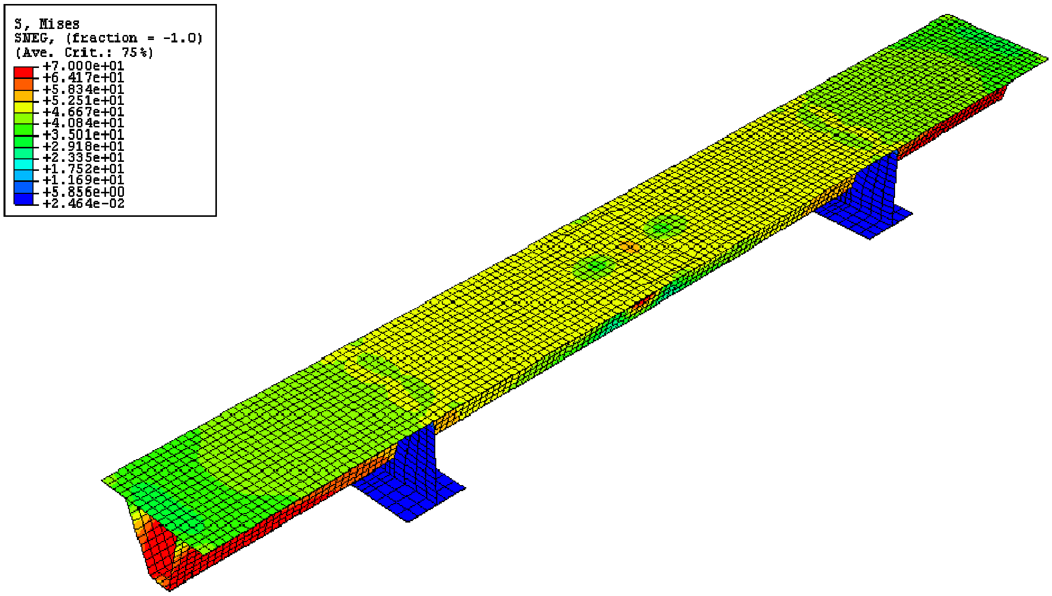

Figure 4-51 Final Appearance of Single-rib Beam-column (SBC) at peak load by FEA

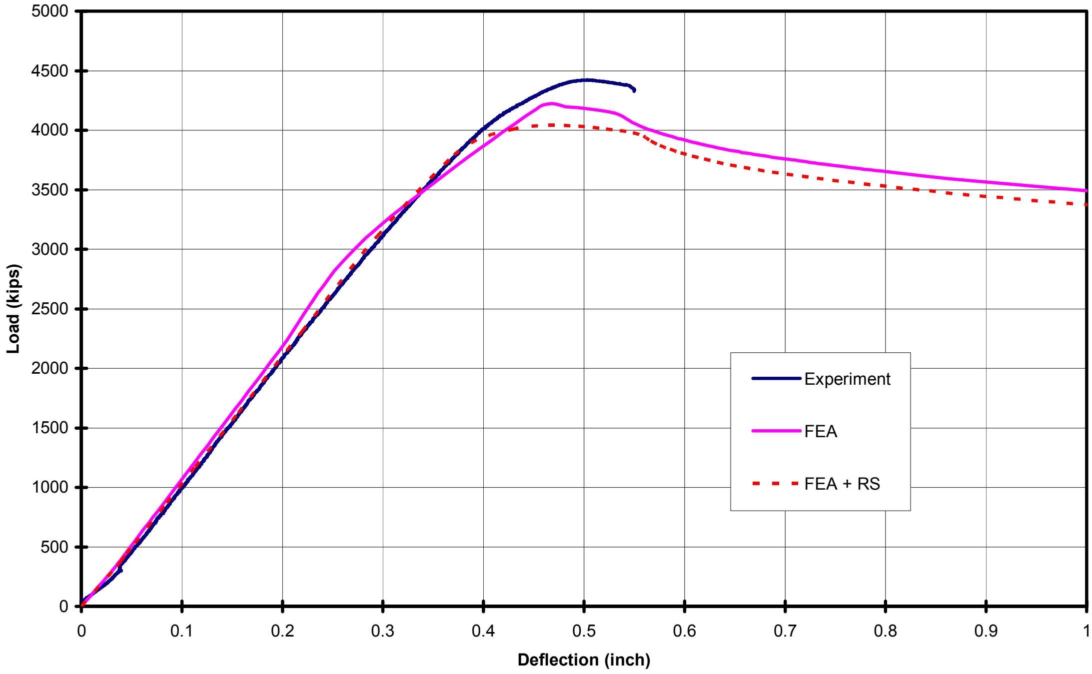

Figure 4-52 The triple beam-column FEA and experimental results

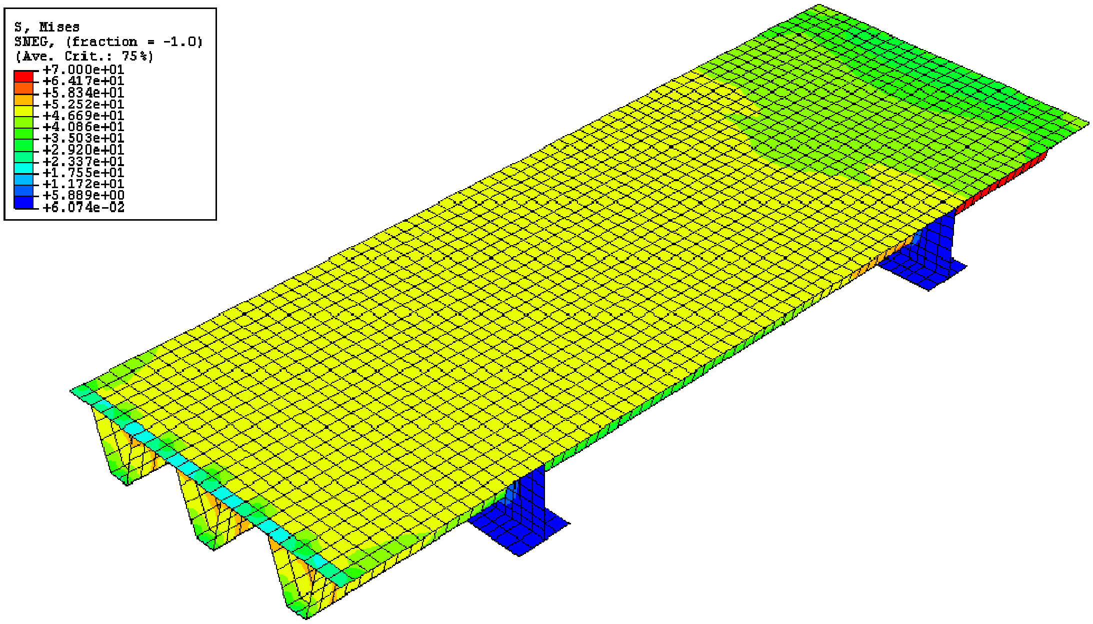

Figure 4-53 Appearance of Triple-rib Beam-column (TBC) at peak load by FEA

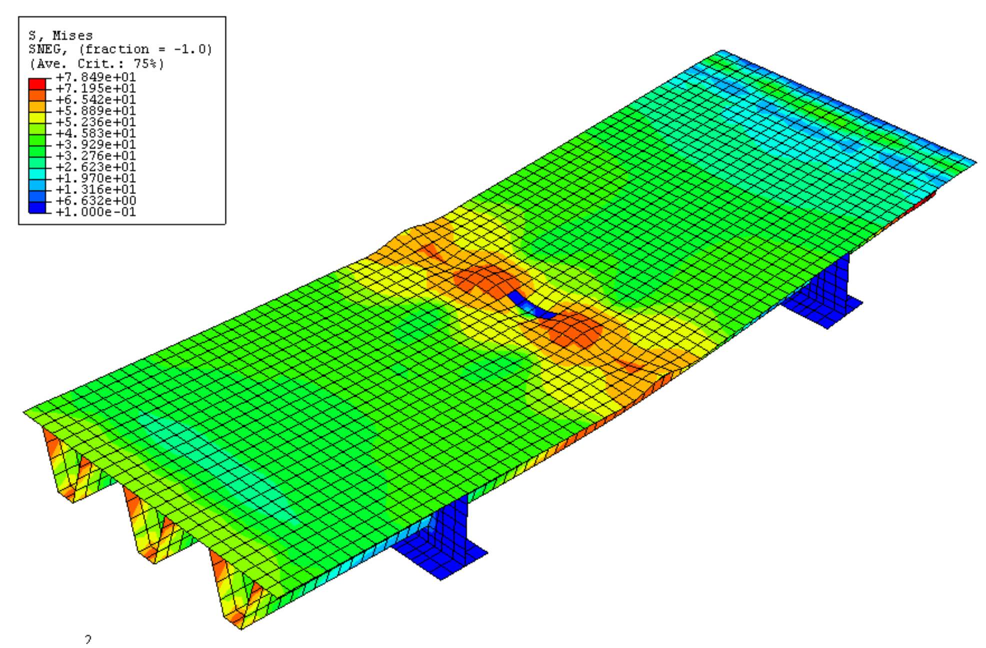

Figure 4-54 Final appearance of Triple-rib Beam-column (TBC) by FEA

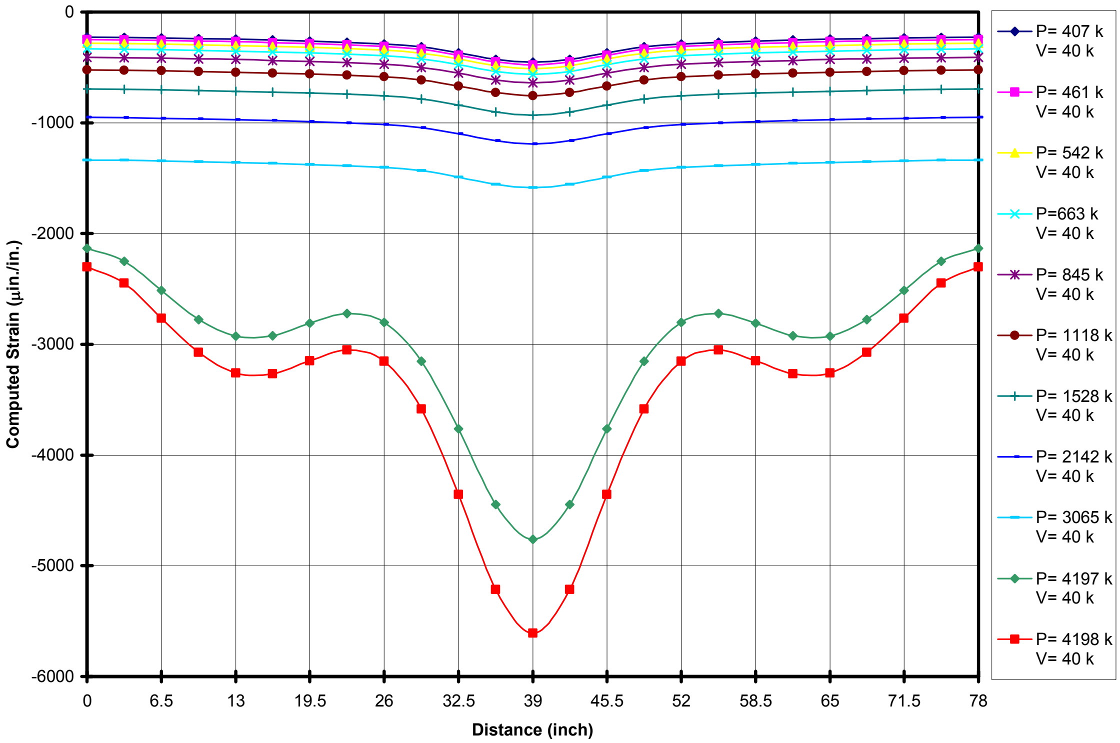

Figure 4-55 Strain Distribution on Surface of Deck at Mid-height of Triple-rib Beam-column (TBC) by FEA

Chapter 5 Estimation of Deck Panel Strength

5.1 Introduction – Method of Summation of Parts (SP)

The results of Chapter 4 on column and beam-column strength of trapezoidal shaped stiffening ribs of an orthotropic deck panel lead to the recommendation of the method of summation of parts (SP) for rib strength evaluation. The compression strength of an individual stiffening rib can be estimated by summing the strength of the component parts. The examination of extending the method of summation for estimating the compression strength of the entire deck panel was the goal of this part of study.

The procedure included computing the compression strength of a single rib as introduced earlier and the summing of individual rib strength as the estimate of the deck panel strength. Because the stiffening ribs were all identical, the strength of the deck panel was simply the multiple of the single rib strength.

The evaluation of this process was carried out using the finite element method. The prototype model deck of Bronx-Whitestone Bridge (BWB) was again used for analysis.

5.2 Finite Element Model for Single Rib

For the reason that deck panels usually contain a fairly large number of identical stiffening ribs, a new finite element model with a coarser mesh then that for the models of Chapter 4 was developed. The single-rib was 10 ft. (3 m) long, the length between diaphragms. The model is shown in Figure 5-1. The ends were assumed being flat. The lower end was fixed and the upper loading end was allowed to deflect along the rib. The longitudinal edges were free from constraint.

The computed relationship between the component forces and the axial deflection of the rib are shown in Figure 5-2. The rib walls failed at an axial shortening of about 0.5 in. (13 mm) while carrying a higher force than did the bottom of the rib, because of the difference in area of these components. The summation of the component forces at an axial deflection provided the force or load on the rib at that deflection. The resulting load-deflection relationship is shown in Figure 5-3, which is the superposition of the lines in Figure 5-2. The strength from the summation of parts (SP) is slightly higher than those from the finite element model in Chapter 4. This is partly due to the condition that no initial imperfection was incorporated in the present model.

Table 5-1 summarized the results of strength estimate. There are differences on the computed values. Discussions will be made later in the chapter.

5.3 Finite Element Model for Multiple Ribs

The models were developed and analyzed using the software ABAQUS (2005) on BWB ribs. Models of single, triple, five, seven and sixteen ribs were studies. The results of stress distribution are shown in Figure 5-1, 5-4, 5-5, 5-6 and 5-7, respectively, at an axial deflection of about 1 in. (25 mm). From the 16-rib model it is seen that there were slight variation of stresses among the ribs although the model was loaded uniformly at one end.

Table 5-2 summarized the computed strength of the models. As the number of ribs increase, the computed strength per rib increase slightly as the effect of free edges diminishes. The comparison of load deflection behavior is presented in Figure 5-8. With the increase of number of ribs, besides the slight increase of ultimate strength, the ductility increases tremendously. Figure 5-9 compares some of the finite element results with the experimental results from specimens SBC1and SBC2. The 16-rib model having a higher strength is again shown. The elastic buckling strength of the 16-rib deck is very high, beyond the range of the plot.

For further examination of the method of summation of parts, another Bridge, RN, was analyzed. The geometry of the trapezoidal shaped stiffening rib is shown in Figure 5-10. The thickness of the deck plate is 0.4 in. (10 mm), the rib plate is 0.24 in. (6 mm) thick. The ribs are spaced uniformly at 12 in. (30 mm). The depth of the rib is 11 in. (27.5 cm). Models of one, three, five, seven and sixteen ribs were analyzed, and the results of stress distribution and deflection are shown in Figures 5-11 to 5-15. The axial deflection of the single-rib in Figure 5-11 is 0.8 in. (20 mm), those in Figures 5-12 to 5-15 are 1 in. (25 mm). The computed ultimate strength values are listed in Table 5-3. The load deflection characteristics are shown in Figure 5-16. For this bridge with rib component plates more slender than those of BWB, the average ultimate strength per rib remains about the same for the models of different number of ribs.

These two bridge models demonstrated the adequacy of the method of summation.

5.4 Discussion and Conclusion

From the finite element analysis of two bridge deck panels, it is conclude that the method of summation of parts can be employed for strength estimate of orthotropic deck panels with trapezoidal shaped stiffening ribs.

The procedure of summation of parts can be applied two ways. The first is through the component parts for individual ribs and then the summation of ribs for the deck panel. The second is by finite element analysis of an individual rib to estimate the strength of the rib and then summation for the strength of the deck.

For BWB Bridge, the first procedure provided a rib strength of 1602 kips (Table 5-1) in comparison to the average of 1603 kips by finite element analysis of the 16-rib deck (Table 5-2). The second procedure provided a single-rib strength of 1357 kips (Table 5-2), which is an underestimate on the safe side.

Considering that deck panels are not subjected to uniform end forces, rather there are the effects of shear lag, of variations of boundary conditions, and of initial imperfection of plate components and rib stiffeners, it is difficult to assess the conservativeness of the two approaches of the procedure. It is, however, definite that the procedure of summation of parts can be applied for estimating the strength of deck panels.

Table 5-1 Comparison of Strength, Single Rib

Procedure	Maximum Axial Load (kips)	Axial Deflection at Max. Load (inch)
Experiment	1385	0.542
FEA (Ch.4)	1569	0.513
FEA + RS* (Ch.4)	1546	0.519
SP Method	1602	0.550

* RS: Residual Stresses

Table 5-2 Summary of Rib Strength, BWB

Number of Ribs N	P_u / N (kips)	$(P_u / N) / P_{u1}$ %	Axial Deflection at P_u (inch)	Aspect ratio
1	1357	100.00	0.338	0.217
3	1357	100.00	0.338	0.650
5	1545	113.90	0.397	1.083
7	1564	115.31	0.394	1.517
16	1603	118.18	0.274	3.467
	1627	119.82	1.317	3.467

(P_u for single rib by SP Method = 1602 kips)

Table 5-3 Summary of Rib Strength, RN

Number of Ribs N	P_u / N (kips)	$P_{u1} / (P_u / N)$ %	Axial Deflection at P_u (inch)	Aspect ratio
1	843.89	100.00	0.24	0.2
3	838.95	99.41	0.23	0.6
5	837.88	99.29	0.25	1.0
7	838.57	99.37	0.25	1.4
16	849.98	100.72	0.20	3.2

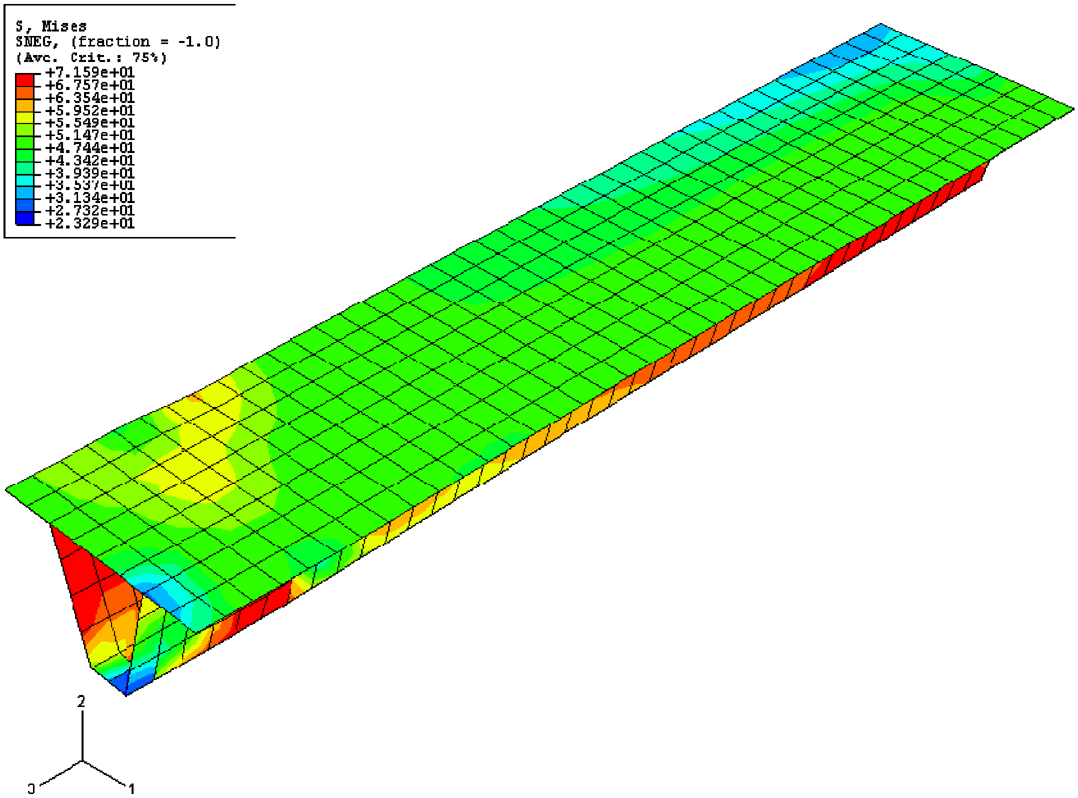

Figure 5-1 Finite Element Model Single Rib

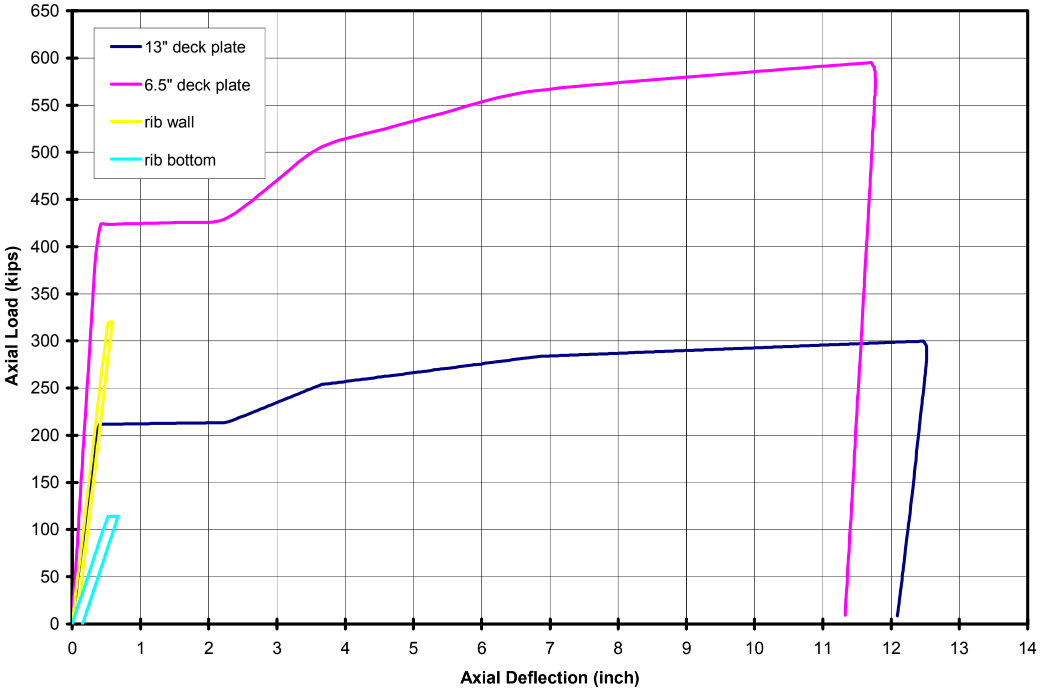

Figure 5-2 Component Strength, BWB

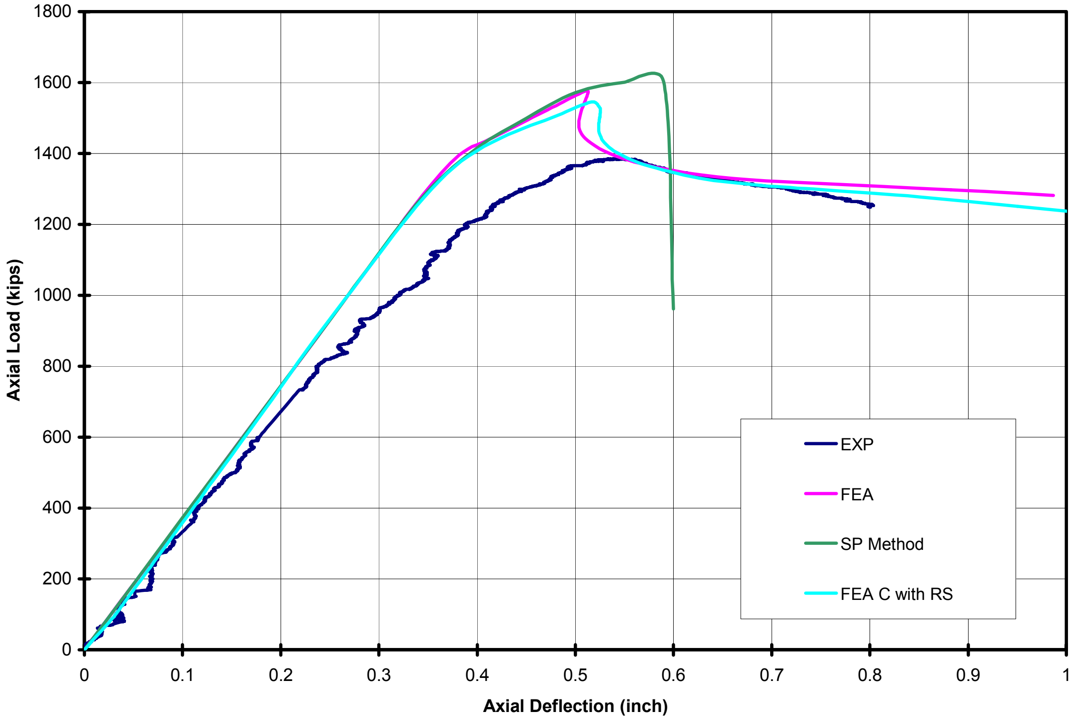

Figure 5-3 Strength of Single Rib

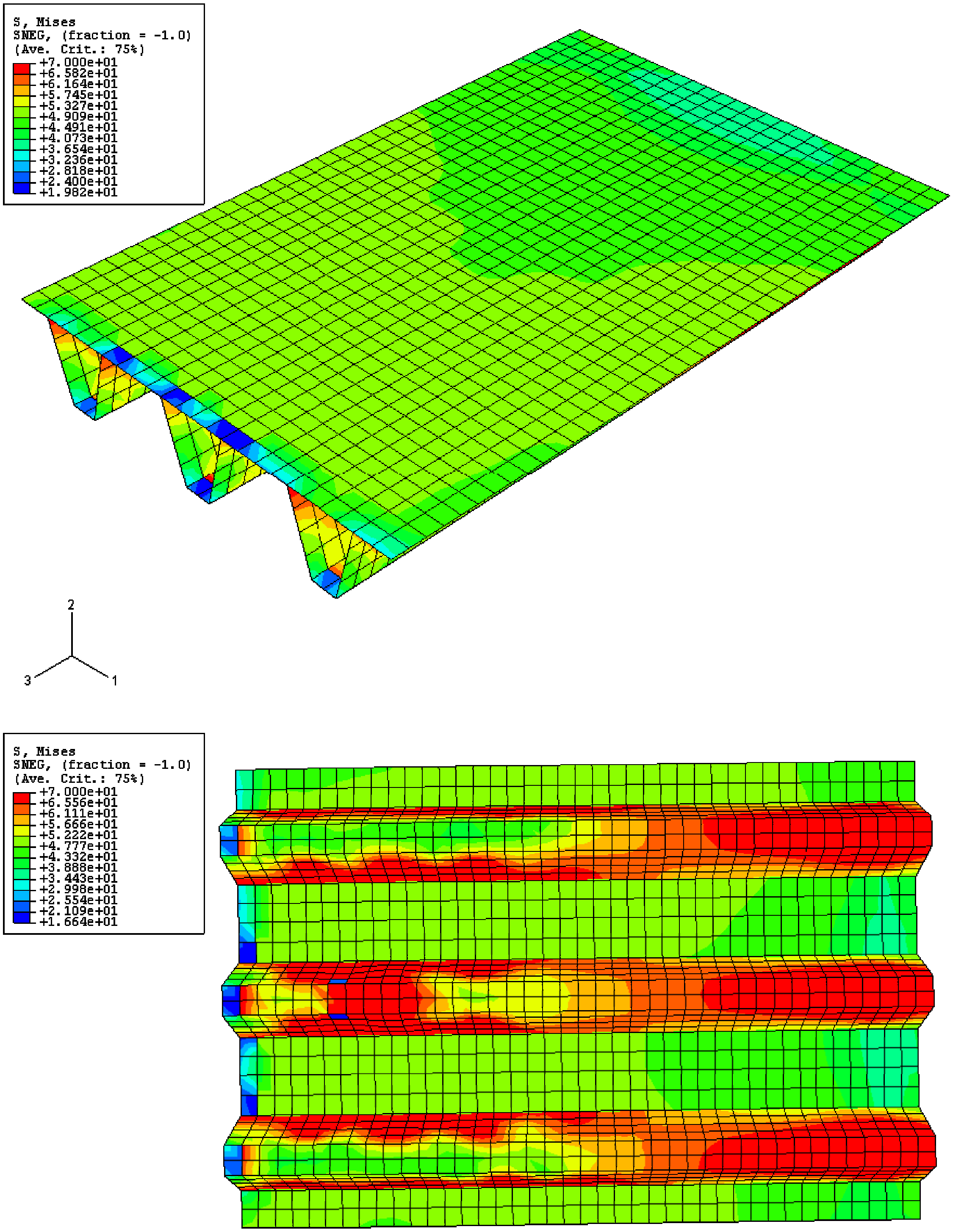

Figure 5-4 Triple Rib Model

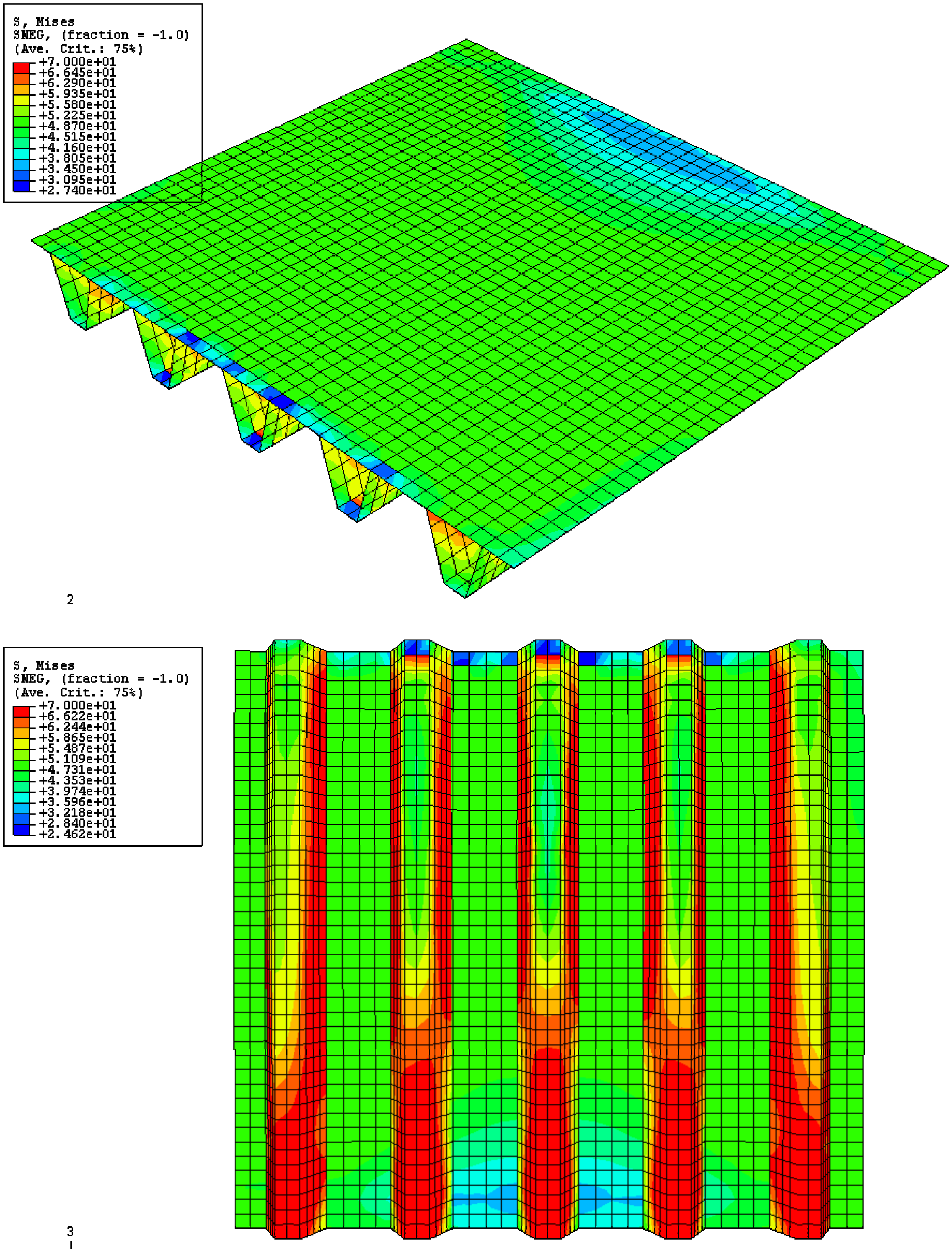

Figure 5-5 Five Rib Model

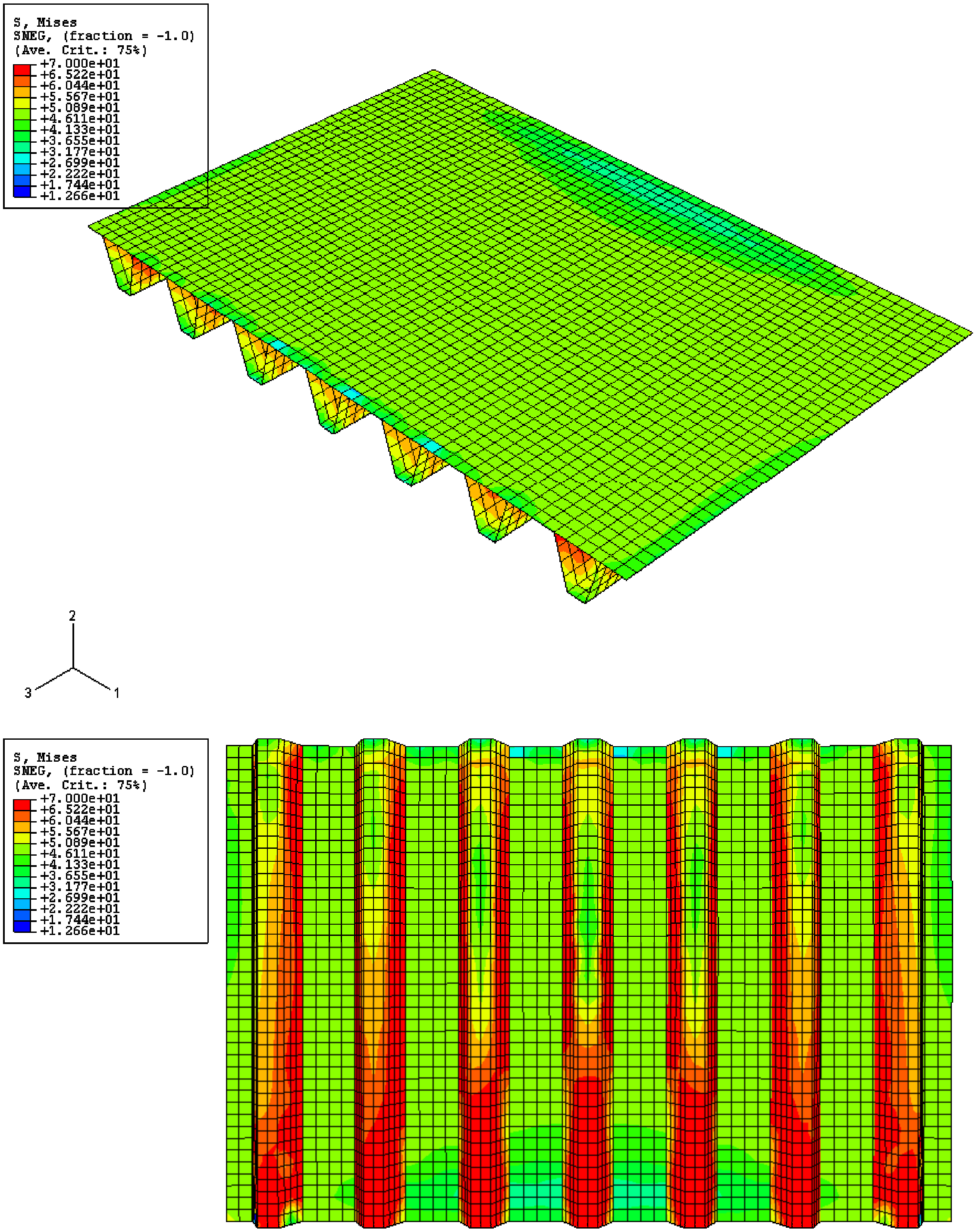

Figure 5-6 Seven Rib Model

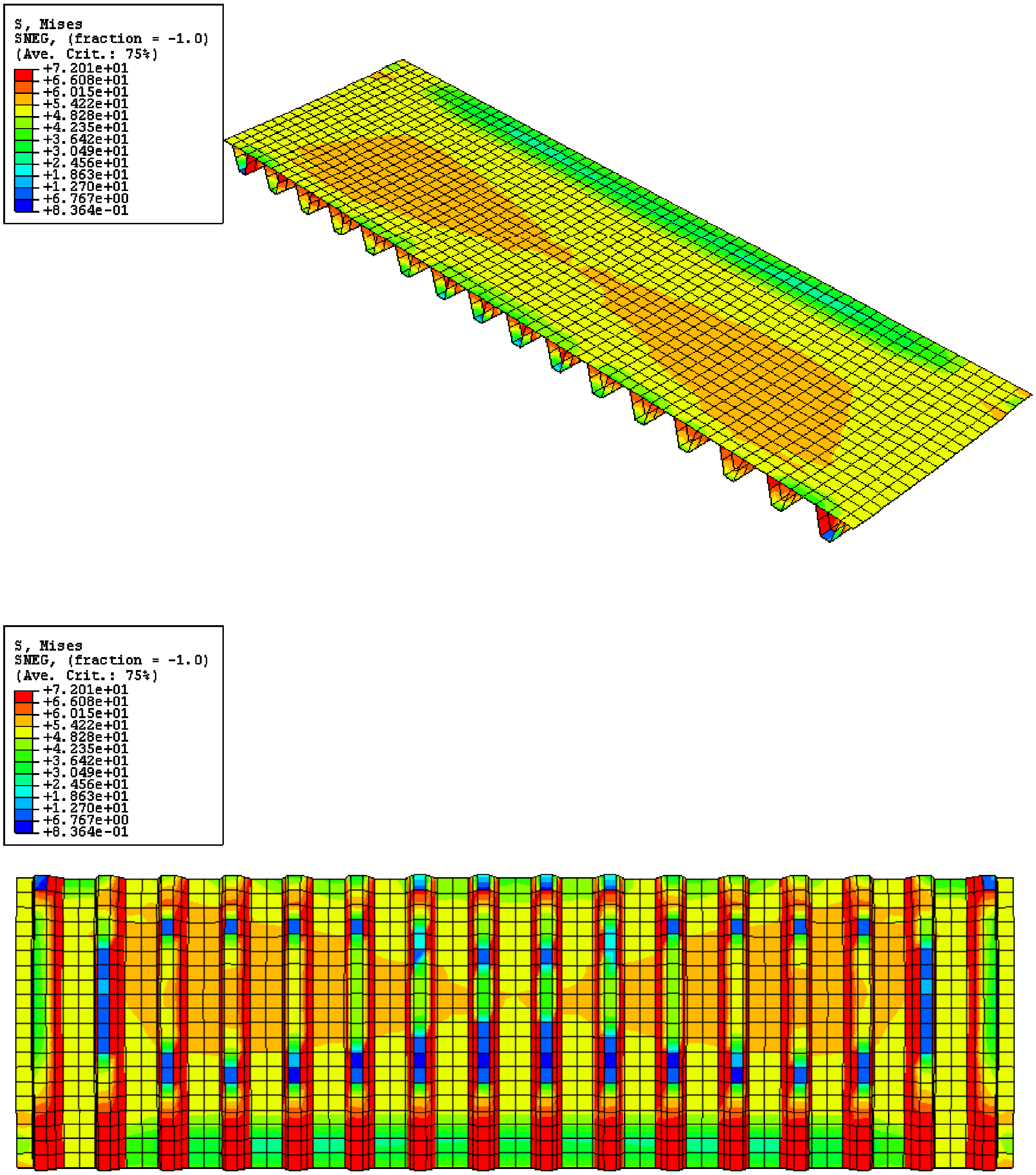

Figure 5-7 Sixteen-Rib Model

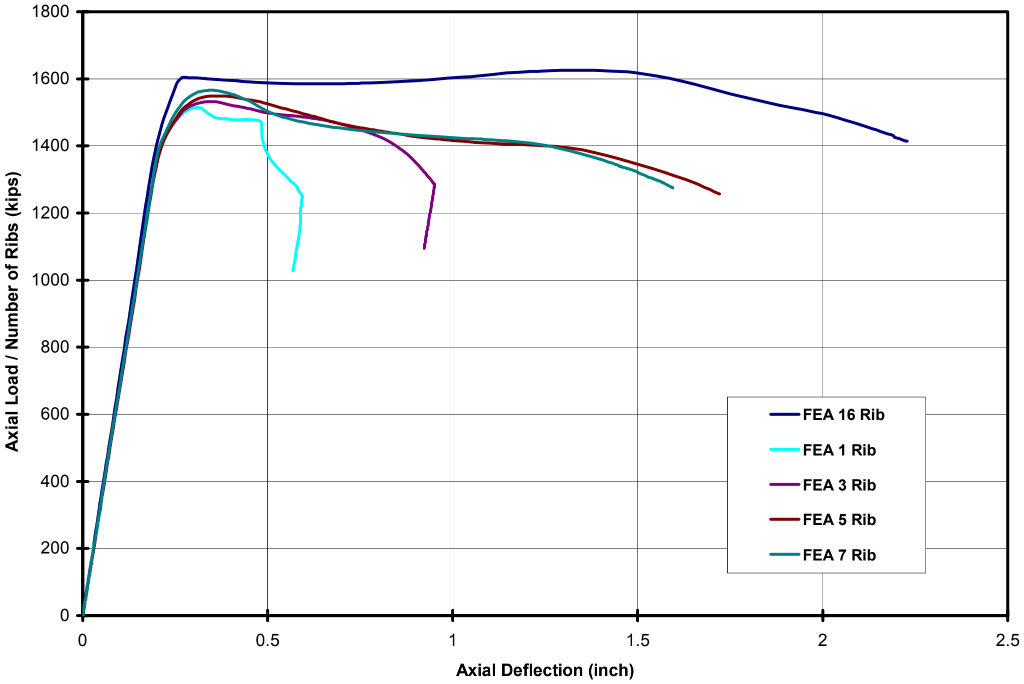

Figure 5-8 Comparison of Different Number of Ribs, BWB

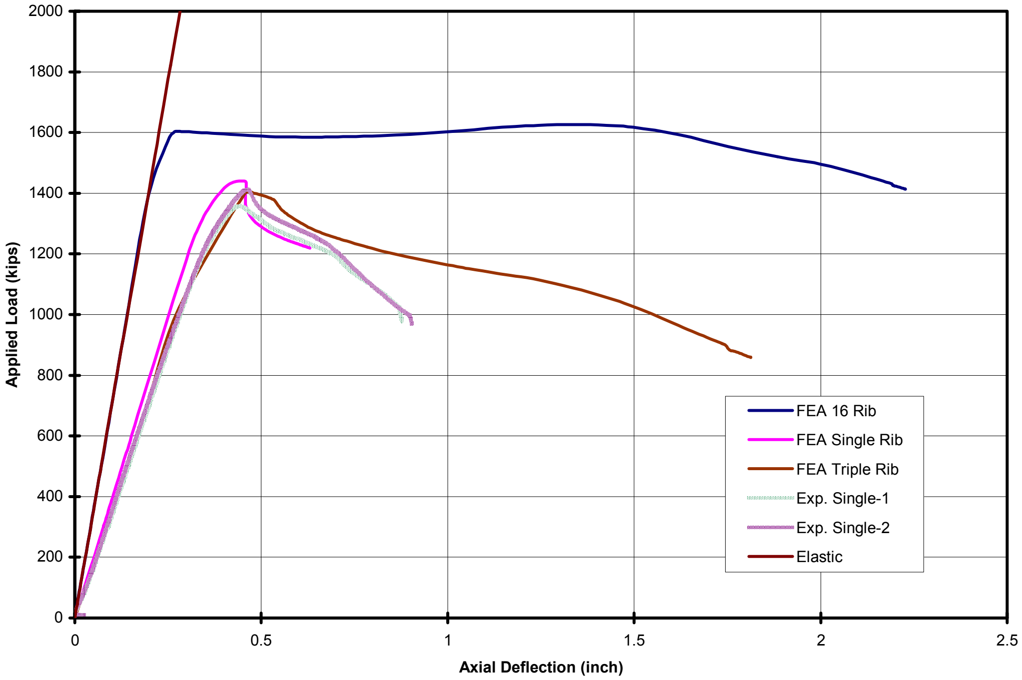

Figure 5-9 Comparison of Experimental and Finite Element Results

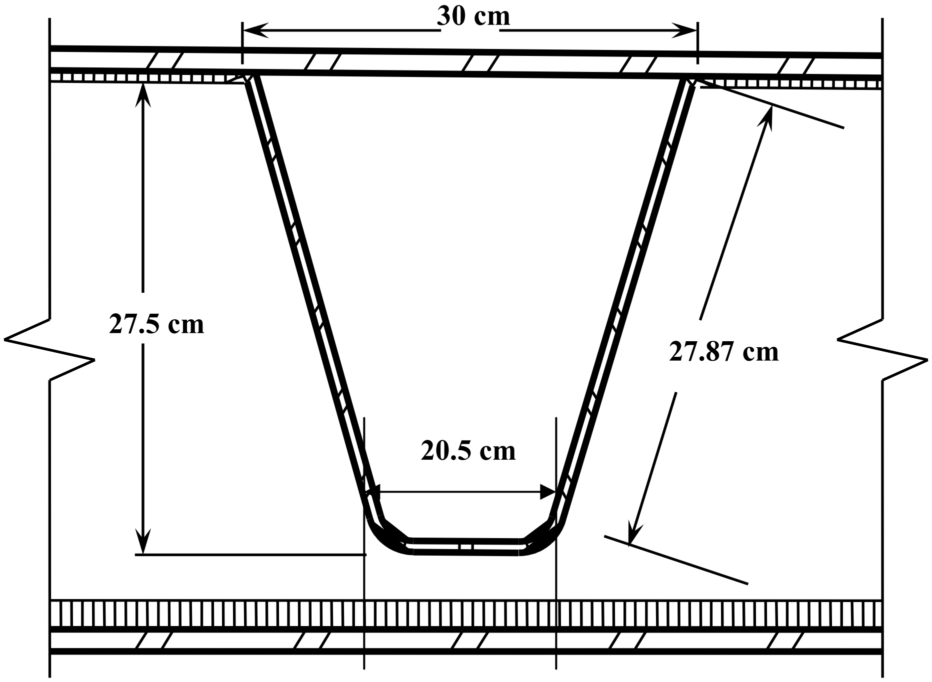

Figure 5-10 Stiffening Rib of Bridge RN

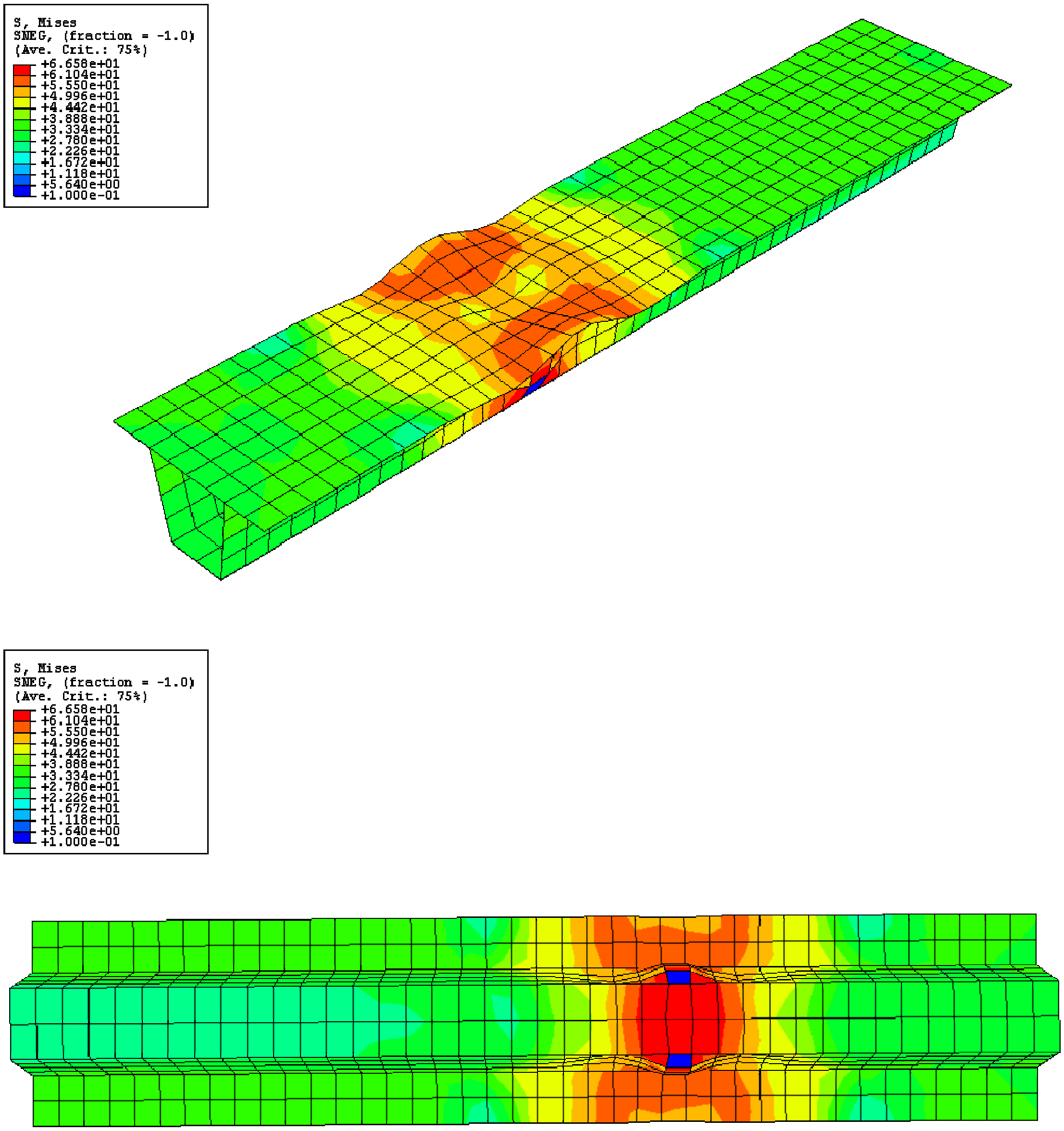

Figure 5-11 Single Rib Model, RN

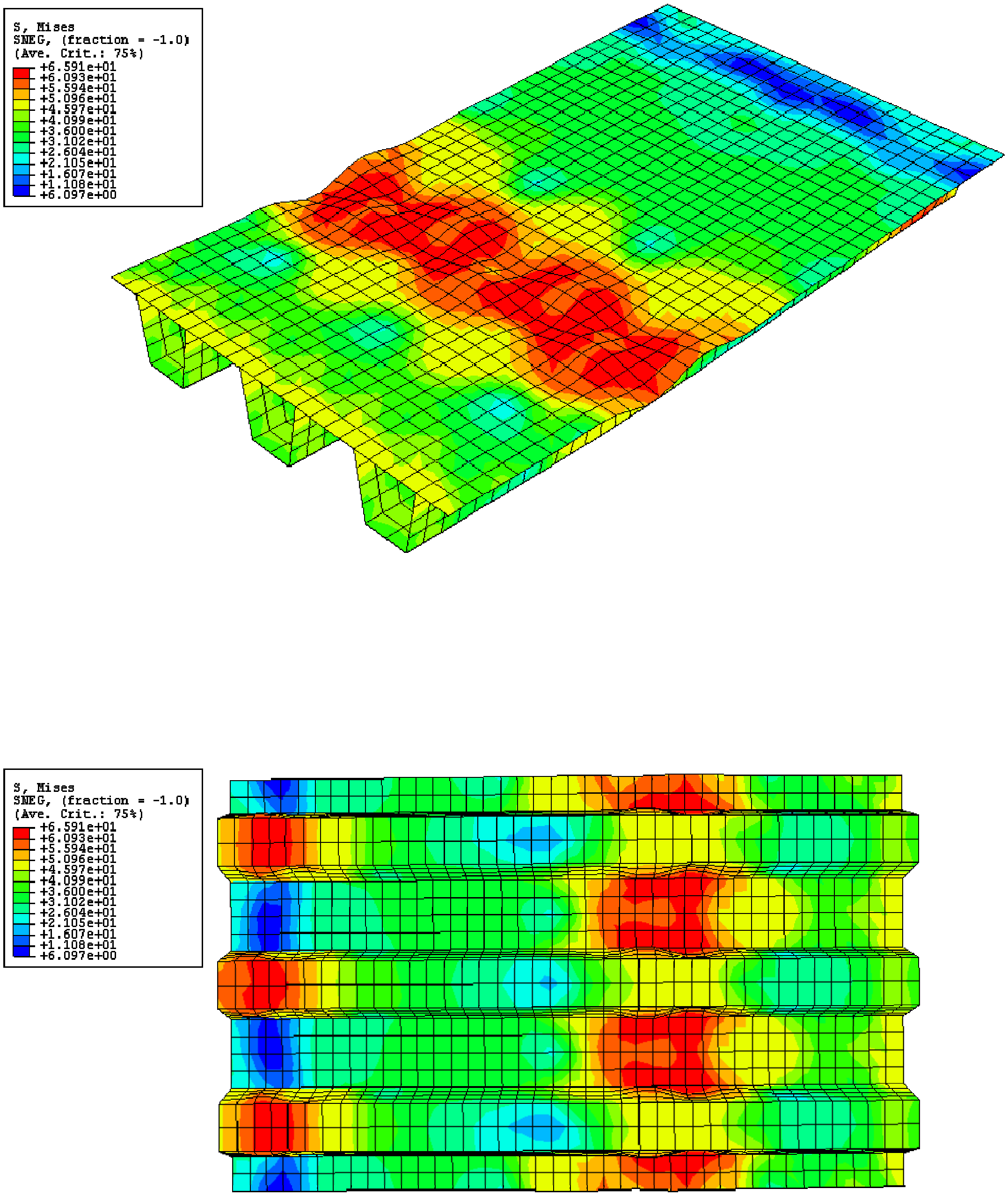

Figure 5-12 Triple Rib Model, RN

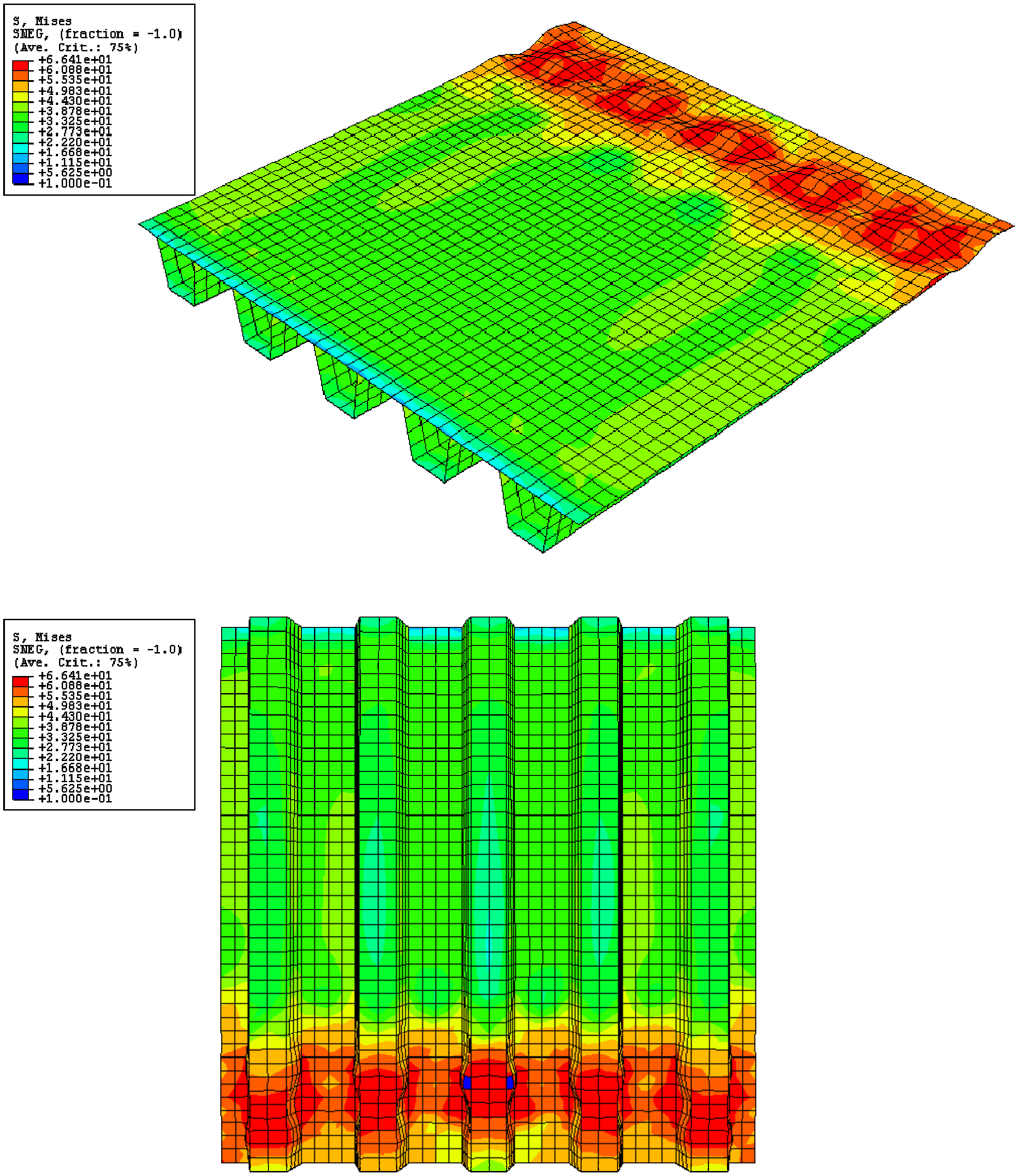

Figure 5-13 Five-Rib Model, RN

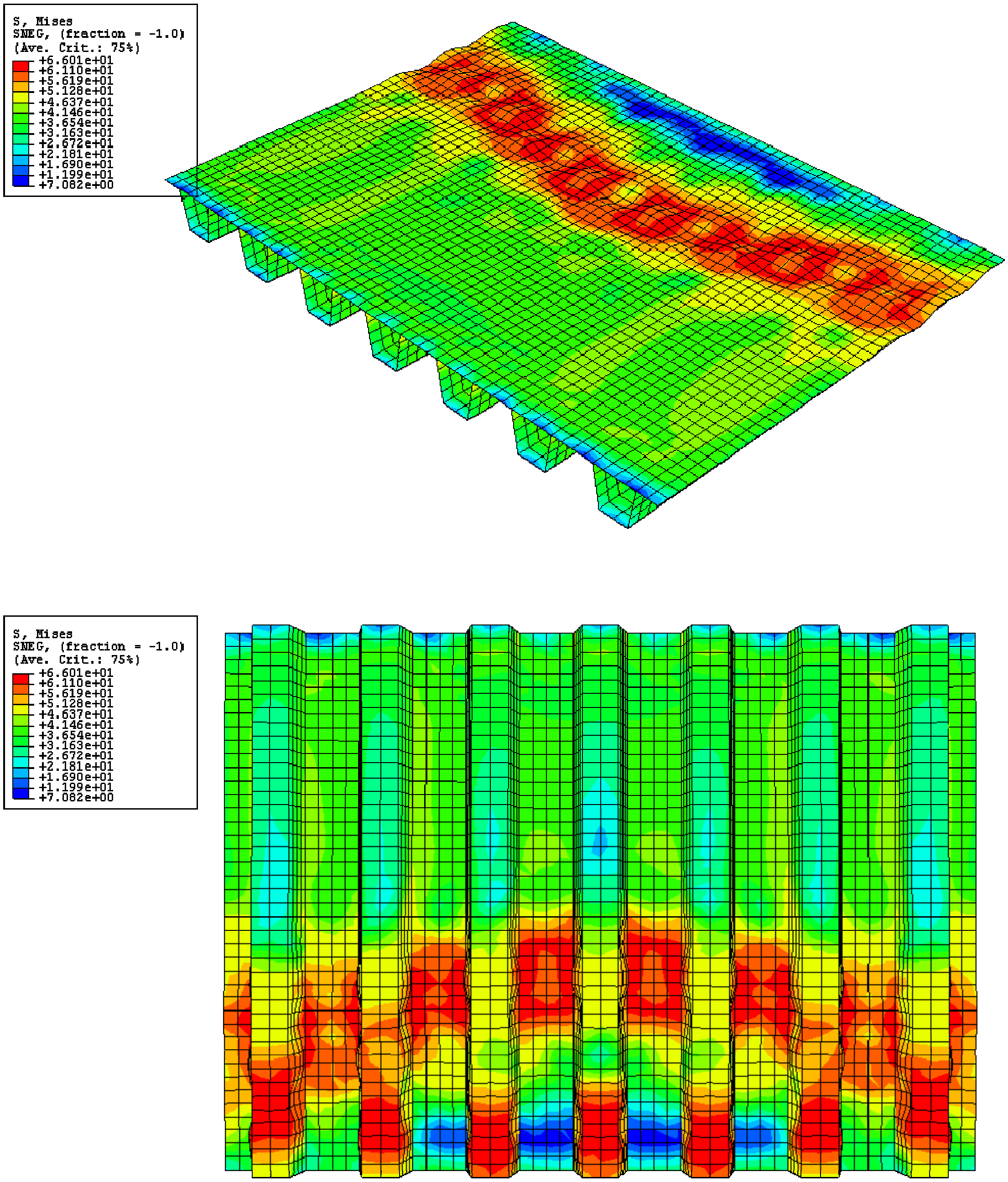

Figure 5-14 Seven-Rib Model, RN

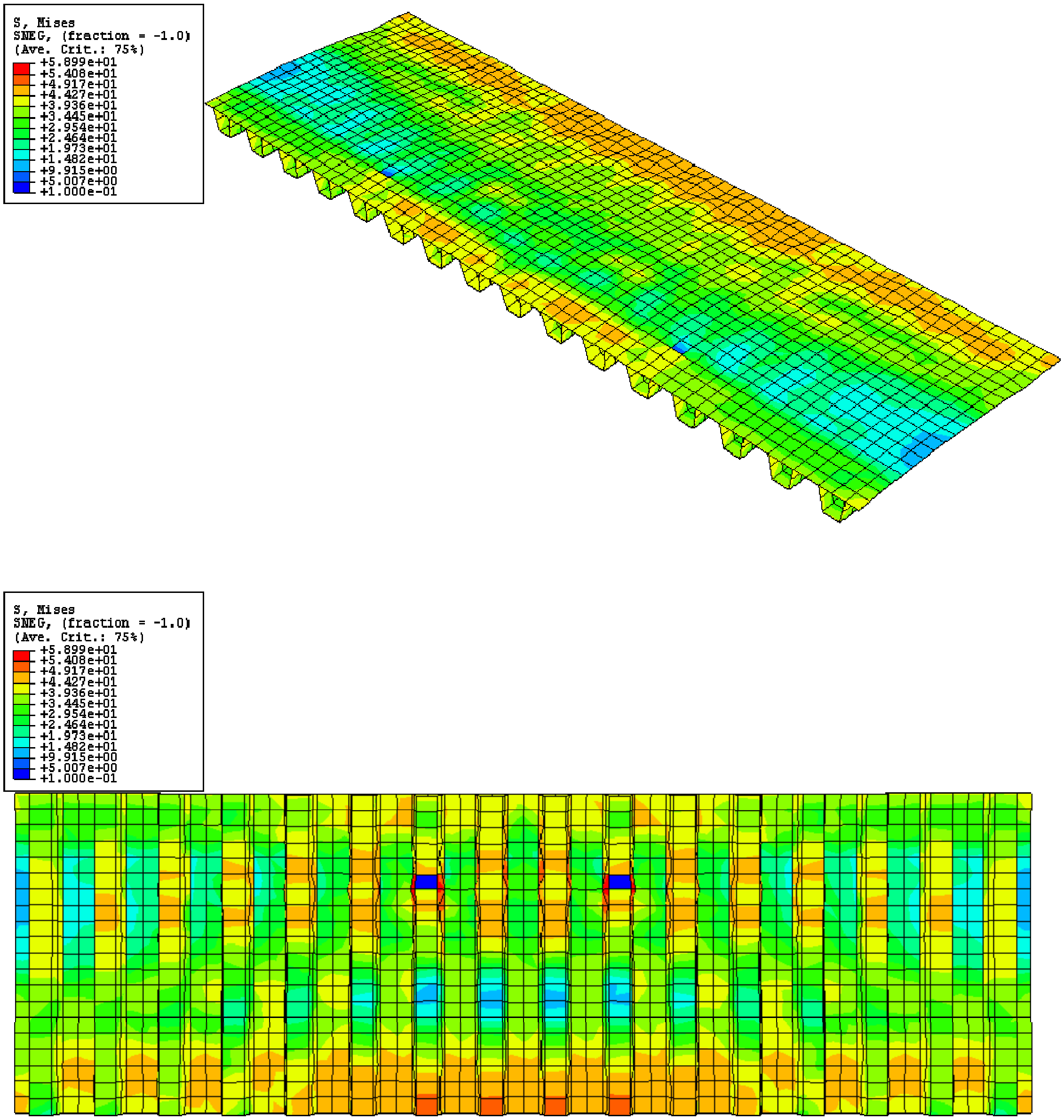

Figure 5-15 Sixteen-Rib Model, RN

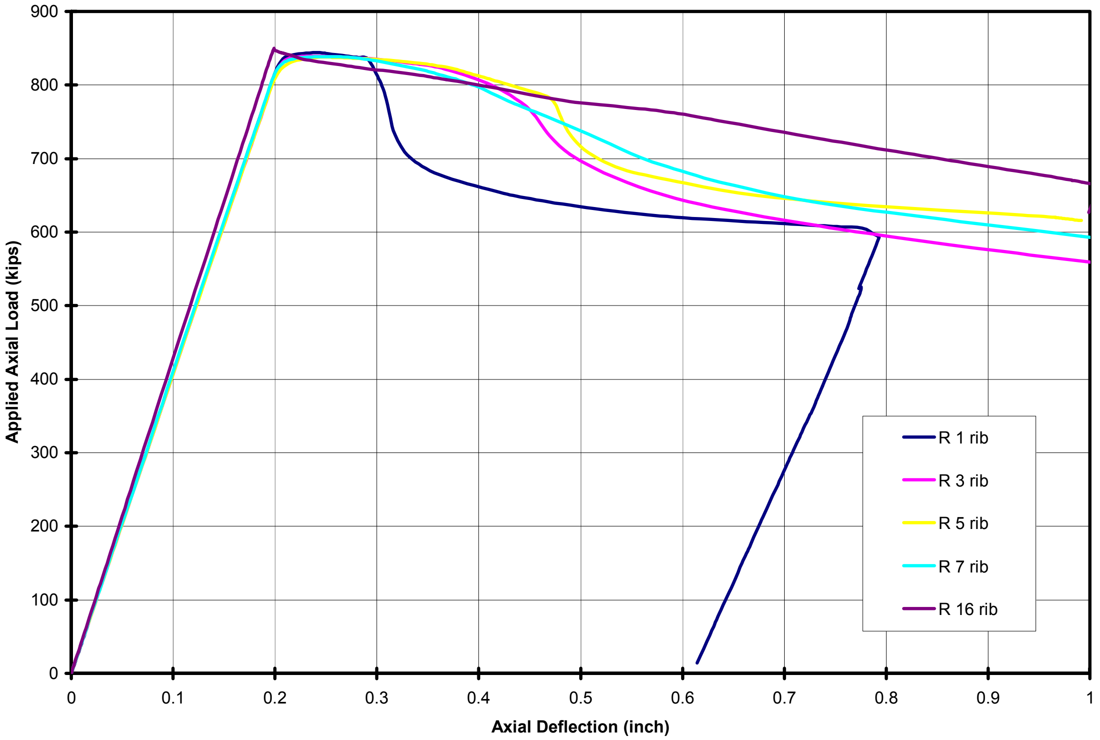

Figure 5-16 Comparison of Different Number of Ribs, Bridge RN

Chapter 6 Summary and Recommendations

6.1 Summary of Results

From the experimental and analytical examination of the behavior and stresses of the model deck panels and components of Bronx-Whitestone Bridge, the following results were obtained.

(1) The wheel loads of trucks affected only one trapezoidal-shaped stiffening rib. This was derived from the results of testing deck panels, ribs in bending and ribs under simultaneous compression and simulated wheel load, as well as from the results of finite element analysis.

(2) The behavior of single-rib and triple-rib specimens under the simulated wheel load and axial loads had similar behavior.

(3) Failure of ribs under compression, and compression with a transverse wheel load, were similar. It was inelastic buckling of the rib walls near the ends of the ribs.

(4) With this failure mode, the ultimate strength of a single-rib specimen and

of the average of triple-rib specimens were essentially the same.

(5) The initial imperfection of component plates had only minor effect on the strength of the ribs.

(6) The ultimate compression strength of ribs could be estimated by finite element analysis, or by the summation of component compressive strength. Component compressive strength could be computed using the classic buckling analysis or by finite element analysis.

(7) Finite element analysis results indicated that the buckling load of the deck panel was very high, being beyond the yielding of the deck. Overall buckling of the deck panel would not be a concern.

(8) The ultimate compressive strength of deck panels could be estimated by the summation of single-rib strength.

6.2 Recommendations

(1) In addition to the current procedure of proportioning orthotropic deck components, the evaluation of deck strength in compression needs to be included in the LRFD design provisions for safety, and for completeness

of the provisions. The method of summation of component part strength is recommended for ultimate strength evaluation.

(2) Buckling of rib components be revisited for the examination of the effects of stress gradient, or non-uniform compressive stresses.

(3) If possible, compression strength testing of adequately small scale orthotropic deck panels be conducted for further verification of the findings from this study.

REFERENCE

1. ABAQUS Standard User's Manual Version 6.51. (2005). Hibbit, Karlsson and Sorensen Inc.
2. American Association of State Highway and Transportation Officials (AASHTO) (2004). *AASHTO LRFD Bridge Design Specifications*, Washington, D.C., USA.
3. American Institute of Steel Construction (AISC) (1963). *Design Manual for Orthotropic Steel Plate Deck Bridges*, New York, USA.
4. Bouwkamp, J.G. and Powell, G.H. (1967). "Structural Behavior of an Orthotropic Steel Deck Bridge," Structures and Materials Research Report No. 67-27, Univ. Calif., Berkeley, Aug.
5. Chen, S.J. and Yang, K.C. (2002). "Inelastic behavior of orthotropic steel deck stiffened by U," Thin-Walled Structures, 40, pp. 537-553.
6. Chen, W.F. and Duan, L. (2000). "Bridge Engineering Handbook, "CRC Press LLC.
7. Connor, R.J. and Fisher, J.W. (2001), "*Results of Field Measurements on the Williamsburg Bridge Orthotropic Deck*," ATLSS Report 01-01.
8. Connor, R.J. and Fisher, J.W. (2004), "*Results of Field Measurements Made on the Prototype Orthotropic Deck on the Bronx-Whitestone Bridge New York City*, *NY,* " ATLSS Report 04-03.
9. De Fries-Suene, A. and Scordelis, A.C. (1964). "Direct Stiffness Solution for Folded Plates," J. Strut. Div. ASCE, Vol. 90, No. ST4, August, pp. 15-47.

10. Dowing, P.J. (1971). “The behavior of orthotropic steel deck bridges,” Developments in bridge design and construction: [proceedings of the International Conference on Developments in Bridge Design and Construction held at the University College, Cardiff, 29 March to 2 April 1971]. Edited by K. C. Rockey, J. L. Bannister and H. R. Evans, International Conference on Developments in Bridge Design and Construction, pp. 557-576.
11. Erzurzmlu, H. and Toprac, A.A. (1970). “The Deck Elements of Ammi System,” Technical Report P550-12, Structures Fatigue Research Lad, Univ. Texas, Austin, March.
12. Faulkner, D. (1975). “A Review of Effective Plating for Use in the Analysis of Steel Plating in Bending and Compression,” Journal of Ship Research, 19(1), pp.1-17.
13. Heins, C. P. and Loony, C.T.G. (1968). “Bridge Analysis Using Orthotropic Plate Theory,” J. Strut. Div. Am. Soc. Civ. Eng., Vol. 93, No. ST2, Feb.
14. Hughes, O.F., Ghosh, B. and Chen, Y. (2004) “Improved prediction of simultaneous local and overall buckling of stiffened panels” Thin-Walled Structures, 42, pp. 827-856.
15. Morice, P.B., Little, G. and Rowe, R.E. (1956). “Design Curves for the Effects of Concentrated Loads on Concrete Bridge Decks,” Publication DB11a, Cement and Concrete Association.
16. Murry, N.W. (1973). “Buckling of Stiffened Panels Loaded Axially and in Bending,” The Structural Engineer, Vol. 51, No. 8, August, pp. 285-301.
17. Ostapenko, A. (1969). “Longitudinal Stiffened Plate under Lateral and Axial

Loads (Ship Bottom Plating)." *Fritz Engineering Laboratory Report No.248.28*, Lehigh University, Bethlehem, PA, U.S.A.

18. Ostapenko, A. (1969). "Longitudinally stiffened plate panels under lateral and axial loads (ship bottom plating)." Fritz Laboratory Report No. 248.28, Lehigh University, August.
19. Paik, J.K., Thayamballi, A.K. (2003). "Ultimate limit state design of steel plated structures," John Wiley & Sons.
20. Rowe, R.E., (1962). "Concrete Bridge Design," C. R. Books, London.
21. Sheikh, I.A., Elwi, A.E., Grondin, G.Y. (2003). "Stiffened Steel Plates Under Combined Compression and Bending," Journal of Constructional Steel Research Vol. 59, pp. 911-930.
22. Troitsky, M.S. (1987). "Orthotropic Bridges - Theory and Design," 2nd ed., James F. Lincoln Arc Welding Foundation, Cleveland, OH, September.
23. Tsakopoulos, P.T., and Fisher, J.W. (1999). "*Williamsburg Bridge, Replacement Orthotropic Deck, As-Built Full-Scale Fatigue Test*," ATLSS Report 99-02.
24. Tsakopoulos, P.T., and Fisher, J.W. (2002), "*Fatigue Resistance Investigation for the Orthotropic Deck on the Bronx-Whitestone Bridge*," ATLSS Report 02-05.
25. Vlasov, V.Z. (1967). "Thin-Walled Elastic Beams, Israel Program for Scientific Translation," for NSF, Jerusalem, (in English; original Russian edition, 1959).
26. Xanthakos, P.P. (1994). "Theory and Design of Bridges," John Wiley and Sons, Inc.
27. Ye, Q., and Fanjiang, G.N. (2004). "*Analysis and Design of Steel Orthotropic Decks*," IABSE, Shanghai, China, Sep. 2004. 222-223.

APPENDICES

Appendix A: AISC / **AASHTO-LRFD Bridge Design Provisions and BWB Components**

An orthotropic deck is defined in AASHTO-LRFD Bridge Design Specification (2005) as a deck plate stiffened and supported by longitudinal ribs and transverse floor beams. The deck plate thickness, t_d, is specified in Section 9.8.3.7.1 to be not less than 0.5625 inch (14 mm) or 4% of the larger spacing of rib webs, that is 4%×13 inch (330 mm) = 0.52 inch (13 mm) for the BWB orthotropic steel deck. The thickness, t_r, of closed ribs shall not be less than 0.1875 inch (6 mm).

Section 9.8.3.7.2 specifies that the dimension of a rib shall satisfy.

$$\frac{t_r \cdot a^3}{t_{d,eff}^3 \cdot h'} < 400 \tag{A-1}$$

where

a = larger of the spacing of the rib,

h' = length of the inclined portion of the rib, and

$t_{d,eff}$ = effective thickness of the deck plate, considered to be the deck plate thickness.

The dimensions and the 5/8 inch (16 mm) and 5/16 inch (8 mm) plates of the BWB satisfy the requirements of the specifications. In Section 9.8.3.6.2 it is started that effects of compressive instability of the orthotropic deck shall be investigated at strength limit states. However, there are no specific equations or guidelines for calculating the buckling strength of the stiffened panel. If stability does no control, the resistance of an orthotropic plate deck shall be based on the attainment of yield strength at any point in the cross section. Section 6.14.3.3.3 describes those longitudinal ribs, including the effective width of the deck plate as a part of the rib, shall be designed as individual columns simply supported at transverse beams. It also states that the elastic stability of ribs under combined loading may be evaluated by formulas in Appendix II of Design Manual for Orthotropic Steel Plate Deck Bridges (Wolchuk, AISC 1963).

Appendix II states that the floor beams of orthotropic steel bridge decks of usual dimensions are usually sufficiently rigid to act as transverse stiffeners of the deck. The deck panel will buckle as an edge-loaded plate with simply supported edges between the floor beams. There are approximate formulas in Section 3.3.2 (AISC 1963) for determining the effective width of girder plate associated with one rib for the calculation of flexural rigidity. The effective width is tabulated to be the spacing of ribs due to dead loads in Section 4.6.2.6.4 of AASHTO LRFD Bridge Design Specification (2005). However, no rule can be found for determining the effective width of a strut under uniform compression in either of these two sets of specifications.

Local buckling of rib plate

Elastic buckling stress

The elastic buckling stress, f_i, for a plate with different loading and boundary conditions can be expressed as:

$$f_i = k\frac{\pi^2 E}{12(1-\nu^2)}\left(\frac{t}{h}\right)^2 \qquad \text{(A-2)}$$

where

ν = Poisson’s ratio (0.3),

h = plate width,

t = plate thickness, and

k = constant, depending on loading case and edge conditions. Values of k for long plates are listed in Table A-1.

Inelastic buckling stress

When the buckling stress exceeds the proportional limit of the material, the inelastic buckling stress, f_{cr}, is given by introducing the tangent modulus (Bleich 1952),

$$f_{cr} = k\frac{\pi^2 E\sqrt{\tau}}{12(1-\nu^2)}\left(\frac{t}{h}\right)^2 = f_i\sqrt{\tau} \qquad \text{(A-3)}$$

where

$$\tau = \frac{E_T}{E}$$

E_T = tangent modulus,

The value τ may be approximated with sufficient accuracy by the flowing equation:

$$\tau = \frac{(f_y - f_{cr})f_{cr}}{(f_y - f_p)f_p} \qquad \text{(A-4)}$$

Introducing Equation (A-4) into Equation (A-3), the following relationship is obtained:

$$\frac{f_{cr}}{f_p} = \frac{1}{1 + \frac{f_p}{f_y}(1 - \frac{f_p}{f_y})(\frac{f_y}{f_i})^2} \tag{A-5}$$

For a steel plate, an average values of $\frac{f_p}{f_y} = 0.75$ may be used, resulting in

$$\frac{f_{cr}}{f_y} = \frac{1}{1 + 0.1875(\frac{f_y}{f_i})^2} \tag{A-6}$$

Overall buckling of rib

Elastic buckling stress

The Euler's buckling formula provides the buckling stress of a rib column,

$$f_i = \frac{\pi^2 E}{(\frac{s}{r})^2} \tag{A-7}$$

where

f_i = elastic buckling stress,

E = modulus of elasticity,

s = span between floor beams, and

r = radius of gyration about the axis of buckling.

Inelastic buckling stress

When the buckling stress exceeds the proportional limit of the material, the inelastic buckling stress, f_{cr}, is given by introducing the tangent modulus (Bleich 1952),

$$f_{cr} = f_i \tau \tag{A-8}$$

where $\tau = \dfrac{E_T}{E}$

with Bleich's approximation for τ as given before.

$$\tau = \frac{(f_y - f_{cr}) f_{cr}}{(f_y - f_p) f_p} \tag{A-9}$$

From these equations,

$$\frac{f_{cr}}{f_p} = 1 - \frac{f_p}{f_y}(1 - \frac{f_p}{f_y})(\frac{f_y}{f_i}) \tag{A-10}$$

Using the value $\dfrac{f_p}{f_y} = 0.75$ as before, the inelastic buckling stress, f_{cr}, can be obtained as

$$\frac{f_{cr}}{f_y} = 1 - 0.1875(\frac{f_y}{f_i}) \tag{A-11}$$

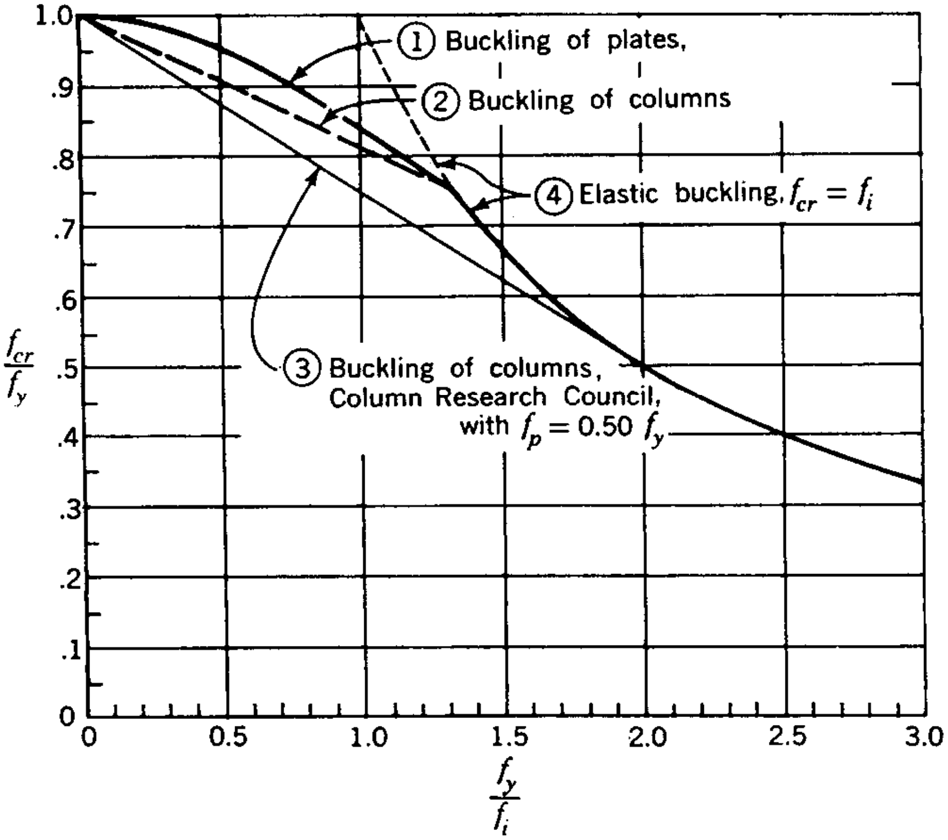

Figure A-1 Buckling curves for plates and columns

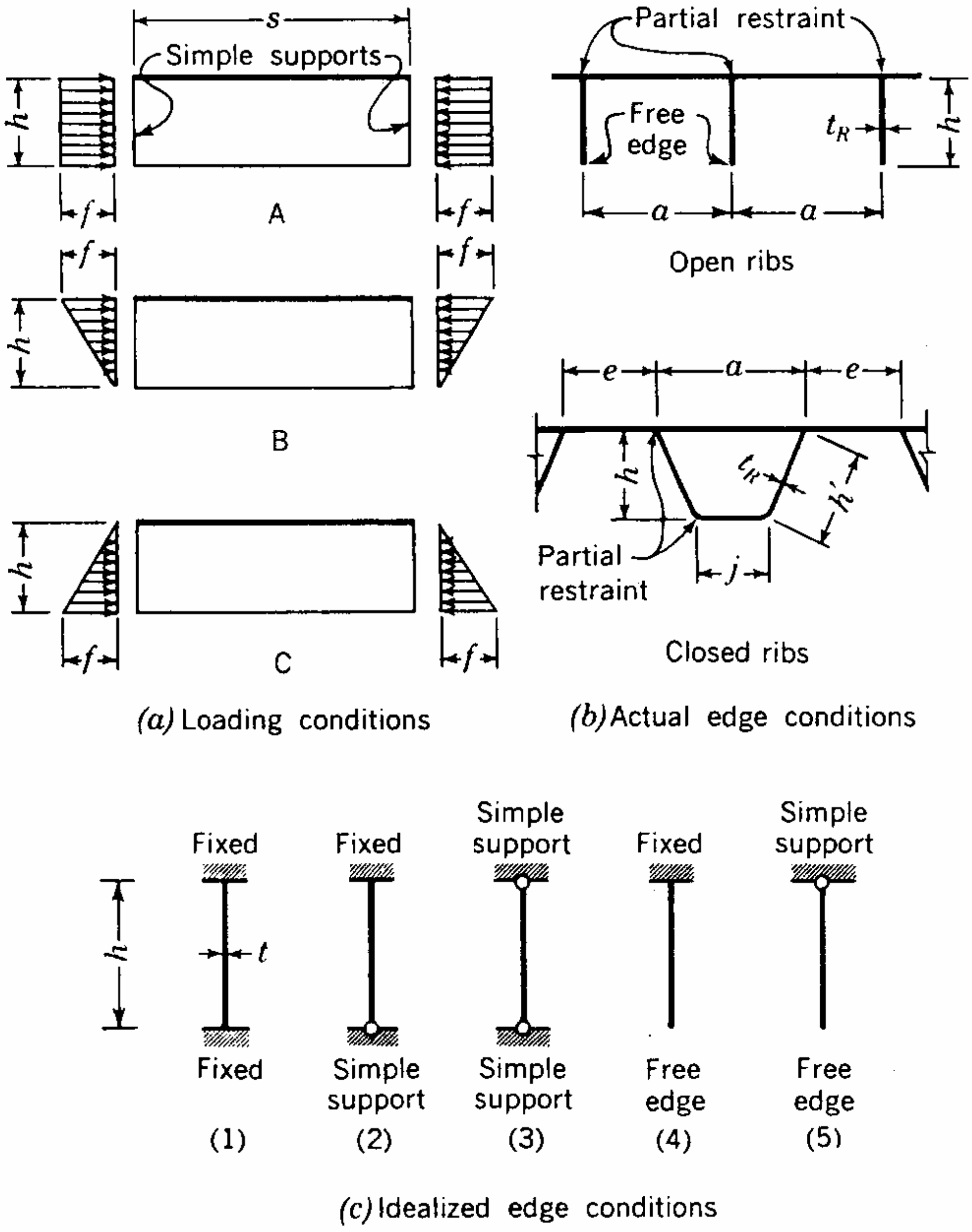

Figure A-2 Loading and Edge Conditions

Table A-1 Values of *k* in equation for loading and edge conditions

Loading	**Edge Conditions**				
	(1)	**(2)**	**(3)**	**(4)**	**(5)**
A	6.97	5.40	4.00	1.28	0.43
B	13.56	12.16	7.81	6.26	1.71
C	13.56	9.89	7.81	1.64	0.57

The prototype model for Bronx-Whitestone Bridge and dimensions are shown in Figure 1-2, and the elevation view is shown in Figure 1-3. There are fourteen trapezoidal shaped stiffeners (ribs). For the convenience of analysis, it was assumed that the deck panel was under uniform compression. In the checking of local buckling strength of the closed ribs, the edges of the rib walls were assumed fixed at the deck plate and simply supported at the bottom (edge condition (2)). This determined that $k = 5.4$ for the uniform loading condition. The elastic local buckling stresses, f_i, was calculated from Equation A-2 to be 69.8 ksi (482 MPa). If the rib walls were assumed simply supported on the both edges (edge condition (3)), $k = 4.0$ for the uniform loading condition. The elastic local buckling stresses, f_i, are calculated to be 51.7 ksi (357 MPa). The inelastic local buckling stresses, f_{cr}, of the rib walls were 58.9 ksi (406 MPa) and 52.1 ksi (359.5 MPa), respectively.

The bottom of ribs was assumed simply supported on both edges (edge condition (3)), with k = 4.0 for the uniform loading condition. The elastic local buckling stress, f_i, was calculated to be 409.5 ksi (2826 MPa). The corresponding inelastic local buckling stress was 69.6 ksi (480 MPa).

The "overhanging" parts of deck plates were assumed fixed at both edges (edge condition (1)), with k = 6.97 for the uniform loading condition. The elastic local buckling stress, f_i, was calculated to be 422.26 ksi (2916 MPa). If both edges of these segments of the deck plates were assumed simply supported (edge condition (3)), k = 4.0 for the uniform loading condition. The elastic local buckling stress, f_i, was calculated to be 242.33 ksi (1672 MPa). The corresponding inelastic local buckling stress was 49.6 ksi (342 MPa).

For overall buckling of the rib columns with a uniform yield stress of 50.0 ksi (345 MPa), the calculated elastic buckling stress was 339 ksi (2339 MPa); the inelastic buckling stress was 48.6 ksi (335 MPa).

Buckling Strength Summary

Component Plates

Table A-2 Elastic Buckling Stress of Components

	f_y	**B.C.**	k	f_{cr}
Deck plate	50	Fixed-Fixed	6.97	422.26
		S.S.-S.S.	4.00	242.33
Rib wall	70	Fixed-S.S.	5.40	69.80
		S.S.-S.S.	4.00	51.70
Rib bottom	70	S.S.-S.S.	4.00	409.50

Table A-3 Inelastic Buckling Stress of Components

	f_y	**B.C.**	k	f_{cr}
Deck plate	50	Fixed-Fixed	6.97	49.87
		S.S.-S.S.	4.00	49.60
Rib wall	70	Fixed-S.S.	5.40	58.9
		S.S.-S.S.	4.00	52.1
Rib bottom	70	S.S.-S.S.	4.00	69.6

Rib Column

Elastic buckling stress

f_{cr} = 339 ksi P_{cr} = 9017 kips

Inelastic buckling stress

Table A-4 Inelastic Buckling Stress of Rib

f_y	f_{cr}
50.00 (deck plate)	48.6
57.64 (weighted)	55.8

Appendix B: **BWB Column Specimen Component Buckling Stress**

Find critical load of deck plate, $P_{d,cr}$, and the critical load of the rib plate, $P_{r,cr}$,

Usami and Fukumoto (1982) conducted experimental works and the results combined with AISC Q-factor method were used to evaluate the strength of box columns. In this method, the stress of a locally buckling column is substituting the corresponding stub-column yield stress, $f_{max} = Qf_y$, Q is a strength reduction factor for the material yield stress.

$$Q \equiv \frac{f_{\max}}{f_y} = \frac{0.737}{R} \tag{B-1}$$

$$\frac{P}{P_u} + \frac{P \cdot e}{M_u (1 - \frac{P}{P_E})} = 1.0 \tag{B-2}$$

Equivalent (modified) slenderness ratio

$$\lambda = \frac{L}{r} \frac{1}{\pi} \sqrt{\frac{\sigma_y}{E}} \tag{B-3}$$

Equivalent width-thickness ratio

$$R = \frac{b}{t} \sqrt{\frac{\sigma_y}{E} \frac{12(1-\upsilon^2)}{\pi^2 k}} \tag{B-4}$$

Interaction buckling stress $\sigma_{\max}^{PC}$

$$\frac{\sigma_{\max}^{PC}}{\sigma_y} = \frac{1}{2\lambda_2}\left[1 + Q\lambda^2 + \eta - \sqrt{\left(1 + Q\lambda^2 + \eta\right) - 4Q\lambda^2}\right] \qquad \text{(B-5)}$$

$$\eta = 0.103(\sqrt{Q}\lambda - 0.15) \qquad \text{(B-6)}$$

Table B-1 Buckling Stress of Components

Components	σ_y **(ksi)**	σ_{cr} **(ksi)**	A **(in.^{2})**	**Component strength (kips)**
Deck plate between walls	***50.00***	81.49	8.45	422.50
Deck plate “overhang”	***50.00***	139.95	8.45	422.50
Rib walls	70.00	***47.07***	8.93	420.42
Rib bottom	***70.00***	94.15	1.51	106.04
			27.35	Total 1371.46

Appendix C: BWB Beam-column strength calculation

Find P_y and M_y

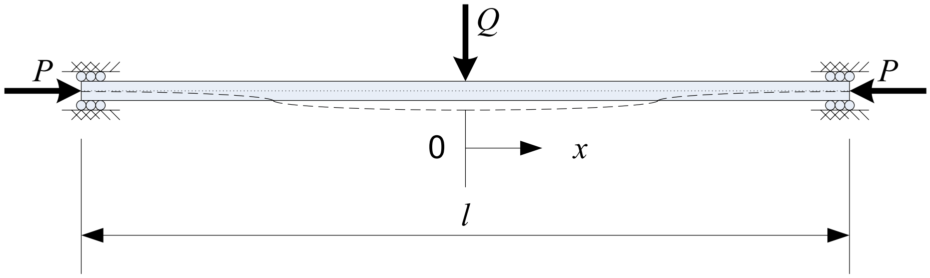

Figure C-1 Beam-Column

Figure C-1 shows a clamped both ends beam-column that is simultaneously acted on by a concentrated load Q at the midspan and axial force P at the ends. Since the shear force $Q/2$ is constant along the member, the governing differential equation for the right half portion, $0 \le x \le l/2$, is given by

$$w''' + k^2 w' = \frac{Q}{2EI} \qquad \text{(C-1)}$$

In which $k = \sqrt{\frac{P}{EI}}$ (C-2)

and the general solution is

$$w = C_1 \cos(kx) + C_2 \sin(kx) + C_3 + \frac{Q}{2k^2 EI} x \qquad \text{(C-3)}$$

$$w' = -kC_1 \sin(kx) + kC_2 \cos(kx) + \frac{Q}{2k^2 EI} \qquad \text{(C-4)}$$

$$w'' = -k^2 C_1 \cos(kx) - k^2 C_2 \sin(kx) \qquad \text{(C-5)}$$

The integration constants C_1, C_2 and C_3 can be determined from the boundary conditions of the beam-column.

$$w(\frac{l}{2}) = w'(\frac{l}{2}) = w'(0) = 0 \qquad \text{(C-6)}$$

Determine the three integration constants

$$w(\frac{l}{2}) = 0 \qquad C_1 \cos(\frac{kl}{2}) + C_2 \sin(\frac{kl}{2}) + C_3 + \frac{Q}{2k^2 EI}\frac{l}{2} = 0 \qquad \text{(C-7)}$$

$$w'(\frac{l}{2}) = 0 \qquad -kC_1 \sin(\frac{kl}{2}) + kC_2 \cos(\frac{kl}{2}) + \frac{Q}{2k^2 EI} = 0 \qquad \text{(C-8)}$$

$$w'(0) = 0 \qquad -kC_1 \sin(0) + kC_2 \cos(0) + \frac{Q}{2k^2 EI} = 0 \qquad \text{(C-9)}$$

$$kC_2 + \frac{Q}{2k^2 EI} = 0 \qquad \text{(C-10)}$$

$$C_2 = \frac{-Q}{2k^3 EI} \qquad \text{(C-11)}$$

Substitution Eq. (1.11) into Eq. (1.8)

$$C_1 = \frac{Q}{2k^3 EI}\left[\frac{1-\cos(\frac{kl}{2})}{\sin(\frac{kl}{2})}\right] \qquad \text{(C-12)}$$

Substitution Eq. (1.11) and Eq. (1.12) into Eq. (1.7)

$$C_3 = \frac{Q}{2k^3 EI}\left[-\frac{1-\cos(\frac{kl}{2})}{\sin(\frac{kl}{2})} + \sin(\frac{kl}{2}) - \frac{kl}{2}\right] \qquad \text{(C-13)}$$

From which maximum bending moment occurs at the midspan, *x=0*, is calculated as

$$M(0) = -EIw''(0) = EIk^2C_1 = PC_1 \tag{C-14}$$

Since the lateral force Q is a constant value in this study, the elastic limit stress occurs generally on the cross section of the maximum bending moment. From the bending moment diagram, the maximum compression stress falls on the top of deck plate. Thus, the elastic limit state for a beam-column is given by

$$\frac{M_{\max}}{S} + \frac{P}{A} = \sigma_y \tag{C-15}$$

This can be written as

$$\frac{M_y}{S_t} + \frac{P_y}{A} = \sigma_y \tag{C-16}$$

$$\frac{P_y C_1}{S_t} + \frac{P_y}{A} = \sigma_y \tag{C-17}$$

Where σ_y, S_t, A are known, and C_1 is a function of P_y

$\sigma_y = 50\ ksi$

$S_{t,} = 138\ in.^3$

$A = 27.35\ in.^2$

$l = 216\ in.$

$Q = 40\ kips$

$E = 29000\ \text{ksi}$

$I = 466.73\ \text{in.}^4$

$\underline{P_y = 1134\ \text{kips}}$

$\underline{M_y = 1177.49\ \text{kips-in.}}$